Investigations of atmospheric condensation induced by femtosecond laser filaments

Im Fachbereich Physik der Freien Universität Berlin
eingereichte Dissertation von

Philipp Rohwetter

April 2011

1. Gutachter: Prof. Dr. Ludger Wöste, Freie Universität Berlin
2. Gutachter: Prof. Dr. Jean-Pierre Wolf, Université de Genève
Datum der Disputation: 15. Juni 2011

Contents

Abstract

The aim of the present work is to gain an understanding of femtosecond laser-induced atmospheric condensation of particles, and to investigate its potential applicability for laser remote sensing of the atmosphere. The primary focus is on terawatt laser pulses undergoing multiple filamentation, and on naturally occuring atmospheric conditions.

The investigations are motivated by previous observations, showing the ability of high intensity femtosecond laser radiation to cause the condensation of fog droplets out of the gas phase, under conditions of high water vapour supersaturation. In the present work similar is shown to hold for multiply filamenting terawatt laser pulses. Furthermore, their ability to cause condensation of particles is observed to remain, to some extent, even under atmospheric conditions of water vapour subsaturation.

An initial attempt to use filament-induced condensation as a tool for atmospheric remote sensing shows its basic feasibility, but it also exposes the technical and fundamental challenges that remain to be overcome.

Using auxiliary results from laboratory experiments conducted by project partners a model for filament-induced condensation is developed, which makes predictions reasonably well in accord with experimental observations.

Kurzfassung

Die vorliegende Arbeit hat zum Ziel, die durch intensive Femtosekunden-Laserpulse induzierten Kondensation von Partikeln aus der Gasphase zu verstehen, und deren Anwendbarkeit im Rahmen der lasergestützten Atmosphärenfernerkundung zu erproben. Dabei liegt das primäre Interesse auf Laserpulsen im Leistungsbereich von Terawatt, die während der Ausbreitung mehrfach filamentieren und auf natürlich in der unteren Atmosphäre auftretenden Bedingungen.

Die Untersuchungen sind motiviert durch bekannte frühere Beobachtungen, durch die die grundsätzliche Fähighkeit hochintensiver Femtosekunden-Laserstrahlung nachgewiesen werden konnte, unter mit Wasserdampf übersättigten Bedingungen die Kondensation von Nebeltröpfchen aus der Gasphase herbeizuführen. Entsprechendes kann im Rahmen dieser Arbeit auch für den Fall der mehrfach filamentierenden Terawatt-Laserpulse gezeigt werden. Darüberhinaus wird beobachtet, dass diese Fähigkeit in gewissem Rahmen auch in Wasserdampf-untersättigter Atmosphäre erhalten bleibt.

Ein erster Versuch, Filament-induzierte Kondensation für die laserbasierte Atmosphärenfernerkundung nutzbar zu machen, zeigt die prinzipielle Machbarkeit, aber auch, welche technischen und fundamentalen Probleme noch zu lösen bleiben.

Unter Zuhilfenahme zusätzlicher Ergebnisse aus Labormessungen von Projektpartnern wird ein Modell für die Filament-induzierte atmosphärische Kondensation entwickelt, dessen Vorhersagen mit den experimentellen Resultaten in Einklang sind.

1. Introduction

The work presented here relies on the peculiar 'self-guided' mode of propagation of optical 'filaments'. These are intense hotspots in the laser beam profile which spontaneously form and stabilize in sufficiently powerful laser beams propagating through transparent dielectric media, including air.

In the case of femtosecond pulsed laser light, a filament represents a large amount of optical energy propagating as a small compact object over longer distances. The relative stability of filaments results from the complex spatio-temporal interplay of nonlinear interactions of light with the optical medium. The nonlinear process actually initiating their formation is the self-focussing of light caused by the intensity dependence of the refractive index of the transparent dielectric which becomes apparent at high optical electric field strengths.

Phenomena related to filamentation of laser beams were observed only a few years after the first working laser had been demonstrated. When laser amplifiers had reached peak powers in excess of about 100 kW, local optical damage in optical elements appeared along extended narrow tracks, even in beams with initially homogeneous intensity profile. Their occurence was interpreted as resulting from "self-trapping" of high power beams caused by a self-induced waveguide (Chiao et al., 1964, 1965). Soon after these first observations J. H. Marburger developed the theory of nonlinear self-focussing in dielectrics (Wagner et al., 1968).

For a long time self-focussing occuring in laser media and other optical components in laser amplifiers imposed a strong limitation on the optical powers achievable by direct amplification, as spontaneously forming self-trapped hotspots easily exceed damage thresholds of optical materials and surfaces, and lead to their destruction. However, the invention of the chirped pulse amplification (CPA) scheme by Strickland and Mourou (Strickland and Mourou, 1985) opened up a new regime of laser pulse peak power by enabling the generation of increasingly shorter pulses, down to few tens of femtoseconds duration, without inducing nonlinear processes inside the amplifier chain.

It was then only a question of time until optical peak powers reached high enough to induce optical self-action already in dilute dielectric materials – such as air. The formation of self-focusing filaments in air at normal atmospheric pressure was reported for the first time by Braun et al. (Braun et al., 1995), initiating the research field of atmospheric nonlinear propagation of high power laser light, and its applications.

In 1999, the Teramobile project was launched as a collaboration of the German DFG and the French CNRS, as a joint effort dedicated to the investigation of self-guided propagation of very intense, femtosecond laser light over long distances in the atmosphere, and in particular of its possible applications for atmospheric remote sensing. In early 2001 the mobile terawatt laser laboratory of the same name was put into service, then the only facility of its kind worldwide. A detailed description of

the system built into a standard freight container can be found elsewhere (Rodriguez, 2004).

In terms of atmospheric sensing with light, the activities of the Teramobile project fairly straightforwardly aim on extending proven concepts by the new possibilities offered by an advanced light source. As an optical analogue of the RADAR technique the LIDAR principle (**LI**ght **D**etection **A**nd **R**anging) consists in sending out a burst of light radiation, and detecting the light scattered or reflected by objects in the path of the outgoing beam. Techniques using light for atmospheric sounding were developed as early as in the 1930s. The acronym was coined already in 1953 (Middleton and Spilhaus, 1953), long before LIDAR was a mainstream tool for atmospheric research.

The first implementations of atmospheric LIDAR used thermal light sources, such as arc flashlamps, with strong limitations of spectral power density and pulse duration. Since pulsed lasers were available, higher sensitivity and range resolution boosted the utility of the technique, and a number of variants were derived.

Today LIDAR is routinely used for gaining information about the atmosphere, such as the determination of cloud base height or the measurement of aerosol profiles or the remote detection of environmentally important trace gases like ozone.

Past achievements of the Teramobile project in the field of atmospheric and general remote sensing are summarized for example in (Kasparian and Wolf, 2008).

About ten years ago, during the startup phase of the Teramobile project, a series of laboratory experiments was conducted by H. Wille and coworkers in L. Wöste's group at the Free University of Berlin (Wille et al., 2001). Motivated by the known ability of femtosecond laser filaments to partially ionize the air through which they propagate, they suspected that laser-generated ions could induce water condensation just like the ions in a Wilson-type cloud chamber.

Because of lack of pulse energy available from their laboratory laser amplifier, they had to simulate the conditions in a filament by focussing lower energy pulses.

Their results indeed showed that a focussed beam of 50 fs short laser pulses, each containing an energy of about 1 mJ, emitted at a repetition rate of 1 kHz, can induce the formation of fog droplets in air containing air supersaturated with water vapour. Their conclusion was that their working hypothesis was corroborated, and that the ions created by the action of the focussed laser served to induce condensation by their electrostatic charge. They also proposed that filament-induced condensation could be used as the foundation for a new method of atmospheric remote sensing (Rodriguez, 2004), actively probing the tendency of the atmosphere to spontaneous condensation of water vapour and precipitation.

In the following years the Teramobile project went ahead and many new and exciting results were obtained – however, the issue of femtosecond laser-induced atmospheric condensation was pending, including the open question of transferability to genuine filaments, the need for a more thorough understanding of the underlying mechanism, as well as the investigation of the potential applicability to atmospheric remote sensing.

At last these were picked up again, and this text reports on the current status of the ongoing efforts. It consists of three main parts. In Chapters 2 and 3 an overview over the nonlinear propagation of intense laser light, and the fundamentals of the remote sensing of atmospheric aerosol, respectively, is

given. Chapter 4 provides a review of the physics of atmospheric condensation and of the possible pathways by which irradiated laser light (in particular, laser filaments) may influence or trigger it. Some focus is put on connecting knowledge from existing literature, which is partially scattered.

Finally, in Chapter 5 experimental results obtained with the Teramobile laser are reported and interpreted. A part of the interpretation is based on a proposed model for filament-induced condensation presented in the same chapter.

2. Laser filamentation in the atmosphere

This chapter very briefly summarizes the main phenomena occuring when a strong femtosecond laser pulse propagates in the atmosphere, the mechanisms leading to filamentation, as well as the main properties of atmospheric laser filaments Some practical aspects of controlling some of their properties are discussed, having in mind the application of filaments in atmospheric remote sensing.

In the following, the laser radiation is generally assumed to be pulsed, with pulse durations shorter than $\tau_p \approx 1\,\mathrm{ps}$. Laser pulses are assumed to be spectrally centered around $\lambda_0 = 800\,\mathrm{nm}$, which is typical for laser amplifiers based on titanium:sapphire (Ti:Sa) as the gain medium. In particular the amplifier of the Teramobile system used in the experiments described in later sections belongs to this class of systems.

Necessarily this short overview can only touch the surface of more than 15 years of research on filamentation of high power laser light in air, and many aspects are omitted. It is also important to note that the discussion about how exactly filamentation in air works is very active (Béjot et al., 2010; Kolesik et al., 2010), fed by unexpected observations waiting for explanation (Diels et al., 2010; Walter et al., 2010).

Comprehensive reviews of the present experimental and theoretical knowledge about filamentation can be found for example in (Bergé et al., 2007), (Couairon and Mysyrowicz, 2007), or (Kandidov et al., 2009). A very comprehensive historical overview is provided in (Boyd et al., 2009).

2.1. Filamentation in air: important phenomena and properties

Experimental evidence shows that to induce the formation of a filament a certain **critical power** propagating in the beam the must be overcome. In the case of air as the medium of propagation, and femtosecond near infrared laser pulses, this critical power amounts to a few GW.

It can be further observed that, once a filament has formed inside the beam cross section, increasing the power does not increase the energy contained in the single filament beyond limit, but above some threshold an additional filament is formed. Each filament and its associated self-focussing 'cell', its surrounding portion of the beam cross section, form a quasi-stable unit, which can contain up to a certain amount of power. Excess of power leads to splitting of the cell and restoration of stability. This type of beam breakup and spontaneous formation of new filaments is the signature of the regime of **multiple filamentation**.

Over a wide range of laser powers a linear scaling of the number of filaments with the input beam power can be observed. On average one filament is formed per about 5 critical powers, in air and for the above assumed laser parameters. This linear scaling of filament number with the input *power* was

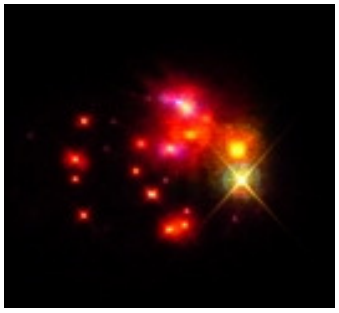

Figure 2.1.: Photograph of a multiply filamenting near-infrared terawatt laser pulse projected on a screen. Filaments show up as colorful spots of visible supercontinuum radiation (see text).

theoretically predicted by Campillo et al. already in 1973 (Campillo, 1973). Only recently experiments using a 100 TW class laser system showed that at high input intensites ($I > 3 \times 10^{11}\,\mathrm{W/cm^2}$) this scaling no longer holds, but the number of filaments per unit area of the beam cross section saturates around $n_{\mathrm{fil}} \approx 10\,\mathrm{cm^{-2}}$.

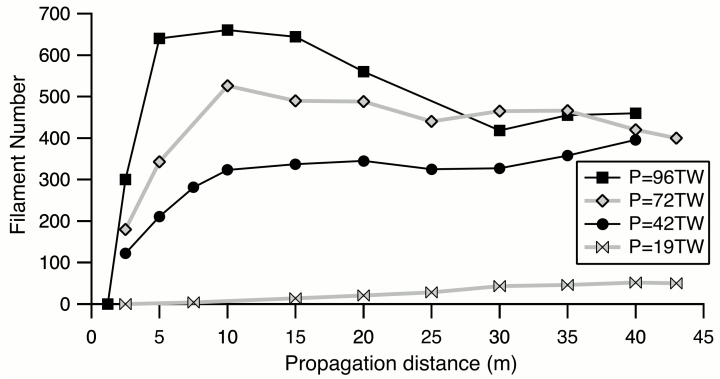

Figure 2.2.: Saturation of the transverse filament number density in very highly supercritical multiple filamentation: number of filaments contained in the 10 cm diameter beam cross section plotted vs. distance of free propagation in ambient air, for different powers of 30 fs long pulses at $\lambda_0 = 800\,\mathrm{nm}$. Clearly the overall number saturates around 400. At the highest input power an initial surge of filament number decays by merging of surplus filaments. Fig. 2 from (Henin et al., 2010).

As far as the 'classical' regime of multiple filamentation is concerned, filaments in air produced from short ($\tau_{\mathrm{p}} < 100\,\mathrm{fs}$) laser pulses typically contain an energy on the order of 1 mJ each, and have diameters on the order of 100 μm (Couairon and Mysyrowicz, 2007), resulting in average fluences of around $10^{12}\,\mathrm{W/cm^2}$. Peak fluences attained in typical filaments in air at normal pressure cannot be measured directly, but are generally agreed to lie between $10^{13}\,\mathrm{W/cm^2}$ and $10^{14}\,\mathrm{W/cm^2}$ (Couairon and Mysyrowicz, 2007).

This phenomenon was termed **intensity clamping** (Becker et al., 2001) and it is a signature of this regime of the self-guided mode of propagation.

First experiments involving long distance atmospheric propagation of terawatt near-infrared laser pulses in air (Nibbering et al., 1996; Wöste et al., 1997) showed that a phenomenon known from filamentation in dense solid media was efficient also in air: spectral broadening or **supercontinuum generation**, mainly caused by processes based on the third-order Kerr nonlinearity of the medium

(see below). In Fig. 2.3 an image of the visible part of the supercontinuum resulting from about 100 m of propagation of slightly prefocussed terawatt laser pulses of initial duration $\tau_p \approx 100$ fs, and a central wavelength of $\lambda_0 = 800$ nm through air is shown. Panel b) of the same figure depicts a typical spectrum of 800 nm-centered supercontinuum, extending from the ultraviolet up to 4 μm wavelength.

Because of the prefocussing and the long propagation path, in Fig. 2.3 a) the emissions from individual filaments are superposed and blurred, in contrary to Fig. 2.1, where individual sources can be identified.

The supercontinuum light emitted by a filament is coherent, in particular meaning that the phase relationship between any two spectral components varies smoothly with their frequency separation. The respective phase relationships are even reproducible on a shot-to shot basis, provided that the laser parameters and conditions of filamentation remain stable enough in time. This for example enables simple generation of shortest optical pulses (Stibenz et al., 2006), and the full characterization of amplitude and spectral phase of the supercontinuum (Schmidt et al., 2008), opening the path to broadband pulse shaping applications.

Perhaps more strikingly, the supercontinuum radiation generated in *different* filaments copropagating within the same laser pulse is coherent as well, and under appropriate conditions interference fringes can be observed (Liu et al., 2004; Nibbering et al., 1996). This is because the processes leading to supercontinuum generation preserve the coherence of the driving electromagnetic field, having a fixed phase relationship for any two points in the beam cross section.

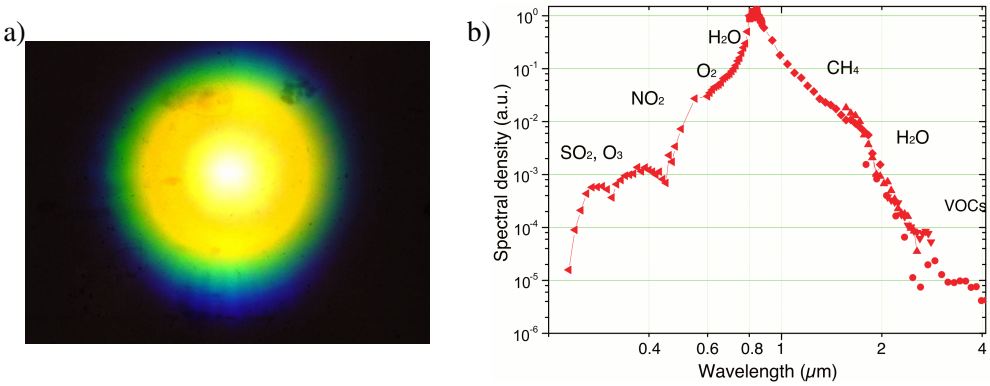

Figure 2.3.: a) Photograph of the visible supercontinuum generated by a high power near-infrared laser pulse propagating in air, projected on a screen; the spectrally dispersed part visible as colorful rings is commonly called "conical emission". b) typical air supercontinuum spectral power density as a function of wavelength for the same type of laser radation; symbols indicate specific absorption bands of environmental trace gases. From (Kasparian and Wolf, 2008).

Supercontinuum generation reflects consequences of nonlinear processes in the high temporal frequency domain. Similar to transverse splitting of the beam profile into filaments, there exists a low-frequency effect resulting in **pulse steepening** and eventual **pulse splitting**. That is, an initially solitary laser pulse splits into two or more sub-pulses during its filamenting propagation (Couairon and Mysyrowicz, 2007).

Another universal property of filaments forming in femtosecond pulses is their dynamical nature: during the lifetime of a filament its diameter, peak intensity, and other properties, do not remain static, but phases of effective **self-focussing and self-defocussing** repeat in **cycles** over propagation distances on the meter scale (Becker et al., 2001). Simulations show a complex three-dimensional redistribution of energy within the filament caused by the dynamical interplay of the various nonlinear processes listed further below.

In the case of multiple filamentation the dynamics become even more complicated. A strong filament distorts its surrounding, potentially giving rise to the nucleation of new filaments (Skupin et al., 2004a). Also already existing, neighbouring filaments mutually interact: they may repel or attract each other, and even merge (Shim et al., 2010).

Multiple filamentation of a laser pulse with an initially smooth transverse profile is governed by **modulational instability**, causing initially small amplitude noise superimposed on the ideally smooth intensity profile to develop into strong modulations, eventually leading to beam break-up.

The growth rate of the different transverse spatial frequency components contained in the intensity noise depends on the transverse wavenumber $k_\perp$ and was shown by Campillo et al. (Campillo, 1973) to be largest for the noise component with

$$k_\perp^{\max} = 2\ \sqrt{\pi\ I_0 / P_{\mathrm{cr,Gauss}}},$$

where $P_{\mathrm{cr,Gauss}}$ is the critical power for a beam with a perfect Gaussian intensity profile. Exponential growth of the dominating noise component leads to the transverse splitting of the beam into filaments with a spacing of $d = 2\pi / {k_\perp}^{\max}$.

It is known since the studies of modulational instability by Campillo that not necessarily the perturbation with the 'optimum' transverse wavenumber finally wins the competition, but it is possible to selectively 'seed' beam break-up by giving certain transverse modulations a "head start" (A.J. Campillo in (Boyd et al., 2009)).

This is the basis of "linear power partitioning" (Roskey et al., 2006) which can be used to manipulate the multifilamentary breakup of a high power laser beam (see later Sec. 2.3).

A well-established filament shows **robustness** even against strong external perturbations.

in the context of multifilamentary beam breakup the strong association of a filament with its surrounding part of the beam cross section and the contained energy became apparent, suggesting to view both as a unit. The "reservoir" or **photon bath** (as it is often termed in the literature) practically is a part of the filament.

This becomes especially apparent in two 'orthogonal' situations tested by experiments. In one case the 100 μm filament core was blocked by a similarly sized water droplet, precisely put in place by a piezoelectric dispenser (Courvoisier et al., 2003). The strong perturbation induced by the droplet was almost without consequence, and the filament quickly self-healed downstream the obstacle. Obviously the co-propagating light outside the filament core was responsible for this stabilization, also corroborated by numerical simulations (Skupin et al., 2004b).

In a complementary experiment a single filament was generated and a diaphragm of about 280 μm ×

1000 μm size was used to transmit the filament core, but to block most of the surrounding radiation (Liu et al., 2005b). After passing the diaphragm the filament was immediately quenched, proving the crucial role of the photon bath.

Other experiments, in which the transmission of filamenting beams through artificial fog or clouds was investigated, showed that mainly the linear extinction due to scattering (see also Sec. 3.1.4) of the photon bath limits the propagation of filaments. Similar was observed for filaments propagating through natural rain, at high altitude (3200 m, 70 % of normal pressure) (Méchain et al., 2005a).

For propagation over long distances in the atmosphere it is important to consider the effect of turbulence-induced refractive index modulations on the propagation of filamenting laser pulses (some further aspects of turbulence in the context of atmospheric remote sensing will be discussed in Sec 3.3, where also the structure parameter C_n^2 of the turbulent medium will be defined).

Experiments investigating the propagation aver distances up to 100 m of femtosecond near-infrared pulses undergoing single filamentation in the presence of moderate turbulence (structure parameters $7 \times 10^{-17}\,\mathrm{m}^{-2/3} < C_n^2 < 2 \times 10^{-15}\,\mathrm{cm}^{-2/3}$) were reported in (Chin et al., 2002), together with consistent numerical simulations of the propagation. Turbulence was shown to have no other effect on the filament than slight shot-to-shot fluctuation of its position on a screen placed at some distance of propagation. The position of the filament fluctuated symmetrically and normally distributed in both orthogonal screen coordinates, resulting in a Rayleigh-distribution with respect to the radial coordinate. Measured peak deviations were as small as about 3 mm from the nominal position after 100 m of propagation.

In laboratory experiments by Salamé et al. (Salamé et al., 2007), very strong turbulence of the refractive index field, far in excess of atmospherically relevant values, was created on a small scale (1.3 m length of the turbulent region). Above a certain threshold filamentation was found to be efficiently quenched. Extrapolating the results to long propagation distances Salamé et al. estimate common atmospheric turbulence to permit filamentation up to the kilometer range.

The length of propagation of an individual filament is difficult to measure unless a single, highly shot-to-shot reproducible filament is generated in a laser beam. Filaments under conditions of turbulent multiple filamentation generally show strong stochastic shot-to-shot variability of the positions of filaments within the laser beam, making it virtually impossible to reproduce exactly the same constellation of filaments in more than one laser shot. In addition to technical issues, in the presence of multiple filamentation the turbulent nature of the process makes it difficult to even define the 'length' of a single filament, at least from an experimental point of view.

femtosecond laser filaments in air are often accompanied by the **formation of a dilute plasma** during phases of propagation when especially high peak intensities are reached in their cores. However, also a non-ionizing mode of filamentation in air has been reported (Méchain et al., 2005b). In the literature, plasma columns left behind by filaments are often termed "plasma strings" or "plasma channels", and sometimes – quite ambiguously – "plasma filaments". To avoid any potential source of confusion, in this text the term *filament* always refers to the self-guided light, and is never used o denote the plasma or any other type of modification of the optical medium *resulting* from a filament.

The electron densities in these plasma columns have been measured by their conductivity (Tzortza-

kis et al., 1999), or interferometric methods (Liu et al., 2005a) or fluorescence imaging techniques, where the decay of singly charged molecular nitrogen ions was used as observable indicating the presence of plasma (see Fig. 2.1). Reported values for the peak electron number concentration

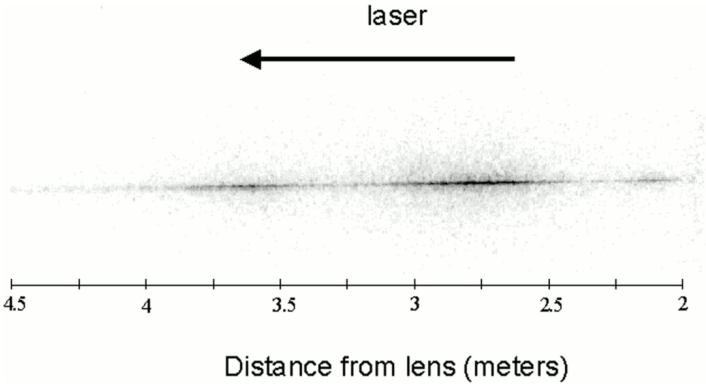

Figure 2.4.: Side-on photograph of the nitrogen fluorescence produced by a single filament formed in a laser pulse ($\lambda_0 = 800\,\mathrm{nm}$, $\tau_\mathrm{p} = 45\,\mathrm{fs}$, $E_\mathrm{p} = 13\,\mathrm{mJ}$) after a $f = 5\,\mathrm{m}$ focussing lens. Fig.2 from (Chin, 2004).

scatter over several orders of magnitude, but they cumulate around $n_e \approx 10^{16}\,\mathrm{cm}^{-3}$. The concentration of ions along the path of a filament shows pronounced signature of the mentioned cyclic focussing-defocussing-refocussing, also nicely visible in Fig. 2.1.

There exists one numerical study of the complex chemistry and thermodynamical in a filament-created air plasma, published by Gordon et al. (Gordon et al., 2003). They considered cases of freely decaying plasma as well as the eolution of the plasma in the presence of a strong external electrostatic field.

In Fig. 2.5 a figure from said publication is shown, indicating the densities of various ionic species as a function of time past the excitation of the freely decaying filament plasma, dominated by singly positively charged molecular oxygen ions. Various excited molecular and atomic species are not depicted in the figure but are included in the simulation. Recombination is the dominant loss mechanism for charged species, but also attachment of electrons to O_2 is an efficient sink for free electrons. The relatively loosely bound attached electrons in O_2^- are the target of attempts to prolong the lifetime of filament generated plasma by sending a trailing detachment/electron heating laser pulse of longer duration (typically nanoseconds) (Méjean et al., 2006).

2.2. Filamentation in air: underlying mechanisms

Filamentation of laser pulses of several tens to several hundreds of femtoseconds duration in transparent dielectric media is based on a few universal mechanisms which govern this mode of propagation of high power light, irrespective of the actual material.

During the past years modeling of filamenting propagation of femtosecond laser light improved along with accumulating experimental data. Over time sort of a ‘standard’ set of involved processes has been identified and more or less agreed upon, together with suitable mathematical formulations and parametrizations. In combination these are able to reproduce many observed features even of long range, multiple filamentation. Last but not least improved numerical methods and increased computer performance have contributed to this achievement.

In the following a present-day model used to describe filamentation in air (Bergé et al., 2007; Couairon and Mysyrowicz, 2007) will be sketched, in order to give a rough idea of what happens when a laser pulse undergoes filamentation.

2.2.1. Qualitative picture of self-guided propagation

Diffraction

A confined beam of light is subject to diffraction. In the special case of a Gaussian transverse intensity profile the beam diffracts self-similarly. A collimated monochromatic Gaussian beam of initial waist w_0 spreads by a factor of $\sqrt{2}$ after propagating a characteristic distance

$$z_{\mathrm{R}} = \frac{w_0^2\, k_0}{2},$$

where $k_0 = 2\pi/\lambda_0$ is the wave vector, and z_{R} is termed the Rayleigh length of the beam.

Consequently, to form a filament, diffraction has to be overcome by a propagating laser pulse.

Diffraction also has a subtle effect on the pulse shape of short (and thus spectrally broad) pulses propagating in narrow beams. Because the angle of diffraction is approximately proportional to the wavelength, spectral components get angularly unmixed. This leads to an increase of the pulse duration at any location within the beam profile, after further propagation. This change of the pulse duration by chromatic diffraction is often called “space-time defocussing”.

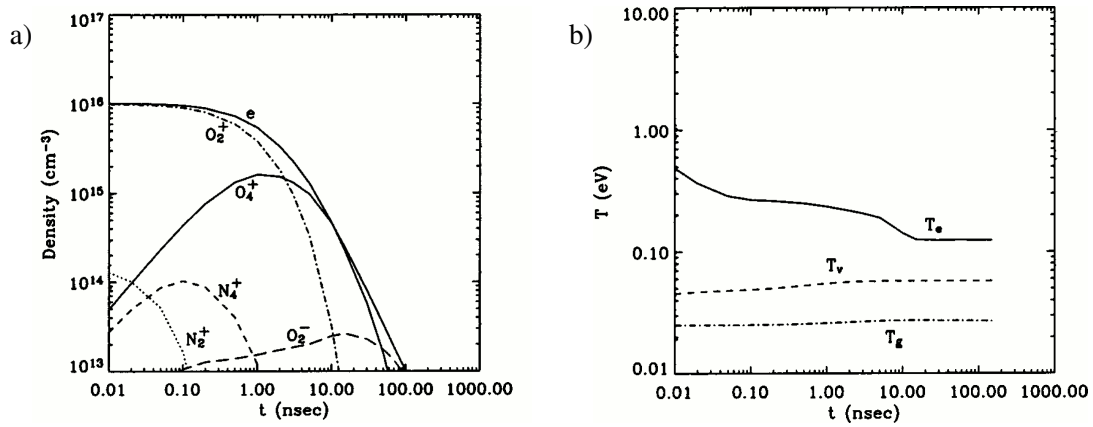

Figure 2.5.: Result of a plasma-chemical simulation by Gordon et al. (Gordon et al., 2003) starting from a plasma composition as assumed in (Tzortzakis et al., 2001), specifically: $[O_2^+] = 1 \times 10^{16}\,\mathrm{cm}^{-3}$, $[N_2^+] = 1.6 \times 10^{14}\,\mathrm{cm}^{-3}$, balanced by equal amount of free electrons; neutral gas assumed to be composed of 80 % N_2 and 20 % O_2; initial electron teperature $T_{\mathrm{el}} = 1\,\mathrm{eV}$, and initial gas temperature $T_{\mathrm{gas}} = 25\,\mathrm{meV}$. Panel a): concentrations of free electrons and the dominating ionic species; Panel b) temperatures of the electron gas (T_{e}), and translational (T_{g}), and (for non-monatomic species) vibrational (T_{v}) temperatures of the filament plasma. Clearly, the heavy species remain cold. Figs. 5 and 6 from (Gordon et al., 2003).

Self-focussing

In linear optics, in an isotropic polarizable medium, where the microscopic constituents have no permanent dipole moments, the macroscopic polarization is directly proportional to the electric field,

$$\mathbf{P} = \varepsilon_0 \, \chi^{(1)} \mathbf{E}.$$

If the response of the medium is instantaneous, this relationship is valid in the time domain, and even in the presence of (not too close) dielectric resonances, that is, chromatic dispersion, a formally similar relationship also holds in the frequency domain.

The resulting linear refractive index of the medium is

$$n_0 = \sqrt{1 + \chi^{(1)}}$$

At high optical field strengths, the optical Kerr effect becomes noticeable, that is, the displacement of bound electrons in the medium is so large that the induced dipole moment is no longer a linear function of the applied field. Then the polarization has to be expressed as a series

$$\mathbf{P} = \varepsilon_0 \, \left(\chi^{(1)} \mathbf{E} + (\chi^{(2)} \mathbf{E}) \mathbf{E} + ((\chi^{(3)} \mathbf{E}) \mathbf{E}) \mathbf{E} + \dots \right).$$

In centrosymmetric media all even order susceptibilities $\chi^{(2n)}$ vanish, and truncating the series expansion after the lowest order nonlinear term yields

$$\mathbf{P} \simeq \varepsilon_0 \, \left(\chi^{(1)} + ((\chi^{(3)} \mathbf{E}) \mathbf{E}) \mathbf{E} \right) \qquad \text{and} \qquad n = \sqrt{1 + \chi^{(1)} + ((\chi^{(3)} \mathbf{E}) \mathbf{E}) \mathbf{E}}.$$

Smallness of the nonlinear term leads to the approximation

$$n(I) \simeq n_0 + n_2 I \qquad .$$

Here the square of the electric field (in $\mathrm{W/m^2}$) is expressed by the intensity $I = \frac{1}{2} n_0 \, \varepsilon_0 \, c |E_0|^2$ of a monochromatic wave with amplitude E_0 (in V/m). For intensity in the customary unit $\mathrm{W/cm^2}$ the nonlinear refractive index n_2 is defined as

$$n_2 = \frac{3 \chi^{(3)}}{4 \varepsilon_0 \, c \, n_0}.$$

Its value for air somewhat depends on the pulse duration (see later sec. 2.2.2) and is about $n_{2,\mathrm{air}}^{800\,\mathrm{nm}} \simeq 3..6 \times 10^{-19}\,\mathrm{cm^2/W}$ for pulses of $\tau_\mathrm{p} \simeq 100..200\,\mathrm{fs}$ duration, centered around $\lambda_0 = 800\,\mathrm{nm}$ (Champeaux et al., 2008).

Because the third order nonlinear susceptibility $\chi^{(3)}$ generally has positive sign, the intensity dependent part of the refractive index, $\Delta n_\mathrm{Kerr} \simeq n_2 I$, expresses a *reduction* of the phase velocity with increasing intensity.

It follows that the self-induced refractive index change of a typical bell-shaped transverse intensity

profile leads to increasing inward curvature of the wavefronts – explaining the observed self-focussing.

Looking for the conditions at which self focussing balances diffraction of a continuous wave beam leads to the identification of a critical power

$$P_{\mathrm{cr}} \simeq \frac{3.72\ \lambda_0^2}{8\,\pi\ n_0\, n2}$$

defining the unstable equilibrium point (Marburger, 1975). A larger power propagating in the beam causes catastrophic transverse collapse due to self-focussing.

Marburger's analysis leads to a semi-empirical expression for the distance z_{c} from the origin at which an initially collimated Gaussian beam with waist ($1/e^2$ half diameter) w_0 and wavenumber $k_0 = \frac{2\pi}{\lambda_0}$, will have collapsed if its power P exceeds the critical power P_{cr}:

$$z_{\mathrm{c}} = \frac{0.184\ w_0^2\, k_0}{\sqrt{\left((P/P_{\mathrm{cr}})^{1/2} - 0.853\right)^2 - 0.0219}}, \tag{2.1}$$

This expression useful for estimating the onset of filamentation of Gaussian beams forming a single filament, but breaks down in the case of multiple filamentation (Couairon and Mysyrowicz, 2007). Its applicability however indicates that filamentation is indeed initiated by self-focussing due to the Kerr-contribution Δn_{K} to the refractive index. Also the existence of a critical power is in accord with experiments.

In reality the collapse is evidently stopped by some negative feedback mechanism. Such a mechanism can be provided by the observed plasma formed during self-guided propagation.

Plasma defocussing

For the moment not asking for the details of plasma generation, it is enough to note that the rate of production is effectively highly nonlinearly dependent on the light intensity.

Once generated, free electrons cause a negative contribution to the refractive index already by their *linear* response to the optical field (Feit and Fleck, 1974) (note however that in short pulse filamentation the quick rate of change of the free electron concentration induces additional more complex spatio-temporal phase distortions (Bergé et al., 2007)).

The resulting plasma-induced shift of the linear refractive index can be expressed as (Feit and Fleck, 1974)

$$\Delta n_{\mathrm{P}} \simeq -\frac{\omega_{\mathrm{p}}}{2\omega},$$

where ω is the frequency of the radiation and $\omega_{\mathrm{p}} = \sqrt{\frac{e^2\,\rho_{\mathrm{e}}}{\varepsilon_0\, m_{\mathrm{e}}}}$ is the plasma resonance (Langmuir-) frequency with ρ_{e} the electron number density, and e and m_{e} electron charge and mass, respectively.

2.2.2. Explicit model for ultrashort pulse propagation in air

Envelope equation

To model nonlinear propagation of laser pulses it is possible to start from the wave equation for the electric field, obtained from Maxwell's equations and assuming a nonmagnetizable, dielectrically polarizable medium, and the presence of free electrons constituting a current density **J** (Couairon and Bergé, 2000),

$$\left(\nabla^2 - \frac{1}{c^2}\frac{\partial^2}{\partial t^2}\right)\mathbf{E} = \frac{1}{c^2\varepsilon_0}\left(\frac{\partial^2}{\partial t^2}\mathbf{P} + \frac{\partial \mathbf{J}}{\partial t}\right) \tag{2.2}$$

where c is the vacuum speed of light and ε_0 is the vacuum permittivity. The macroscopic polarization **P** and the current density **J** depend nonlinearly on the optical electric field **E**. All involved quantities are coupled and change on very different time and length scales. The relevant couplings have to be identified, correctly modeled and implemented, and finally tested by comparison with experiment, a still ongoing process in the case of laser pulse filamentation.

In models of nonlinear laser puse propagation the wave equation is reformulated invoking simplifications permitted by the spatial and temporal shape of the light field $\mathbf{E}(x, y, z, t)$ at $t = 0$.

One of the simplifications is based on the requirement that the dependence of the optical field on the transverse coordinates fits the usual notion of a 'beam'. This means that amplitude and phase of the optical field vary slowly in the transverse direction as compared to the rapid variation along the direction of propagation: $(\frac{\partial^2}{\partial x^2} + \frac{\partial^2}{\partial y^2})\mathbf{E} \ll \frac{\partial^2}{\partial z^2}\mathbf{E}$.

Additionally assuming that the polarization **P** and the current density **J** are dominated by their linear components, with relatively small contributions of the nonlinear terms, allows to describe the electric field as purely transversally polarized (Bergé et al., 2007).

Next the field is described as a carrier wave oscillating with the central frequency ω_0 and propagating with wave vector $k_0 = c/\omega_0 = 2\pi/\lambda_0$, modulated with a complex envelope $U(x, y, z, t)$,

$$E = \sqrt{c_1}(\mathcal{E} + \mathcal{E}^*) \qquad \text{and} \qquad \mathcal{E} = U \exp\{\mathrm{i}\, k_0 z - \mathrm{i}\, \omega\, t\},$$

where $c_1 = \frac{\omega_0 \mu_0}{2\, k_0}$.

The time variable is transformed as $t \to t - z/v_\mathrm{g}$ with $v_\mathrm{g} = \frac{\partial k}{\partial \omega}|_{\omega=\omega_0}$ being the classical group velocity of the pulse.

In (Bergé et al., 2007) it is shown that as a result the wave equation can be cast into the form

$$\left(\mathrm{i}\frac{\partial}{\partial z} + \mathcal{D}\right)U \simeq -\frac{1}{2\, k_0} T^{-1}(\nabla_\perp^2 U) - \frac{\mu_0 \omega_0^2}{2\, k_0\, \sqrt{c_1}}\, T F_{NL}^{env}(U) \tag{2.3}$$

where

$$k(\omega) = k_0 + \left.\frac{\partial^n k}{\partial \omega^n}\right|_{\omega=\omega_0} (\omega - \omega_0) + \mathcal{D},$$

and the operators

$$\mathcal{D} = \sum_{n\geq 2}^{\infty} \frac{1}{n!} \left.\frac{\partial^n k}{\partial \omega^n}\right|_{\omega=\omega_0} \left(\mathrm{i}\frac{\partial}{\partial t}\right)^n \qquad \text{and} \qquad T = \left(1 + \frac{\mathrm{i}}{\omega_0}\frac{\partial}{\partial t}\right)$$

introduced by Brabec and Krausz (Brabec and Krausz, 1997) extend the applicability of the slowly varying envelope approximation down to pulse durations of only a few optical cycles.

Above, $\nabla_\perp^2 = \frac{\partial^2}{\partial x^2} + \frac{\partial^2}{\partial y^2}$, and the containing term in first order describes linear diffraction.

The operator $\mathcal{D}$, describing chromatic dispersion, is practically truncated at some order. Its leading term describes the group velocity dispersion (GVD) which has practical use in applications where filamentation is to be delayed to some propagated distance. Its sign is positive in normally dispersive media, and it leads to entirely linear temporal spreading of an initially transform limited, broadband femtosecond laser pulse. Precompensating GVD by applying a so called negative "chirp", a negative quadratic spectral phase, can be used to let an initially linearly propagating pulse become recompressed at some distance where nonlinear effects set in due to the restored high power.

Any nonlinear source terms appearing in the original wave equation are contained in $F_{NL}^{env}(U)$ (in correspondingly transformed form). The corresponding term vanishes in the case of a linearly propagating low power, short laser pulse, and Eq. 2.3 then just describes spatial and temporal broadening of the optical wave packet due to dispersion and diffraction.

If the temporal and spectral properties of the laser pulse undergoing filamentation are not so much of interest, but rather the transverse structure of the filamenting beam, Eq. 2.3 is often further simplified (Kandidov et al., 2009) by replacing $T \to 1$, resulting in

$$\mathrm{i}\frac{\partial}{\partial z} U \simeq -\frac{1}{2\,k_0}(\nabla_\perp^2 U) - \mathcal{D}\; U - \frac{\mu_0 \omega_0^2}{2\,k_0\,\sqrt{c_1}}\; F_{NL}^{env}(U) \tag{2.4}$$

Kerr response of air

In the current 'mainstream' models of filamentation in air the highest order term of the nonlinear dielectric response considered is the quintic nonlinear polarization, meaning that the series expansion of the polarization is truncated after the fifth order term, $\mathbf{P}^{(5)}$. The latter is considered to be necessary to recover experimental observations with sufficient fidelity, especially allowing for the observed merging of two filaments (Champeaux et al., 2008).

There is an ongoing discussion (Béjot et al., 2010; Kolesik et al., 2010) if especially filamentation of short, near-infrared laser pulses in air involves – and even relies on – higher order terms of the polarizability.

Justified by the centrosymmetry of gaseous media, the susceptibilities $\chi^{(3)}$ and $\chi^{(5)}$ corresponding to cubic and quintic Kerr nonlinearities are treated as scalars. Peculiar to filamentation air (often treated as 80:20 mixture of diatomic gases N_2 and O_2), inclusion of a delayed nonlinear dielectric response has turned out to lead to better agreement of simulations of the dynamics of filamentation with experiment.

The delayed Kerr response of such a gas has been modeled by the excitation of rotational states via

Raman transitions (Sprangle et al., 2002), modulating the third order susceptibility on characteristic timescales of around 60..80 fs (Bergé et al., 2007), which is on the order of typical pulse durations. Experiments have shown that the magnitude of the contribution of the Raman-related delayed part of the Kerr response may be as large as that of the instantaneous part. This can be inferred from a strong observable pulse-duration dependence of the effective nonlinear refractive index, directly affecting the critical power and the distance of self-focussing collapse (Eq. 2.1) (Champeaux et al., 2008).

The corresponding modified expression for the Kerr-induced change of the index of refraction, Δn_K, including the quintic nonlinearity, reads (Champeaux et al., 2008)

$$\Delta n_\mathrm{K} = n_2 \Big\{ (1 - x_\mathrm{K}) I + x_\mathrm{K} \left(\frac{1 + \omega_\mathrm{R}^2 \tau_{dk}^2}{\omega_\mathrm{R} \tau_{dk}^2} \right) \int_{-\infty}^{t} e^{(t-t')/\tau_{dk}} \sin\left(\omega_\mathrm{R}(t-t')\right) I(t') \mathrm{d}t' \Big\} + n_4 I^2 \tag{2.5}$$

Here $x_\mathrm{K} \simeq 1/2$ is the fraction of the delayed part in the total Kerr response, and typical choices for the fundamental rotational frequency ω_R and the dephasing time constant τ_dk are $\omega_\mathrm{R} = 1.6 \times 10^{13}\,\mathrm{s}^{-1}$ and $\tau_\mathrm{dk} = 77\,\mathrm{fs}$ (Bergé et al., 2007; Champeaux et al., 2008).

A different kind of delayed Kerr response has recently been reported by Varma et al. (Varma et al., 2008). They observed that a first filamenting laser pulse can strongly affect the filamentation of a subsequent second pulse, following with a delay of preferentially $1/4$ of the fundamental rotational period T of air molecules ($T_{\mathrm{O}_2} = 11.6\,\mathrm{ps}$, $T_{\mathrm{N}_2} = 8.3\,\mathrm{ps}$).

The first laser pulse aligns air molecules by acting on the induced dipole moments, however without changing their rotational quantum numbers, merely initializing their rotational phase. This corresponds to the creation of a rotational wave packet $|\psi\rangle = \sum_{j,m} a_{j,m} |j,m\rangle \exp(\mathrm{i}\omega_j t)$ in which all phases of the amplitude coefficients $a_{j,m}$ are reset to achieve alignment of the molecule with the laser field at $t = 0$. The eigenfrequencies of the superposed states, $\omega_j = E_{j,m}/\hbar = \frac{2\pi}{c} B\, j(j+1)$ are inverse integer multiples of the fundamental rotational period, and as each component of the superposition independently propagates in time. Because of this, after finite time the situation at $t = 0$ is restored, recovering the initial molecular alignment.

Oscillation of net molecular alignment corresponds to a modulation of the nonlinear polarizability, and thus the nonlinear refractive index. The revival of the rotational wave packet prepared by a first laser pulse can be probed by sending a properly delayed second pulse. The corresponding action on the filamentation of the second pulse was called “quantum wake effect”. Cross-modulation via the molecular alignment-related delayed Kerr component has been shown to strongly influence various aspects of the filamentation process in the trailing pulse (Wu et al., 2009), and was proposed to be useful for engineering multiple filamentation (Varma et al., 2008; Wu et al., 2009).

Ionization processes

The observed formation of a plasma in filaments is based on two main processes, the relative contribution of which depends mainly on pulse peak power and duration. These are direct photoionization

of neutrals by multiphoton absorption, and collisional absorption by the free electrons of forming plasma, driven by the laser field.

One prerequisite of filamentation is the large gap between the photon energy and the lowest excited state of the medium. Thus, in the absence of preexisting free charges, the premier source of free electrons is **multiphoton absorption**, where several photons are absorbed by an electron 'at an instant'.

There are two regimes of multiphoton absorption of importance for filamentation in air, which were both described in a unifying theory for the first time by Keldysh (Keldysh, 1965). The magnitude of the parameter

$$\gamma = \omega_0 \frac{\sqrt{2 m_\mathrm{e} U_\mathrm{i}}}{|e E_\mathrm{peak}|}$$

indicates the asymptotic 'weak' and 'strong' field regimes, namely, (nonresonant) multiphoton ionization ('MPI', $\gamma \gg 1$) and tunneling ionization ('TI', $\gamma \ll 1$). Here ω_0 is the dominant optical frequency, U_i is the ionization potential, E_peak the peak amplitude of the optical field, and e and m_e are electron charge and mass, respectively.

Up to $I \approx 10^{13}\,\mathrm{W/cm^2}$ the MPI limit is applicable, expressing the change of the free electron number concentration as

$$\frac{\partial \rho_\mathrm{e}}{\partial t} = (\rho_\mathrm{neutr} - \rho_\mathrm{e})\, W(I) = (\rho_\mathrm{neutr} - \rho_\mathrm{e})\, \sigma_K\, I^K, \qquad K = \mathrm{mod}\left(\frac{U_\mathrm{i}}{\hbar\omega_0}\right) + 1.$$

The number of absorbed photons K is $K_{\mathrm{O}_2} = 8$ ($U_\mathrm{i}^{\mathrm{O}_2} = 12.1\,\mathrm{eV}$) and $K_{\mathrm{N}_2} = 11$ ($U_\mathrm{i}^{\mathrm{N}_2} = 15.6\,\mathrm{eV}$), for $\lambda_0 = 800\,\mathrm{nm}$. Values for the corresponding absorption coefficients calculated from Keldysh theory are $\sigma_8 = 2.8 \times 10^{-96}\,\mathrm{s^{-1}\,cm^{16}/W^8}$, and $\sigma_{11} = 6.3 \times 10^{-140}\,\mathrm{s^{-1}\,cm^{22}/W^{11}}$ (Couairon and Mysyrowicz, 2007), indicating that oxygen is ionized much more efficiently than nitrogen.

Intensities in filaments exceed the range of validity of the asymptotic MPI limit, and ionization rates have to be calculated from the detailed model. The original Keldysh theory describes the special case of hydrogen-like atoms, and was extended by Perelomov, Popov, and Terent'ev ("PPT") to describe multi-electron atoms, including coulomb attraction between the ion and the leaving electron, and different initial states for the ionization.

Further refinements of Keldysh theory exist (Bergé et al., 2007; Couairon and Mysyrowicz, 2007), however it was shown by Talebpour et al. (Talebpour et al., 1999) that for molecular nitrogen and oxygen and for $\lambda = 800\,\mathrm{nm}$ radiation the PPT model, although constructed for atoms, can be semi-empirically adjusted by making the effective ion charge a tunable parameter to agree well with experiment up to $I = 10^{15}\,\mathrm{W/cm^2}$. The resulting parametrizations of the multiphoton ionization rates $W_{\mathrm{O}_2}(I)$ and $W_{\mathrm{N}_2}(I)$ are often used when filamentation in air is modeled (Bergé et al., 2007; Couairon and Mysyrowicz, 2007; Kandidov et al., 2009).

The next important source of free electrons in laser filamentation is **collisional absorption** by inverse bremsstrahlung. In this process free electrons get accelerated by the laser field and couple out energy when colliding with heavy plasma species (Kruer, 1988). Depending on the laser field strength direct laser-driven collisional ionization dominates, or the electron gas gradually heats up

until electrons in the hot tail of the thermal distribution are energetic enough to knock off additional electrons from neutrals.

The electron temperature in femtosecond laser filament-generated air plasma remains on the order of $T_\mathrm{e} \approx 1\,\mathrm{eV}$) (Couairon and Mysyrowicz, 2007). Resulting from the relatively much higher ionization potential of the medium, ionization due to thermal collisions of electrons with neutrals can be neglected (assuming a Maxwell-Boltzmann energy distribution of the electron gas).

The directly laser-driven collisions are usually described by a Drude model, resulting in the expression for the consequent rate of change of the electron number density (Bergé et al., 2007):

$$\frac{\partial \rho_\mathrm{e}}{\partial t} = \frac{\sigma_\mathrm{coll}}{U_\mathrm{i}} \rho_\mathrm{e}\, I, \qquad \sigma_\mathrm{coll} = \frac{e^2}{\varepsilon_0\, m_\mathrm{e}\, n_0 c\, \nu_\mathrm{e} \left(1 + \frac{\omega^2}{\nu_\mathrm{e}^2}\right)},$$

where in particular $\nu_\mathrm{e} \approx (350\,\mathrm{fs})^{-1}$ (for air under normal conditions) (Couairon and Mysyrowicz, 2007) is the collision frequency of electrons with neutrals, and ω is the laser frequency. Here ohmic heating of the electron gas was neglected.

The collisional ionization rate is proportional to the laser intensity and, more importantly, proportional to the number density ρ_e of electrons already present. As a result, especially in the trailing part of longer pulses ($\tau_\mathrm{p} > \nu_\mathrm{e}^{-1}$), collisional ionization becomes more important. Positive feedback of the electron density on the ionization rate leads to the onset of an electron avalanche, influencing the dynamics of filamentation.

Nonlinear envelope equation modelling filamenting laser pulse propagation in air

After ionization losses of the laser field are included in the wave equation by the requirement of energy conservation, the envelope equation describing the previously listed effects may look like this:

$$\mathrm{i}\frac{\partial}{\partial z} U = \overbrace{-\frac{1}{2k_0} T^{-1} (\nabla_{bot}^2 U)}^{\text{diffraction}} \overbrace{-\mathcal{D}\, U}^{\text{dispersion}} \overbrace{-k_0 T \Delta n_\mathrm{K}\, U}^{\text{Kerr effect}} \overbrace{+\frac{k_0}{2\rho_\mathrm{c}} T^{-1} \rho_\mathrm{e} U}^{\text{plasma defocus.}} \underbrace{-\mathrm{i}\frac{\sigma_\mathrm{coll}}{2}\rho_\mathrm{e}}_{\text{collisional loss}} \underbrace{-\mathrm{i}\,\rho_\mathrm{neutr} U_\mathrm{i} \frac{W(I)}{2I} U}_{\text{photo-ionization loss}}.$$

The operators $\mathcal{D}$ and T, as well as the Kerr-induced index change n_K, including the delayed response and the quintic nonlinearity, appear as defined above. The same holds for the multiphoton absorption rate $W(I)$.

Equation 2.2.2, together with the coupled equation for the evolution of the electron density containing the contributions of multiphoton absorption and collisional absorption, constitute the final model.

Propagation models like the one sketched here are able to reproduce many of the observed features of (multiple) filamentation in air. Spectral broadening as well as characteristic deformations of the

envelope such as pulse steepening, pulse splitting, and complex three-dimensional dynamics, resulting in the observed cyclic focussing and defocussing phases, can be observed in model results.

Also the crucial role of the photon bath, mutual interactions of filaments, seeding of new filaments, as well as the turbulent transverse redistribution of energy, and the formation of persistent "optical pillars" (Bergé et al., 2004; Skupin et al., 2004a) forming around input inhomogeneities of the transverse intensity profile, are reproduced.

Features of filamentary structures like peak intensity and root-mean-square diameter of the intense core resulting from model calculations come close to measured experimental observations even quantitatively (Champeaux et al., 2008).

From a practical perspective, the added understanding gained from simulations can be used to obtain some control over filamentation. This can be done by preparing and optimizing various parameters of the laser pulse, in order to suppress or emphasize the one or the other of the involved mechanisms, guiding the complicated dynamics of filamentation in the desired direction.

2.3. Influencing multiple filamentaton in air

In reality there are practical limitations for the degree of control attainable over multiple filamentation. In principle, virtually all parameters characterizing a laser pulse can be manipulated and tuned: the transverse envelope (intensity profile) by a suitable amplitude mask, and longitudinal envelope, spectral phase, and even the direction of polarization by more complicated, but well established pulse shaping techniques (Weise and Lindinger, 2010).

Difficulties arise when exceptionally high powers and short pulses are involved, putting strong constraints on the optical elements which can be used for tuning these parameters. Besides, in most circumstances where high powers and pulse energies are desired, loss of a substantial fraction of the (expensive) pulse energy is no option.

Additionally, there are inherent limitations of the quality of the beam profile obtainable from a real high power amplifier, for example also the Teramobile system used in the experiments described in later chapters.

In this section some practical methods to influence high power femtosecond filamentation in air are described.

2.3.1. Beam expansion and focussing

Considering the expression for the self focussing collapse distance z_c (Eq. 2.1), increasing the beam width before transmitting it into the atmosphere should be an efficient way to delay the onset distance of filamentation, and in fact it is, and has been used extensively since the first experiments on atmospheric multiple filamentation.

Already Marburger derived this simple lens formula for the modified distance $\frac{1}{z_c^f}$ of global collapse of a Gaussian beam due to Kerr self-focussing when a lens of focal length f is inserted at the beam

waist:

$$\frac{1}{z_c^f} = \frac{1}{z_c} + \frac{1}{f},$$

where the focal length may be positive or negative.

Fibich et al. (Fibich et al., 2006) theoretically and experimentally showed that the above formula even applies to the distance of onset of multiple filamentation. Besides they showed that delaying filamentation in this way causes an increase of the length of the filaments.

2.3.2. Pre-chirping

Applying a (linear) "chirp" to a short laser pulse amounts to displacing its spectral components of frequency ω in time by an amount proportional to $\omega - \omega_0$, where ω_0 is the central frequency of the pulse spectrum. A linear chirp affects both duration and peak power. For a Gaussian-shaped pulse with transform limited duration τ_0 and peak power P_0 the corresponding quantities for the chirped version of the same pulse are

$$\tau_C = \tau_0(1 + C^2)^{1/2}, \qquad P_C = P_0(1 + C^2)^{-1/2}.$$

The chirp parameter C can have positive or negative sign. $C > 0$ means lower frequencies propagate ahead of higher frequencies, and vice versa for $C < 0$.

Peak power reduction directly affects the self-focussing distance, irrespective of the sign of the chirp. A slightly more subtle effect is related to group velocity dispersion (GVD) affecting spectrally broad femtosecond laser pulses.

In media with normal GVD such as air, that is, with positive $k'' = \frac{\partial^2 k}{\partial \omega^2}|_{\omega_0} \approx 0.2\,\mathrm{fs}^2/\mathrm{cm}$ at $\lambda_0 = 800\,\mathrm{nm}$ (Bergé et al., 2007), an initially unchirped pulse acquires a chirp and broadens during propagation.

A properly chosen negative chirp applied before launching the pulse into the atmosphere results in the automatic compensation of the chirp and recompression at a distance

$$z_{\min} = \frac{|C|\,\tau_0^2}{(1 + C^2)\,k''\,\ln(2)}.$$

Exactly such recompression of negatively prechirped high power laser pulses at has been observed by Rodríguez et al. (Rodriguez, 2004; Rodriguez et al., 2004), by enabling supercontinuum generation at a distance of about 2 km.

A numerical study by Nuter et al. (Nuter et al., 2005) predicts a similar effect of initial chirp on filamentation dynamics.

In another experimental study by Méchain et al. (Méchain et al., 2005b) initially chirped high power femtosecond pulses were sent collimated along a horizontal path and filamentation and associated ionization of air were monitored along an extended path. Fig. 2.6 shows the strong effect of initial chirp on position and strength of observed filaments. Also pre-chirping is an easy and standard method to influence high power femtosecond multiple filamentation, as the chirp can be chosen by detuning

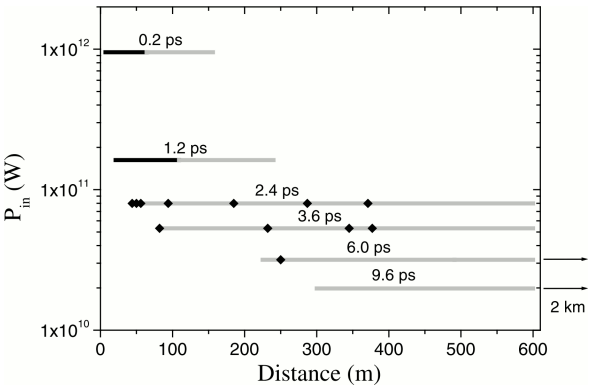

Figure 2.6.: Dependence of length of filamentation on the initial negative chirp imposed on laser pulses of 100 fs transform limited duration, energy $E_p = 190$ mJ, emitted collimated with diameter $d = 34$ mm. Black symbols and lines indicate detectable air ionization, gray lines indicate filamentation without detectable plasma. Fig. 8 from (Méchain et al., 2005b).

the pulse compressor of the laser amplifier, and no additional optics are needed.

2.3.3. Patterning multiple filamentation

It also follows from the considerations in (Fibich et al., 2006) that ideally beam expanding/focussing and pre-chirping do not affect the pattern of multiple filamentation. Also in a moderately convergent beam, the multifilamentary break-up is still governed by modulational instability seeded by the inhomogeneities in the intensity pattern resulting from imperfect amplification.

One of the methods which have been used to affect the pattern of multiple filamentation consists in shaping the transverse amplitude profile of the laser beam by amplitude masks with a spatially varying transmittance. However, the very high intensities attained by high power femtosecond laser pulses powers in this case prevent smooth amplitude modulation. Practically, only wire meshes (Kandidov et al., 2004) or apertures (Méchain et al., 2004) placed in the beam could be used, as they mainly reflect or scatter light out of the beam and withstand the intense laser radiation, while any transmitted partially absorbing material would be immediately destroyed.

Certainly, blocking amplitude masks are far from being the ideal solution, as the inherent side effects of substantial loss of laser energy from the beam and large-angle diffraction at the sharp edges are highly unwanted. Energy loss may be compensated by brute force, but diffraction can lead to premature filamentation seeded by near field diffraction maxima (Roskey et al., 2006). Even disregarding diffraction, already the steep intensity gradients at the edges of the transmitted beam profile lead to self-focussing collapse exactly there, which imposes a severe limit on the freedom where filaments can be placed within the beam.

It was shown by Roskey et al. (Roskey et al., 2006) that the initial phase of propagation of high power femtosecond laser pulses even with many critical powers is dominated by linear diffraction, and that intensity maxima induced by linear diffraction act as nucleating germs for filaments. Thus, as an alternative to directly shaping the transverse intensity profile of the beam, modulation of the transverse *phase* offers another opportunity for steering multiple filamentation.

Consequently, applying an appropriate phase pattern which transforms to an intensity pattern during the initial quasi-linear phase of pulse propagation should allow to relatively freely choose the pattern of multiple filamentation. In Campillo's terms (see Sec. 2.1), the resulting slight but well controlled

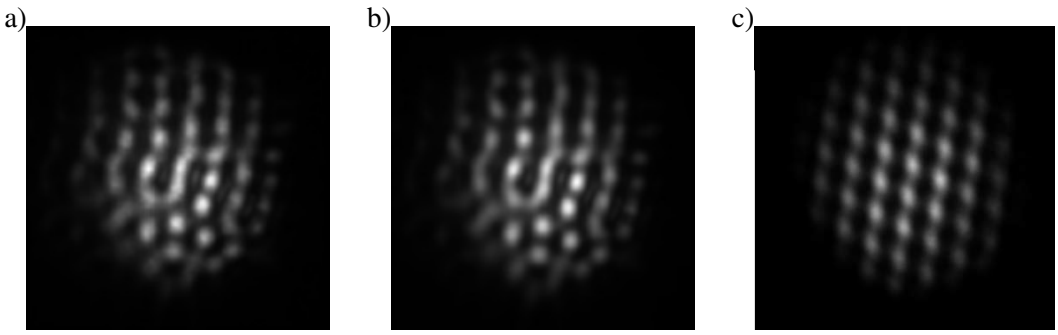

Figure 2.7.: Shot-to-shot stability of the far-field patterns generated with the SDDM demonstrated by visual comparison of a single shot image (a) with a 100-shot exposure (b). The corresponding far-field pattern calculated from the reconstructed mirror surface profile is sown in panel (c).

deformation of the intensity profile building up during the linear propagation phase would provide for the "head start" of the desired transverse modes to dominate the collapse due to modulational instability.

Apart from the attempts mentioned above, other ways to achieve control of the pattern of multiple filamentation have been tried before (see references in (Rohwetter et al., 2008)), but due to lack of suitable optical elements a fine grained control of filamentation in air using transverse phase modulation had not been achieved.

To demonstrate the feasibility of multifilamentation patterning in air our group proposed an unconventional optical device which we called 'strobed dynamic deformable mirror', consisting of a perfectly smooth surface of liquid gallium. It was driven vertically by an oscillating force, inducing the formation of self-organized, regular patterns of standing "Faraday waves" (Cross and Hohenberg, 1993).

The peculiarity of these parametrically driven surface waves is the nonlinear coupling of modes even at smallest amplitudes (Chen and Viñals, 1997). This lead to regular patterns with amplitudes on the order of only 100 nm, verified by comparison with calculated far field patterns obtained from a simplified parametrization of the wave pattern of the deformable mirror surface (for details see (Rohwetter et al., 2008)).

The surface oscillations had a multiple frequency of the laser repetition rate of 10 Hz and were synchronized with the laser clock, so that each laser pulse was reflected at the identical phase of oscillation. In Fig. 2.7 a single shot far field pattern is shown together with a 100 shot average to visualize the high shot-to-shot reproducibility of the resulting far field intensity profiles. The same figure shows the calculated far field pattern obtained from the reconstructed mirror surface profile. The peak-to-peak amplitude of the surface modulations in the depicted case was found to be about 220 nm.

Using laser pulses with $\tau_p = 120$ fs duration, a central wavelength of $\lambda_0 = 801$ nm, and an energy of $E_p = 30$ mJ, shot-to-shot reproducible, structured multifilament patterns could be generated in the ≈ 15 mm diameter beam. Figure 2.8 shows a multi shot burn pattern created by 100 successive

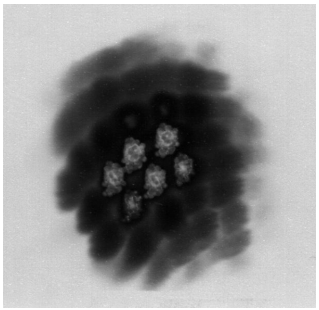

Figure 2.8.: Burn pattern on photographic paper showing the traces of 100 laser shots with an imprinted filamentation pattern. Filaments cause characteristic local point-like surface ablation while non-filamenting parts of the beam profile only cause blackening of the photographic paper.

patterned filamenting laser shots. Traces of six persistent and highly stable filaments can be identified.

Although the variety of obtainable surface patterns was limited for this particular device, it could clearly be shown that a smooth phase mask can be used to efficiently induce controlled transverse alignment of multiple filaments.

3. Optical remote sensing of aerosol

In this section some aspects of optical remote sensing of the atmosphere are summarized, which will later be applied in the context of remote sensing of laser-induced atmospheric condensation. A brief summary of the relevant atmospheric optical parameters is given, and the principles of aerosol backscattering LIDAR is outlined.

A comprehensive overview of the technique can be found in (Measures, 1984), and some more recent developments are described for example in (Weitkamp, 2005).

3.1. Atmospheric scattering and absorption

Some aspects of atmospheric light scattering and absorption will be briefly introduced here, as the phenomenological parameters resulting as the average of microscopic scattering processes involving atmospheric molecules and particles, the atmospheric backscattering and extinction coefficients, are the primary observables in the technique of atmospheric LIDAR. Here only those quantities are defined which are used in later sections.

3.1.1. Absorption

The gaseous atmosphere as well as the suspended aerosol contain substances absorbing light. In the visible spectral range of the electromagnetic spectrum absorption involves electronic transitions, while atmospherically relevant infrared absorption almost generally occurs by the excitation of molecular rotational-vibrational transitions (Measures, 1984). Generally, if the optical irradiance is low, as it is the case for sunlight propagating in the atmosphere, or for low power laser radiation, the optical power absorbed by a body (a molecule, cluster, or particle) is proportional to the flux of the incoming radiation, $W_{\mathrm{abs}} \propto I_{\mathrm{inc}}$.

A prominent example of the absorption of light by atmospheric trace gas is the efficient filtering of ultraviolet radiation with wavelength shorter than about 290 nm out of the sun spectrum by molecular oxygen (O_2) and ozone (O_3).

Water vapour, in several bands above $\lambda \approx 800\,\mathrm{nm}$, and carbon dioxide ($CO_2$) above $\lambda \approx 2\,\mu\mathrm{m}$ wavelengths are responsible for most of the atmospheric infrared absorption (Seinfeld and Pandis, 2006).

The spectral signatures of different absorbers can be used to identify them and quantify their atmospheric abundance, as it is embodied in the DIfferential Absorption LIDAR (DIAL) technique applied for example to tropospheric ozone (Measures, 1984).

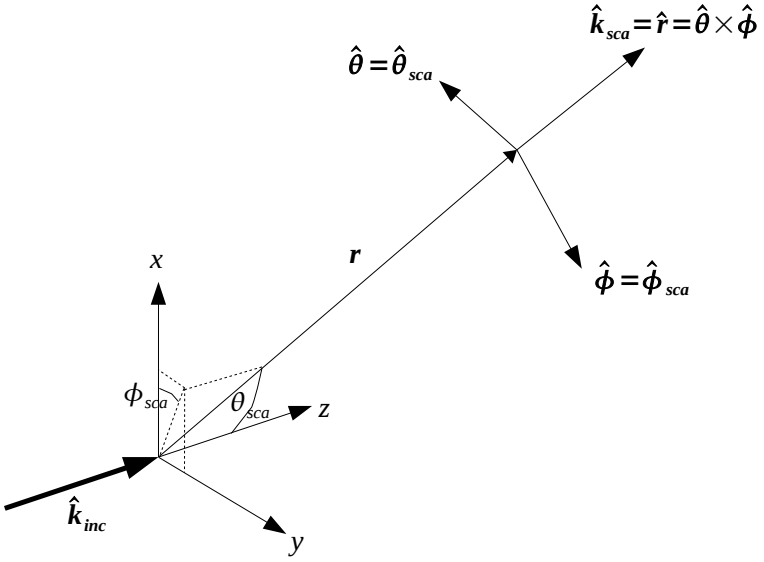

Figure 3.1.: Illustration of relationships defining the scattering geometry.

Also aerosol substance can absorb light, although in the visible part of the spectrum absorption by aerosol is much less important than scattering processes (Kokhanovsky, 2008). For the purpose of this work linear atmospheric absorption is not important and will not be detailed further. Later in this text absorption by aerosol will be discussed again, but in the context of nonlinear absorption of intense laser light.

3.1.2. Phenomenology of light scattering

Scattering geometry

The scattering geometry is sketched in Fig. 3.1. The incoming light propagates in direction of the unit vector $\hat{\mathbf{k}}_{\text{inc}}$, which coincides with the z-axis by choice of the reference coordinate system. The observation point $\mathbf{r}$ (together with the origin) defines the scattering direction $\hat{\mathbf{k}}_{\text{sca}}$ and the local coordinate system $(\hat{\mathbf{r}}_{\text{sca}}, \hat{\theta}_{\text{sca}}, \hat{\phi}_{\text{sca}})$ with $\hat{\mathbf{r}}_{\text{sca}} = \hat{\mathbf{k}}_{\text{sca}}$ and $\hat{\mathbf{r}}_{\text{sca}} = \hat{\theta}_{\text{sca}} \times \hat{\phi}_{\text{sca}}$.

The plane containing $\mathbf{r}$ and the z-axis is the scattering plane (if $\mathbf{r} \nparallel \hat{\mathbf{z}}$).

Scattering matrix

When the electric field of the incident light is decomposed into components parallel (index $\parallel$) and perpendicular (index $\perp$) to the scattering plane, a similar decomposition follows for the field at the observation point. By construction $\hat{\theta}_{\text{sca}}$ and $\hat{\phi}_{\text{sca}}$ lie parallel and perpendicular to the scattering plane, respectively, and the corresponding components of the scattered electric field are defined by the corresponding projections.

Using this decomposition the dependence of the scattered field components at a large distance from the scatterer can be expressed by the scattering amplitude matrix $\mathbf{S} = ((S_2, S_3), (S_4, S_1))^T$, which is a

function of the scattering direction expressed by θ_{sca} and ϕ_{sca}.

$$\begin{pmatrix} E_{\parallel,\text{sca}} \\ E_{\perp,\text{sca}} \end{pmatrix} = \frac{\exp(ikr)}{-ikr} \begin{pmatrix} S_2 & S_3 \\ S_4 & S_1 \end{pmatrix} \begin{pmatrix} E_{\parallel,\text{inc}} \\ E_{\perp,\text{inc}} \end{pmatrix}$$

Here all amplitudes and matrix elements are complex numbers, the arguments of which encode phases.

Phenomenological quantities related to scattering

Some phenomenological quantities can be introduced, the definitions of which are independent of the nature of the underlying microscopic scattering processes. They describe the result of a scattering process observable in the far field, and depend on the size, geometry, and material properties of the scatterer, as well as on the wavelength and polarization of the incident light.

'Extinction' is the total of all effects leading to loss of radiation flux in the original direction $\hat{\mathbf{k}}_{\text{inc}}$. These are absorption, effectively removing energy out of the light field, and extinction due to scattering of radiation into directions other than $\hat{\mathbf{k}}_{\text{inc}}$

Given an incident radiation flux I_{inc} entering a volume containing the scatterer, one defines the corresponding cross sections

$$C_{\text{abs}} = \frac{W_{\text{abs}}}{I_{\text{inc}}} \qquad C_{\text{sca}} = \frac{W_{\text{sca}}}{I_{\text{inc}}} \qquad C_{\text{ext}} = C_{\text{abs}} + C_{\text{sca}},$$

where W_{abs} and W_{sca} denote the energy per unit time absorbed and scattered by the scattering body, respectively. The cross sections have the unit of area. In the geometrical optics picture the extinction cross section can be visualized as the effective area of the scattering body, represented by an equivalent disk acting as a sink for all rays which are intercepted by it.

The amount of light, as well as its polarization properties, that are observed in the far field, are functions of the scattering angle, the initial polarization, and generally of the orientation of the scattering body with respect to $\hat{\mathbf{k}}_{\text{inc}}$. The last dependence vanishes in the case of spherically symmetric scatterers. The directional characteristic of scattering is expressed by the differential scattering cross section, symbolically denoted by the expression $dC_{\text{sca}}/d\Omega$. It has the unit of area per unit solid angle. The total cross section for scattering into a certain sufficiently small solid angle element $\Delta\Omega$ on the unit sphere accordingly is given by

$$C_{\text{sca},\Delta\Omega} = \int_{\Delta\Omega} \mathrm{d}\hat{\mathbf{r}} \, \frac{dC_{\text{sca}}}{d\Omega} \simeq \Delta\Omega \, \left.\frac{dC_{\text{sca}}}{d\Omega}\right|_{\Delta\Omega},$$

where $dC_{\text{sca}}/d\Omega|_{\Delta\Omega}$ denotes the differential scattering cross section evaluated for the scattering direction centered on $\Delta\Omega$.

In a typical LIDAR configuration the detector is situated in almost ideal backward direction at a scattering angle $\theta \approx \pi$. This motivates the definition of the backscattering cross section

$$C_{\text{back}} = \left.\frac{dC_{\text{sca}}}{d\Omega}\right|_{\theta=\pi}$$

The normalized function describing just the angular characteristic of scattering is traditionally and misleadingly called the 'phase function' and is obtained by scaling the differential scattering cross section by the inverse of the total scattering cross section

$$p = \frac{1}{C_{\mathrm{sca}}} \frac{dC_{\mathrm{sca}}}{d\Omega}.$$

It is normalized to 1 in the sense of its integral over the unit sphere. Some authors normalize the phase function to 4π, so one has to be careful when intercomparing data from different sources.

The scattering properties expressed as cross sections with the unit of area, like C_{sca}, C_{ext}, are often divided by the geometrical cross section of the scatterer, which is $\pi D_{\mathrm{p}}^2/4$ in the case of a sphere of diameter D_{p}, and equivalently stated as the corresponding efficiency factors. For example

$$Q_{\mathrm{sca}} = \frac{C_{\mathrm{sca}}}{(\pi D_{\mathrm{p}}^2/4)}$$

is the scattering efficiency factor.

From the cross sections of an individual microscopic scatterer (including absorption) and the volume number concentration n_{p} of similar scatterers one can obtain the average scattering properties of a volume element. Under the assumptions that individual scattering bodies of species i are distributed in space sparsely enough not to mutually modify their scattering properties, and that their positions in space are random and independent, one can define the volume scattering coefficients according to

$$\alpha_i(\lambda) = n_{\mathrm{p}} C_{\mathrm{ext}}^{(i)}(\lambda) \qquad \beta_{\pi,i}(\lambda) = n_{\mathrm{p}} C_{\mathrm{back,sca}}^{(i)} \tag{3.1}$$

Under the same assumptions as above these quantities are additive when different scattering species are present. The range dependent total volume extinction coefficient and volume backscattering coefficient are the primary quantities inferred from a classical backscattering Lidar signal, as will be outlined below.

Atmospheric scattering has an impact on the transmission of light in the sense of radiation transport as well as imaging and the ability to optically resolve distant objects. The meteorological observable '(daylight) visibility' is defined as the maximum range at which an object (brightness b) can be distinguished from its background (brightness b_0) by a human observer. The definition of standard visibility assumes that atmospheric extinction alone causes degradation of visual contrast. Assumption of a homogeneous atmosphere results in an exponential relationship between contrast c and range r (Kokhanovsky, 2008),

$$c(r) := \frac{b - b_0}{b_0} = \exp(-\alpha_{\mathrm{tot}} r).$$

The definition of standard visibility v assumes a minimum required contrast of $c(r) = 2\,\%$ at range $r = v$, and atmospheric extinction is evaluated at at a wavelength of 550 nm, yielding the equation

$$v = -\frac{\ln(0.02)}{\alpha_{\mathrm{tot,\,550\,nm}}} \simeq \frac{3.91}{\alpha_{\mathrm{tot,\,550\,nm}}}, \tag{3.2}$$

where v has the unit m if the total extinction coefficient $\alpha_{\text{tot, 550 nm}}$ is given in units of m^{-1}. The choice of reference wavelength is based on the fact that human daytime visual sensitivity attains its maximum at about 550 nm.

3.1.3. Molecular (Rayleigh) scattering

The term 'Rayleigh scattering' has many uses, and its actual meaning depends on the context. It may stand for scattering by a single ideal dipole, by a *small, spherical* scatterer (small compared to the considered wavelength), and, finally, the actual scattering of light by air molecules. This is the meaning assumed in the following paragraphs. Often the label 'Rayleigh' scattering is used in a way implying elastic scattering, where again the meaning of the word 'elastic' is context-dependent, and eventually is defined by the spectral selectivity of the observation. Atmospheric molecular scattering is a mixture of scattering on static and propagating refractive index fluctuations, as well as rotational and rotational-vibrational Raman scattering. The rotational-vibrational raman components of the scattered spectrum of nitrogen and oxygen are shifted in energy by around $2300\,\text{cm}^{-1}$ and $1500\,\text{cm}^{-1}$, respectively. In the case of incident light at a wavelength of 532 nm this corresponds to wavelength shifts of roughly 65 nm and 45 nm. The lines of the rotational Raman band, on the other hand, are much less displaced from the incident wavelength. Again in the case of 532 nm laser light the total width of the corresponding band is around ±4 nm. Due to the different involved scattering mechanisms, in cases when the observation is spectrally selective and/or is sensitive to polarization, this affects the corresponding scattering cross sections (Young, 1981, 1982).

In monochromatic Lidar setups vibrational Raman scattering adds to extinction but not to the detected backscattering signal, simply because of the relatively large molecule-specific wavelength shift. However, this part only adds a small contribution to overall molecular extinction. In fact the backscattered raman-shifted component is detected in explicit Raman Lidar setups and used to obtain concentration profiles of specific molecular scatterers such as water vapour.

If the bandwidth of the detection is sufficiently large to cover the rotational Raman components, the overall molecular scattering cross section (neglecting the very small contribution of vibrational Raman scattering) can be written (Bucholtz, 1995)

$$C_{\text{sca,Mol}} = \frac{24\,\pi^3}{\lambda^4 N^2}\left(\frac{n^2-1}{n^2+2}\right)\left(1+\frac{2\,\varepsilon}{9}\right),$$

where N is the number density of molecules, and n is the refractive index of the medium. The last term in brackets on the right side is a correction factor derived by King (King, 1923), taking into account the anisotropy of the molecular polarizability of diatomic air molecules (N_2 and O_2) averaged over a randomly oriented ensemble, and expressed by the molecular anisotropy factor ε. As the quantities N, n, and ε depend on the physical state, and/or the chemical composition of the atmosphere, and n and ε additionally are subject to dispersion, the explicit frequency dependence of the molecular scattering cross section, $C_{\text{sca,Mol}}$ varies depending on the atmospheric conditions. Calculated cross sections for various model atmospheres are presented in (Bucholtz, 1995).

The molecular backscattering cross section ($\theta = \pi$) then is

$$C_{\text{back,Mol}} = \frac{3}{8\pi} C_{\text{sca,Mol}}.$$

3.1.4. Aerosol scattering

Mie theory The sizes of atmospheric aerosol cover a very broad range, from fractions to multiples of an optical wavelength. For most part of this range the particles cannot be assumed to be much smaller or larger as compared to the wavelength (Rayleigh resp. geometrical optics approximations). The calculation of scattering properties of particles in this intermediate size range requires a more rigid approach. Unfortunately, the precise treatment of optical scattering is a complicated task if particles of arbitrary shape, material composition (including inhomogeneous mixing of different materials), are to be considered.

The special case of scattering of electromagnetic radiation by (optically) homogeneous spherical particles is covered by a theory commonly associated with the name of Gustav Mie (Mie, 1908), which however was independently developed by Ludvig Lorenz, as well as Peter Debye. It is often referred to briefly as 'Mie theory', or 'Lorenz-Mie theory'. A short outline and some results which will be invoked later in the text are given in the following.

In its original form Mie theory describes the scattering of monochromatic radiation, incident as a plane wave, by a perfectly spherical object. Generalizations involve spectral decomposition in terms of frequecy/wavelength and angular spectrum, and allow for the description of scattering of (Gauß-shaped) beams or short pulse radiation. There also exists a generalization to spheroidal particles[1].

Detailed derivations of Mie theory can be found in many text books, for example (Bohren and Huffmann, 1983; Mishchenko et al., 2002; Morse and Feshbach, 1953), following different conventions regarding the involved functions and coefficients. The results summarized in the following match the conventions of Bohren and Huffman (Bohren and Huffmann, 1983).

Although strictly valid only for ideally homogeneous spherical scatterers, Mie theory yields useful results for real atmospheric aerosols, and frequently is applied in atmospheric optics. It can provide a good approximation to reality, and often is directly applied to atmospheric aerosols, as in many cases the assumptions of sphericity and homogeneity of scatterers are sufficiently well fulfilled (Mishchenko et al., 2002).

Without loss of generality linearly polarized light with the electric field vector lying in the $\phi = 0$ plane is assumed. Because of the symmetry of the scattering geometry and the linearity of the wave equation and the boundary conditions, only the relative angle between the plane of polarization of the incident light and the scattering plane is physically relevant, and rotating the plane of incident polarization is equivalent to rotating the scattering geometry around the z-axis. The scattered field of arbitrarily polarized incident light is found by linear superposition.

The results of Mie theory which are the most important for aerosol LIDAR are the expressions for

[1] S. Asano and G. Yamamoto, 'Light Scattering by a Spheroidal Particle', Appl. Opt. **14**:29 (1975)

the scattering cross sections defined above. They are stated here without derivation:

$$\begin{aligned} C_{\text{sca}} &= \frac{\pi}{k^2}\sum_{\ell=1}^{\infty}(2\ell+1)\left(|a_\ell|^2+|b_\ell|^2\right) \\ C_{\text{ext}} &= \frac{\pi}{k^2}\sum_{\ell=1}^{\infty}(2\ell+1)Re(a_\ell+b_\ell) \\ C_{\text{abs}} &= C_{\text{ext}} - C_{\text{sca}}. \end{aligned} \tag{3.3}$$

The differential scattering cross section reads

$$\left.\frac{dC_{\text{sca}}}{d\Omega}\right|_{(\theta,\phi)} = |S_2(\theta)|^2\cos^2(\phi) + |S_1(\theta)|^2\sin^2(\phi) \tag{3.4}$$

where

$$\begin{aligned} S_1(\theta) &= \sum_{\ell=1}^{\infty}\frac{2\ell+1}{\ell(\ell+1)}\left(a_\ell\pi_\ell(\theta)+b_\ell\tau_\ell(\theta)\right) \\ S_2(\theta) &= \sum_{\ell=1}^{\infty}\frac{2\ell+1}{\ell(\ell+1)}\left(a_\ell\tau_\ell(\theta)+b_\ell\pi_\ell(\theta)\right). \end{aligned}$$

The dependence on the scattering angle is contained in the functions $\pi_\ell(\theta)$ and $\tau_\ell(\theta)$, which are derived from the associated Legendre functions P_n^ℓ:

$$\begin{aligned} \pi_\ell(\theta) &= \frac{P_n^\ell(\cos\theta)}{\sin\theta} \\ \tau_\ell(\theta) &= \frac{d}{d\theta}P_n^\ell(\cos\theta). \end{aligned} \tag{3.5}$$

The expansion coefficients a_ℓ and b_ℓ depend only on the size parameter and the relative refractive index, and they are calculated as

$$a_\ell = \frac{m\psi_\ell(mx)\psi'_\ell(x) - \psi_\ell(x)\psi'_\ell(mx)}{m\psi_\ell(mx)\xi'_\ell(x) - \xi_\ell(x)\psi'_\ell(mx)} \qquad b_\ell = \frac{\psi_\ell(mx)\psi'_\ell(x) - m\psi_\ell(x)\psi'_\ell(mx)}{\psi_\ell(mx)\xi'_\ell(x) - m\xi_\ell(x)\psi'_\ell(mx)}$$

where $\psi_\ell(z)$ and $\xi_\ell(z)$ are the Riccati-Bessel functions (Bohren and Huffmann, 1983).

Polarization-dependence of the far-field scattered intensity is conveyed by the ϕ-dependence of the right side of eq. 3.4.

Fortunately there are well-tested and published codes available which can be readily used to calculate the expansion coefficients, the internal and scattered electromagnetic fields, or the derived quantities listed above. These are for example the BHMIE code for homogeneous spherical scatterers by Bohren and Huffman (Bohren and Huffmann, 1983), or the collection of programs by Barber and Hill described in (Barber and Hill, 1990).

Scattering by a polydisperse aerosol The scattering properties of a polydisperse mixture of scatterers is found by averaging over a statistical ensemble. In the special case of homogeneous spherical scatterers this reduces to integrating the respective size-dependent quantity, weighted by the volume number concentration $n(D_\mathrm{p})$. In the case of the scattering and backscattering cross sections this reads

$$\langle C_\mathrm{sca} \rangle_\mathrm{p} = \int_{D_\mathrm{min}}^{D_\mathrm{max}} \mathrm{d}D_\mathrm{p}\; n(D_\mathrm{p})\, C_\mathrm{sca}(D_\mathrm{p}) \tag{3.6}$$

$$\langle C_\mathrm{b} \rangle_\mathrm{p} = \int_{D_\mathrm{min}}^{D_\mathrm{max}} \mathrm{d}D_\mathrm{p}\; n(D_\mathrm{p})\, C_\mathrm{sca}(D_\mathrm{p})\, p(D_\mathrm{p}; 180^\circ) \tag{3.7}$$

where $C_\mathrm{sca}(D_\mathrm{p})$ and $p(D_\mathrm{p}; 180^\circ)$ are the size-dependent scattering cross section and phase function, respectively.

The above equations consider homogeneous aerosol particles of uniform chemical composition, meaning that the optical refractive index is the same for all particle sizes. This assumption is often well met by pure water aerosol such as clouds or fog. In the more general case the aerosol particles are allowed to have different chemical composition. Even in the relatively simple case of binary homogeneous mixing, where the composition can be parametrized by the mixing ratio, this would add another dimension to the integrals in eq.3.7. Practically often the effective refractive index is assumed to be a function just of the particle size. This is physically grounded in the case when cloud droplets form around approximately similar germs of, say, sulphuric acid. Then the degree of acid dilution (and therefore the refractive index) is approximately a function of droplet size only.

Averaging over an ensemble means loss of information. The independent inference of both $n(D_\mathrm{p})$ and the scattering properties $C_\mathrm{sca}(D_\mathrm{p})$ and $p(D_\mathrm{p})$ is not possible without some degree of a priori knowledge. This is a fundamental problem of the remote sensing of aerosol properties via their scattering of light.

3.2. Atmospheric scattering LIDAR

A schematic atmospheric LIDAR setup is sketched in Fig. 3.2. Its main components are the transmitter, the receiving optics, an optical wavelength analyzer or filter, optional polarization analyzing optics, one or multiple optical detectors with fast response, and a correspondingly fast electronic data acquisition system.

Depending on the particular LIDAR variant implemented, the transmitter emits one or multiple wavelengths, and the tuning and transmitted bandwidth of the wavelength analyzer, and the number of wavelength channels may differ.

In the simple case of monochromatic aerosol backscattering LIDAR considered in the following only narrowband radiation around a single wavelength is emitted, and the same wavelength is transmitted by a matching narrow bandpass filter on the detection side.

Another class of LIDAR setups exist where collected radiation is brought to interference with radiation from a local reference oscillator before detecting it with an intensity sensitive detector, so

called ‘heterodyne’ or coherent LIDARs (Belmonte, 2004; Henderson et al., 2005). These are not considered here.

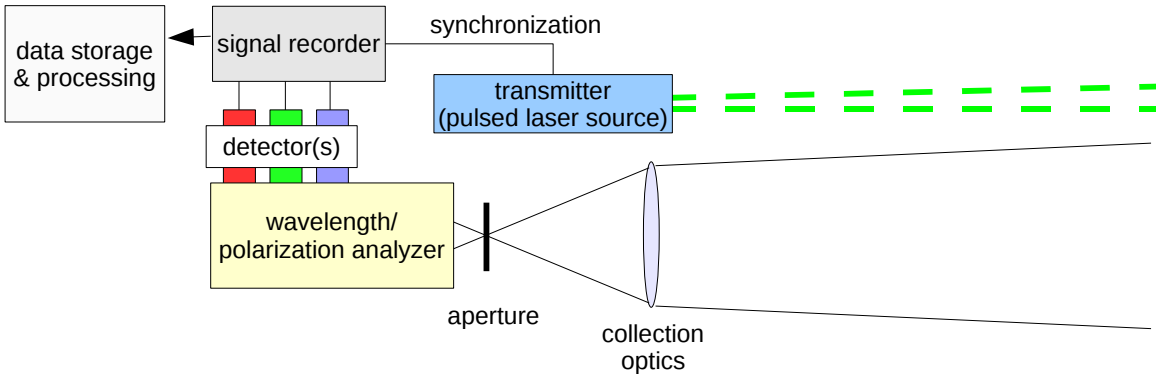

Figure 3.2.: Schematic of a generic atmospheric LIDAR setup.

3.2.1. The elastic scattering LIDAR equation

The measured quantity in any sort of (incoherent) LIDAR scheme is the instantaneous optical power $P(r, \overline{\lambda})$ in the wavelength interval $\overline{\lambda}$, arriving from the detection volume at range r of thickness $\Delta r = c\tau_p/2$, where c is the speed of light in air and τ_p is the laser pulse duration.

Assuming that only singly, elastically scattered radiation reaches the detector, $P(r, \overline{\lambda})$ can be expressed as

$$P(r, \overline{\lambda}) = P_0 \, \frac{c \, \tau_p}{2} \, \eta(\lambda) \, G(r) \, \Delta\Omega(r) \, \beta(r, \overline{\lambda}) \, \exp\left\{-2 \int_0^R \alpha(r', \overline{\lambda}) \, \mathrm{d}r'\right\}, \tag{3.8}$$

where P_0 is the transmitted power, $\eta(\lambda)$ is an instrument-specific efficiency factor, and $\Delta\Omega(r) = A/r^2$ is the range dependent solid angle filled by the pupil of the detection optics (cross sectional area A) when seen from the scattering volume at range r (Measures, 1984).

The function $G(r)$ describes the fraction of the light backscattered at range r and entering the pupil of the detection optics, which actually reaches the detector. Nonunity $G(r)$ is caused by imperfect imaging due to defocus and/or offset between the optical axis of the detection optics and the LIDAR beam. The related range-dependent signal distortion is commonly called ‘geometrical compression’ and can be determined from the geometry of the LIDAR setup (Stelmaszczyk et al., 2005) (see also later Sec. 5.2.2). In a standard LIDAR setup $G(r) < 1$ for short distances, and $G(r)$ approaches 1 for longer distances. This behaviour results as generally the collection optics are adjusted for infinite object distance, and their optical axis is aligned collinear to the transmitter axis.

The exponential term describes the integrated extinction along the optical path outward to range r and back to the detector, leading to the factor of 2 in the exponent of the Beer-Lambert term. The signal $P(r, \overline{\lambda})$ in the above equation is assumed to be already background-corrected.

Note also that the total atmospheric extinction coefficient $\alpha(r, \overline{\lambda})$ includes scattering and absorption by both gaseous and aerosol components, that is, no simplifying assumptions have been made yet.

3.2.2. Evaluation of elastical backscattering LIDAR signals

Proper choice of the transmitted laser wavelength avoids extinction due to molecular absorption by trace gases. Then no loss channels are important but extinction due to scattering. Later, in sec. 5.2, the interpretation of elastical LIDAR returns will be reconsidered in the new context of differential elastical backscattering LIDAR. For this reason the usual method to deal with elastical backscatter returns will be outlined in the following. The single scattering LIDAR equation 3.8 simplifies when absorption (including loss at the laser wavelength due to inelastical scattering) can be neglected. Assuming only one narrow wavelength band removes the $\overline{\lambda}$-dependence. Also treating the absorption by aerosols as negligible, and including the correction for geometrical compression in the signal ($P(r) \rightarrow P(r)/G(r)$), leads to some simplification of the LIDAR equation. After defining the total of molecular (Rayleigh) and aerosol scattering parameters

$$\beta(r) = \beta_{\mathrm{R}}(r) + \beta_{\mathrm{A}}(r) \qquad\qquad \alpha(r) = \alpha_{\mathrm{R}}(r) + \alpha_{\mathrm{A}}(r)$$

The LIDAR equation now looks like this:

$$P(r) = \frac{C}{r^2}\beta(r)\exp\left\{-2\int_0^r \alpha(r')\mathrm{d}r'\right\}$$

The quantities $\alpha(r)$ and $\beta(r)$ contain range-resolved information about optical properties of the aerosol, and are to be retrieved from the power of backscattered light at the detector, $P(r)$. The main difficulty consists in the fact that the information about two independent unknown quantities is compressed in a single measured quantity $P(r)$. The de facto standard method for retrieving the unknown scattering parameters $\alpha(r)$ and $\beta(r)$ from the measured LIDAR return was introduced into the context of atmospheric LIDAR by James D. Klett (Klett, 1981), and since then is commonly reffered to as 'the Klett method'. In fact, the analytical solution to the problem had already been found long before (Hitschfeld and Bordan, 1954), but had been literally used in 'reverse gear' – in an analytically unstable form, which was recognized and resolved by Klett. A relatively general variant of the Klett method will be quickly sketched in the following. The first step is to rephrase the LIDAR equation introducing the 'extinction/backscatter ratio'- or 'LIDAR ratio' $g(r)$. No assumptions are made on $g(r)$ (yet), and no information is gained or lost:

$$g(r) = \frac{\alpha(r)}{\beta(r)}, \qquad\qquad \alpha(r) = g(r)\beta(r).$$

Note that here $g(r)$ denotes the ratio of the *total* extinction coefficient and the *total* volume backscattering coefficient, unlike in many cases where the 'LIDAR ratio' is defined to relate the aerosol scattering parameters α_{A} and β_{A}. Besides this substitution, the LIDAR equation is multiplied with

r^2/C and logarithmized, and finally reads

$$\begin{aligned} X(r) &= \ln\left(\frac{r^2 P(r)}{C}\right) \\ &= \ln\beta(r) - 2\int_0^r g(r')\beta(r')\mathrm{d}r'. \end{aligned} \tag{3.9}$$

Taking the derivative with respect to range r of both sides of Eqn. 3.9 leads to a differential equation for $\beta(r)$:

$$\beta'(r) = X'(r)\beta(r) + 2\,g(r)\beta^2(r)$$

which has the form of a Bernoulli equation, and which is solved by

$$\beta^{-1}(r) = e^{-X(r)+C_1}\left(C_1 - 2\int e^{-X(r')+C_1} g(r')\mathrm{d}r'\right). \tag{3.10}$$

Klett showed that analytical stability is obtained when the integral is evaluated between r and a reference range r_m at the *upper* end of the inversion interval, instead of setting the reference range to $r = 0$. Loosely speaking, analytical stability means that solutions for 'close' initial conditions at the reference range do not diverge exponentially with increasing distance from the reference range, but remain 'close' to each other throughout the whole considered range interval. Said way to evaluate the integral is common to all flavours of the Klett method, which mainly differ in the assumptions on the relation of $\alpha(r)$ and $\beta(r)$ and the computational scheme. The unique solution of Eqn. 3.10 is found by fixing $\beta(r_\mathrm{m}) = \beta_\mathrm{m}$ after factoring out the term $\exp(C_1)$ and lumping all constants into one, leading to the final result

$$\beta(r) = \frac{e^{X(r)-X(r_\mathrm{m})}}{\beta_\mathrm{m}^{-1} + 2\int_r^{r_\mathrm{m}} e^{X(r')-X(r_\mathrm{m})} g(r')\mathrm{d}r'}. \tag{3.11}$$

The problem that remains is the complete ignorance of $g(R)$. The molecular contribution to backscattering and extinction can be relatively accurately determined from temperature and pressure profiles obtained from balloon sonde data, or from a standard model atmosphere. The molecular LIDAR ratio is known and constant (see Sec.3.1.3),

$$g_\mathrm{R} = \frac{\alpha_\mathrm{R}}{\beta_\mathrm{R}} = \frac{8\pi}{3}\,\mathrm{sr},$$

while the aerosol LIDAR ratio $g_\mathrm{A}(r)$ can be highly variable in space and strongly depends on the aerosol type and factors such as the space and time dependent relative humidity (see 4.1.2). Therefore it contains valuable information itself. This information is largely discarded when plugging in an assumed $g_\mathrm{A}(r)$. When LIDAR returns are measured simultaneously at different wavelengths, the unknown functions $g_\mathrm{A}(\lambda; r)$ that now are functions with the wavelength as a parameter, are not independent, as they originate from the same type of scatterers at any range r. This dependence can be used to gain information about the scatterers. However, the problem of retrieving, for example, the

range-dependent aerosol size distribution from a finite number of LIDAR returns is mathematically ill-posed. This means that two 'completely different' candidate size distributions $n_1(D)$ and $n_2(D)$ can possibly each produce a family of Lidar ratios $(g_{A,1}(\lambda_i))_i$ and $(g_{A,2}(\lambda_i))_i$ which are close to each other, and which are consistent with the observed data. The ill-posedness results from $\beta_A(\lambda)$ and $\alpha_A(\lambda_i)$ being average quantities, and from the loss of information entailed in the averaging process (see also Sec. 3.1.4). Therefore, cross-linking the analysis of polychromatic elastical backscattering LIDAR returns via a model for aerosol scattering does not easily resolve the problem of two unknowns. An elegant but technically more challenging way to get access to $g_A(r)$ is implemented in High Spectral Resolution Lidar (HSRL) (Piironen and Eloranta, 1994), where the LIDAR return of narrowband transmitted laser pulses is detected in two separate channels: One channel is precisely tuned to the narrow transmitted wavelength interval, while the other channel registers LIDAR return in an extended wavelength interval. This allows to discriminate the Doppler-broadened molecular backscatter from the unbroadened aerosol backscatter, and yields direct information on aerosol extinction. This is, however, at the cost of more complex instrumentation.

3.3. The impact of atmospheric turbulence on LIDAR signals

Turbulence occurs on all atmopheric length scales, from several thousands of kilometres down to the millimetre scale. In contrast to laminar flow with a homogeneous, essentially one-dimensional velocity field, turbulence is characterized by random inhomogeneous, three-dimensional flow.

The Reynolds number $Re = vL/\nu = vL\rho/\mu$, (v being the velocity, L a characteristic length, ρ the fluid mass density and μ the bulk viscosity, and $\nu = \rho/\mu$) relates inertial and viscous forces acting on some moving fluid element. Values of $Re > 5000$ indicate instability of the flow towards turbulence. This is practically always the case for atmospheric flows.

Strong *microscale* turbulence on scales below 1 km is characteristic for the lowest part of the troposphere and determines its physical properties. On this scale, shear forces caused by the no-slip condition on ground, emphasized by surface relief and thermic convection, seed initial turbulent structures.

Kolmogorov theory is widely used to describe atmospheric optical turbulence (Goodman, 1985) and to approximate its effects on real optical systems.

According to A.N. Kolmogorov, the energy contained in structures of some size scale cascades down to smaller and smaller scales in a self-similar way. This cascade continues until the smallest vortex structures are efficiently consumed by diffusive energy loss. The main assumptions of the theory are isotropy and homogeneity of the random flow field. This roughly means that the statistical properties of the velocity field are independent of absolute position in space, as well as of direction. Conequently, the resulting spectral power density of the turbulent wind velocity field, $\Phi_v(|\kappa|)$, depends only on the spatial wavenumber $|\kappa| = 2\pi/l$. The characteristic length scale l is the size of the turbulent structure corresponding to the respective wavenumber.

The spectral power density of the velocity field directly translates to temperature and refractive index fields, and the results of Kolmogorov theory can be applied to predict the effect of atmospheric

turbulence on the propagation of light. This was initially done by V.I. Tatarskii, using the Kolmogorov spectral power density of the refractive index fluctuations as a starting point:

$$\Phi_n(\kappa) = 0.033\, C_n^2\, \kappa^{-11/3}, \tag{3.12}$$

This expression is valid in the range $2\pi/L_0 < \kappa < 2\pi/l_0$. The *outer scale* L_0 is defined by the size of the largest turbulent structures for which the above initial assumptions hold; the *inner scale* l_0 demarks the length below which flow kinetic energy is efficiently dissipated by diffusion. On scales smaller than l_0 turbulent structures quickly dissolve, and $\Phi(\kappa)$ rapidly drops off. Close to ground level, l_0 is on the order of millimetres, while L_0 is on the order of metres to hundreds of metres (Goodman, 1985).

C_n^2 is called the 'structure parameter' of the turbulent refractive index field, and is a measure for the degree of turbulence. Generally it is a function of the height coordinate, and typically assumes values between $10^{-17}\,\mathrm{m}^{-2/3}$ and $10^{-13}\,\mathrm{m}^{-2/3}$ corresponding to 'weak' and 'strong' turbulence (Andrews, 2004).

There are approximations that extend $\Phi_n(\kappa)$ outside the range of validity of Eqn. (3.12) to account for efficient dissipation at the small scale end (Tatarskii spectrum), and to avoid divergence for $\kappa \to 0$ (von Kármán spectrum).

The greatest detrimental effect of turbulence is observed in *coherent* LIDAR systems using heterodyne detection schemes (Belmonte, 2004; Henderson et al., 2005). This is not too surprising, as these systems, by their principle of operation, are sensitive to the phase of the incoming backscattered radiation. In such cases, turbulence-related optical path differences on the order of fractions of a wavelength that appear across the entrance pupil, can have strong impact on the actually measured signal.

Although *incoherent* LIDAR systems are sensitive just to the amplitude squared of the light reaching the detector, they are affected by turbulence. As a result the effect of turbulence has to be taken into account regarding the specific experiment described later in this text, which will be done in sec. 5.2.4, discussing the experimental results. The general pathways through which turbulence can affect incoherent LIDAR signals shall be listed subsequently.

Laser beam wandering affects overall pointing of laser beams transmitted through the atmosphere.

Laser beam spreading increases the effective diameter of the laser beam.

Image degradation leads to spread of the incident light energy in the image plane of the receiving optics. Generally it causes some variation in time of the distribution of light flux on the detector, although the imaged object and its illumination may be invariant in time.

Turbulence-induced enhanced backscattering of laser radiation on randomly dispersed scatterers, commonly referred to simply as 'enhanced backscattering' in the literature, may significantly increase the amount of light scattered in the direction of the receiver for truly monostatic LIDAR setups.

Turbulence-induced 'enhanced backscattering', is a more subtle effect which may affect LIDAR measurements, and which was observed by Gurvich and Kashkarov for the first time in 1977 (Gurvich

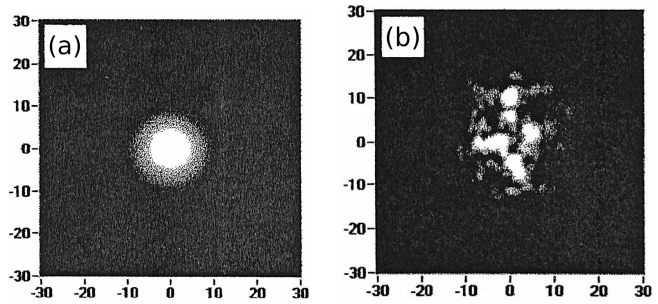

Figure 3.3.: (a) original ground level and (b) distorted laser beam profile after numerical propagation through a strongly turbulent atmosphere ($C_n^2 = 10^{-13}\,\mathrm{m}^{2/3}$) over a distance of 1 km; adapted from (Banakh et al., 2000), Figs. 1 and 2.

and Kashkarov, 1977).

It is important to note that, awkwardly, there is another entirely different phenomenon of importance for aerosol LIDAR, which is sometimes referred to as 'enhanced backscattering' as well. Other terms for this other phenomenon used in the literature are 'coherent backscattering' or 'weak photon localization' (Mishchenko et al., 2002). It is caused by the constructive interference of mutually reciprocal light paths under conditions of *multiple* aerosol scattering in an otherwise optically homogeneous atmosphere, and it occurs when light source and observer lie in exactly the same direction from the scattering ensemble of particles. This type of 'enhanced backscattering' is not meant in this context, besides it is of no importance under the conditions of low aerosol densities encountered in the present study.

The turbulence-induced enhanced backscattering considered here involves just single scattering and appears even under conditions of dilute aerosol. It has been shown to be capable of increasing the amount of light scattered back to the detector by a factor greater than 2 in a monostatic LIDAR setup (Chrzanowski et al., 2002), potentially leading to gross overestimation of the aerosol concentration.

The effect can be qualitatively explained as follows: firstly, wavefront deformations, continually picked up by the laser beam propagating through the turbulent refractive index distribution, transform into intensity modulations during further propagation. An initially Gaussian beam profile becomes inhomogeneous, and irradiance is distributed unevenly. This phenomenon is often termed 'scintillation'.

A simulated case is shown in fig. 3.3 b), where the initial beam profile, shown in panel a) of the same figure, was numerically propagated over 1 km through an atmosphere with $C_n^2 = 10^{-13}\,\mathrm{m}^{2/3}$ (strong turbulence) (Banakh et al., 2000). Besides apparent overall beam spreading, considerable resulting inhomogeneity of the intensity distribution (scintillation) can be observed.

To understand the effect of enhanced backscattering, one now can think of the bright spots in the beam profile as caused by net focusing lenses, resulting from the action of the refractive index inhomogeneities along the entire beam path. Accordingly, the bright spots represent the 'focal regions' of these lenses. The sequence of 'atmospheric lenses' thus image the light source to the bright spots.

They also reciprocally image the bright spots back to the light source: a ray of light scattered from some point inside one of the focal regions will more likely be sent back close to the source than a ray emanating from outside such a focal region. Stated differently, optical turbulence concentrates light energy in the same volume which is favourably imaged back towards the source – leading to enhancement of the relative amount of light energy propagating back towards the source even under conditions of isotropic scattering.

The strength of scintillation is greatest at distances Z_{str} on the order of 1 km under realistic conditions of atmospheric turbulence (Banakh et al., 2000; Chrzanowski et al., 2002). In fig. 3.4 the range dependence of the enhancement factor affecting an ideally monostatic incoherent backscattering LIDAR measurement is sketched as a function of range. It peaks close to the range Z_{str} where strongest scintillation occurs. However, also at a range of 100 m enhancement on the order of $\sim 10\,\%$ can be expected. Being naturally stochastic on a shot-to-shot basis, the enhancement represents a considerable contribution to random measurement noise.

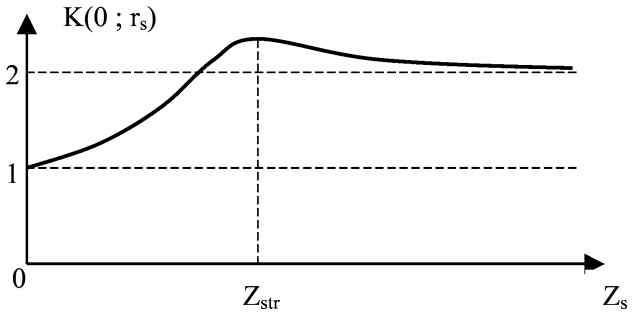

Figure 3.4.: Turbulence induced (single-scattering) backscattering enhancement factor K as a function of the distance between light source/receiver (LIDAR setup) and the scatterer (Fig. 2 from (Chrzanowski et al., 2002)).

Some of the effects of atmospheric turbulence may be reduced by design of the LIDAR optical system. It was shown by Chrzanowski *et al.* (Chrzanowski et al., 2002) that this noise source can easily be eliminated. According to their analysis, turbulence-enhanced backscattering can be practically completely avoided by displacing the detection optics from the transmitter optical axis by a few centimeters.

Other turbulence-induced noise sources may be reduced as well. Laser beam wandering and spreading, which increase the effective divergence of the LIDAR laser beam, may be accounted for by using detection optics offering a sufficiently large acceptance cone.

Image degradation, including displacement of the image due to global wavefront tilt, may modulate the amount of energy that reaches the detector. In a LIDAR system the spatial distribution of the collected light that is concentrated on the detector will generally differ on a shot-to-shot basis. The amount of fluctuation is related to the strength of the causing turbulence. This effect is expected to have the greatest influence in the close range, as here image degradation modulates geometrical compression (see sec. 5.2.2) in a random way.

Randomly varying inhomogeneities of the light distribution on the detector may also modulate the resulting signals indirectly. Spatial inhomogeneities of the detector may lead to slightly different electrical output signals, even though the integrated amount of received light energy is the same, and only the distribution across the sensitive area of the detector differs. Similar effect can be caused

by spatial inhomogeneity of the net coupling efficiency at the input face of an optical fibre bundle, representing the effective detector area in a LIDAR detection setup. If present, the effect of image fluctuations caused by turbulence is a random modulation imposed on each individual LIDAR transient. It may be reduced by inserting a homogenizing optical element, such as a diffusor, in front of the effective detector area, removing at least part of its spatial inhomogeneity, but at the cost of loss of overall optical transmittance.

Furthermore, in the presence of aerosol particles, the turbulent velocity field of the air can translate to local inhomogeneities of their number concentration, leading to additional shot-to-shot fluctuations of the backscattered LIDAR return signal.

To conclude this this section: turbulence can have a large impact on aerosol scattering measurements. One particular, potentially strong source of noise is turbulence-induced enhanced backscattering. It can be eliminated by proper design of the measurement geometry. Still, turbulence-induced fluctuations of atmospheric optical properties are a major source of unavoidable measurement uncertainty, affecting single-shot LIDAR return signals.

4. Inducing and sensing atmospheric condensation with light – background and preliminary considerations

4.1. Initial steps of natural cloud or fog droplet formation

Before turning to the issue of laser-induced (or, generally, light-induced) condensation of water out of the gas phase, in this section the mechanisms important in the initial steps of naturally occuring atmospheric condensation of water vapour will be discussed. This is done keeping in mind the goal to search for pathways by which laser light, and specifically filaments, can influence these processes, which is the subject of the subsequent section.

4.1.1. Nucleation

When new fog or cloud droplets are created, a liquid phase is newly formed out of vapour. At its onset, condensation does not proceed continuously and homogeneously, because the creation of a new phase requires the formation of a phase boundary. In fact, condensation starts suddenly and at discrete locations, and the vapour concentration of a condensable substance in a clean carrier gas (atmosphere) can be driven above the equilibrium vapour concentration which would prevail at the given pressure and temperature above an already existing extended liquid phase of the same substance. The atmosphere is then 'supersturated' with with vapour and with respect to the extended liquid phase.

Similar phenomena occur at the onset of boiling or freezing of initially homogeneous liquid substance. Under certain conditions liquids can be heated above their boiling point, resulting in eventual sudden and explosive boiling (see also sec. 4.3). Similarly, pure liquids can be supercooled below their freezing temperatures without actually changing to the crystalline state, because of the lack of impurities which could offer some starting point for crystallization.

The process of the creation of a new phase and a phase boundary starting from an initial seeding inhomogeneity is called nucleation. Inhomogeneities which have the ability to grow by continued transfer of substance from the old to the new phase are termed nuclei, and specifically condensation nuclei in the case of condensation out of the gas phase.

Nucleation is classified according to some basic criteria. If the condensation nuclei consist of the vapour substance alone, one speaks of *homogeneous* nucleation. If nucleation takes place on foreign preexisting nuclei, for example on solid particles or droplets of a different substance, this is called *heterogeneous* nucleation. Finally, nucleation of a single vapour substance is called *homomolecular*,

whereas nucleation involving two ore more vapour substances condensing into one mixed liquid phase is termed *heteromolecular*.

Under natural atmospheric conditions, especially in the troposphere, homogeneous nucleation is strongly competed by heterogeneous nucleation on ubiquitous aerosol. This especially holds in the tropospheric mixing layer where the earth's surface continually injects particles. However, it appears as if under the more extreme conditions which are created when an intense laser pulse interacts with the atmosphere, homogeneous nucleation may play a more important role. This is part of the results of the present work and will be discussed in the following. Therefore the subsequent sections will provide a brief summary of the main contributing effects in atmospheric fog or cloud droplet nucleation in order to allow to refer to them later in the context of laser-induced atmospheric condensation. Detailed introductory treatments of nucleation in the context of atmospheric physics can be found in the literature, such as (Seinfeld and Pandis, 2006) or (Pruppacher and Klett, 1997).

Classical nucleation theory was developed by J.W. Gibbs in the second half of the 19th century as part of his works in which he developed much of what is the basis of chemical physics. The thermodynamic potential of choice in the case of droplet nucleation is the Gibbs energy of the combined system of vapour and condensed phases, where the equilibrium state is the one minimizing the total Gibbs energy G of the gas phase–droplet system.

It is defined by

$$G = U + pV - TS,$$

where U is the internal energy, and T and S are temperature and entropy of the system, V is the occupied volume, and p is the pressure. At constant temperature and pressure the Gibbs energy is equivalently given by the sum of the products of the chemical potential of each species and the respective number of moles,

$$G = \sum_{i=1}^{k} \mu_i n_i.$$

The chemical potentials μ_i express how much the energy of the system changes upon addition of an amount of species i.

All gaseous species are assumed to behave as ideal gases, which is generally well justified under atmospheric conditions (Pruppacher and Klett, 1997; Seinfeld and Pandis, 2006), resulting in gas phase chemical potentials of the form

$$\mu_i(T) = \mu_i^\circ(T, p_\circ) + RT \ln(p_i/p_\circ),$$

where $p_\circ$ denotes standard pressure, and $\mu_i^\circ(T, p_\circ)$ is the chemical potential at standard pressure and temperature T.

In classical nucleation theory the liquid phase is assumed to have the same thermodynamic properties as the bulk liquid substance. This specifically entails that the chemical potentials are treated as independent of droplet size. Besides ignoring that nanometer sized aggregates can rarely be treated

as bulk substance, classical nucleation theory also neglects possible effects of molecular orientation or conformation which have been shown to be important for cluster-sized atmospheric nuclei (Yu, 2005). Still classical nucleation theory serves as a basis for theories taking into account such size effects (Seinfeld and Pandis, 2006). Such theories often involve assumptions about the dependence of surface tension on curvature.

The most important factor in the nucleation of cloud or fog droplets is the increase of total Gibbs energy change due to the work needed to form the phase boundary. Classical nucleation theory assumes a spherical droplet with radus r, and the surface energy to be equal to the bulk surface tension σ times the surface area,

$$\Delta G_{\text{surface}} = 4\pi r^2 \sigma. \tag{4.1}$$

The assumption of a surface tension which is equal to that of the bulk under any set of conditions, is commonly called the 'capillarity approximation'. Just like the assumption of bulk thermodynamic properties, this is sure to fail for sufficiently small clusters.

While the surface term $\Delta G_{\text{surface}}$ always leads to a positive change of Gibbs energy when a vapour molecule is added to the droplet, a chemical potential μ_l in the liquid phase, which is lower than the corresponding potential μ_v in the gas phase, leads to a negative contribution to the total change of Gibbs energy. Based on the assumption of ideal gas behaviour, the difference of the chemical potentials can be expressed in terms of the actual vapour pressure p_v and the saturation vapour pressure over a flat phase boundary p_v°,

$$\mu_l - \mu_v = -R\,T \ln(p_v/p_v^\circ), \tag{4.2}$$

where, in the case of pure vapour and a pure liquid phase, the ratio $p_v/p_v^\circ := S$ is called the saturation ratio, and in the case of water is equivalent to the 'relative humidity', stated in percent. The total Gibbs energy change due to condensation of n moles of vapour substance into a spherical liquid droplet, under the previously mentioned assumptions, is

$$\Delta G = n(\mu_l - \mu_v) + \Delta G_{\text{surface}}. \tag{4.3}$$

An existing droplet will grow if the first term is negative and dominates the positive surface term. Different scenarios of nucleation differ in the way in which the chemical potential μ_l of the vapour substance in the liquid phase is influenced by the presence of other substances and/or a soluble or insoluble solid phase.

Homogeneous homomolecular nucleation is the simplest of all cases, as only one single substance is involved. The change of Gibbs energy due to formation of a droplet of liquid of radius r in an atmosphere containing vapour with a saturation ratio S takes on the form (Seinfeld and Pandis, 2006)

$$\Delta G = -\frac{4\pi}{3}\frac{k_{\text{B}}T}{v_\ell}\ln(S)\,r^3 + 4\pi r^2\sigma, \tag{4.4}$$

where again σ is the bulk surface tension, k_B is Boltzmann's constant, and v_ℓ is the volume occupied per molecule in the liquid phase. As mentioned before, the surface term involving σ is always positive. The bulk term switches sign when the atmosphere is saturated with vapour, *i.e.* when $S = 1$. The plot in Fig. 4.1 illustrates how the sign of the bulk term influences ΔG as a function of radius r. For $S > 1$ the Gibbs energy change will attain a maximum at some finite radius $r = r_{crit}$, because the bulk term is proportional to r^3, while the surface term scales as r^2. The maximum is located at

$$r_{crit} = \frac{2\sigma v_\ell}{k_B T \ln(S)},$$

which can be rearranged to yield the equilibrium saturation ratio $S_{equ}(r)$ for a given radius r,

$$S_{equ}(r) = \exp\left(\frac{2\sigma v_\ell}{k_B T r}\right). \tag{4.5}$$

The height of the Gibbs energy barrier is

$$\Delta G^* := \Delta G(r_{crit}) = \frac{4\pi}{3}\sigma r_{crit}^2 = \frac{16\pi}{3}\frac{\sigma^3 {v_\ell}^2}{(k_B T \ln(S))^2}. \tag{4.6}$$

Because $\Delta G(r)$ is monotonically decreasing for $r > r_{crit}(S)$ and fixed S, any droplet exceeding the critical radius will further grow. Correspondingly, droplets with $r < r_{crit}$ tend to evaporate. In the case $S > S_{equ}(\tilde{r})$, similar holds for droplets larger or smaller than $\tilde{r}$, respectively. Under conditions

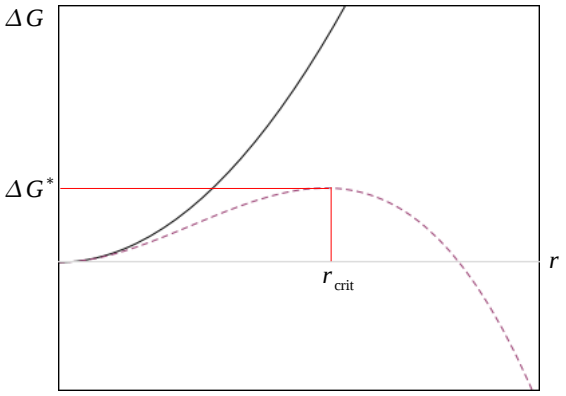

Figure 4.1.: Sketch of the Gibbs energy change of condensation, ΔG, as a function of droplet radius r when the droplet is formed out of the vapour phase. Under conditions of supersaturation (saturation ratio $S > 1$) the curve $\Delta G(r)$ attains a maximum at the critical radius r_{crit}, and a Gibbs energy barrier of height $\Delta G^* = \Delta G(r_{crit})$ results.

of $S \leq 1$ homogeneous homomolecular nucleation cannot occur, as $\Delta G(r)$ is nowhere a decreasing function of r.

Vapour molecules permanently collide with each other due to thermal motion. A certain fraction of such collisions leads to formation of dimers, which either break apart at some rate, or which collide with another vapour monomer, and with some probability form a trimer, and so on. In classical homogeneous nucleation theory the equilibrium distribution of vapour substance i-mers in a Gibbs-potential according to Eqn. 4.4 is derived. The system of agglomeration reactions underlying the latter is illustrated in Fig. 4.2. The nucleation rate J in terms of number of nucleated droplets per unit

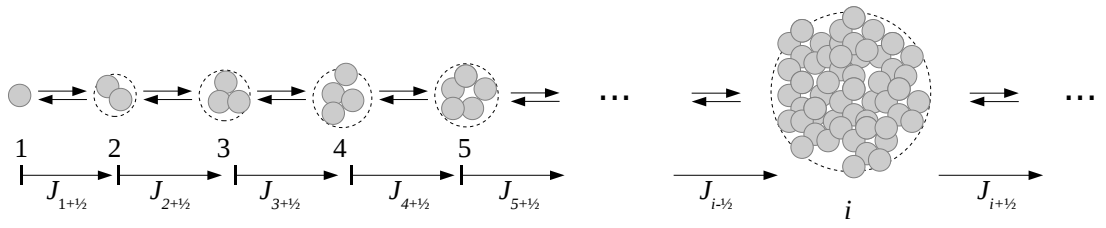

Figure 4.2.: System of agglomeration reactions considered in classical nucleation theory used to derive the equilibrium distribution of vapour substance i-mers and finally the nucleation rate J. In each step only one monomer is added or removed. After (Seinfeld and Pandis, 2006)

time per unit volume is equivalent to the flux of i_{crit}-mers per unit volume that eventually surpass the critical number of constituent molecules corresponding to the critical radius r_{crit}, and slide down on the right side of the Gibbs energy barrier towards ever increasing radii. It is generally expressed by

$$J = A \exp\left[-\frac{\Delta G^*}{k_{\mathrm{B}} T}\right], \tag{4.7}$$

Where A is a function of the vapour pressure of the condensing species, and also depends on the composition of the critical cluster when multicomponent nucleation is considered. The expression for J derived in (Seinfeld and Pandis, 2006) for homogeneous unary nucleation is just stated here:

$$J = \left(\frac{2\sigma}{\pi m_v}\right)^{1/2} \frac{v_\ell N_v^2}{S} \exp\left[-\frac{\Delta G^*}{k_{\mathrm{B}} T}\right], \tag{4.8}$$

where N_v is the number concentration of vapour monomers, m_v is the mass of a vapour monomer, and the other symbols are defined as in Eq. 4.4. It is obvious that the Gibbs energy barrier ΔG^* in the exponent to a large extent determines the dependence of J on the thermodynamic state of the overall system. Reconsidering the form of ΔG^* (Eq. 4.6), one sees that the term $\ln(S)^{-2}$ in the exponent quenches J close to $S = 1$ and makes it very sensitive to S above. Table 4.1.1 shows calculated nucleation rates as well as critical i-mer sizes for water and a range of saturation ratios. Note that even at $S = 3$, the nucleation rate corresponds to about one nucleation event per two weeks per cm^3, while at $S = 4$ there is appreciable nucleation flux. This fits well to the threshold for visible spontaneous water fog formation of $S \gtrsim 4$ which was observed already in early experiments with cloud chambers (Tohmfor and Volmer, 1938). It should also be noted that at very high nucleation rates for large initial S the limited amount of available vapour per volume is quickly consumed, which quenches nucleation and sets a limit to the growth of the nuclei. The most important result here is that homogeneous homomolecular nucleation of water vapour is totally irrelevant in the natural atmosphere where S rarely exceeds unity by a few percent (Pruppacher and Klett, 1997; Seinfeld and Pandis, 2006). The formation of fog and clouds must rely on different mechanisms. As mentioned in the introduction to this section, the reason for this is the presence of further agents that lower the Gibbs energy barrier to be overcome.

S	i_{crit}	r_{crit}(nm)	$J(cm^{-3}s^{-1})$
2	525	1.55	2×10^{-54}
3	132	0.98	1.2×10^{-6}
4	66	0.78	0.84×10^{6}
5	42	0.67	1.33×10^{11}
6	30	0.60	1.08×10^{14}
7	24	0.56	0.8×10^{16}
8	19	0.51	1.6×10^{17}
9	16	0.49	1.5×10^{18}
10	14	0.46	8.5×10^{18}

Table 4.1.: Homogeneous nucleation rate and critical cluster size for water at $T = 293\,K$, after (Seinfeld and Pandis, 2006), Table 11.4; calculated using Eq. 4.8.

Homogeneous heteromolecular nucleation Homogeneous nucleation can be substantially facilitated when two or more vapor substances are involved. In the atmosphere these are typically water and trace gases that dissolve in water undergoing ionic dissociation, such as H_2SO_4 or HNO_3. In this case the dissolution reaction lowers the Gibbs energy of the resulting mixed liquid phase, or, stated differently, the equilibrium vapour pressures of both components over the mixed liquid phase, are reduced as compared to those over the respective pure phases. In the case of two nucleating substances, the Gibbs energy change upon formation of a nucleus that consists of a mixture of molecules of substances A and B now is given by

$$\Delta G = n_A(\mu_{Al} - \mu_{Av}) + n_B(\mu_{Bl} - \mu_{Bv}) + \Delta G_{surface}. \tag{4.9}$$

Indices v and l again denote vapour and liquid phases.

As ΔG depends on the size and composition of the respective droplet, the system moves on a Gibbs energy hypersurface during its time evolution. It has been shown by Reiss (Reiss, 1950) that $\Delta G(n_A, n_B)$ is saddle-shaped. A growing binary mixed droplet must pass the ridge of the saddle surface to eventually nucleate, and it will probably do so close to the saddle point. In this case the latter defines the effective Gibbs energy barrier of nucleation. The nucleation rate can be estimated from the height of the saddle point, provided that the path in the (n_A, n_B)-plane actually taken by the growing droplet passes there (Reiss, 1950).

A number of additional difficulties arise in the theoretical treatment of binary nucleation. To mention two of them, the path across the saddle surface, influencing the preexponential factor of the nucleation rate, is a priori unknown. Also the evaluation of ΔG is more complicated than in the homomolecular case, as not only the chemical potentials, but also the surface tension entering the surface energy term are functions of the mixing ratio (Seinfeld and Pandis, 2006).

Heteromolecular homogeneous nucleation of new particles out of the gas phase actually happens and plays an important role in the aerosol production and cloud formation in the stratosphere and in the troposphere. The binary system H_2O–H_2SO_4 is considered the most important in this regard (Seinfeld and Pandis, 2006), not only because sulphuric acid is very hygroscopic and an efficient nucleation partner for water, but also because it is relatively abundant. Stratospheric aerosol even mainly consists of a concentrated aqueous sulphuric acid solution and is present in a liquid state even at

temperatures down to −85 °C. Also in the troposphere, a major fraction of particles smaller than 1 μm are sulphuric (Jaenicke, 1993). Atmospheric sulphuric compounds have various origins, but most of the gaseous sulphur in the troposphere is biogenic (~ 80 %). The remaining part stems from volcanoes and fuel burning (Jaenicke, 1993). The final step of sulphuric acid production in the atmosphere is the gas phase oxidation of SO_2 to SO_3 involving ·OH radicals. The SO_3 then quickly reacts with water vapour to form H_2SO_4 (Seinfeld and Pandis, 2006).

Another highly hygroscopic compound involved in heteromolecular atmospheric nucleation is nitric acid, HNO_3. It is found in tropospheric aerosol and results from the oxidation of nitric oxide and nitrogen dioxide NO_x. The ambient concentrations of its precursors vary from 0.02 ppb up to 1000 ppb in polluted urban regions. It is of special interest here because various oxides of nitrogen result as chemical products from laser generated air plasmas.

More recently experiments performed in the atmospheric chamber at Paul Scherrer Institute in Switzerland showed that H_2SO_4 formed by oxidation of photolytically produced ·OH radicals very efficiently nucleates with organic compounds (Metzger et al., 2010). Concentrations were varied up to $n_{H_2SO_4} \simeq 4 \times 10^7$ cm^{-1}, which is the range typical for naturally observed nucleation events. The nucleating organic was present at similar concentrations. In these experiments the critical nuclei consisted of only one molecule of H_2SO_4 and organic substance, respectively, resulting in nucleation rates way higher than would result from the usually considered sulphuric acid–water binary nucleation.

Binary homogeneous nucleation of H_2SO_4 from SO_2 oxidation by ·OH radicals with gaseous organic substance, probably also partially oxidized by ·OH may explain the observed stronger production of new particles by nucleation. The bimolecular critical nuclei of said process imply a linear dependence of the nucleation rate on the sulphuric acid vapour concentration. Already before (Spracklen et al., 2008), this dependence had been shown to lead to better agreement of concentrations of Cloud Condensation Nuclei (CCN, see sec. 4.1.2) obtained from model calculations when compared with observations.

Heterogeneous nucleation Especially in the lower atmosphere the ubiquitous presence of aerosol makes heterogeneous nucleation an important mechanism for the production of water droplets. Preexisting solid aerosol offers a large surface area per volume, and the particles act as favourable landing sites for impinging vapour molecules. At the onset of heterogeneous nucleation on a solid

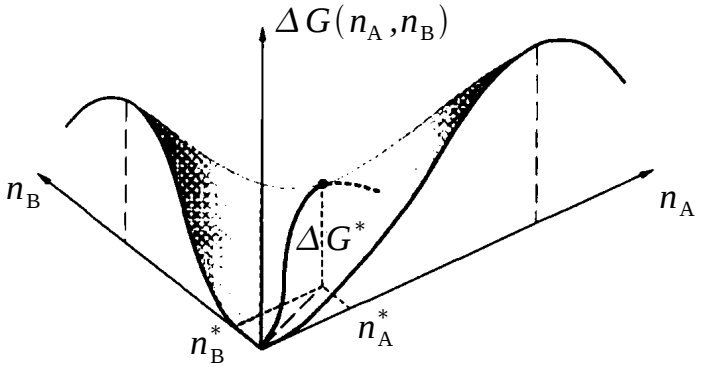

Figure 4.3.: Saddle surface $\Delta G(n_A, n_B)$ of Gibbs energy change in classical binary homogeneous nucleation. Figure adapted from (Seinfeld and Pandis, 2006).

nucleus, adhesion counteracts surface tension and reduces the expense of Gibbs energy needed to add another vapour molecule to the emerging liquid phase. Macroscopically this corresponds to a reduced contact angle between the solid and the liquid phase. Additionally, the solid particle surface can aid nucleation by facilitating vapour transport: adsorbed vapour substance can redistribute itself by surface diffusion and may more efficiently form a liquid nucleus somewhere on the particle. This effect increases the effective surface area of the nucleus for catching vapour molecules, leading to its accelerated growth.

Aerosol particles that are soluble or partly soluble in water (for example, inorganic salts) or particles partly composed of such) are efficient nucleation sites, as the Gibbs energy barrier for condensation is further lowered by the solvation energy. Generally the transition from solid to liquid occurs abruptly once a critical water relative humidity, the 'deliquescence relative humidity' (DRH) is overcome. Typical salt aerosols deliquesce at rather low relative humidities, and are then treated as solution droplets interacting with the vapour phase. Very hygroscopic substances like sulphuric acid take up water at any ambient relative humidity and do not possess a DRH. Typical values for DRH at 298 K of common salt subtances are RH = 84.2 ± 0.3 % for KCl, RH = 75.3 ± 0.1 % for NaCl, and as low as RH = 40.0 % for NH_4HSO_4 (values from (Seinfeld and Pandis, 2006)).

The presence of atmospheric aerosol reduces the critical saturation ratio for water vapour condensation to ~ 102 % or less (Hobbs, 1993). This is the other reason why homogeneous nucleation of pure water substance is basically irrelevant for the atmosphere. As a consequence, the presence of aerosol can suppress the formation of new condensation nuclei in favour of the growth of already existing particles, even under conditions which would make homogeneous nucleation possible. The preexistent aerosol acts in two ways: firstly it represents a sink for precursor substance, lowering its vapour concentration. Secondly, even if homogeneous nucleation were possible, aerosol particles tend to withdraw the small freshly generated nuclei by coagulation.

Ion-induced nucleation J.J. Thomson recognized that the presence of electric charges may reduce the threshold saturation ratio for the nucleation of droplets forming out of the vapour phase (Thomson, 1906). This is caused by charge-induced additional lowering of the Gibbs energy for a vapour molecule entering the charged cluster or droplet, leading to a reduction of the equilibrium vapour pressure over its surface.

In his original theory J.J. Thomson treated the forming water droplets as conducting spheres, which is apparently justified by the large DC dielectric constant $\varepsilon_{H_2O,bulk} \simeq 80$ of water. Later Tohmfor and Volmer (Tohmfor and Volmer, 1938) showed that the physical reality is better described if water is treated as a dielectric, leading to a correction factor $1 - \varepsilon_{H_2O}^{-1}$ in the charge-related contribution to the Gibbs energy change as compared to the corresponding expression for the case of a conducting sphere. Including the correction by Tohmfor the equilibrium vapour saturation ratio S_{CKT} over a spherical charged dielectric liquid surface is

$$S_{CKT} = \exp\left\{\frac{m_v}{k_B T \rho_l}\left(\frac{2\sigma}{r} - \frac{\left(1-\varepsilon_l^{-1}\right)q^2}{32\pi^2\varepsilon_0 r^4}\right)\right\}. \tag{4.10}$$

Including the contribution of surface curvature (due to Lord Kelvin) and electrostatic energy (due to J.J. Thomson), this is also known as the classical Kelvin-Thomson equation (CKT).

Tohmfor and Volmer were able to show that much more realistic nucleation rates are predicted when explicitly treating water as a dielectric. However, to achieve this agreement, a dielectric constant of $\varepsilon_{H_2O} \simeq 1.85$ had to be assumed, which is far below the bulk DC value. Tohmfor and Volmer offered the explanation that probably the reorientation of permanent water dipole moments is responsible for this deviation.

The additional stabilization of small clusters or droplets due to single elementary charges is rather weak. In particular, single elementary charges are generally not sufficient to reduce the equilibrium vapour pressure above small water drops enough to result in appreciable nucleation under conditions of less extreme supersaturation. This is illustrated in Fig. 4.1.1, where the equilibrium saturation ratio S_{sat} over a cluster/droplet of pure water is plotted for different numbers of elementary charges, as it is predicted by the classical Kelvin-Thomson equation Eq. 4.10. The range where the droplet approximation is valid starts above $r \cong 0.4\,\mathrm{nm}$, corresponding to a cluster of approximately 10 water molecules (Yu, 2005) and is marked by a vertical gray line.

One clearly sees that $S_{equ} \gg 1$ even for multiply charged water clusters. Figure 4.5 illustrates the

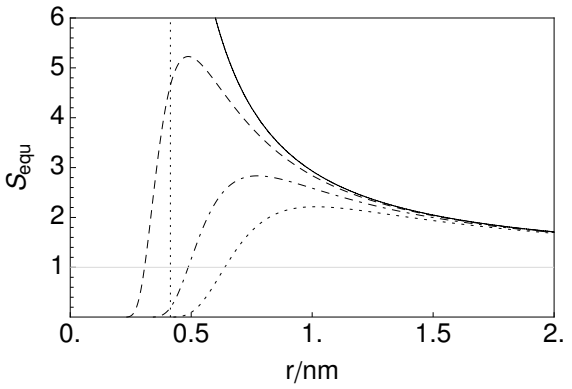

Figure 4.4.: Equilibrium water vapour saturation ratio over a water droplet as a function of radius according to the Kelvin-Thomson equation, $T = 293K$ $\varepsilon_{H_2O} = 1.85$ (see text). Vertical gray line: approximate start of validity of the droplet approximation (see text). solid, dashed, dash-dotted, dotted: zero to three elementary charges, respectively.

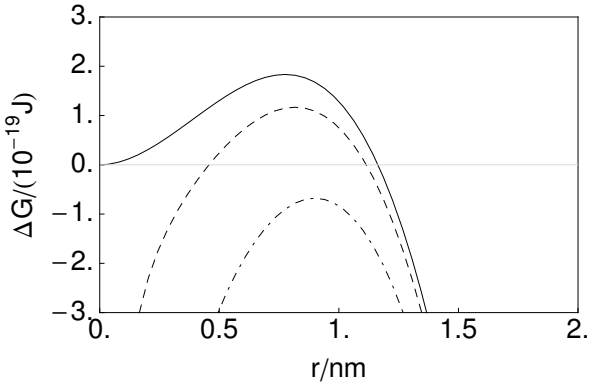

Figure 4.5.: Total Gibbs energy change of formation of a water droplet with radius r according to the Kelvin-Thomson equation. Plotted for $T = 293\,\mathrm{K}$, $S = 4$. Black: uncharged droplet, dashed: single elementary charge, dash-dotted: double elementary charge.

effect of charge on the Gibbs energy barrier. Under the conditions of strong supersturation assumed in plotting the curves, a single elementary charge shifts the top of the energy barrier down by about 30 % a double elementary charge even removes the barrier completely. Experiment shows that under the considered conditions of high supersaturation the presence of a singly charged ion in a water cluster

lowers the energy barrier sufficiently to cause an observable nucleation rate. This is however not the case for the atmospherically relevant levels of water vapour supersaturation.

One can easily see that the classical Thomson theory of ion-induced nucleation does not predict stabilized droplets larger than a few nanometers under just saturated conditions. The size $r = r_{\mathrm{stab}}$ of stabilized clusters is given by the intersection of the rising slope of the $S_{\mathrm{equ}}(r)$ curve with the $S = 1$ line. Clusters smaller than this size grow until the equilibrium saturation ratio over their surface equals the ambient saturation ratio. Figure 4.6 shows r_{stable} as a function of the number of elementary charges under similar conditions as for Fig. 4.1.1. It is obvious that even large numbers of elementary charges may not account for stabilized droplets bigger than a few nanometers.

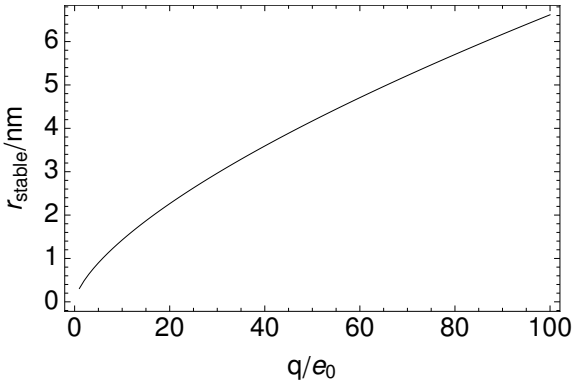

Figure 4.6.: Size of the charge stabilized pure water droplet under conditions of $S = 1$ as a function of number of elementary charges, according to the classical Kelvin-Thomson theory (see text). Temperature $T = 293\,\mathrm{K}$. Note that this plot is rather a caricature as it does not consider the Rayleigh limit of charge beyond which Coulomb self-repulsion of the confined charge would not be balanced by surface tension any more, leading to disruption of the droplet.

The simple picture of ion-induced nucleation can be refined to accomodate effects which are important especially when the forming clusters are too small to treat them as drops of a continuous fluid. Modern theories of ion-induced nucleation explicitly consider the microscopic structure and water dipole-dipole interaction in pre-nucleating embryo clusters (Kusaka et al., 1995). The additional feature predicted when molecular dipoles are considered is an asymmetry of the interaction energy with respect to the sign of the ion charge, resulting in a sign preference of the respective nucleation rates, which have actually been observed for polar condensing molecules (Adachi et al., 1992). The classical Kelvin-Thomson theory can be modified by explicitly considering the microscopic interaction of condensing dipolar molecules with each other, as well as with the core ion (Yu, 2005), leading to a more accurate description.

For pure water, all these refinements do not lead to dramatic changes of the critical charged cluster size and the degree of supersaturation where a considerable nucleation rate is reached.

A step beyond the strongly simplified Kelvin-Thomson approach may however be of great benefit for the description of heteromolecular nucleation, where the critical clusters are smaller and the critical cluster size is potentially more affected by steric effects. Some models of heteromolecular homogeneous nucleation actually include effects of electrical charge (Yu, 2006; Yu and Turco, 2001). Specifically, such models suggest that ions may play an important role in the binary homogeneous nucleation of water and sulphuric acid (H_2SO_4) even in the lower atmosphere, and even in the planetary boundary layer, where it is strongly competed by heterogeneous nucleation (Yu, 2006).

The Nucleation Theorem relates the work of critical cluster formation with the size of the critical nucleus. It was firstly formulated by Kashchiev (Kashchiev, 1982) for unary nucleation, extended to multicomponent systems by Oxtoby and Kashchiev (Oxtoby and Kashchiev, 1994), and critically analyzed and generalized by Schmelzer (Schmelzer, 2001). The nucleation theorem allows to infer properties of the critical clusters directly from experimentally measured nucleation rates.

One of its formulations, given by Oxtoby and Kashchiev for isothermal multicomponent nucleation, is

$$\frac{\partial \Delta G(n^*, \Delta\mu)}{\partial \mu_{v,i}} = -\Delta n_i^*. \tag{4.11}$$

Here $\Delta G(n^*, \Delta\mu)$ denotes the height of the Gibbs energy barrier, that is, the Gibbs energy change required to reach the critical number of molecules of the ith nucleating substance, n_i^*, in a cluster. According to the nucleation theorem its derivative with respect to the chemical potential of the ith component in the vapour phase determines the 'excess number' of molecules of species i in the critical cluster. The excess number n_i^* is given by the number of molecules in the volume occupied by the critical cluster minus the number of molecules which would occupy the same volume when still in the vapour phase.

The general expression for the nucleation rate, Eq. 4.7, also holds for multicomponent nucleation. Then, further following Oxtoby and Kashchiev, the nucleation theorem for isothermal binary nucleation can be restated as

$$\Delta n_i^* = \frac{\partial (k_\mathrm{B} T \ln J)}{\partial \mu_{v,i}} - c, \tag{4.12}$$

where c is a small number typically between 0 and 1. Additionally assuming the vapour phase as an ideal gas mixture (with component chemical potentials according to Eq. 4.1.1), one obtains a very useful relationship of nucleation rate, vapour concentration, and critical cluster composition and size:

$$\frac{\partial \ln J}{\partial [\, i \,]} \simeq n_i^*. \tag{4.13}$$

This is due to Eq. 4.12 and the assumption of a cluster density much higher than the gas phase density, leading to $\Delta n_i^* \simeq n_i^*$. The critical cluster size is obtained within an uncertainty of about one molecule of either component.

In the special case of binary nucleation of two gaseous components A and B following power laws with respect to the concentration of either component, $J \propto [A]^{m_A}$ when $[B]$ is held fixed, and $J \propto [B]^{m_B}$, for fixed $[A]$, directly tells the number of molecules of components A and B in the critical nucleus:

$$J = k[A]^{m_A} \Rightarrow n_A^* \simeq m_A$$

In this form the nucleation theorem was used by Metzger et al. (Metzger et al., 2010) to gain insight in the binary nucleation of H_2SO_4 and volatile organic compounds (see the previous section on binary homogeneous nucleation in the atmosphere). In the present work the nucleation theorem will not be directly applied in the evaluation of experimental results. It may however be of use in future investigations of laser induced condensation.

4.1.2. Activation of atmospheric particles

If particles initially residing in a minimum of Gibbs energy are exposed to a different atmosphere, this may result in their present size not to be in equilibrium with the surrounding anymore. A change of the ambient vapour saturation ratio will lead to evaporation or growth until the equilibrium is established again. Provided the saturation ratio rises and eventually overcomes the critical saturation ratio, the growth will continue – in principle – indefinitely. Under such conditions the particles are said to be *activated*.

In some contexts calling a particle a 'droplet' is equivalent to saying it is activated (Laaksonen et al., 1998). Note that in this text the word 'droplet' does not entail this implication.

Those initially stable particles may be droplets of ionic solutions, charge-stabilized droplets, or solid or partially solid particles, which may also contain a water soluble fraction. Activation may result from an actually rising ambient vapour pressure of condensable substance, but also from changes of the chemical composition of the (at least partially liquid) particle. The latter may result from the uptake of dissociating gaseous substance, such as HNO_3(g) or H_2SO_4(g). Some consequences of such processes will be discussed in a subsequent paragraph.

Activation of a particle or droplet is closely related with heterogeneous nucleation, because growth starts from an already existing phase boundary.

In the case of a mixed aerosol population, consisting of particles of different sizes and chemical compositions, only part of it may become activated and eventually grow to cloud droplets, while the other part remains unactivated. Even not being able to grow indefinitely, the equilibrium sizes of the unactivated part may well shift towards larger diameters, causing an overall change of the scattering properties of the aerosol. In cloud physics, unactivated particles are commonly called 'haze'. In other contexts the term 'haze' may imply specific properties of the particles. Throughout the present text the more general cloud physics definition is used.

One common classification of atmospheric aerosol is based on the threshold vapour supersaturation above which a particle gets activated. Any particle which is activated at a saturation ratio below the threshold of homogeneous nucleation is considered a condensation nucleus (CN). The subclass of particles which get activated at atmospherically relevant saturation ratios up to 102 % are often classified as 'cloud condensation nuclei' (CCN). It is also common to explicitly specify the level of supersaturation parting CCN from CN to remove ambiguity.

Under conditions of water vapour pressure levels close to saturation, tropospheric air contains wetted background aerosol ('haze' according to the convention of cloud physics). The larger of these wetted aerosol particles can heterogeneously nucleate water vapour at saturation ratios just slightly exceeding unity (Pruppacher and Klett, 1997), qualifying them as cloud condensation nuclei. Even in 'clean' maritime air their concentration is $n_{\mathrm{CCN}} \sim 100 - 1000\,\mathrm{cm}^{-3}$. This class of particles has minimum diameters between $D_{\mathrm{P}} = 0.05\,\mu\mathrm{m}$ and $D_{\mathrm{P}} = 0.14\,\mu\mathrm{m}$ (Seinfeld and Pandis, 2006), depending on the individual content of soluble material.

4.1.3. Köhler theory

The inclusion of Gibbs energy gain due to the dissolution of solids, such as NaCl or NH_4NO_3 in the equations describing the equilibrium vapour pressure over a spherical droplet was firstly done by H. Köhler (Köhler, 1936). In the simplest case a single, fully soluble, dilute substance which has a vanishing equilibrium vapour pressure is dissolved in the initial CN. The latter means that it is strongly solvated and practically does not evaporate from the droplet, which is true for NaCl and other inorganic ionic compounds, but not, for instance, for CO_2. Inclusion of the solute effect leads to a modified Kelvin equation Eq. 4.5

$$S_{\mathrm{equ}}(r) = \exp\left(\frac{2\,\sigma\,v_\ell}{k_{\mathrm{B}}T\,r} - \frac{3\,\nu_s n_s v_\ell N_{\mathrm{A}}}{4\pi r^3}\right) \simeq 1 + \frac{2\,\sigma\,v_\ell}{k_{\mathrm{B}}T\,r} - \frac{3\,\nu_s n_s v_\ell N_{\mathrm{A}}}{4\pi r^3}. \tag{4.14}$$

The solute-related negative term in the exponent depends on the number of moles of solute, n_s, and the number of ions resulting from each dissociating solute molecule, ν_s. As before v_l is the molecular volume of the condensing liquid (water) and r is the droplet radius. Similar to the charge-related term in the Kelvin-Thomson equation the negative sign of the solute term counteracts the surface energy-related positive term. It however generally cannot dominate it. This is why the effect of a soluble core particle on the critical supersaturation may well lead to a considerable reduction close to unity, but not below.

The classical Köhler theory can be extended by inclusion of the dissolution of gaseous soluble substance, as it was already mentioned in a previous paragraph. Taking into account the Gibbs energy change of droplet growth due to the free energy change due to the total of dissolution, dissociation, and solvation of the soluble gas molecules leads to the result that the presence of soluble gases can lead to conditions which allow cloud droplets to form and exist even in atmospheres subsaturated with water vapour (Laaksonen et al., 1998; Seinfeld and Pandis, 2006).

The expression derived by Laaksonen et al. for the equilibrium water vapour saturation ratio over a nucleus of radius r_{p}, containing a soluble core of n_s moles, and surrounded by an atmosphere containing soluble dissociating trace gas, is given by Eq. 4.15. This expression is analogous to Eq. 4.14,

$$\begin{gathered} S_{\mathrm{equ}}(r_{\mathrm{p}}) \simeq 1 + \frac{2\,\sigma\,v_\ell}{k_{\mathrm{B}}T\,r_{\mathrm{p}}} - \frac{B_s}{r_{\mathrm{p}}^3} - \frac{B_a}{r_{\mathrm{p}}^3}, \\ B_x = \frac{3\,\nu_x n_x v_\ell N_{\mathrm{A}}}{4\pi} \quad \text{with} \quad x = s \text{ or } x = a. \end{gathered} \tag{4.15}$$

The additional term $-B_a/r_{\mathrm{p}}^3$ has similar form as the term $-B_s/r_{\mathrm{p}}^3$, in the corresponding expression resulting from the classical Köhler theory. It describes the influence of a fixed number of moles n_s of highly soluble dissociating substance on the equilibrium water vapour pressure over the solution droplet of radius r_{p}. The new term involving B_a depends on n_a, the number of moles of dissolved soluble gas contained in the droplet. This number is *not* fixed but it is determined by an equilibrium

between dissolution and outgassing of the soluble gas a. Consequently it is a function of the ambient vapour pressure p_a of soluble gas, the droplet radius r_p, and the specific tendency of the gas to dissolve and dissociate in water.

The latter is encoded in its Henry's law constant H_a. According to Henry's law the equilibrium concentration of dissolved soluble gas in a dilute solution is proportional to its partial pressure over the flat phase boundary between the gas phase and the solution:

$$[a(\mathrm{aq})] = H_a p_a$$

Laaksonen et al. (Laaksonen et al., 1998) derive the equilibrium value $n_a(r_\mathrm{p}, p_a, H_a)$ assuming that Henry's law holds, and that each soluble gas molecule dissociates into exactly one cation and one anion (as it is the case for HNO_3). This leads to Eq. 4.15 taking on the form

$$S_\mathrm{equ}(r_\mathrm{p}) \simeq 1 + \frac{2\,\sigma\,v_\ell}{k_\mathrm{B} T\,r_\mathrm{p}} - \frac{B_s}{r_\mathrm{p}^3} - 2\sqrt{p_a H_a} \tag{4.16}$$

It is important to note that tabulated Henry's law constants usually do not include the shifting of the dissolution equilibrium caused by dissociation reactions. For example, solvated HNO_3, being a strong acid, undergoes complete dissociation at not too low pH values, making this effect very pronounced for this type of gas. Inclusion of the equilibrium reaction $HNO_3(\mathrm{aq}) \rightleftharpoons NO_3^-(\mathrm{aq}) + H^+(\mathrm{aq})$ with the equilibrium constant K_diss leads to the effective Henry's law constant $H^*_{HNO_3}$ which turns out as

$$H^*_{HNO_3} = H_{HNO_3}\left(1 + \frac{K_\mathrm{diss}}{[H^+]}\right) \tag{4.17}$$

In Fig. 4.7 an example of the effect of a soluble gas on the equilibrium saturation ratio over a CN is shown for the case of gaseous HNO_3 at a concentration of 10 ppb, corresponding to moderately polluted conditions. Growth of existing CN by uptake of dissociating gaseous species may be one of the important pathways to laser induced condensation of water vapour.

As Laaksonen et al. remark (Laaksonen et al., 1998), the stabilization of droplets in a water-subsaturated atmosphere caused by the uptake of dissociating gaseous substance generally does not entail their 'activation' according to the traditional definition. Nevertheless it may lead to stable droplets having diameters up to $\sim 10\,\mu$m, which are typical of larger cloud droplets. As a consequence, the total amount of condensed mass may substantially grow, and the generated particles will take part in microphysical processes such as coagulation, altering the subsequent evolution of the aerosol, as compared to the case of no soluble gas. Besides these direct effects, the droplets stabilized at relatively larger diameters are expected to "interact significantly [...] with electromagnetic radiation" (Laaksonen et al., 1998), that is, the light scattering properties of the aerosol are changed by the action of the soluble gas.

Laaksonen et al. expect the exceptionally large particles ($r_\mathrm{p} > 1\,\mu$m) to form on relatively long timescales of several tens of seconds, as the "transfer of soluble gas to a growing droplet becomes a rate-limiting factor". This estimation of course applies to the typically low ambient concentrations

of soluble gas considered in their study, and may be exceeded when higher local concentrations are produced by a laser.

4.1.4. Diffusive evaporation and growth of a droplet

Comparing the equilibrium vapour pressure over a droplet or a nucleation germ to the actual ambient vapour pressure allows to predict whether the droplet will shrink or grow in the next instance. To estimate the actual velocity of size change one has to model the heat and mass transport through the droplet surface and through its surrounding. A frequently applied model for the diffusive growth or evaporation of an isolated spherical droplet in still air is reviewed in detail for example in (Pruppacher and Klett, 1997; Seinfeld and Pandis, 2006). Here only the main ingredients of the model and some general results will be summarized. Although the implied assumptions are usually not strictly fulfilled under realistic conditions, comparing results from such a simplified growth model to actually observed growth rates can tell, for instance, if additional pathways beyond diffusion are at play.

The geometry of the model is sketched in Fig. 4.1.4. The vapour density is described as a continuous function of the radial coordinate r. At steady state, that is, when the radial concentration profile has attained its equilibrium shape, the molar vapour flux through the droplet surface (radius r_p) can be shown to be

$$J_s = 4\pi\, r_\mathrm{p}\, D\, (c_\infty - c_s).$$

Here c_∞ and c_s denote the molar vapour concentrations far away from the droplet and just at the droplet surface, respectively, and D is the diffusivity of vapour in air. Relating J_s to the mass change

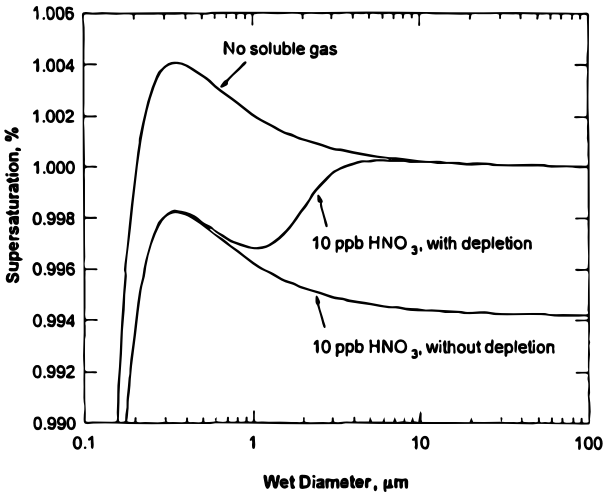

Figure 4.7.: Example for the effect of soluble trace gas on the critical water vapour saturation ratio over a deliquesced ammonium sulfate CN of 50 nm dry diameter. The critical saturation ratio (i.e. the maximum of the curve) is reduced below unity by the presence of initially 10 ppb of HNO_3(g). The curve including depletion of HNO_3(g) was calculated assuming 1000 cm^{-3} identical nuclei consuming the available HNO_3. Figure from (Seinfeld and Pandis, 2006).

of the droplet one then obtains a differential equation for the droplet radius r_p:

$$\frac{\mathrm{d}r_\mathrm{p}}{\mathrm{d}t} = \frac{D\, v_\ell\, N_\mathrm{A}}{r_\mathrm{p}}(c_\infty - c_s), \tag{4.18}$$

where once more v_ℓ is the molecular volume of the liquid.

This can equivalently be expressed as

$$\frac{\mathrm{d}r_\mathrm{p}}{\mathrm{d}t} = \frac{D\, v_\ell\, N_\mathrm{A}}{r_\mathrm{p}\, R}\left(S_\infty \frac{p_v^\circ(T_\infty)}{T_\infty} - S_s \frac{p_v^\circ(T_s)}{T_s}\right), \tag{4.19}$$

where $p_v^\circ(T)$ denotes the equilibrium vapour pressure at temperature T over a *flat* phase boundary (see sec. 4.1.1). If $T_\infty \sim T_s$, the largest contribution to the right hand side of the previous equation comes from the difference of the saturation ratios S_∞ and S_s. The latter in particular depends on the surface curvature (Kelvin effect), solute effects, and charge, which were discussed earlier (see Eqns. 4.5, 4.10, 4.14). Because of this it is generally a function of the droplet radius r_p. When more coupled equilibria are involved (as resulting from including solvation and dissociation of gaseous substance, see sec. 4.1.3), diffusion of substances in the liquid phase, chemical reactions between them, etc., the model becomes increasingly complex.

The vapour concentration profile equilibrates quickly. The corresponding characteristic time can be estimated by (Seinfeld and Pandis, 2006)

$$\tau \simeq \frac{r_\mathrm{p}^2}{4\, D},$$

which is as short as a few microseconds even up to droplet sizes of $r_\mathrm{p} = 10\,\mu$m. The assumption of a steady state is valid as long as the droplet size change occurs on a much slower timescale.

The latent heat released by condensing vapour molecules (or taken away by evaporating ones) may significantly heat or cool the droplet. Considering this, the heat conduction through the droplet surface, and the resulting temperature profile outside the droplet connected to a heat bath at $r \to \infty$ leads to another differential equation for the temperature at the droplet surface, T_s, in which the thermal conductivity of the surrounding gas, k, takes the role of the diffusivity D in eq. 4.19. Both equations are coupled and have to be solved simultaneously. The temperature dependence of the equilibrium

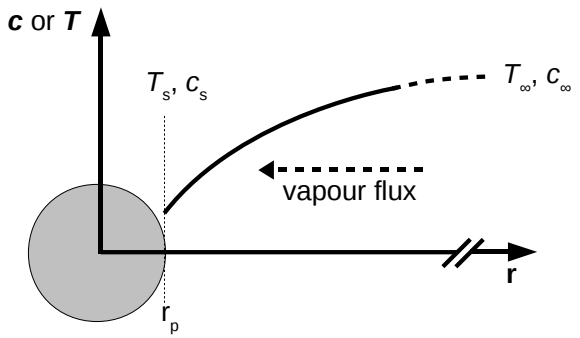

Figure 4.8.: Geometry of the diffusive growth model.

vapour pressure causes latent heat release to have some impact on condensational growth. It was thus included in corresponding calculations in this work.

Treating the vapour concentration as a continuous function of space requires that any characteristic length must be much larger than the mean free path of the vapour molecules in the gas phase, which is on the order of 100 nm. The range of validity of the continuous model can be extended down to this length scale by introducing size-dependent expressions for the diffusivity D and the thermal conductivity k. These result from an approximate procedure where the vapour and heat fluxes through the immediate surrounding of the droplet are treated with gas kinetic theory, yielding more appropriate boundary conditions for the corresponding continuous problems outside this surrounding (Pruppacher and Klett, 1997). The additional phenomenological parameters ('accomodation coefficients') appearing in these expressions are difficult to measure (Laaksonen et al., 2005; Winkler et al., 2004), and there is no common agreement about their exact values. It was argued that it is conceptionally least awkward, and leads to best agreement with observed droplet growth rates, if unity accomodation coefficients are assumed for atmospheric diffusional droplet growth (Laaksonen et al., 2005; Winkler et al., 2004), and this recommendation is adopted in the present work.

The larger a droplet grows the more S_s gets independent of the droplet radius r_p. Then, Eq. 4.19 becomes approximately

$$\frac{\mathrm{d}r_\mathrm{p}}{\mathrm{d}t} = C\, r_\mathrm{p}^{-1},$$

where C is a constant. For the case of $C > 0$ (conditions of droplet growth) this leads to

$$r_\mathrm{p}(t) = \sqrt{r_0^2 + 2\, C\, t^2}.$$

Even without considering vapour depletion the velocity of increase of the droplet radius decelerates with time. This sets an effective size limit up to which diffusional growth is fast enough to be important. In natural clouds the typical size of diffusionally grown droplets is not much greater than abut $\sim 10\,\mu$m (Pruppacher and Klett, 1997).

4.2. Laser-induced condensation

The term 'laser-induced condensation' should be understood in a quite general sense: it comprises all possible mechanisms driven directly or indirectly by the action of laser light which can lead to a transfer of atmospheric gaseous substance to the liquid phase.

To affect atmospheric condensation the composition and/or physical properties of the gas phase must be suitably changed, and/or the natural background of unactivated atmospheric condensation nuclei has to be modified to allow for condensation under conditions otherwise preventing it.

This section aims on give an overview of mechanisms able to lead to condensation of atmospheric water out of the gas phase, which are triggerable by laser light, and especially by the action of filaments occurring in high power laser pulse propagation.

4.2.1. Previous demonstrations of laser-induced condensation of water

Apart from the early experiments by Wille et al. (Wille et al., 2001) there are hardly any reports of attempted or successful laser induced condensation of water vapour to be found in the literature. In these experiments a diffusion cloud chamber was used to create conditions of extreme water vapour supersaturation. A focused femtosecond beam of $\tau_p \geq 50\,\text{fs}$ laser pulses with energy $E_p = 1\,\text{mJ}$ and central wavelength $\lambda_0 = 810\,\text{nm}$ from a Ti:Sa amplifier created observable formation of fog droplets. Focussing of the laser beam by a $f = 600\,\text{mm}$ lens, with a spot size of about 0.2 mm (Luderer, 2001), was relatively tight. Lacking the necessary laser pulse power to support a genuine filament, this was the only available method to create peak intensities comparable to those in the core of a strong filament, or even in excess.

The produced fog particles were detected by measuring the extinction of a $\lambda = 633\,\text{nm}$ helium-neon laser beam sent through the chamber collinearly with the femtosecond beam.

The interpretation of the observed effect offered by the experimenters suggested classical Kelvin-Thomson charge-induced nucleation, which was discussed in Sec. 4.1.1, as the underlying mechanism. Under conditions of very high supersaturation up to 400 % which were accessible with the cloud chamber used by Wille et al. this effect may indeed play an important role. However, the possibility of the existence of further mechanisms potentially leading to formation of water fog was not considered.

It was also mentioned before that in these early experiments no genuine femtosecond laser filaments were utilized, but a filament was simulated by the narrow waist of a focused 'low power' femtosecond laser beam. In this sense the question if also a filament is able to induce water condensation in air was not closed yet.

One more report of observed laser induced water condensation can be found in the literature. The laser source used by K. Yoshihara was an ArF excimer laser emitting $\tau_p = 10\,\text{ns}$ long pulses of up to $E_p = 250\,\text{mJ}$ in a beam of $24 \times 10\,\text{mm}^2$ cross section, yielding peak intensity of 'only' about $I \approx 10^7\,\text{W/cm}^2$. The emitted wavelength was $\lambda = 193\,\text{nm}$ corresponding to a photon energy of about 6 eV, insufficient for single photon ionization of any of the present gases (the ionization potential of water is just above at about 6.5 eV (Couairon et al., 2006), and those of molecular nitrogen and oxygen are about double the photon energy (Couairon and Mysyrowicz, 2007)).

According to Yoshihara the only potential source of ions under these conditions could be resonance-enhanced two-photon absorption of water molecules. His preliminary interpretation of UV-laser induced condensation includes a number of reactions starting from the photodissociation of molecular oxygen (^{1}P), leading to the formation of ozone (O_3), which in a subsequent photodissociation releases singlet oxygen (^{1}D). This would in turn react with water to form ·OH radicals, starting a sequence of reactions ending in the production of hydrogen peroxide H_2O_2.

Interestingly, Yoshihara seems unaware of the fact that ultraviolet light induced formation of fog from moist air has a long history of experimental observation and of search for (as well as debate about) the underlying mechanisms. Part of this will be summarized below, as the potentially involved cascades of chemical reactions may as well be started under the extreme conditions of irradiation created by a filamenting laser pulse.

4.2.2. Known and potential mechanisms of laser-induced condensation in the atmosphere

Photonucleation

The relatively recently reported capability of UV laser radiation to induce the formation of fog from moist air (Yoshihara, 2005), as it was already summarized in the previous section, is not too surprising regarding the long history of the phenomenon often termed "photonucleation", dating back to more than 100 years ago. Despite the long time passed the discussion about how exactly water photonucleation works is still not settled. Because of some very interesting properties of the phenomenon, and a possible link to ultra high power laser-induced (respectively, filament-induced) atmospheric water nucleation, the main observations and interpretations are summarized in the following.

Discovery of photonucleation The formation of fog induced by the action of light on mixtures of air and vapour of organic compounds had been reported by J. Tyndall, already in 1868 (Tyndall, 1868). He obtained best results using vapours of alkyl nitrites, which constitute a class of simple organic compounds with the structure formula R–O–N=O, where R is an alkyl group. In his experiments Tyndall observed that light from the violet end of the visible spectrum was able to induce the formation of fog in such mixtures. Fog was not induced when he used light of longer wavelengths, or when no alkyl nitrite vapour was present. His experimental apparatus had coloured glass windows to filter the spectrum of light emitted by an arc lamp. This means that the shortest transmitted wavelengths were around 360 nm, as glass is typically opaque for shorter wavelengths. The outcome of Tyndall's experiments has a straightforward qualitative explanation: it is evident that the underlying mechanism is based on the photochemical transformation of a substance with high saturation vapour pressure (the alkyl nitrite) into a less volatile substance. In the case of alkyl nitrites, the initial absorption of light results in the formation of an alkoxy radical (Orlando et al., 2003),

$$\mathrm{RONO} \xrightarrow{h\nu,\Delta} \mathrm{RO}\cdot + \mathrm{NO},$$

which is the starting point of the subsequent chemistry. In air typically oxygen is the next reaction partner. Using pure air/alkyl nitrite mixture, Tyndall observed relatively weak fog formation. Adding substantial concentrations of gaseous HCl strongly enhanced the effect (Tyndall, 1868).

Photochemical production of fog involving organic compounds at first sight may seem artificial and of lesser relevance for the atmosphere. However, particle production by photochemical processing of volatile organic compounds is an important source of atmospheric organic aerosol (Seinfeld and Pandis, 2006), and it may also affect laser-induced condensation in real atmosphere (see later Sec. 5.4).

As important as the photochemical modification of organics may be in the total atmospheric budget, their local concentrations are generally low. Typical mixing ratios of volatile organic compounds (VOC) are in the range from a few to a few tens of ppbC[1] (Seinfeld and Pandis, 2006). Butyl nitrite (1-

[1]ppbC: parts per billion of carbon atoms, the volume mixing ratio of the gaseous VOC times the number of carbon atoms

nitrosooxybutane), a substance prototypical for those used by Tyndall, has the sum formula $C_4H_9NO_2$ and an equilibrium vapour pressure at normal conditions of about 130 hPa. Tyndall filled his apparatus with dry air which had been bubbled through liquid butyl nitrite at ambient temperature (Tyndall, 1868). It is safe to assume a resulting saturation ratio of several tens of percents. The volume mixing ratio of butyl nitrite thus was on the percent level – far above the ppb levels of VOCs encountered in the ambient atmosphere.

Because the main interest here is on the natural atmosphere, the results which C.T.R. Wilson obtained 30 years after Tyndall's first observations of light-induced fog, are somewhat more exciting.

Carrying out research in J.J. Thomson's laboratory, Wilson examined the ability of various kinds of radiation to induce fog in an expansion cloud chamber (Wilson, 1899). He had earlier found that X-rays and "uranium rays" induce the same type of electrically charged nuclei that lead to condensation of water vapour mixed with some non-condensible carrier gas (air in most of the cases). These observations motivated the refinement of the cloud chamber, eventually enabling the observation of ionization paths of energetic particles in 1911 (Wilson, 1911), for which Wilson was awarded the Nobel Prize in 1927, which he shared with A.H. Compton. Wilson's findings showed that condensation nuclei generated by either type of radiation – "uranium rays" and X-rays – require precisely the same supersaturation of water vapour to observe condensation. His aim then was to see if this threshold supersaturation was universal, and he conducted studies on the induction of condensation by "any of the known methods to be capable of allowing the passage of electricity through them [gases]".

Motivated by observations of Lenard and Wolf published already ten years earlier (Lenard and Wolf, 1889), one of the types of radiation examined by Wilson was ultraviolet light. Indeed he found that under certain conditions, ultraviolet light from an arc lamp could generate condensation nuclei which were electrically neutral and very efficient. Lenard and Wolf had attributed similar observations to contamination from the windows of their chamber, but Wilson was able to exclude any such influence in his experiment.

Wilson soon recognized that the UV generated condensation nuclei were quite special. He was able to show that they were able to induce fog formation at way lower saturation ratios than required for the ions generated by X-rays or "uranium" rays (see also sec.4.1.1).

Wilson's original apparatus was an early ancestor of his Nobel-awarded cloud chamber: a sealed glass tube with a quartz lens at each end, containing a non-condensible carrier gas, initially saturated with some vapour substance. The gas mixture was driven into supersaturation by adiabatic expansion. At about room temperature, and using water vapour in air atmosphere, the expansion ratio needed for ion-induced condensation found by Wilson (and later others (Tohmfor and Volmer, 1938)) was about 1.25, corresponding to a saturation ratio of $S \simeq 4$. The smallest expansion ratio found by Wilson for UV light induced nucleation of water vapour was equal to 1 (no expansion), meaning that just saturated conditions were sufficient.

Encouraged by these findings Wilson prepared an atmosphere with less than unity saturation ratio,

per molecule

and still was able to observe formation of fog:

> "Over aqueous caustic potash, containing about 17 per cent. of KOH, a fog was readily obtained. The relative humidity over such a solution is less than 90 per cent. Experiments have not been tried with humidity between 50 and 90 per cent. These experiments then show that both air and water vapour are necessary for the production of the ultra-violet light fogs; it is not necessary that the air should be saturated." (Wilson, 1899)

Wilson observed that under similar conditions, and without further irradiation, the UV generated fog persisted "for some hours at least". This indicates, according to classical nucleation theory, that the generated droplets were residing in a local minimum, with respect to their diameter, of the Gibbs energy. The equilibrium diameter corresponding to this minimum was large enough for visual observation of the droplets in the light of the arc lamp, and at the same time small enough for a sufficiently slow settling speed, indicating a size about between an optical wavelength and a few micrometers.

Assuming that classical nucleation theory can describe the observations, this indicates that a species with low volatility and/or *very* hygroscopic substance must have been created in large amounts due to the UV irradiation, as Wilson found evidence against electrical charge being the stabilizing agent. In Wilson's own words:

> "[. . .] yet in spite of their small size there is no indication of any tendency for them to evaporate again. It is probable, therefore, that the drops do not consist of pure water. We might, it is true, account for their persistence by supposing each to have become charged with electricity under the influence of the ultra-violet rays. In the light of later experiments, however, the former view appears to be the more probable."

After systematically excluding any other kind of contamination or experimental error, Wilson came to the conclusion that, besides water vapour, most likely oxygen is the other essential agent. He concluded this from the observation that fog was formed in atmospheres of air, as well as in those of pure oxygen, but not of pure nitrogen alone. In his conclusion Wilson singles out hydrogen peroxide as the most probable candidate for the substance is formed in the atmosphere containing water and oxygen, and which then induces and stabilizes the fog:

> "The view here taken is then, that under the action of the ultra-violet light small drops of water combine with the oxygen in contact with them, and in consequence of the lowering of the equilibrium vapour pressure by the dissolved H_2O_2 they are able to grow, when similar drops of pure water would evaporate."

Modern interpretations in the light of newer experiments support Wilson's conclusion that the reaction partners are most likely water and oxygen. The pathway leading to fog formation, however, may be more involved.

Newer experimental evidence and modern interpretation Wilson's initial experiments were repeated and refined by different researchers (for example (Farley, 1951; Hoppel and Dinger, 1973; Reiss et al., 1977; Wen et al., 1978)). The results obtained by Farley (Farley, 1951) support Wilson's conclusions that the presence of oxygen plays a crucial role in the phenomenon, and that the generated condensation nuclei are electrically neutral. In his experiments Farley also found that, contrary to classical ion-induced nucleation, UV photoinduced nucleation did not show saturation with respect to the degree of expansion (this corresponds to the vapour saturation ratio). This fact points towards a fundamental difference between the two phenomena. In the former case, the number of ion-induced nuclei, and thus the density of the resulting cloud, are limited by the number of available ions, but not by the saturation ratio of the condensible substance. This obviously leads to the interpretation that more available vapour substance not only feeds growth of a certain number of preexisting nuclei, but it also contributes to the ongoing formation of more and more *new* nuclei.

Farley describes the influence of the UV radiation as "to modify the value of the cloud limit", which means that spontaneous nucleation of vapour substance occurs at lower saturation ratios than without the radiation. He found that neither the radiation intensity nor the exposure time alone were important, but that the radiation *dose* determined the obtained cloud density.

One more important result obtained by Farley was the seemingly limited lifetime of the produced "u.v.-factor", as he intentionally vaguely names whatever caused the enhancement of condensation. He was not able to decide if the reduction of its efficiency was caused by diffusion and removal by contact with the chamber walls, or if the "u.v.-factor" was unstable and decayed into products which did not enhance condensation.

W.A. Hoppel and J.E. Dinger (Hoppel and Dinger, 1973) investigated the creation of condensation nuclei (CN) and cloud condensation nuclei (CCN) by the irradiation with ultraviolet light in cleaned natural air samples at a water vapour saturation ratio of $S = 1.007$. They were able to show that CCN at concentrations exceeding 10^4 cm^{-3} were produced in their apparatus. They also compared air sampled at different locations and altitudes during sounding flights over Hawaii and Alaska, and found that especially under conditions free from influence of the earth surface (sea salt, dust) the volatility of the natural CCN resembled that of the UV induced nuclei generated in purified air under laboratory conditions, indicating that they may be of similar nature.

In their report they do not explicitly state spectral properties of the irradiated light nor the radiation dose. They used a 200 W high pressure mercury lamp, and the irradiated air was flowing through quartz tubes, but it is particularly not possible to precisely tell which was he shortest irradiated wavelength. However, they also found that water vapour had to be present during the irradiation of the air sample to cause the formation of nuclei. Primary irradiation of a dry air sample and subsequent addition of water vapour did not cause the formation of nuclei, which proves that water takes part in essential steps of the formation of nucleus precursor substance.

Wen, McLaughlin and Katz (Wen et al., 1978) used an upward diffusion cloud chamber with H_2 as the buffer gas to quantitatively measure the UV induced nucleation rates of pure water vapour as a function of wavelength and light intensity. Furthermore they measured the delay time between the start of the exposure to the radiation and the onset of nucleation events. Figure 4.9 a) shows a

plot of nucleation rate vs. the irradiated light intensity at a wavelength of 200 nm as shown in (Wen et al., 1978). The lowest saturation ratio considered in the plot is $S = 1.797$. In their report, Wen et al. however state that they were able to detect photoinduced condensation at a saturation ratio of just $S = 1.00042$, which is practically just saturated. This limit was not fundamental, but imposed by the maximum light intensity of $0.2\,\mathrm{W/m^2}$ available from their source.

Interpreting the notion of 'detectability' as a nucleation rate of 1 drop $\mathrm{cm^{-2}s^{-1}}$, being the lowest abscissa value plotted in the original figure shown in 4.9 a) this data point can be included and compared. This is done in 4.9 b), where the required light intensity to observe a nucleation rate of 1 drop $\mathrm{cm^{-2}s^{-1}}$ is plotted versus the saturation ratio S. The solid line is an exponential fit to the data obtained from the original plot shown in 4.9 a). Note that the choice of an exponential function is entirely heuristic and based on the observation that most of the data points appear to lie on a straight line.

The additional extremal data point at $S = 1.00042$ seems to fit the picture quite well, if one keeps in mind that the choice of 1 drop $\mathrm{cm^{-2}s^{-1}}$ as the detection limit was somewhat arbitrary.

The delay times until onset of nucleation observed by Wen et al. were systematically dependent on the radiation intensity and the saturation ratio. Delays spanned the entire range up to almost 20 s. Furthermore nucleation remained active for times on the same scale after the irradiation actually stopped, indicating a corresponding lifetime of the agent produced under the influence of UV radiation and causing the nucleation. This observation is in full agreement with what Wilson and Farley had reported earlier based on studies of nucleation strength as a function of delay between exposure and expansion (Farley states a typical maximum delay of 30 s after which no more nucleation could be observed (Farley, 1951)).

Wen et al. claim to have found no evidence for a special role of oxygen in the photonucleation process, which had earlier been identified by Wilson and Farley. They found no change in the photonucleation spectrum after introducing 5 Torr (~ 660 Pa) of O_2 into the chamber, and concluded that it did not participate in the photochemical reactions leading to the production of condensation

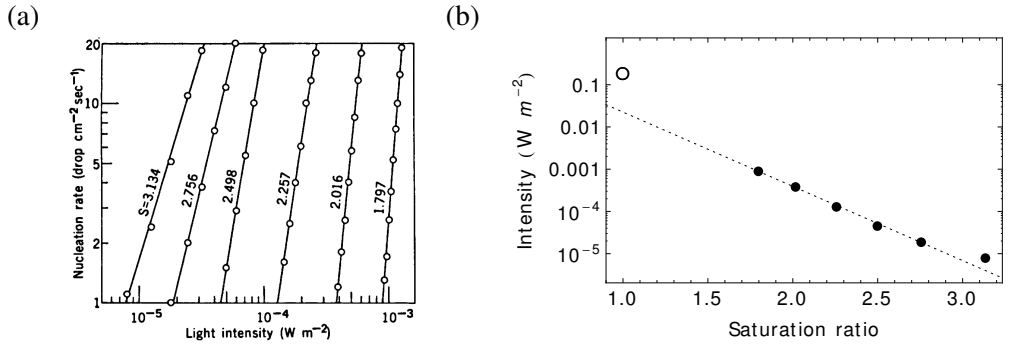

Figure 4.9.: a) Figure 2 from (Wen et al., 1978) showing the dependence of photoinduced droplet nucleation rate upon the intensity of the irradiated UV light at a wavelength of 200 nm for various saturation ratios of water vapour in a buffer gas of H_2; b) plot of intensity vs saturation ratio S as read from a) for a nucleation rate of 1 drop $\mathrm{cm^{-2}s^{-1}}$ with an additional data point mentioned in the text of (Wen et al., 1978). The dashed line is an exponential fit to the data points from a).

nuclei. In a later publication (Wen et al., 1982), however, they conceded that likely their apparatus was polluted with "an unidentified water soluble impurity from the gaskets of the cloud chamber". This impurity could well have consisted of traces of molecular oxygen, which reopens the question about its role.

A few years earlier I.D. Clark and J.F. Noxon had conducted related experiments under slightly different conditions, and using even shorter wavelength radiation (150 nm $\leq \lambda \leq$ 170 nm) (Clark and Noxon, 1971). Their most spectacular result was the generation of photoinduced water fog even at highly undersaturated conditions (typically down to $S \simeq 0.5$). They used helium as the buffer gas and could exclude any other impurity than water vapour by mass spectrometry. They found a wavelength dependence of the photonucleation rate indicating direct absorption by water molecules as the initial step (note that this is contrary to the results of Wen et al.). Another peculiarity consisted in the observation of strictly positively charged droplets, as confirmed by a Millikan type electrostatic balance incorporated in their apparatus. Interestingly they observed an unusually low mass density of the aggregated material, leading them to the conclusion that "the particles themselves were not composed of H_2O in its usual liquid or solid form". This is certainly a strong claim, but it does not seem to have been discussed a lot in the literature until today.

The addition of molecular oxygen increased the rate of particle production, but so did that of CO_2. On the other hand, simultaneous addition of N_2 reduced the enhancing effect of oxygen. This was interpreted as evidence for the involvement of singlet oxygen, $O(^1D)$, produced in the photolysis of O_2 or CO_2, respectively, which they presumed to be quenched more efficiently by N_2 than by CO_2 (in fact, in a later publication (Clark and Noxon, 1971), they reported improved measurements showing almost twice as fast quenching by CO_2 as compared to N_2. Therefore, this part of the argument has to be taken with a bit of caution).

Clark and Noxon concluded that under their experimental conditions ·OH radicals may play the most important role, noting that they are produced in the reaction of singlet oxygen with water. They did not consider O_2 an essential ingredient (contrary to the conclusions of Wilson and Farley), because the more energetic UV radiation used by them allowed for the production of ·OH by direct photolysis of water.

Summarizing, photonucleation of water induced by UV light with wavelengths shorter than $\lambda \sim$ 170 nm is highly efficient and requires clearly less than unity saturation ratios, but it seems to involve somewhat different photochemical pathways than photonucleation induced by longer wavelength UV light. The former is not fully understood but may rely on ·OH radicals. The mechanism underlying the latter may be explainable by a model which will be outlined in the following paragraph.

Models for UV-induced photonucleation of water vapour Wen, Laughlin and Katz (Wen et al., 1978) were able to identify a phenomenological kinetic model which was very well supported by their data. This model involves a species of excited water molecules (H_2O^*) which are able to form mixed clusters with additional unexcited water molecules. The nature of this 'excitation' remains unspecified. Wen et al. made no a priori assumptions about the absorption mechanism, and initially allowed for sequential absorption of an unspecified number of photons (their measured data later

required to assume a one-step, single-photon absorption for consistence).

The system is modelled as a set of equations, displayed in Eq. 4.20, describing the photochemical production of excited water molecules and their sequential addition to clusters $(H_2O^*)_n$, containing n such excited water molecules plus an unspecified number of 'ordinary' water molecules. In this model, addition of the c-th excited water monomer leads to nucleation and production of a visible droplet and terminates the reaction sequence. The critical number c of excited water molecules per cluster may depend on environmental conditions, especially on the saturation ratio.

$$\begin{aligned} H_2O &\xrightarrow{mh\nu} (H_2O^*) \\ (H_2O^*)_n + (H_2O^*) &\longrightarrow (H_2O^*)_{n+1} \quad (\text{for } c-1 > n > 1) \\ &\vdots \\ (H_2O^*)_{c-1} + (H_2O^*) &\longrightarrow (H_2O^*)_c \longrightarrow \text{nucleus} \longrightarrow \text{droplet} \end{aligned} \tag{4.20}$$

Using measured steady state nucleation rates and delay times before the onset of nucleation, Wen et al. were able to show that the rate equations of their model yield consistent values for the critical number c in both limiting cases of initial time solution and steady state solution of the system in Eq. 4.20. In fig. 4.10 values for the critical number of excited water molecules per cluster are plotted vs. the

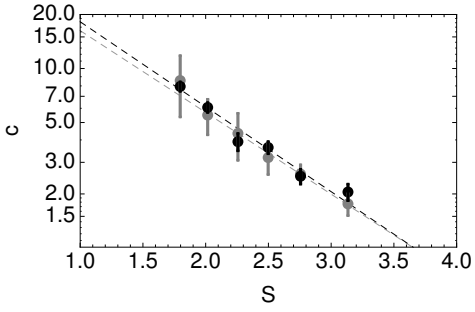

Figure 4.10.: Critical number c of molecules of excited water species per cluster vs. saturation ratio S; data from Table 1 in (Wen et al., 1978). Black dots: c from measured steady-state nucleation rates; gray dots: c from delay times. Error bars denote uncertainties of c (3σ) as stated by Wen et al.; Black and gray lines: exponential fits (see text).

saturation ratio S. These are the values calculated by Wen et al. from the steady state nucleation rate (implicitly using a variant of the nucleation theorem 4.1.1), and the delay time data, respectively, and are given in Table 1. of (Wen et al., 1978). The black dots correspond to the values obtained from the steady state nucleation rates, and are less affected by measurement uncertainty than those obtained from the delay time measurements, represented by gray dots. The straight lines correspond to exponential fits to the data. Note that the choice of an exponential function is not a result of the model. The straight lines in fig. 4.10 are merely intended to indicate a gross trend. Keeping this in mind one may obtain a rough estimate of c at $S \simeq 1$, resulting in $c_{\text{sat}} \simeq 20$ with considerably large uncertainty, but relatively certainly $c_{\text{sat}} > 10$.

Despite the phenomenological predictive power of the proposed model, several important questions remained unanswered by Wen et al.:

– Pure water vapour does not absorb light in the range between 200 nm and 320 nm. In fact, light from this spectral range was able to induce nucleation. What actually *does* absorb?

– How can the second-long persistence of the effect be explained regarding the much shorter typical lifetimes of electronic excitations? How are the 'excited' water monomers, which are at the foundation of the model, stabilized over such long times?

– Energetic excited molecules embedded in a cluster, once their excitation decays, are supposed to deposit heat. This heating rather should *counteract* nucleation due to the enhancement of evaporation. Then, what is the mechanism which, despite of this, makes the clusters containing excited molecules so attractive, that they still serve as efficient promoters of condensation? After all "it is unclear how a cluster of excited molecules can cause other molecules to condense on it".

Much later, in 1995, W. Byers Brown gave possible answers to some of the open questions, when he proposed a model based on photochemistry of gas phase van der Waals complexes of water and molecular oxygen (Byers Brown, 1995; Byers Brown et al., 1995). He noticed similarities of the spectral dependence of the rate of UV-induced nucleation reported by Wen et al.(Wen et al., 1978) and the absorption spectrum of oxygenated liquid water as it had been measured by Heidt et al. (Heidt and Ekstrom, 1957; Heidt and Johnson, 1957) in the wavelength range between 200 nm and 260 nm.

From measurements conducted by Quickenden and Irvin (Quickenden and Irvin, 1980) it was meanwhile known that highly purified liquid water practically does *not* absorb light in the same wavelength region. The same holds for molecular oxygen (Heidt and Ekstrom, 1957), proving that the observed absorption originates from oxygen in water, supposedly present in a special solvated state. Already Heidt had speculated about the origin of the peculiar absorption of oxygenated bulk water as being due to electron transfer within $H_2O \cdot O_2$ solvation complexes (he acknowledges R. S. Mulliken to have suggested the idea to him), the oxygen acting as electron acceptor.

Byers Brown's new idea then was to assume that the hydrated oxygen molecules also exist in the gas phase, and that they have similar UV absorption characteristics as in the liquid phase. The excited charge transfer state already proposed by Heidt then takes on a key role in his photonucleation theory.

The argument based on experimental observations was already backed up by preliminary ab initio quantum chemical calculations, which had been published some time before by the same author and coworkers (Byers Brown et al., 1992). They had shown that loosely bound van der Waals complexes of water and oxygen, $H_2O \cdot O_2$, likely exist in the gas phase under common atmospheric conditions. The lowest energetic charge transfer state was found to lie at a level approximately 6 eV above the Van der Waals ground state, corresponding to an excitation wavelength of about 200 nm, in agreement with the spectroscopic observations mentioned before. The same calculations showed that the dipole moment of the charge transfer state is considerably large, at least about 6 D[2].

According to the model, the large dipole moment of the charge transfer complexes (CTCs) leads to the formation of "Wilson clusters" (the naming proposed by Byers Brown) by the strong attraction of polar water molecules, but also of more CTCs in the vicinity. Byers Brown identified the CTCs with the unknown excited water species of the heuristic model by Wen et al., resulting in a similar set

[2] 1 D = 1 Debye $\simeq 3.33564 \times 10^{-30}$ Cm

of equations as in Eq. 4.20 (Byers Brown, 1995). The symbols $(H_2O)_n$ then denote Wilson clusters containing a number of n CTCs (or, more precisely, classes of Wilson clusters, as the number of aggregated H_2O is not specified in this notation).

Estimated from their excitation energy, the lifetime of the charge transfer complexes most likely does not exceed microseconds. Recognizing this, Byers Brown was aware that a satisfying explanation for the observed long lifetime of the nucleation-enhancing effect was lacking. In his original publication (Byers Brown, 1995) he proposed resonance stabilization of excited complexes $(H_2O)_n^+ \cdot O_2^-$ by nearby water molecules present in a Wilson cluster, which could lead to an extended radiative lifetime of the excitation. Alternatively, to explain how radiative loss of excitation energy may be circumvented, he proposed the accelerated production of the presumed final photochemical product, H_2O_2. The Wilson clusters (already delaying radiative decay), by spatially confining the reactants, would act as nanometric reactors. The production rate of H_2O_2, under otherwise similar conditions would then far exceed that in the gas phase, and the electronic excitation would be consumed in the chemical reaction before being lost as radiation. Finally, the H_2O_2 would have to play the role of the "excited water species" in the reaction system Eq. 4.20.

The structure and potential energy surfaces of the involved collision and charge transfer complexes have been investigated in improved quantum chemical calculations (Palmer et al., 1996; Sabu et al., 2004), and the structure and energetic properties of Wilson clusters have been calculated using computational molecular dynamics and Monte Carlo methods (Dos Santos et al., 1997). The calculated absorption spectra of the van der Waals complexes $H_2O \cdot O_2$ as presented in (Byers Brown et al., 1995; Palmer et al., 1996) show some qualitative agreement with experiment. Especially the long tail of the main absorption band extending into the longer wavelength region is reproduced.

In their calculations, for mostly computational reasons, the authors of (Byers Brown et al., 1995) and (Palmer et al., 1996) assumed C_{2v} symmetry of both the van der Waals and the charge transfer complexes. The calculated excitation energies for the transition $H_2O \cdot O_2 \xrightarrow{h\nu} H_2O^+ \cdot O_2^-$ are about $h\nu \simeq 5.9\,\mathrm{eV}$, or $h\nu \simeq 5.7\,\mathrm{eV}$, depending on the computational method used (Palmer et al., 1996). This energy gap corresponds to the vertical transition at the intermolecular coordinate (along the C_2 axis) minimizing the energy of the ground state configuration (see Fig. 4.11). Note that due to the shallowness of the ground state potential minimum both bound and continuum states act as initial states for the transition, and the stated transition energies are not sharply defined. The variety of possible initial states leads to the broad absorption spectra obtained from the calculations and may explain the measured absorption and nucleation spectra.

According to the more exhaustive numerical exploration of the conformation space done by Sabu et al., the structure with C_{2v} symmetry appears not to be the lowest energetic one (in approximate agreement with results of Robinson et al. (Robinson and Kjaergaard, 2003)). The C_{2v}-symmetrical structure however agrees with microwave spectroscopic results (Sabu et al., 2004), and its theoretically predicted optical excitation energy is well in agreement with experiment (see above).

While the quantum chemical calculations of the properties of the hydrated oxygen complexes lead to results with semi-quantitative agreement to experiments, the situation is somewhat less satisfactory when the theoretically predicted properties of the Wilson clusters are considered. Byers Brown et

al. (Byers Brown et al., 1995), as well as Dos Santos et al. (Dos Santos et al., 1997), carried out molecular dynamics calculations on clusters of water molecules containing a single CTC. They found that the most favourable configuration of the CTCs was – quite surprisingly – not fully solvated inside the cluster, but close to its surface, the dipolar axis being aligned almost parallel to the surface. Both groups determined the energies of a small water cluster (eight molecules in total) with a CTC at the periphery, and of a similar cluster with a fully embedded CTC, using ab initio mehods. Doing so the favourable energetic situation of the cluster with the peripheral CTC could be reproduced by both groups. They took this as indication that the results of the molecular dynamics simulations were not an artefact of the crude interaction models used, but that they resemble the true physical situation.

Dos Santos et al. point out that, to assess the role of CTCs as initiators of water vapour nucleation, besides looking at the energetic stabilization of the clusters one should take into account entropic (mixing) stabilization, which was beyond the capabilities of their method. This relates to the basis of classical nucleation theory: the system comprising vapour and condensed phases tends to minimize its Gibbs energy, including the maximization of its entropy (see Sec. 4.1.1).

Another important piece of evidence was contributed by Cacace et al. when they used neutralization-reionization mass spectrometry to prove the existence of relatively long lived $H_2O^+ \cdot O_2^-$ charge transfer complexes in the gas phase (Cacace, 2001, 2002; Cacace et al., 2000).

They used ion-molecule collisions for preparing singly charged water-oxygen adducts $(H_2O \cdot O_2)^+$ or $(H_2O \cdot O_2)^-$, which were accelerated to a kinetic energy of $4 - 8\,\mathrm{keV}$ and mass selected. The ion beam was sent through a cell with neutral target gas, in which part of the ions were neutralized. After electrostatically deflecting all charged species the beam of neutrals was allowed to propagate through some distance until being reionized by collision with neutrals in another gas cell. The propagated distance was used to probe the lifetime of the neutrals by varying their time of flight.

By a combination of isotope labelling the oxygen in the original H_2O and O_2, enabling the observation of the fragmentation patterns in a neutralization–reionization/ collisionally-activated dissociation type experiment, Cacace et al. were able to prove that neutral, relative strongly bound complexes of water and molecular oxygen exist, and that they have a lifetime of greater than $0.5\,\mu\mathrm{s}$. The fact that the complexes survived the reionization collisions allowed them to estimate the binding energy as being greater than about $25\,\mathrm{kJ/mol}$ (about $260\,\mathrm{meV}$ per complex). In fact, the binding

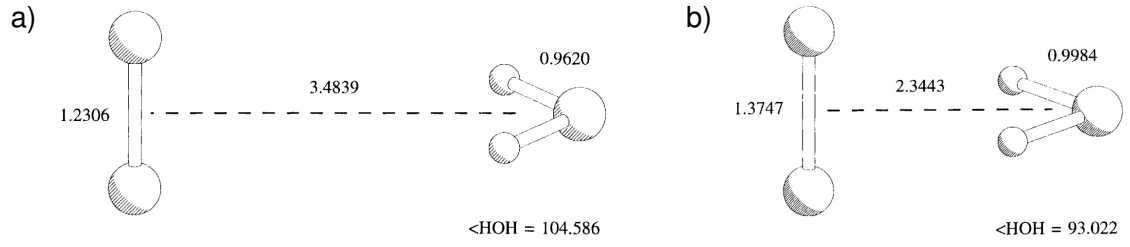

Figure 4.11.: C_{2v} optimized geometries of the a) $H_2O \cdot O_2$ van der Waals complex ground state, b) $H_2O^+ \cdot O_2^-$ charge transfer state. All distances are in Ångströms and angles in degrees. Figures reproduced from (Byers Brown et al., 1995).

energy of the C_{2v} symmetric charge transfer state, as calculated by Palmer and Byers Brown, even amounts to about 0.2 Hartrees, which is roughly 5.4 eV, an order of magnitude larger than the lower limit estimated by Cacace and coworkers.

The authors of (Cacace, 2001, 2002; Cacace et al., 2000) interpret the large lower limit of 0.5 μs for the lifetime of gas phase $H_2O^+ \cdot O_2^-$ as strong evidence for the mechanism proposed by Byers Brown. Summarizing the preceding section, the existence of non-ionic pathways for UV photoinduced water vapour nucleation has been proven by many observations. Their atmospheric relevance is supported by experimental evidence, while the magnitude of the impact of related phenomena on the chemistry and absorption properties of the atmosphere is still not fully understood (Vaida and Headrick, 2000). Apart from the role played by the photochemical products in the nucleation of atmospheric water vapour, the additional absorption of sunlight due to collision-enabled electronic transitions in complexes may have a direct impact the radiative balance of the atmosphere, but also opens up channels for sunlight-driven photochemical processes which would otherwise not be efficient enough to be of importance (Sennikov et al., 2005; Vaida and Headrick, 2000).

Irrespective of the discussion about the role of such processes under general atmospheric conditions, in the present context of laser induced water condensation, there is enough evidence that they have to be considered.

This value of the is at the upper boundary of the nanosecond to lower microsecond interval of possible lifetimes estimated by Byers Brown for absorption features as experimentally observed (Byers Brown, 1995; Byers Brown et al., 1995). It is not fully clear from his statements whether microsecond scale lifetimes of the complexes should be considered sufficient for efficient cluster formation mainly by the dipole moment, or if additional chemical reactions still have to be invoked.

Ion-chemical production of aerosol precursor substance

With regard to the partially ionized channels left by laser filaments, besides direct optical excitation of air molecules leading to the formation of neutral reactive species, ions may as well provide for the necessary activation energy, releasing it during ion-molecule charge transfer reactions.

In most interpretations of UV light-induced water vapour photonucleation (except the mechanism proposed by Byers Brown) the ·OH radical plays a key role, because it is highly reactive and is a precursor of the stable and hygroscopic H_2O_2. The ·OH radical is known to have an atmospheric lifetime of less than 10 ms, leading to a transport scale of only about 1 cm (Seinfeld and Pandis, 2006). This is valid for common atmospheric conditions, and may be strongly reduced in the presence of efficient reaction partners. For example, in the presence of ozone the following reactions may lead to the production of H_2O_2:

$$\cdot OH + O_3 \longrightarrow HO_2 + O$$
$$HO_2 + HO_2 \longrightarrow H_2O_2 + O_2.$$

It is long known that ozone is produced in laser filaments in air, yet only recently its production has been quantified (Petit et al., 2010). Ozone concentrations extrapolated to the volume occupied by

the filament core were found to be as high as 400 ppm (on the order of the initial concentration of free electrons). This makes the above reactions likely to happen, especially as the heavy species in filament plasma are known to remain relatively close to ambient temperature (diffractometric measurements show a rise of about 100 K (Tzortzakis et al., 2001), supported by plasma dynamic simulations (Gordon et al., 2003)).

In an upward diffusion cloud chamber experiment involving a helium atmosphere containing water vapour, sulphur dioxide (SO_2) and traces of the radioactive rare gas radon, F. He and P.K. Hopke observed the oxidation of gaseous SO_2 to sulphuric acid H_2SO_4 happening along the ion tracks left by fast α-particles emitted in the decay of radon atoms (He and Hopke, 1995). They could show the observed efficient formation of H_2SO_4 to be mainly caused by ·OH radicals formed in positive ion charge transfer reactions

$$N_2^+ + H_2O \longrightarrow N_2H^+ + \cdot OH$$
$$O_2^+ + H_2O \longrightarrow O_2H^+ + \cdot OH.$$

In the plasma created in filaments the reaction involving O_2^+ is likely to dominate, as according to simulated filament plasma dynamics (Gordon et al., 2003) the concentration of singly ionized molecular oxygen is at least 100 times greater than that of corresponding molecular nitrogen ions and reaches a number concentration on the order of $10^{16}\,cm^{-3}$.

In Sec. 4.1.1 the role of the oxidation of SO_2 by ·OH radicals in natural atmospheric particle formation was mentioned. In the presence of higher concentrations of nitric oxide (NO) and nitrogen dioxide (NO_2) the following reactions are possible (Seinfeld and Pandis, 2006):

$$\cdot OH + NO + M \longrightarrow HONO + M$$
$$\cdot OH + NO_2 + M \longrightarrow HNO_3 + M$$

Here the symbol M stands for a collision partner (an air molecule) needed to remove excitation energy liberated in the association reaction, according to the more explicit notation $A + B \rightleftharpoons [AB]^* \xrightarrow{M} AB$.

The association of ·OH and NO_2 leads to direct formation of gas phase nitric acid, which is an efficient agent in atmospheric nucleation and condensation of water vapour. Recent observations of the formation of NO and NO_2 in filament plasma at high concentrations by Petit et al. (Petit et al., 2010) suggest that the above reactions actually occur. The proposed pathways for the production of the nitrogen oxides involve N^+ ions and singly ionized molecular nitrogen N_2^+, as well as electronically excited atomic and molecular nitrogen. The importance of these will become evident when interpreting experimental observations in a later Sec. 5.3.2.

Nucleation enhanced by laser-generated ions

In an earlier section 4.1.1 the phenomenon of ion induced nucleation was briefly discussed and it was demonstrated that it is negligible for the condensation of pure water under common atmospheric conditions, where no extreme levels of water supersaturation are reached. It was also mentioned

that modern extensions of the classical Kelvin-Thomson model include microscopic interactions of dipolar molecules to more accurately describe small clusters of dipolar molecules.

These models predict a stronger enhancing influence of charge on the binary nucleation of water and dipolar precursor substances such as H_2SO_4 for the following two reasons (Yu, 2006): Similar to the simplified classical Kelvin-Thomson description the charge acts to stabilize small charged clusters thermodynamically, enhanced by the orientation of dipolar molecules. In the case of strongly dipolar co-condensing precursor substance, the attractive electrostatic forces acting on precursor molecules accelerate the growth of small charged clusters, additionally increasing the nucleation rate.

Almost expectedly no published research specifically dealing with laser generated ions influencing atmospheric binary condensation could be found. However, a theoretical study by F. Yu and R. P. Turco (Yu and Turco, 2001) considers the situation in an expanding and cooling lightning channel, where the concentrations of ions and precursor gas molecules are relatively high. Their considerations start at about 50 ms after the lightning strike, when the initial lightning channel has explosively expanded from an initial diameter of a few centimeters to about 2 m. At this time the ion density is about $10^8\,\mathrm{cm}^{-3}$ and the temperature is (still) in excess of 500 K.

Besides the presence of ions, in the study it is assumed that all sulphate aerosol initially present in the lightning channel has been evaporated due to the pre-expansion plasma temperature of about 30000 K, and is present as H_2SO_4. Assuming initial total background sulphate mass concentrations of $1.5 - 8\,\mu\mathrm{g\ m}^{-3}$, corresponding to up to about 2 ppb H_2SO_4(g) in the lightning channel before expansion, the authors of the study predict strong new particle formation of sizes larger 3 nm within one to ten seconds after the expansion of the channel. A typical number stated for typical assumed conditions is a total of $10^5 - 10^6\,\mathrm{cm}^{-3}$ newly nucleated particles.

The presence of ions as well as of precursor substance is found to be a critical factor. As it can be expected considering the discussion in Sec. 4.1.1, the influence of charge on the growth of larger particles with diameters $D_\mathrm{p} > 100$ nm turns out to be negligible.

It may seem odd to consider the situation of a cooling lightning channel for assessing the role of laser-generated ions in the context of atmospheric condensation. However, the ion number densities resulting from the simulations presented in in (Yu and Turco, 2001) attained when the lightning channel has cooled sufficiently to allow for particle formation (that is, it has reached close to ambient temperature which occurs about 1 s after the stroke), are just around $10^7\,\mathrm{cm}^{-3}$ (see Fig. 4.12), and are easily reached by a cooling flament plasma, which additionally has a heavy species temperature close to ambient from the start (Couairon and Mysyrowicz, 2007; Tzortzakis et al., 2001).

Later in this text it will become clear, and it will be discussed in detail, that the concentration of comparably efficient gaseous aerosol precursor substance produced in a filament, taking the role of H_2SO_4 in Yu and Turco's study, can be up to three orders of magnitude higher than that of H_2SO_4 considered for the cooling lightning channel (that is, up to ppm concentrations instead of ppb).

Consequently, although having almost certainly negligible effect on homogeneous nucleation of pure water particles, the electrostatic effect of ions produced in filament plasma may most probably add to the efficiency of new particle formation in filament plasma channels.

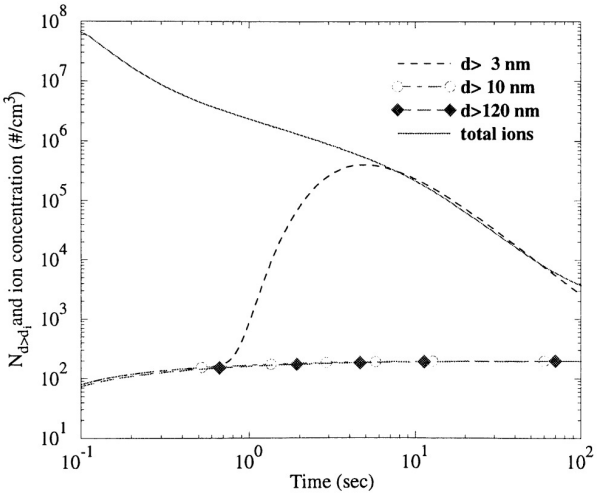

Figure 4.12.: Fig. 1 from Yu and Turco's study on electrostatically enhanced binary nucleation of water and H_2SO_4 in an expanding lightning channel (Yu and Turco, 2001). It can be seen that new particle formation sets in at about $t = 1$ s after the stroke, at which the temperature in the lightning channel has reached near ambient values. The ion concentration at that time is about 10^7 cm^{-3}, easily matched by the naturally cold filament plasma. Plotted curves are the ion concentration and cumulative changes of particle number concentrations above background; the assumed background sulphate mass concentration is $4.0\,\mu$g m^{-3}.

Indirect photochemical effects

In natural atmosphere containing a background of condensation nuclei too small to be activated under realistic conditions of water vapour saturation ratio (see sec. 4.1.2) photochemically or ion-chemically produced reactive substances may chemisorb to the surfaces of such particles, changing their surface properties and eventually enhance their ability to capture further molecules from the gas phase.

Such effect will be considered in the discussion of experimental results in a later section 5.3.4.

Besides directly forming hygroscopic species, reactive gaseous substances created due to the action of laser light, such as ozone or the ·OH radical, may also react with organic substances present in the atmosphere. On a global average biogenic sources, mostly vegetation, contribute the largest fraction of these volatile organic compounds (VOC) emitted into the atmosphere. They are present typically at ppb levels throughout the lower troposphere. VOC can lose their 'volatility' when they are oxidized by radicals. Several such oxidation steps may repeat, eventually resulting in supersaturation and condensation of the now involatile organic compound onto, for instance, a preexisting aerosol particle. In atmospheric chemistry condensed phase organic compounds formed in such a way are called 'secondary organic carbon'(Seinfeld and Pandis, 2006).

In normal atmosphere VOC are present at low concentrations, and the formation of secondary organic carbon due to their oxidation by laser induced radicals can not be expected to lead to reasonably quick and intense production of new particles.

However, in Sec. 4.1.1 the findings of Metzger et al. were referred to, who reported evidence for co-nucleation of H_2SO_4 with oxidation products of the initially very nonpolar VOC 1,3,5-

Trimethylbenzene, oxidized by ·OH radicals. One of the conclusions Metzger et al. draw from their results is the importance of specific functional groups added to the organic, serving as docking site for H_2SO_4.

Simultaneous high abundance of laser-generated radicals, processing available VOC, and precursor substance (specifically, of HNO_3 generated in filament plasma), could thus be another pathway to enhanced new particle formation induced by laser filaments.

4.2.3. Potential advantages of high power femtosecond laser radiation

The bottom line of the previous sections is that several pathways appear to exist to use light for inducing net condensation of vapour substance out of air. Especially the relatively well reproduced (but less well understood) photonucleation and light-induced condensation of water vapour using ultraviolet light indicates that electronic excitation of air molecules is necessary to induce some sort of initial aggregation of molecules to form critically sized clusters, on which further condensation of 'ordinary' vapour substance is possible.

The wavelength dependence of water photonucleation shows that the necessary excitation can be accomplished by light of photon energy in excess of $5 - 6\,\mathrm{eV}$.

The observed induction of water condensation by high intensity femtosecond radiation of about 1.5 eV photon energy shows that the necessary excitation can also be provided by effectively multiphotonic processes. These are direct multiphoton absorption, and probably more important, the creation of a plasma in which excitation can be built up by cascaded absorption mediated by the free electrons in the plasma. In Sec. 4.2.2 some reactions were listed by which the ions in a plasma created from moist air could produce similar excited species as they are created by the direct absorption of sufficiently energetic ultraviolet light.

There are two factors which make UV light less attractive with regard to a possible application of laser-induced condensation for atmospheric remote sensing.

Firstly, while direct absorption of UV light of wavelengths $\lambda \leq 200\,\mathrm{nm}$ by moist air is efficient, quite naturally the corresponding strong atmospheric absorption automatically entails limited range. Linear absorption leads to Beer-Lambert exponential decay of light intensity with distance, and a corresponding profile of deposited energy and density of excited molecules (at least as long saturation of the absorption does not occur).

Secondly, molecular (Rayleigh) scattering increases as λ^{-4} (see later Sec. 3.1.3), leading to a relative penalty of a factor of 256 between the molecular scattering attenuation coefficients at the two wavelengths $\lambda = 800\,\mathrm{nm}$ and $\lambda = 200\,\mathrm{nm}$. The result is a relatively stronger exponential attenuation of UV light due to molecular scattering, in addition to linear absorption. The net effect is impressive: the transmittance through air at sea level over a distance of 1828 m (about one nautical mile) is about 70 % at $\lambda = 800\,\mathrm{nm}$, and practically zero at $\lambda = 200\,\mathrm{nm}$ (Measures, 1984).

Not only the exponentially decaying irradiance resulting in limited range of *action* makes linear absorption unfavourable. Also in terms of remote *detection* an effect with such an exponential range profile is unfavourable, as a strong signal from close distances is likely to shadow an exponentially

weak signal from large distances (adding to one of the basic difficulties of laser remote sensing).

Besides reduced scattering losses, nonlinearly propagating near infrared laser light producing multiple filamentation has some properties which would make it more promising for inducing atmospheric condensation for the purpose of remote sensing.

In a multiply filamenting laser beam most energy is contained in the background photon bath and is only successively fed into filaments, where it is consumed by multiphoton ionization and inverse bremsstrahlung. This causes deposition of energy to be relatively evenly distributed along the direction of propagation in contrast to the Beer-Lambert profile of (non-saturating) linear absorption of UV light.

Moreover, the possibility to place the position of filament onset in space, within certain limits, yields additional control of the range where optical energy will be efficiently absorbed.

It is also important to note that not just processes happening in femtosecond near-infrared laser-induced plasma may turn out to eventually cause net water condensation. The high intensities reached close to the ionizing cores of filaments may as well produce non-ionic excited species taking part in relevant chemical reactions sketched in previous sections, leading to known aerosol precursor substances.

Finally, non-ionic pathways appearing in interpretations of the known UV-light induced photonucleation (Sec. 4.2.2) may be enabled by multiphoton (specifically: 4-photon) absorption of high intensity radiation propagating close to the ionizing filament cores.

4.3. Aspects of Laser-aerosol interaction

This section specifically deals with the action of a strong laser beam on preexisting suspended particles and droplets already present in the gaseous atmosphere. The lower atmosphere is never perfectly free of particles (solid or liquid), and their presence may have an impact on laser induced condensation processes, as aerosol particles may be modified, and their properties as condensation nuclei may change.

In this section experimental and theoretical results from previous studies on general laser-aerosol interaction are collected. Then the specific case of watery aerosol will be considered with a focus on intense femtosecond laser light. Finally the important question of femtosecond laser-induced fragmentation of such aerosol will be addressed.

4.3.1. Brief overview of processes involved in laser-aerosol interaction

The different cases of laser-aerosol interaction can be classified according to the combination of a number of key parameters: The **linear optical properties of the aerosol substance** at the laser wavelength are described by the complex refractive index $\tilde{n} = n + i\kappa$, where n is the 'usual' real refractive index and the imaginary part κ is related to absorption. Together with the size and morphology of the aerosol particles they determine the intensity distribution of the internal optical field. The material dependence of the latter can have subtle consequences for the localization of energy

absorption, in particular when the real part of the refractive index of absorbing particles is less than unity (Astafieva and Prishivalko, 1998). This is for example the case for mineral dust (Al_2O_3) and 10.6 μm laser wavelength, where $\tilde{n} = 0.78 - 0.049i$.

The **physical and thermodynamic properties of the aerosol substance** such as their enthalpies of melting and evaporation, thermal conductivity, and state of matter under atmospheric conditions, are important for the case when enough energy is absorbed by a particle to cause notable change of temperature or even to induce phase transitions. These parameters also determine how the interaction with the laser beam will proceed after such changes have been initiated, and what are the relevant time scales.

In the case of pulsed laser radiation, these timescales automatically are the reference for the **laser pulse duration**, allowing to classify the pulses as relatively 'long' or 'short'. In most of the literature the reference time scale is that of heat diffusion within the aerosol particle.

Besides the purely temporal aspect, the pulse duration together with pulse energy determine the **maximum Intensity** reached under the prevailing conditions, which is another important parameter. Additionally, the laser pulse can have an internal time structure, such as a multipulse, reducing the tradeoff between achievable peak intensity and total interaction time.

The uptake of energy from the laser beam is also strongly influenced by the **size of the particles** relative to the laser wavelength. Especially in the case of (partially) transparent material, particle size and refractive index together determine the internal intensity distribution.

The previously mentioned criteria are mainly related to single particle effects. In some situations, effects involving many neighbouring particles can introduce collective interaction and additional nonlinearities. An aerosol particle absorbing energy from the laser beam heats up and emits part of the generated heat to the surrounding. Evaporation or fragmentation lead to emission of gaseous or condensed phase material. The affected volume expands as heat and gas diffuse or produce a shock wave, and expelled fragments ballistically propagate. Therefore the affected volume may be significantly larger than the original particle volume, and neighbouring volumes may overlap. If irradiation persists in this situation, multiple particle effects may develop due to the interaction of the expanding volumes.

Accordingly, besides number density and size distribution of the aerosol, the time structure of the laser irradiation is important for the occurence of such effects.

Altogether, the interplay of the mentioned parameters determines how individual aerosol particles and their surroundings, and consequently the aerosol as a whole, are left after the interaction. How much of the absorbed energy is actually turned into heat determines the absolute and relative amounts of vaporized aerosol substance, and the amount of material forming fragments. The chemical composition of the debris after the laser interaction, and the state of electronic excitation or even ionization, especially of gaseous substance, are determined by details of the absorption process. The very local deposition of energy, which is finally turned into heat, can cause shock waves or strong acoustic waves that sweep the surrounding medium and that can transiently create extreme conditions of pressure and temperature even at some distance from the location of the original aerosol particle. These observable effects mainly root in the different **dominating mechanisms of absorption** of

energy from the laser beam: **Linear absorption** is important as soon as light at the laser wavelength matches an electronic or dipole-active vibrational transition of the aerosol substance. Soot is a typical example for an absorber in the visible, and water shows strong absorption accessible to CO_2 laser radiation at a wavelength of 10.6 μm.

Sufficiently intense laser light can induce the formation of a plasma. The initial step of plasma formation in aerosol particles or droplets which do not linearly absorb at the laser wavelength is due to **multiphoton ionization** which was introduced in sec. 2.2 (Eickmans et al., 1987; Kandidov and Militsin, 2004). Following a similar formalism as for hydrogen-like atoms Keldysh derived his theory also for interband transitions in crystalline solids, and found the same regimes of interaction as they were identified in the case of a single atom (Keldysh, 1965), again separated by the parameter γ_K.

In insulating solids multiphoton-ionization leads to population of the conduction band where electrons move freely and can be accelerated by an external field. Also in the case of solids it is the initiating process for generating a plasma. Again, the associated cross section $\sigma^{(K)}$ strongly depends on the number $K = \mathrm{mod}(\frac{\Delta E}{\hbar\omega}) + 1$ of photons of energy $\hbar\omega$ needed for surpassing the ionization barrier of height ΔE (Bergé et al., 2007; Keldysh, 1965). Also in condensed media tunneling ionization can be neglected up to irradiated intensities of about $I \approx 10^{13}\,\mathrm{W/cm^2}$, and the multiphoton ionization rate can be well expressed by the relationship $\mathrm{d}n_e/\mathrm{d}t = \sigma^{(K)} \times I^K$. Besides its influence on the K-photon absorption cross-section $\sigma^{(K)}$ the number K of required photons explicitly enters the expression for $\mathrm{d}n_e/\mathrm{d}t$ as the exponent of the laser intensity I, making the multiphoton ionization rate highly nonlinear with respect to K as well as to I.

Thus there are different factors determining the actual importance of MPI in a given situation: laser light intensity and pulse duration, as well as the ionization potential of the aerosol material together with the ability of the particles to locally enhance the optical field strength (Kandidov et al., 2004). The latter again depends on material properties, but also on particle morphology. Figure 4.13 illustrates the role of the ionization potential. It shows multiphoton ionization rates obtained from Keldysh theory for crystals (Keldysh, 1965) (see also sec. 2.2.2) for fused silica and water at an excitation wavelength of 800 nm. The double-logarithmic plot, adapted from Fig. 2 in (Bergé et al., 2007), extends over the intensity range between $I = 10^{12}\,\mathrm{W/cm^2}$ and $I = 10^{15}\,\mathrm{W/cm^2}$. The lower ionisation potential of water (7 eV vs. 7.8 eV for fused silica) (Bergé et al., 2007) results in an MPI rate that is greater by more than 2 orders in the 'lower' intensity range.

Very few initially present free electrons, that may have been generated by MPI, can be multiplied to immense numbers by **avalanche** or **cascade ionization**, by collisional absorption as it was described in Sec. 2.2.2.

The process of laser filamentation described in the first chapter involves short pulses, a relatively dilute medium, and a geometry, which together have the consequence that the electron avalanche cannot develop catastrophically until the laser pulse is over. In a condensed medium the collision rate of electrons with neutrals is considerably higher. The number of free electrons rises more steeply. Additionally, due to the more frequent collisions, the electron gas heats up by inverse bremsstrahlung, and collisional ionization by thermal electrons becomes more important than directly laser driven collisional ionization (Peñano et al., 2005).

Heating of the electron gas is even more efficient in the case of longer laser pulses, which are able to sustain the electron multiplication to high number densities, eventually leading to **optical breakdown**.

Above an electron density of $n_e = n_{\mathrm{crit}}$, the refractive index of the plasma (see also sec. 4.3.3) becomes imaginary and the laser light can no longer propagate, but it is backreflected. As the energy supply to the plasma is practically cut off, this sets an end to the electron avalanche. The critical electron density n_{crit} is defined as the one leading to a plasma frequency $\omega_{\mathrm{pl}} = \sqrt{n_e e^2/\epsilon_0 m_e}$ which, for $n_e = n_{\mathrm{crit}}$ equals the optical frequency ω_{l} of the laser light (Kruer, 1988).

This is the case for $n_{\mathrm{crit}} = \omega_{\mathrm{l}}^2 m_e \epsilon_0 / e^2$, or

$$n_{\mathrm{crit}} \simeq \frac{1.11 \times 10^{21}}{\lambda^2},$$

where n_{crit} is in units of cm^{-3}, and the laser wavelength λ in μm.

Finally, the modified medium in the beam path affects subsequent laser radiation. In general, any additional inhomogeneity of the refractive index will increase total scattering. If present, newly formed particles will be major contributors to this increase, but in priciple scattering can also occur on inhomogeneities of temperature or mixing ratio of gaseous substances (e.g. air/water vapour) with different refractive indices at the laser wavelength.

4.3.2. Important specific cases of 'classical' laser-aerosol interaction

The majority of published studies of laser action upon aerosol addresses cases of micosecond pulsed/cw infrared (CO_2) or nanosecond Q-switched laser radiation interacting with water and various solid aerosols. Some important results on this 'classical' type of interaction are summarized in this section. The types of aerosol considered here comprise water aerosol and micrometer or sub-micrometer sized solid dielectric particles. The atmospherically less relevant case of laser interaction with aerodisperse metal particles (see (Lushnikov and Negin, 1993)) is not included here. The same holds for coarse solid aerosol like mineral dust with particle sizes of several tens of micrometers, which sediment

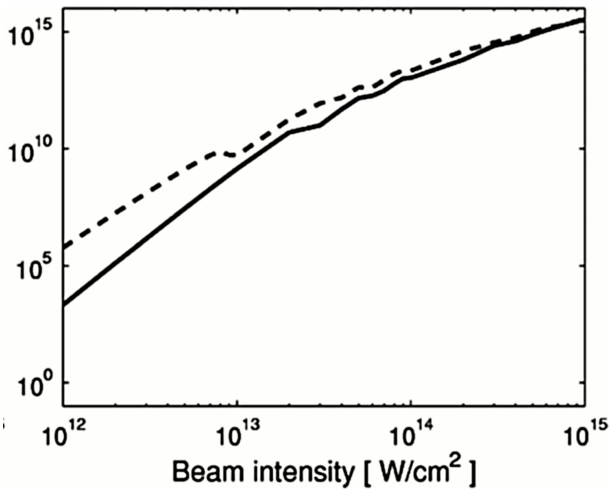

Figure 4.13.: Multiphoton ionization rates obtained using Keldysh theory as function of intensity I, plotted for liquid water (dashed) and silica (solid) and an excitation wavelength of $\lambda = 800$ nm(Fig. 2 b) from (Bergé et al., 2007))

quickly and generally stay close to ground level.

Liquid water aerosol

One of the best studied scenarios of laser-aerosol interaction is that of strong cw or microsecond pulsed CO_2 laser radiation propagating through water fogs and clouds, and relatively much work on this subject has been published. According to A.A. Lushnikov (Lushnikov and Negin, 1993) the idea to use infrared laser light for evaporating water aerosol was first formulated by A.V. Kuzikovskii et al. in 1968 (Kuzikovskii and Khmelevtsov, 1968). Since then there has been a lot of activity in this field, starting from initial experiments on single suspended drops (Bukatyi and Pogodaev, 1970; Kuzikovskii et al., 1971). Only a fraction of the published material on this subject is represented by the works (Almaev et al., 1985; Caramana et al., 1991; DeForest et al., 2002; Pustovalov and Khorunzhii, 1992), and the many references in the latter three.

The main goal of this research was to delineate conditions under which the clearing of a channel through an atmospheric water cloud or fog would be possible using a high power laser. The cleared channel then would permit unscattered propagation of subsequent laser radiation of the same or of a different wavelength. Besides the goal of mere reduction of scattering due to cloud droplets, laser clearing of clouds has been suggested as a means to gain information, enabling remote sensing of cloud properties and turbulence (Caramana et al., 1991). Most of these 'cloud hole boring' studies consider laser radiation at a wavelength of $\lambda = 10.6\,\mu$m, as this wavelength is strongly absorbed by liquid water, less strongly by water vapour and only weakly by air (Caramana et al., 1991), making it preferential for heating up and evaporating liquid water droplets, with otherwise low transmission loss. The absorption of light at $\lambda = 10.6\,\mu$m is due to the molecular bending modes of liquid water (Zhang et al., 1987) and thus entirely linear. The corresponding absorption coefficient is about $\alpha \sim 10^5\,\mathrm{m}^{-1}$ (Zhang et al., 1987).

As water droplets absorb energy from the laser field they heat up. The irradiated isolated droplets can be strongly superheated to about 305 °C without actually boiling, that is, without a new gas phase forming inside the droplet. On the basis of modelling and numerical calculations two distinct regimes were identified in this regard: slow and fast heating (Park and Armstrong, 1989). Slow heating is dominated by thermal diffusion of vapour from the droplet surface, equally removing water vapour and heat from the droplet. The fast heating regime is entered when heat losses at the droplet surface due to evaporation and heat conduction are insufficient to prevent the core of the droplet from overheating.

When CO_2 laser radiation is considered, the microsecond pulsed laser heating of small water droplets ($D_\mathrm{p} < \lambda$) is practically homogeneous, mainly because of the evenly distributed energy deposition in the droplet volume. This is because internal focusing of the laser light is rather weak in this size range. It is more remarkable that homogeneous heating can be assumed even up to a diameter of $D \simeq 70\,\mu$m, by far exceeding the size of typical cloud droplets ($D_\mathrm{p} \leq 10\,\mu$m). In the case of large droplets (here $\lambda \gtrapprox D_\mathrm{p}/5$), even though the internal distribution of light intensity is noticeably inhomogeneous, heat production can still be assumed homogeneous. Calculations by Carls et al. (Carls and Brock, 1988) showed that flow-based heat equilibration during the time of irradiation can smooth

out inhomogeneities providing that the laser pulse is long enough and not too intense, in accordance with experimentally observed explosion thresholds for large droplets ($D_\mathrm{p} \cong 60\,\mu\mathrm{m}$) (Kafalas and Herrmann, 1973). Specifically, the laser pulse parameters discussed in the cited publications are a pulse duration of $\tau \simeq 200\,\mathrm{ns}$ and an intensity of about 10 to $70\,\mathrm{MW/cm^2}$.

Because of the generally homogeneous heating, the onset of internal boiling is mainly a function of the laser intensity and the droplet size. One more result is a generally spherically symmetric pattern of droplet explosion (Carls and Brock, 1988).

The situation already becomes more complex if the laser light is not strongly absorbed by the aerosol or liquid droplet material, and at the same time the laser intensity and photon energy are greater than in the previous case. This happens for example when radiation from a strong Q-switched, frequency doubled Nd:YAG laser is applied, where pulse durations are often on the order of a few nanoseconds, and intensities can reach values on the order of $\mathrm{GW/cm^2}$. The absorption coefficient of pure water at a wavelength of $\lambda = 532\,\mathrm{nm}$ is about $\alpha \sim 10^{-4} \ldots 10^{-3}\,\mathrm{cm^{-1}}$ which is negligibly small for drops of even several tens of micrometers size (Zhang et al., 1987). As for the infrared case, the optical field strength and, thus, the intensity inside droplets small compared to the wavelength, are practically uniform. This is true for sizes where $x = k\ r_\mathrm{p} = \frac{2\pi r_\mathrm{p}}{\lambda} \lessapprox 2$, the so called Rayleigh size range (k is the wavenumber of the laser light). Because of the shorter wavelength this criterion fails for correspondingly smaller droplets when 532 nm laser light is irradiated, in this case for diameters $D_\mathrm{p} \gtrapprox 340\,\mathrm{nm}$. Above this diameter the intensity distribution inside the droplets becomes increasingly inhomogeneous.

The extreme case of a large, transparent spherical droplet can be visualized by the action of a ball lens in geometrical optics. In calculations, to accurately handle also intermediate droplet sizes, the exact solutions for the optical fields inside and outside the irradiated droplet provided by Mie theory are used (Alexander et al., 1991; Astafieva and Prishivalko, 1998; Kandidov et al., 2004). These will be revisited later in sec.3.1. In such a case, the strong enhancement of the optical intensity in parts of the aerosol particle, in combination with the nonlinear microscopic interaction of the laser light with the aerosol material, can lead to very localized deposition of energy within the particle. The size dependence of the internal intensity exaggeration is literally potentiated by the nonlinearity of the absorption, making all accompanying processes strongly size dependent. Especially the fragmentation of larger droplets and particles can be expected to have a pronounced size dependence under conditions of effectively nonlinear absorption. The asymmetry of energy deposition causes an asymmetry of the explosion dynamics as well, leading to additional complication of the fragmentation process(Zhang et al., 1987).

Solid aerosol

Besides watery liquid aerosol there is a vast variety of solid aerosol present in the troposphere. A major component of it consists of inorganic material, mainly sea salt, volcanic ash, ashes from wildfires and desert dust. There is also a fraction stemming from biogenic sources, which comprises pollen, algae, bacteria and other microorganisms, as well as dead biogenic material from soil and vegetation.

The biogenic fraction may represent up to half of the aerosol particles with a radius smaller than $r_P \approx 1\,\mu$m (Jaenicke, 1993).

Laser action upon, and interaction with, solid aerosol has been studied mainly for some artificially prepared aerosols. These were for example clouds of mineral dust (Al_2O_3, SiO_2), or metal powders (Lushnikov and Negin, 1993). There appear to be no published studies specifically addressing the interaction of strong laser light with organic or generally biogenic aerosol. (There *do* exist studies about, for example, the fluorescence of substances contained in watery solution droplets (Hill et al., 2000; Méjean et al., 2004), or solid aerosol substance (Pinnick et al., 2004), but the question of irreversible action of the laser radiation on the aerosol particles generally is not addressed therein.)

The imaginary parts of the refractive indices of Al_2O_3 and SiO_2, which are typical compounds found in aerosol of crustal origin, are only about three times smaller than that of water at the CO_2 laser wavelength of $\lambda = 10.6\,\mu$m. Under appropriate conditions of irradiation the resulting efficient absorption leads to strong heating of the mineral substance, even up to the boiling point, which is as high as $\sim 4000\,$K in the case of Al_2O_3. The high temperature leads to considerable population of the conduction band from which electrons are freed by thermoemission or by photoexcitation. Thus mineral aerosol offers an additional pathway to plasma formation which is distinct from the mono- or multiphotonic optical excitation of molecules in the watery aerosol case. During the processes of thermoemission the aerosol particles are positively charged. This proceeds until the kinetic energy of emitted electrons is insufficient for overcoming the growing attractive coulomb potential, that is, until the particle is charged up to its equilibrium charge corresponding to the present conditions.

Another mechanism by which mineral aerosols acquire charge is the desorption of molecules adsorbed to the aerosol particle surface, accompanied by matrix-assisted desorption and ionization. The adsorbed molecules are bound with energies between $100\,$meV and $2\,$eV and can be released with low energy photons. The process of desorption can involve a charge transfer from the desorbed molecule to the aerosol particle.

Once electrons are created by the latter two effects at a sufficiently high rate, the electron avalanche can proceed as in the previously discussed cases. The elevated temperature close to the hot aerosol further facilitates the avalanche process because of the locally reduced density of the surrounding air. (Lushnikov and Negin, 1993). Unlike the case of initially liquid aerosol, where temperature gradients arising during the heating process can equilibrate on the same timescale as the gradients build up (Carls and Brock, 1988), initially solid aerosol can heat up in a substantially inhomogeneous way. This may lead to stress induced cracking and fragmentation way below the threshold for explosive boiling (Astafieva and Prishivalko, 1998).

The absorption mechanisms at shorter pulse durations and wavelengths (this is, for intense nanosecond visible or near infrared laser pulses), resemble those encountered in the case of liquid watery aerosol. The linear absorption coefficients of typical oxide minerals are on the same order of magnitude as that of water, and linear absorption is likewise unimportant. The absence of efficient heating and thus thermoemission of electrons makes multiphoton ionization the only available process to initiate the formation of plasma. Differences of multiphoton absorption cross sections and the ionization potential influence the threshold irradiance above which avalanche ionization sets in. Theoretically

obtained multiphoton ionization rates of water and SiO_2 are displayed in Fig. 4.13, indicating that modest differences of ionization potential may substantially influence the MPI rate. The mostly irregular morphology of mineral aerosol particles complicates the theoretical treatment of the interplay between the internal intensity distribution and energy deposition.

Irrespective of the laser parameters, a special role is played by solid carbonaceous aerosol which is highly absorbing throughout an extended spectral region, and especially in the visible range. This is, for example, atmospheric soot particles from fossil fuel burning. Aerosol particles of this type efficiently couple energy out of the laser beam on any time scale. The material is able to react with the atmospheric oxygen, and the chemical reactions following the laser ignition strongly impact the atmosphere in the surrounding of the original aerosol particle.

4.3.3. Action of intense femtosecond laser light on watery aerosol particles

A relatively limited amount of experimental data on the action of femtosecond laser radiation on water aerosol is available in the literature. One single publication by Lindinger and coworkers (Lindinger et al., 2004) is concerned with the explosion dynamics of large water droplets of $D_p \approx 100\,\mu$m diameter when irradiated with a focused beam of high power femtosecond laser pulses (~ 1 mJ, ~ 60 fs, focused to a beam diameter of about $100\,\mu$m). By time resolved imaging they qualitatively showed that the explosion dynamics become even richer than in the nanosecond case and vary strongly with the irradiated pulse energy and duration. Geometrical features (symmetry) of the explosion dynamics and explosion velocities were studied, and a variety of features and explosion patterns were identified which were very reproducible.

Lindinger et al. identified aspects peculiar to ultrashort pulse durations, most notably the greatly reduced fluence threshold for observable plasma generation when compared to the nanosecond laser pulse case, and attributed this to the more efficient multiphoton ionization, enabling the fast ignition of an electron avalanche.

The observations of large droplets exploding in intense femtosecond near infrared laser light allowed them to draw conclusions on the explosion mechanism along the theoretically calculated distribution of peak intensities inside the droplet resulting from short-pulse irradiation.

Once optical breakdown commences in one of the zones, the trailing part of the laser pulse is effectively cut off. If the pulse peak intensity is sufficiently high, breakdown sets on already during the leading part of the pulse, resulting in practically all pulse energy to being intercepted (not necessarily fully absorbed) in that zone, and determines the strong dependence of the directionality of fragment ejection on the laser pulse parameters. It was also observed that the visual impression of droplet explosion processes were comparable between the case of shortest pulse at highest obtainable peak intensity ($\tau = 60$ fs, $I_0 = 1.8 \times 10^{14}$ W/cm^2) and a not too long stretched pulse with lower peak intensity ($\tau = 260$ fs, $I_0 = 1.7 \times 10^{13}$ W/cm^2). This manifests the frequently observed phenomenon that once the intensity is high enough to liberate sufficient electrons by multiphoton ionization to *start* an electron avalanche, a longer pulse is generally more efficient in *driving* it.

The work reported in (Lindinger et al., 2004) is not concerned with determining the result of the

droplet explosion, that is, the size distribution of the fragments or the mass lost by evaporation, but with the dynamics of the initial few microseconds alone.

A little earlier an optical time delayed transient scattering technique had been applied by Courvoisier et al. to investigate the plasma formed in relatively large ($D_\mathrm{p} \approx 50\,\mu$m) water droplets irradiated by intense near infrared femtosecond laser pulses. Also they found the plasma to be generated in a very localized spot at the expected position.

In a numerical study Kandidov et al. examined the initial stages of of the plasma density evolution inside relatively large water droplets ($D_p = 30\,\mu$m). In the calculations an approximate phase-aware raytracing method was compared with Mie theory (Kandidov et al., 2004). The time-dependent optical field was coupled into a model for the electron density evolution incorporating multiphoton and collisional ionization, and Drude-type collisional heating of the plasma.

These calculations were limited to the time when the most dense regions in the distribution of free electrons in the material parts reached 1 % of the concentration of neutrals. The main result of these calculations was the proof that the locations of plasma formation, for sufficiently large droplets, can be well predicted by the geometric optics picture of focusing due to refraction and internal reflection. More importantly, the determined approximate threshold irradiance for the commence of internal optical breakdown in the large water droplet agrees quite well among experiment (Lindinger et al., 2004) and theory (Kandidov et al., 2004) (see Fig. 4.14) for comparable pulse durations. Note however that although the droplets are not exactly of the same size. With regard to the finding that the geometrical optics picture approximately holds in this droplet size range ($x \approx \frac{\pi D_\mathrm{p}}{\lambda} > 200$).

Another important observation reported in (Lindinger et al., 2004) is that, under conditions typical for the core of a strong filament ($I_0 > 10^{13}\,\mathrm{W/cm^2}$ for near infrared filaments), the threshold for droplet explosion is overcome. In a large cloud drop ($D_p \approx 100\,\mu$m) directly hit by a filament a substantial fraction of the irradiated energy will drive an electron avalanche, and the droplet eventually will fragment.

The relative amount of plasma generated inside a large water droplet under various conditions of irradiation can be estimated from measurements reported by Henin et al. (Henin et al., 2009) who used, as a proxy for the number of initially present free electrons, the ion current through a biased plate capacitor enclosing the volume around the exploding droplet. A train of $D_\mathrm{p} \approx 100\,\mu$m water droplets was irradiated with intense, strongly focused femtosecond laser pulses (duration $\tau_\mathrm{p} = 65$ fs) to which an increasing chirp was applied, stretching them to up to 10 ps duration. The reported observation of strongly enhanced plasma creation, peaking at about 8 ps pulse duration, is in qualitative accordance with the previously described time resolved imaging study.

The locally augmented concentration of excited species in the cooling plasma could have an influence on the ion and radical chemistry following the irradiation. Questions related to this will reappear later in this text.

Regrettably there appear to be no published studies of the action of intense femtosecond laser radiation on water droplets of smaller sizes in the range down to $D_\mathrm{p} \approx 1\,\mu$m more typical for clouds and larger haze droplets, nor do such studies exist for non-water materials. For even smaller (sub-μm) particles or droplets, the situation appears similar. To my knowledge there is no published systematic

work devoted to the action of ultrashort laser pulses upon atmospherically relevant aerosols (or artificial aerosols serving as models of these), under conditions of irradiation causing irreversible modification of the aerosol particles.

In the context of laser-induced explosion of large water droplets nonlinear self focussing inside the droplet can be observed (Lindinger et al., 2004), leading to a different shape and size of the region where plasma is formed. Similar can be expected to happen in solid media, the more the larger the nonlinear refractive index. The more localized energy deposition may reduce the threshold for stress cracking and enhance the fragmentation of solid particles.

4.3.4. Extrapolation to small watery aerosol particles

The intensity enhancement factor relative to the incident radiation determined by Kandidov et al. for $D_p = 60\,\mu$m water droplets attains a maximum value of about 100 on the droplet's axis, after internal reflection from the shadow face. Before being internally reflected the light passes a conically shaped region close to the shadow face, where the intensity is enhanced by a factor of about 20. In the case of just threshold irradiance the former is the location where the electron avalanche sets off, as only there the local intensity is high enough to liberate the necessary amount of seed electrons by multiphoton ionization.

This means that roughly $I_{\max} \approx 10^{13}\,\mathrm{W/cm^2}$ (at $\tau = 45\,$fs) is reached there, suggesting that also in smaller water aerosol droplets, once about this peak intensity is reached, optical breakdown occurs.

In droplets larger than the spatial extent of the laser pulse along its direction of propagation

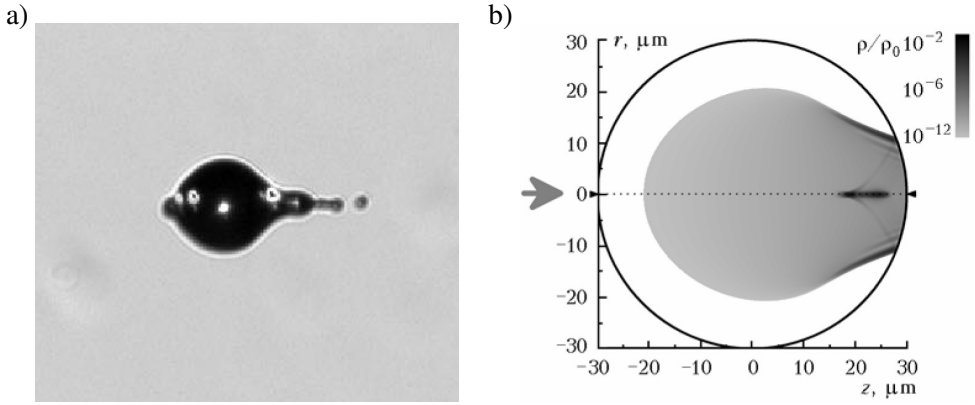

Figure 4.14.: a) Water droplet ($D_\mathrm{p} \approx 100\,\mu$m) irradiated by a laser pulse ($\tau = 60\,$fs, $\lambda_0 = 805\,$nm,$I_0 = 3.3 \times 10^{11}\,\mathrm{W/cm^2}$) photographed by Lindinger et al. at time $t = 8.4\,\mu$s after the laser pulse (Fig. 3d from (Lindinger et al., 2004)). **b)** Calculated free electron density inside a water droplet ($D_\mathrm{p} = 60\,\mu$m) irradiated by a laser pulse ($\tau = 45\,$fs, $\lambda_0 = 800\,$nm, $I_0 = 3 \times 10^{11}\,\mathrm{W/cm^2}$) at time $t = 330\,$fs measured from the time at which the pulse maximum enters the droplet on axis (Fig. 7d from (Kandidov et al., 2004)). In the zones of highest degree of ionization the calculated electron density reaches about 1 % of the bulk density of neutral molecules $n_0 = 3.34 \times 10^{22}\,\mathrm{cm^{-3}}$. In panel a) it can be seen that the resulting shock wave deforms the shadow face of the droplet and leads to the ejection of a few fragment drops, while most of the liquid volume remains in the mother droplet.

(which can be described by the phase-aware ray optical approximation in (Kandidov et al., 2004)) the maximum achieved enhancement of the internal intensity depends on the time-dependent overlap of the refracted and reflected fields, as the optical wave packet is localized within the droplet. Such overlap constraints become less important the more the droplet dimensions come close to (or go below) the spatial laser pulse length $L = c\tau/n$ (c being the speed of light and n the refractive index of the external medium), as then the external optical field can better and better be approximated not by a wave packet, but by a slowly amplitude modulated plane wave. This means that the internal intensity distribution can be increasingly well be approximated by the one caused by an incoming monochromatic plane wave. This is the case described by the classical Mie theory (see Sec. 3.1.4).

If the droplets are *even* smaller, of the size of an optical wavelength, $D_\mathrm{p} << \lambda$, the exciting laser pulse can be approximated by a slowly amplitude modulated time harmonic field. More specifically, if $x << 1$ and $|mx| << 1$, where $x = \pi D_\mathrm{p}/\lambda_\mathrm{ext}$ and $m = n_\mathrm{int}/n_\mathrm{ext} << 1$ is the ratio of internal and external refractive indices, the Rayleigh approximation is valid and the optical electric fields in a sphere of diameter D_p and close to it can be treated as if they were static fields. With the approximation $n_\mathrm{ext} = 1$ the internal intensity then is given by

$$I_\mathrm{int} = \frac{9}{|\epsilon_\mathrm{int} + 2|^2}\, I_\mathrm{ext}, \tag{4.21}$$

where ϵ_int is the (complex) dielectric function of the dielectric, related to the refractive index n_int by $n_\mathrm{int} = \sqrt{|\epsilon_\mathrm{int}|}$. This expression corresponds to the 'Rayleigh approximation' and results from dropping all but the lowest order terms from the Mie expansion of the internal field.

In the case of water with $n \approx 1.33$ ($\lambda = 800\,\mathrm{nm}$) this means $I_\mathrm{int}/I_\mathrm{ext} \approx 0.63$. Consequently, very small water droplets do not show the immense reduction of the breakdown (and explosion) irradiance threshold which is produced by the concentration of light energy in large droplets. On the contrary, the intensity distribution is rather homogeneous, at a level below the external intensity.

To illustrate this, in Figure 4.15 the deviation of the internal intensity distribution in small silica spheres surrounded by air, calculated using the exact expressions from Mie theory for plane wave illumination, from that resulting from the Rayleigh approximated internal optical field is shown for diameters D_p of 10 nm, 50 nm and 100 nm. The assumed optical wavelength is $\lambda = 800\,\mathrm{nm}$. Clearly, the Rayleigh approximation gradually underestimates the average intensity and the homogeneity of its distribution in the sphere. It is however evident that the internal optical field is close to homogeneous, and no notable enhancement of optical breakdown occurs.

In Fig. 4.16 the internal intensity distributions in the equatorial planes of water droplets of sizes between $D_\mathrm{p} = 0.5\,\mu\mathrm{m}$ and $100\,\mu\mathrm{m}$ are visualized for monochromatic illumination with $\lambda = 800\,\mathrm{nm}$ light. It is apparent that already at $D_\mathrm{p} = 1\,\mu\mathrm{m}$ notable concentration of optical energy towards the shadow face takes place. For the reasons given above, considering a laser pulse of $\tau = 100\,\mathrm{fs}$ duration (corresponding to a thickness of about $L = \frac{c}{n}\tau \approx 30\,\mu\mathrm{m}$) the continuous wave field gives a reasonable approximation for the field excited by the pulsed radiation.

Also for larger drops and short pulse irradiation the continuous wave (cw) approximation gives a good idea if the pulse duration is long enough according to the requirement $c\tau >> R$.

As pointed out in (Kandidov et al., 2004), in large droplets and under conditions far above threshold for explosion, breakdown sets on in the conically shaped volume close to the shadow face, where the intensity enhancement is relatively moderate as compared to the internal focal region located on-axis (see also Fig. 4.14 b). As it can be inferred from actually observed explosion dynamics (Lindinger et al., 2004) the plasma formed in the conical region of moderate intensity enhancement, which is reached by the laser pulse first, blocks the trailing part of the pulse from reaching the central focal region. This means that under these conditions the enhancement on the order of ≈ 20 is sufficient to set off the catastrophic electron avalanche leading to efficient coupling of energy out of the light field.

With regard to the estimated peak intensity enhancement for smaller droplets (Fig. 4.16) it is then possible to conclude that under the same above-threshold conditions also smaller droplets down to sizes of single micrometers concentrate the incident light sufficiently to initiate and fully develop optical breakdown.

Evidently the intensity levels in the core of a filament belong to this regime. As a conclusion, water droplets down to sizes on the order of a micrometer hit by a filament will almost certainly undergo explosive fragmentation.

Some conclusions can be drawn also for the dependence of the threshold irradiated intensity for optical breakdown on the initial droplet diameter D_p. Evidently the threshold irradiated intensity for the observable onset of plasma formation in $D_\mathrm{p} = 100\,\mu$m water droplets is below $I_{\mathrm{thresh},100\,\mu\mathrm{m}} \approx 3 \times 10^{11}\,\mathrm{W/cm^2}$ for laser pulses of $\tau = 60\,$fs duration and a central wavelength of $\lambda_0 = 805\,$nm (Lindinger et al., 2004), as the plasma created at this intensity is already strong enough to produce a shock wave leading to deformation of a corresponding droplet and the emission of a few small fragments (see also Fig. 4.14).

Based on the calculated internal intensity enhancement (Kandidov et al., 2004) of a factor of 100 in that particular case this translates to a minimum required internal intensity of $I_{\mathrm{thresh,\,int}} \approx$

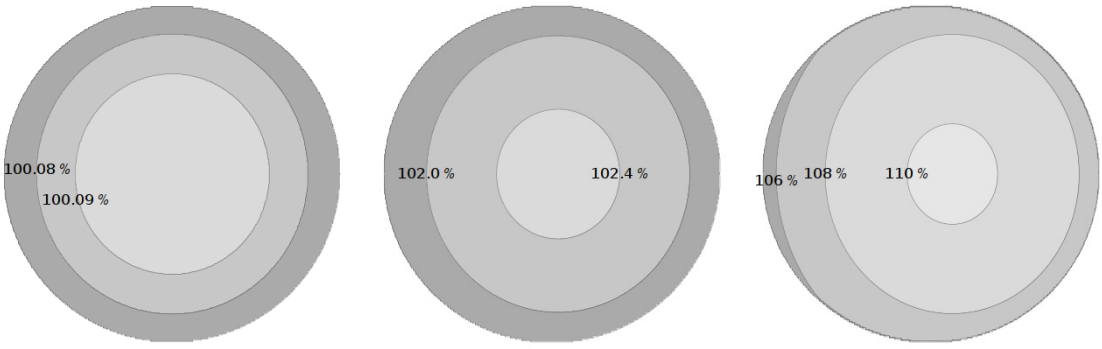

(a) $D_\mathrm{p} = 10\,$nm (b) $D_\mathrm{p} = 50\,$nm (c) $D_\mathrm{p} = 100\,$nm

Figure 4.15.: Ratio of exact and Rayleigh-approximated internal intensity distributions ($I_{\mathrm{int,Mie}}/I_{\mathrm{int,Rayleigh}}$) in silica spheres (refractive index $n = 1.45$) of three representative sizes. Plots show the equatorial plane, also being the plane of polarization of the incident linearly polarized light of wavelength $\lambda = 800\,$nm. Labels on isolines express intensity ratios in percent. Note that the three plots have individual gray scales; laser polarization is in the equatorial plane, laser beam propagates to the right

$3 \times 10^{13}\,\mathrm{W/cm^2}$.

The peak intensity enhancement $R_I = I_{\mathrm{int,max}}/I_{\mathrm{ext}}$ obtained from a cw Mie calculation should be compared with the corresponding time-dependent result from (Kandidov et al., 2004) Inspection shows that the cw intensity distribution on the droplet axis, where breakdown sets on at threshold, resembles the result obtained from the time dependent calculation by Kandidov et al. . Agreement within 20 % of the peak intensities is found.

The agreement is considered sufficient to use the values of R_I for an order of magnitude estimation of the required irradiated peak intensity to overcome the breakdown threshold, as a function of droplet size. Results are summarized in Tab. 4.3.4. They delineate the peak intensities below which internal breakdown is unlikely to occur for given water droplet diameters.

It is difficult to tell without detailed modelling how the optical breakdown sets on and proceeds in droplets of sizes around and below an optical wavelength, where the Rayleigh approximation Eq. 4.21 holds. Probably, because of the relatively uniform internal optical field, the plasma formation starts

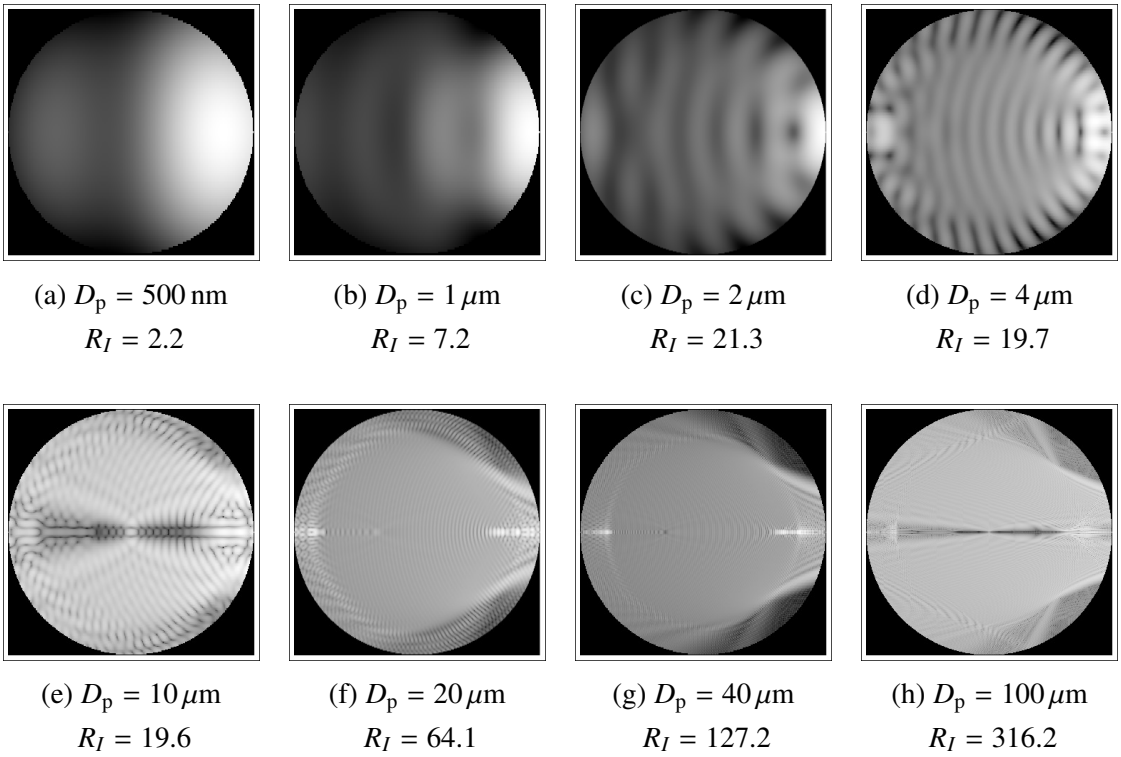

(a) $D_{\mathrm{p}} = 500\,\mathrm{nm}$, $R_I = 2.2$ (b) $D_{\mathrm{p}} = 1\,\mu\mathrm{m}$, $R_I = 7.2$ (c) $D_{\mathrm{p}} = 2\,\mu\mathrm{m}$, $R_I = 21.3$ (d) $D_{\mathrm{p}} = 4\,\mu\mathrm{m}$, $R_I = 19.7$

(e) $D_{\mathrm{p}} = 10\,\mu\mathrm{m}$, $R_I = 19.6$ (f) $D_{\mathrm{p}} = 20\,\mu\mathrm{m}$, $R_I = 64.1$ (g) $D_{\mathrm{p}} = 40\,\mu\mathrm{m}$, $R_I = 127.2$ (h) $D_{\mathrm{p}} = 100\,\mu\mathrm{m}$, $R_I = 316.2$

Figure 4.16.: Internal intensity distributions in the equatorial planes of water droplets of various diameters (incoming monochromatic plane wave, $\lambda = 800\,\mathrm{nm}$). Logarithmic grayscales are chosen per panel and cannot be compared among any two panels. Peak intensity enhancement ratios $R_I = I_{\mathrm{int,max}}/I_{\mathrm{ext}}$ provide a first order estimate of the breakdown threshold intensity compared to the 'reference' size range $D_{\mathrm{p}} \approx 100\,\mu\mathrm{m}$; laser polarization is in the equatorial plane, laser beam propagates to the right. Note the secondary internal focus appearing in the illuminated half of larger droplets. This feature results from another internal reflection mainly of light which has already been internally reflected once and passed the primary internal focus. This is why in the case of irradiation above breakdown no significant amount of light will reach the secondary internal focus.

D_p (μm)	estimated I_{thresh} (W/cm^2)
0.5	3×10^{13}
1	9×10^{12}
2	3×10^{12}
4	3×10^{12}
10	3×10^{12}
20	1×10^{12}
40	5×10^{11}
60	3×10^{11}
100	2×10^{11}

Table 4.2.: Estimated threshold irradiated intensity I_{thresh} to initiate internal breakdown in water droplets, extrapolated to droplet diameters $D_p < 60\,\mu$m based on calculated internal intensity peak enhancement factors for cw plane wave irradiation. As this is an order of magnitude estimation results are rounded to one siginificant digit.

homogeneously throughout the entire droplet, leading to qualitatively different explosion behaviour and a relatively larger fraction of material which evaporates and does not contribute to the fragmented portion of the former droplet.

4.3.5. Estimation of filament-induced fragmentation of watery aerosol droplets

In the course of the present work the question will arise to what extent laser induced fragmentation of a preexisting aerosol may impact the optical scattering properties of real atmospheric (watery) aerosol. The variety and complexity of the interaction of laser radiation with an aerosol or even just one aerosol particle makes it difficult to formulate a comprehensive model of laser-induced fragmentation. Apart from the results reviewed in the previous paragraphs it appears as if in particular the case of femtosecond laser induced fragmentation of watery aerosol has not been investigated in detail previously. Similarly, no published works on the corresponding case of nanosecond laser excitation could be found, either.

To approach the problem, the extensively studied case of infrared laser "cloud hole burning" was examined for aspects that could be transferred to the short pulse regime.

In the classical field of long pulse infrared CO_2-laser/water aerosol interaction it is generally assumed that droplet explosion occurs once the droplet as a whole has been heated up by linear absorption of laser radiation to the critical temperature of 305 °C, above which water vapour bubbles can homogeneously nucleate in the superheated liquid (Caramana et al., 1991; Park and Armstrong, 1989), leading to immediate evaporation of a large fraction of the liquid mass (between 10 % and 75 %, depending on laser fluence (DeForest et al., 2002)).

Some authors consider the threshold temperature to be somewhat lower (i.e. about 80 % of the critical temperature of 305 °C) (DeForest et al., 2002), and some effects related to not perfectly homogeneous heating have been observed (Kafalas and Herrmann, 1973) and theoretically explained (Carls and Brock, 1988). The distinction between different heating regimes has been proposed based on theoretical considerations (Caramana et al., 1991), determined by relative importance of heat and vapour loss through the droplet surface compared to the volume process of linear absorption. These

considerations lead to a threshold laser intensity ($\lambda = 10.6\,\mu$m, multi-μs pulse duration) of

$$I_{\mathrm{thresh}} \approx 50\frac{100}{D_{\mathrm{p}}^2}\,\mu\mathrm{m}^2\mathrm{kW/m}^2,$$

required to reach the point of critical superheating in the center of the droplet. In the equation, the droplet diameter D_{p} is assumed to be given in micrometers. For a fixed prescribed laser intensity this relationship can be alternatively interpreted as stating the minimum droplet diameter required for superheating and consequent explosive fragmentation.

Because of the essentially nonlinear absorption mechanism in the case of optically transparent watery droplets illuminated by visible or near infrared short pulse laser radiation, it is clear that these criteria for explosive fragmentation cannot be directly transferred. It is frequently observed and is theoretically understood (Caramana et al., 1991) that the explosion of superheated water droplets generally proceeds from their center, where the critical temperature is reached first. It is thus possible, that knowledge about the mechanics of the fragmentation process could be transferred to the case of localized internal plasma formation where the driving force also comes from a small volume inside the droplet.

However, no experimental or theoretical studies concerned with the details of the evaporative fragmentation process and the shape of the size distribution of the remaining droplet fragments could be found, which would provide a hint how to treat the nonlinear optical breakdown case. Some authors assume that a fragmenting initially monodisperse distribution also results in a monodisperse size distribution of the fragments (Pustovalov and Khorunzhii, 1992). Others choose both initial and fragmented size distributions to be Gamma distributions (Almaev et al., 1985) with freely assumed parameters. DeForest et al. (DeForest et al., 2002) used angularly resolved light scattering and two-colour extinction measurements to estimate the width of the fragment size distribution, assuming a log-normal shape.

Probably one complicating factor in the scenario of droplet disruption by explosive boiling is the uncertainty about the fraction of the droplet mass which actually evaporates. The latter has been observed to be sensitive, for example, to the heating rate (DeForest et al., 2002) (corresponding to the different ‘heating regimes’ of Caramana et al. (Caramana et al., 1991)).

It is obvious that the situation encountered in the present work differs from the scenario of infrared CO_2-laser cloud hole burning in many aspects. However, irrespective of how the energy is transferred to the droplet, there appears to be no established view how it is turned into fragmentation, and how this affects the resulting fragment size distribution, also in the latter, better investigated case. That is why the estimation of femtosecond filament induced droplet fragmentation had to be approached differently.

For reasons that will be explained in the actual experimental context just the impact of a filament on a droplet is considered here, that is, the irradiated intensity is assumed well above threshold for fragmentation of a broad range of droplet sizes.

The second assumption, based on what is known from the details of the optical breakdown mechanism, is that of a fast, localized ‘detonation’ of a relatively small plasma in the droplet interior,

leading to relatively little heating and evaporation of the larger part of the droplet material. It is well possible that this assumption breaks down for droplets approaching a size on the order of an optical wavelength, as then the plasma is expected to spread over a relatively larger volume (see the previous section), entailing additional loss of material by vaporization. This has to be kept in mind and reconsidered later.

One more assumption is also based on the results reviewed in the previous section. It concerns the amount of energy transferred from the laser beam (i.e. the filament) to the droplet, and it depends on the incident irradiation to be well above the threshold for optical breakdown. The localized plasma evident in the case of short pulse optical breakdown comes from the concentration of the optical energy incident on the largest fraction of the illuminated face of the droplet. This leads to the conclusion that firstly, the amount of energy *potentially* available for the optical breakdown can be assumed about proportional to the geometrical cross section of the droplet (note that this is a main difference to the linear volume absorption case). The fact that well above threshold the optical breakdown sets in already in the leading slope of the pulse leads to the second conclusion that the actually absorbed fraction of the energy reaching the breakdown zone is mainly independent on the degree of internal focussing, and thus droplet size. Summarizing it follows that the energy *actually* absorbed in the plasma created in a droplet, which is hit by an optical filament, can be assumed to be about proportional to the geometrical cross section of the respective droplet as well.

The next questions to be answered are: how does the absorbed energy turn a single droplet into a collection of fragments? How many fragments are to be expected, and what are their sizes?

For problems of this kind R.D. Cohen formulated a generic solution based on a statistical argument which is essentially independent on the details of the fragmentation process, but which is able to make predictions about the number of resulting fragments and their approximate size distribution, based on a few general assumptions and the knowledge of the energy available for the fragmentation (Cohen, 1991).

It was chosen here because it yields an estimate based on considerations of the fundamental quantities energy and entropy, without the need for adjustable parameters. The generality of this approach evidently limits its quantitative predictive power (Cohen, 1991), and one cannot expect it to give absolutely accurate results such as the precise size distribution of droplet fragments. In the case of fragmentation of water drops in a sudden air blast, that is, their disintegration on a low-viscosity medium after a brief shock, the predicted total number of fragments as a function of impact energy and the relative widths of the fragment size distributions have however been found in good agreement with experiment (Cohen, 1991). In fact it is the *scaling* of position and width of the fragment size distributions with the applied energy as well as the size of the mother droplet which is of greatest interest here, and their absolute values need not be known with high accuracy.

Cohen's considerations start from one initial droplet of diameter D_0 and some amount of energy E_T available to be turned into additional surface energy, while the total liquid volume $V = \pi\, D_0^3/6$ is assumed to be conserved (no material loss due to evaporation). The energy balance in the process is

$$E_T + \sigma\, \pi\, D_0^2 = E_{Surf} + E_{Loss},$$

where σ is the surface tension, E_{Surf} is the total surface energy after the fragmentation process, and E_{Loss} is that part of the initially available energy E_{T} which is lost as heat, kinetic energy of the fragments, energy stored in oscillatory motion, rotational energy of liquid blobs or any imaginable form other than surface energy (Cohen, 1991).

Next, two extreme outcomes are considered: In the one extreme case of total conversion of E_{T} to surface energy the result is a monodisperse collection of a number of N_0 fragments with a minimal diameter D_{min}, because, as Cohen shows, the monodisperse distribution is the unique distribution with the property of maximizing the surface energy under the constraint of mass conservation. The number N_0 of such minimal fragments is shown to be given by

$$N_0 = (1 + \hat{E}_{\mathrm{T}})^{1/3}, \tag{4.22}$$

where $\hat{E}_{\mathrm{T}} = E_{\mathrm{T}}/\sigma\,\pi\,D_0^2$ is the dimensionless absorbed energy obtained by relating the actual absorbed energy to the initial surface energy.

The other extreme case consists of E_{T} being entirely lost, leaving the initial droplet unfragmented. It is obvious that neither of these two extremal cases is likely to occur.

Cohen then describes the general outcome of a fragmentation event as an intermediate case where each actual fragment is imagined as being composed of a number of elementary fragments of diameter D_{min} (the minimal size that would result from optimally efficient conversion to surface energy) so that

$$N_0 = \left(\frac{D_0}{D_{\mathrm{min}}}\right)^3 = \sum_{i=1}^{i_{\mathrm{max}}} i\,N_i. \tag{4.23}$$

Here N_i denotes the occupation number of size class i (the one containing fragments composed of exactly i elementary fragments), and the index i_{max} is the index of the largest occupied size class, that is, the individual volumes of the largest fragments are $V_{\mathrm{max}} = i_{\mathrm{max}}\,\pi\,D_{\mathrm{min}}^3/6$, and their diameter is $D_{\mathrm{max}} = (6V_{\mathrm{max}}/\pi)^{1/3} = i_{\mathrm{max}}^{1/3}\,D_{\mathrm{min}}$.

Note that this part of the derivation can be argued about (Cohen, 1991; Villermaux, 2007) because the ‘elementary fragments’ are treated as fundamental volume units of the liquid drop. This is not strictly physically grounded and is known to become awkward if the number of hypothetical elementary fragments becomes very small (Cohen, 1991).

The next step consists of finding the ‘most probable’ outcome of a fragmentation event with a maximum expendable energy E_{T}, fulfilling mass conservation. Probability is measured by counting the number of ways the N_0 distinguishable elementary fragments can be combined to result in the same macroscopic outcome, that is, in the same distribution $\{N_i\}$ of clusters composed of of $1, 2, \ldots, i_{\mathrm{max}}$ elementary fragments.

The result is a distribution

$$\tilde{N}_i = Z^i/i!$$

where the distribution parameter Z is found from the requirement of mass conservation

$$N_0 = \sum_{i=1}^{i_{\max}} i\, Z^i/i!.$$

The last ingredient to make the definition of $\tilde{N}_i$ unique is defining $i_{\max}$ so that $\tilde{N}_{i_{\max}} = 1$. Via Eq. 4.22 Z is directly related to the amount of energy available for fragmentation, as plotted in Fig. 4.17. In fact, it is a one-to-one function of $\hat{E}_{\mathrm{T}}$ alone (Cohen, 1991). Also plotted is the total number of fragments as a function of the dimensionless impact energy. When the distribution of fragment sizes $\tilde{N}_k$ (size

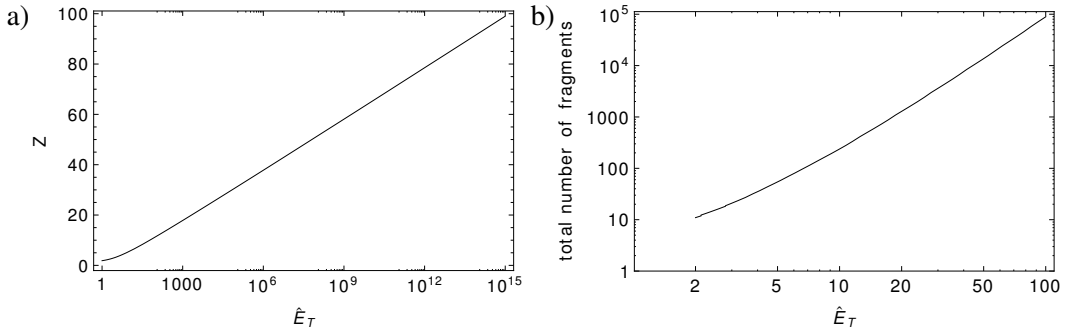

Figure 4.17.: a) Width parameter Z of the fragment size distribution interpreted as the mean number of 'elementary fragments' which an actual fragment is composed of, plotted as a function of the dimensionless impact energy $\hat{E}_{\mathrm{T}}$. b) the total number of fragments in the most probable post-fragmentation distribution plotted vs. $\hat{E}_{\mathrm{T}}$. One reads, for example, that absorption of about 10 times the initial surface energy on average will result in a total of more than 200 fragments.

measured as the number k of minimal unit volumes $V_{\min} = \pi D_{\min}^3/6$ in a fragment) is normalized by the total number of fragments one gets the probability distribution for a particular randomly chosen fragment to consist of exactly k elementary fragments:

$$p(k, Z) = \frac{\tilde{N}_k}{\sum_{i=1}^{i_{\max}} N_i} = \frac{Z^k/k!}{\sum_{i=1}^{i_{\max}} Z^i/i!}.$$

For large enough $i_{\max}$ this is approximately a Poisson distribution

$$p(k, Z) \approx \tilde{p}(k, Z) = \frac{Z^k}{k!} \exp(-Z).$$

As $k = D/D_{\min}$, transformed to the continuous variable of fragment diameter D this becomes

$$\tilde{p}_{\mathrm{D}}(D, Z) = 3\frac{D^2}{D_{\min}^3} \frac{Z^{(D/D_{\min})^3}}{\Gamma(1 + (D/D_{\min})^3)} \exp(-Z), \tag{4.24}$$

which is the probability that a randomly chosen fragment is contained in the interval $[D, D + dD]$. Here the Euler gamma function $\Gamma(1 + x)$ replaces the factorial $x!$ for non-integer x.

In the previous expression the diameter of the elementary fragment, $D_{\min}$ and the distribution parameter Z depend on the dimensionless impact energy $\hat{E}_{\mathrm{T}}$, which may generally be a function of the initial droplet diameter D_0. Earlier in the text arguments were given why in the case of a filament hitting a water droplet larger than sizes belonging to the 'Rayleigh' range the energy absorbed by the forming internal plasma should be approximately proportional to the geometrical cross section $\pi D_0^2/4$ of the droplet. The consequence of this is that $\hat{E}_{\mathrm{T}}$ becomes relatively independent of the droplet diameter, as in the case of strict proportionality $E_{\mathrm{T}} = C\pi D_0^2/4$ it would follow $\hat{E}_{\mathrm{T}} = E_{\mathrm{T}}/(\pi D_0^2/4) = C$.

Then the size distribution $F(D, D_0)$ has only the explicit dependence on D_0, and the single $\hat{E}_{\mathrm{T}}$ is a parameter common to all fragment distributions originating from mother drops of diameters D_0 for which the above mentioned proportionality holds. Then

$$F(D, D_0) = F(D, D_0, \hat{E}_{\mathrm{T}}) = 3\,\frac{D^2}{D_0^3}\left(1+\hat{E}_{\mathrm{T}}\right)^3\,\frac{Z^{\left(\frac{D}{D_0}(1+\hat{E}_{\mathrm{T}})\right)^3}}{\Gamma\{1+(\frac{D}{D_0}(1+\hat{E}_{\mathrm{T}}))^3\}} \tag{4.25}$$

is the total number of fragments appearing in the diameter interval $[D, D + dD]$, originating from a single droplet of initial diameter D_0, using Eqs. 4.23 and 4.22 to substitute $D_{\min}$.

A continuous distribution of mother droplets $n_{\mathrm{mother}}(D)$ from this interval of constant $\hat{E}_{\mathrm{T}}$ undergoing fragmentation results in a fragment size distribution n_{frag} according to

$$n_{\mathrm{frag}}(D) = \int_D^\infty n_{\mathrm{mother}}(D_0)\; F(D, D_0)\; \mathrm{d}D_0, \tag{4.26}$$

of course assuming that all droplets fragment independently.

The lower integration boundary is D because naturally no fragments of size D are expected from droplets originally smaller than D. Integration to $D_0 \to \infty$ means that $n_{\mathrm{mother}}(D_0)$ should vanish quickly enough for large D_0. To approximately treat the effect of a threshold size $D_{0,\mathrm{thresh}}$ below which no fragmentation occurs, the lower integration boundary can be set to $\max(D, D_{0,\mathrm{thresh}})$.

Equation 4.26 will later be used to estimate the effect on the optical scattering properties of a haze aerosol by partial fragmentation due to the influence of laser filaments.

5. Inducing and sensing atmospheric condensation with light – experiments

5.1. Filament-induced condensation of water under artificial atmospheric conditions

The aim of the initial experiments described in this section was to firstly transfer the results earlier obtained by Wille et al. (Wille et al., 2001), using a tightly focused beam of millijoule level femtosecond laser pulses, to the case of a multifilamenting terawatt laser beam. This was to eventually test if self guided filaments have the proposed ability to initiate processes necessary to induce water condensation in air. The next objective was to explore the range of conditions under which condensation would be observable, respectively, to advance in the identification of the underlying mechanism.

Two different experimental setups were used to create particular atmospheric conditions and to optically detect filament-induced scatterers forming in the Teramobile beam.

5.1.1. Experimental setup

Laser source

The Teramobile laser system provided the beam which was emitted via the horizontal exit port of the container. After propagating through free space over a distance of approximately 15 m the laser beam entered the respective experimental setup. Laser performance at the time of experiment allowed for a maximum pulse energy of $E_p = 240\,\mathrm{mJ}$ with a minimum duration of $\tau_p \approx 60\,\mathrm{fs}$.

The Teramobile beam was emitted slightly focused and generated a bunch of $20 - 30$ intense filaments starting roughly half way between the laser output and the experiment. In the present experiments with the cloud chambers at such relatively close distance, the pulses were only slightly negatively chirped in order to have the distance of most intense filamentation centered around the position of the respective chamber.

The Teramobile container was located next to the building of the FU physics department. The laser beam entered the basement of the building (normally serving as a car park), through a clear opening in the wall. The cloud chambers and auxiliary experimental apparatus were placed in the basement, protected from rain and other precipitation, and to some degree shielded against wind.

Cloud chambers

Two cloud chambers were used, complementing each other in terms of the achievable atmospheric conditions. The first setup (Cloud chamber #1) consisted of a modified and enlarged version of the diffusion cloud chamber used by Wille et al. (Luderer, 2001; Wille et al., 2001). The most important distinction from Wille's chamber was the availability of additional lateral ports for optical access to the center of the chamber.

Its principle of operation was that of a downward diffusion cloud chamber as invented by A. Langsdorf in the 1930's as a tool for detecting tracks of energetic particles (Langsdorf, 1939). In this type of cloud chamber a vertical temperature gradient is established by cooling the bottom of the enclosed volume filled with a carrier gas (in this case, air), and heating the top, where vapour of condensable substance (in this particular case, water) is generated by evaporation from a reservoir. The vapour diffuses towards the bottom plate, where it eventually condenses and freezes.

Because of the temperature dependence of the thermal conductivity of the carrier gas and similarly of the diffusivity of the vapour substance in it, this results in a vapour saturation profile which has a maximum close to the bottom of the chamber. Appropriate choice of top and bottom temperatures allows to reach high levels of supersaturation, up to the value of $S \approx 4.0$, which is the limit for spontaneous homogeneous nucleation of water droplets (see Sec. 4.1.1). Details on the determination of the saturation profile in this particular cloud chamber under typical conditions of operation are given below.

The aluminium bottom plate was cooled by indirect contact to a reservoir of liquid nitrogen, via a wire mesh immersed in the coolant. Its typical temperature was $-60\,^{\circ}\mathrm{C}$. The air at the top of the chamber was heated by a thermostated laboratory circulator (RTE-110, Neslab Instruments), pumping water through a copper pipe serving as heat exchanger, to typically $10\,^{\circ}\mathrm{C}$. The air temperature at the level of the laser beam was constantly monitored by a thermocouple thermometer.

The body of the chamber consisted of polystyrene foam (outer dimensions $1.00 \times 0.50 \times 0.44\,\mathrm{m}^3$) with a clear enclosed volume of $0.60 \times 0.30 \times 0.20\,\mathrm{m}^3$. Lateral ports, vertically centered at a height of 40 mm above the cooled bottom plate, allowed for optical access to the centre of the chamber. Optical ports were equipped with double windows to minimize thermal perturbation of the chamber interior, and to prevent condensation of ambient humidity on the outer faces.

The input and putput ports (clear diameter 40 mm) for the filamenting Teramobile laser beam, had manually operated sliding shutters made of 1 mm strong teflon plates, sealing the chamber interior from the environment except for the brief moments when they were simultaneously opened for about 1 s in order to transmit one single, or a short burst of filamenting laser pulses. This was necessary because the multifilamenting beam would have immediately destroyed any optical window. It was checked before that perturbations of the chamber interior caused by opening the ports were limited to a short range of a few centimeters from the inner chamber wall, leaving the observed volume at the centre of the chamber uninfluenced.

In Fig. 5.1 a sketch of the arrangement of the ports and a photograph of the setup, mounted on an aluminum frame to match the height of the Teramobile beam, are shown.

In order to literally wash out aerosol particles from ambient air entering the chamber during installation, 'cleaning cycles' were executed, meaning that temporarily stronger evaporation from the reservoir was obtained by more intense heating of the chamber top. This lead to higher vapour supersaturation and a the temporary formation of a dense fog of large droplets around preexisting aerosol particles, which precipitated and were captured on the bottom plate, and hence removed. Setting standard heating rate and waiting for thermal conditions to settle competed the cycle.

The instrument used for retrieving time-dependent size information about scatterers inside the cloud chamber was a commercial near-forward scattering based particle sizer (Spraytec, Malvern Instruments Ltd.) originally designed for the characterization of sprays. It was chosen because of the large nominally covered detectable particle size range between 0.1 μm and 900 μm, at the same time having a large permitted working distance and probing a relatively large volume. It was however known from the start that the expected low signal levels (as compared to those from a dense spray of droplets) would require operating the instrument at the edge of its sensitivity range. The principle of operation of the instrument is to send a expanded and collimated helium neon laser beam (diameter $\approx$ 15 mm) through the probed volume, and focusing the transmitted and scattered light by a large, low F/#, lens onto a proprietary large multielement photodiode detector in its Fourier plane. The detector consists of elements of increasing size, placed at increasing radii from a central pinhole behind which another photodiode registers the amount of unscattered light. Together with the probing laser output power measured in the transmitter module the total extinction of the space in between transmitter and detector is calculated.

The result of a measurement is angularly resolved information of scattered intensity (that is, of the scattering phase function (see Sec. 3.1.2), as well as the total extinction due to the aerosol.

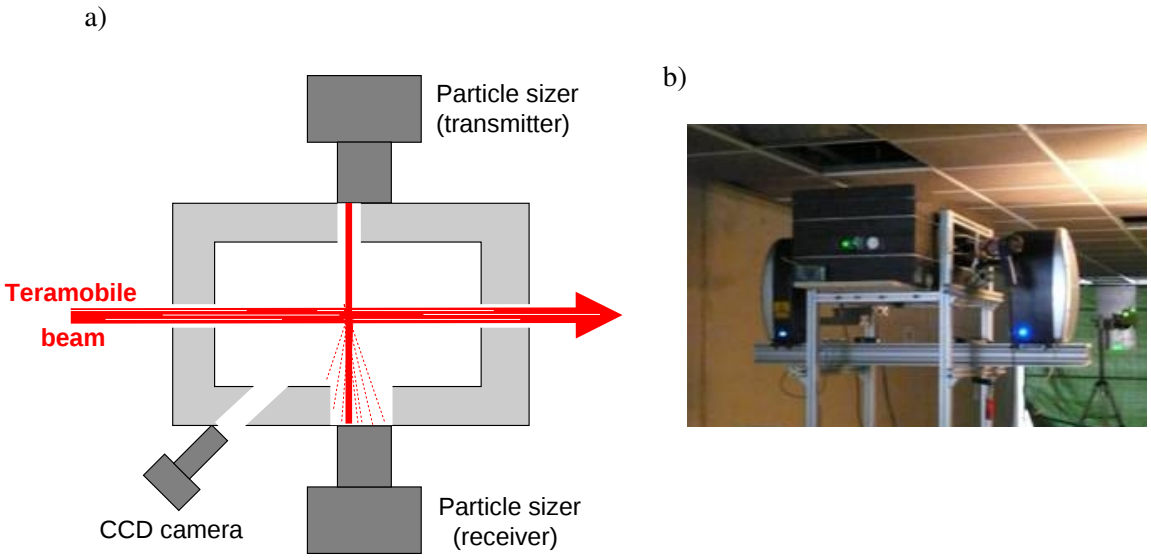

Figure 5.1.: a) Sketch of the location of optical ports in cloud chamber #1 seen from top; b) photograph of cloud chamber #1 with mounted Spraytec instrument.

The automated measurement routine includes fine alignment of the internal detector array and and calibration of the extinction measurement and does not require interference by the user.

As the Spraytec instrument is designed for free space operation, care had to be taken when inserting the additional windows in the beam path. Previous tests in the laboratory had shown that the additional windows, having an anti-reflective coating for the laser wavelength of 633 nm, did not impose a problem, if the window normals and the Spraytec beam were set slightly off-parallel.

Alternatively the centre of the chamber at the height of the transmitted Teramobile beam could be observed by a digital monochrome CCD camera (Focolus432B, Net GmbH) equipped with a macro zoom objective (Navitar). In this case the volume traversed by the filamenting beam was illuminated by a nearly counterpropagating expanded and collimated beam from a microchip diode pumped, frequency doubled ND:YAG laser (Lasiris Inc.). The camera was mounted at a 45 ° angle with respect to the Teramobile beam.

The second chamber was constructed for providing a water subsaturated atmosphere at higher temperature in order to reach high absolute humidities. It consisted of a thermally insulated steel pipe (length 1.2 m, diameter 0.3 m), in which a temperature gradient could be established by heating the top with a digitally temperature-controlled ohmic heater (maximum rated power 500 W) and cooling the bottom part by thermostated water circulating through several windings of copper pipe in close thermal contact with the chamber wall.

A total of five optical ports were available, three of which were on level around the circumference of the pipe, and two more on its axis, on top and bottom. The top port allowed to send in a slightly expanded and collimated green He:Ne laser beam ($\lambda = 543\,\mathrm{nm}$, $P = 1\,\mathrm{mW}$, diameter $\approx 5\,\mathrm{mm}$) down the central axis of the chamber, ending in a beam dump fixed on the opposite side. The window of the top port was mounted on a tube constantly flushed with a minute flow of dry air to prevent condensation of moisture from the inside.

Two lateral ports located on opposite sides on the circumference served to transmit the Teramobile beam, and another at right angle to accept the detection system. The ports for the Teramobile beam were kept closed except when firing the laser. To minimize leaking in of ambient air during periods when they were opened, 2 m long PVC pipes (inner diameter 40 mm) could be attached to both Teramobile beam input and output ports. The port for the detection optics was fitted with a lens tube with a cold trap, preventing condensation of humidity on the optical window protecting the optical elements of the detection system.

Temperature was monitored at three positions along the pipe using simple semiconductor thermometers. Just below the path of the Teramobile beam a combined temperature/relative humidity sensor was mounted (HD-3008, Lutron) to record these parameters close to the optically monitored volume throughout the experiment.

Using chamber #2 the absolute humidity at the position of the Teramobile beam could reach values in excess of $100\,\mu\mathrm{g\ cm^{-3}}$, corresponding to a relative humidity of 80 % at a temperature of 60 °C.

Compared to the previously described setup chamber #2 was equipped with a much more sensitive optical detection setup, also having a much higher dynamic range. However, these had to be traded against loss of size information about the detected scatterers, because only one scattering angle could

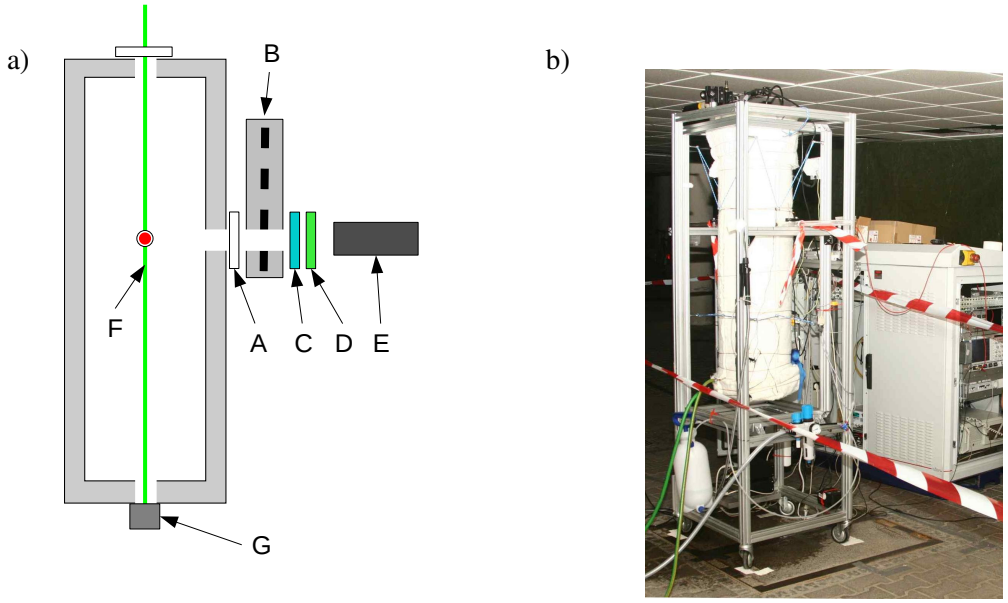

Figure 5.2.: a) Front view sketch of the geometry of cloud chamber #2 (not to scale) as seen along the Teramobile beam (red circle); A: detection window, B: optical chopper, C: BG18 colour glass filter, D: bandpass interference filter, E: photomultiplier module, F: probing laser beam, G: beam dump ; b) photograph of cloud chamber #2, aligned for experiment and thermalizing with beam input and output shielding tube extensions dismounted.

be observed.

The detection system of chamber #2 consisted of a sensitive photomultiplier module (Licel GmbH) based on a Hamamatsu R7400-P03 photomultiplier tube (PMT) with a cathode sensitive diameter of 8 mm, operated in photon counting mode. It was mounted at right angle with respect to the probe beam coming from the top, staring at its intersection with the filamenting Teramobile beam. The detector was protected against scattered Teramobile laser light by an optical chopper (Oriel) synchronized with the 10 Hz clock of the Teramobile laser. For safety reasons an additional 3 mm thick BG18 colour glass filter (Schott) was inserted in the optical path. A bandpass interference filter ($\lambda = 543.5 \pm 2$ nm, FWHM $= 10 \pm 2$ nm, Thorlabs) was used to suppress wavelengths other than that of the probing beam. A schematic sketch of the geometry of the setup and the detection system is shown in Fig. 5.2.

Single photon current pulses from the PMT were counted using a fast event timer (Model P7888, FAST ComTec GmbH) and registered together with temperature and humidity data, together with information when the Teramobile laser was fired through the chamber.

5.1.2. Data evaluation

Estimation of the vapour saturation profile

The height profile of the water vapour saturation ratio S inside chamber #1 could not be measured directly, especially in the region where $S > 1$ and where any inserted object would have distorted the profile due to condensation on its surface. Under static conditions with low concentration of spontaneously formed fog the determination of the temperature profile was however possible in the laboratory, using a vertically shiftable thermocouple sensor.

Knowledge of the temperature profile given standard heating and cooling rates, as well as the vapour saturation ratio at the level of the water reservoir allowed to estimate the vapour saturation profile based on the theory for the binary thermal diffusion in a cloud chamber developed by I. Saavedra (Saavedra, 1958).

The appropriate diffusion equation (15) for the mass density of a dilute (water) vapour diffusing in a carrier gas in the presence of a steep temperature gradient derived by Saavedra reads

$$\frac{\partial \rho_{\mathrm{H_2O}}}{\partial t} = D_{\mathrm{H_2O}}\, \nabla^2(\rho_{\mathrm{H_2O}} + k'_{\mathrm{T}} \ln T), \tag{5.1}$$

where $D_{\mathrm{H_2O}}$ is the diffusivity of water vapour in air and

$$k'_{\mathrm{T}} = \frac{D^{\mathrm{T}}_{\mathrm{H_2O}}}{D_{\mathrm{H_2O}}} = \frac{n^2 m_{\mathrm{H_2O}} m_{\mathrm{air}}}{\rho}\, k_{\mathrm{T}}$$

is the inverse ratio of $D_{\mathrm{H_2O}}$ and the binary thermal diffusivity of water in air, $D^{\mathrm{T}}_{\mathrm{H_2O}}$. Here m_{air} and $m_{\mathrm{H_2O}}$ are the molecular masses of air and water, respectively, ρ is the mass density of the gas mixture, and n its number density. The quantity k_{T} is the so called thermal diffusion ratio of water in air. The latter can be approximated (Yoshitake, 1961) by $k_{\mathrm{T}} \approx 0.32\, \frac{p_{\mathrm{H_2O}}}{p}$, with $p_{\mathrm{H_2O}}$ being the water partial pressure and p the total (atmospheric) pressure. Thus, for the case of dilute vapour ($\rho \approx \frac{m_{\mathrm{air}} p}{k_{\mathrm{B}} T}$) this results in

$$k'_{\mathrm{T}} \approx 0.32 \rho_{\mathrm{H_2O}}$$

and Eq. 5.1 becomes

$$\frac{\partial \rho_{\mathrm{H_2O}}}{\partial t} = D_{\mathrm{H_2O}}\, \nabla^2(\rho_{\mathrm{H_2O}}(1 + 0.32 \ln T)). \tag{5.2}$$

As the steady state density profile in the case of one-dimensional temperature and density profiles is of interest, this simplifies to a differential equation for the water vapour density $\rho_{\mathrm{H_2O}}$ in one coordinate

$$D_{\mathrm{H_2O}}(T) \frac{\partial^2}{\partial x^2}[\rho_{\mathrm{H_2O}}(x)(1 + 0.32 \ln T(x))] = 0,$$

which is readily simplified, as always $D_{\mathrm{H_2O}}(T) > 0$:

$$\frac{\partial^2}{\partial x^2}[\rho_{\mathrm{H_2O}}(x)(1 + 0.32 \ln T(x))] = 0. \tag{5.3}$$

Plugging in the measured temperature profile and solving with the boundary conditions given by the measured water vapour density at the height of the reservoir, and $\rho_{H_2O} = 0$ at x=0, yields the desired estimate of the saturation ratio as a function of the height coordinate x for the typical conditions encountered in the experiment, shown in Fig. 5.3. This treatment assumes mass and heat transport to

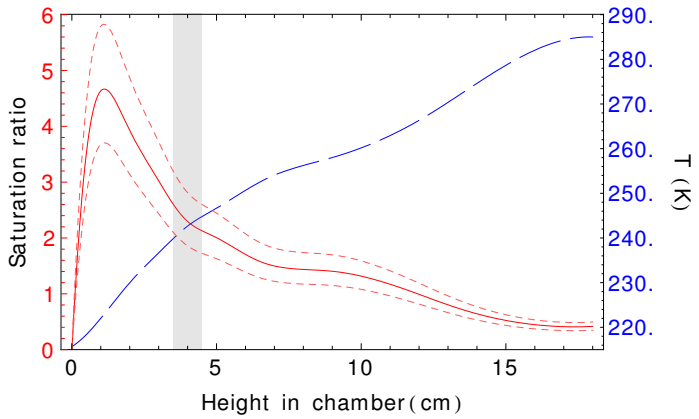

Figure 5.3.: Water vapour saturation profile estimated from the measured temperature profile $T(x)$ and water saturation ratio at the level of the water reservoir, $S(x = 18\,\text{cm})$. The saturation profiles plotted with dashed red lines correspond to those that would result from unfavourable combinations of 2σ measurement errors of $T(x)$ and $S(x = 18\,\text{cm})$. The vertical bar indicates the position of the Teramobile laser beam.

be solely due to diffusion and heat conduction. The presence of a background fog of droplets adds additional transport pathways and invalidates the assumptions underlying this idealized treatment. The above saturation profile can thus only serve as an estimation for the case of negligible background of particles.

Retrieval of the droplet size distribution

The retrieval of the size distribution of droplets in chamber #1 will only be sketched here. It was done by J. Kasparian using a multiparameter fitting routine based an evolutionary algorithm.

The scattering was treated using the geometrical optics approximation, valid in the case of particles considerably larger than the scattered wavelength, and treating the spherical scatterers as opaque circular disks. In this approximation the intensity scattered into an angle θ away from the original direction of propagation is proportional to (Bohren and Huffmann, 1983)

$$I_{\text{sca}}(\theta) \propto x^2\,(1+\cos(\theta))^2\left(\frac{J_1(x\sin(\theta))}{\sin(\theta)}\right)^2,$$

where $x = \pi D_\text{p}/\lambda$ is the size parameter of the droplet, and $J_1(z)$ is the Bessel function of the first kind and order 1.

A discrete size distribution of droplets across size bins i of width ΔD_p, which are centered at respective diameters $D_{\text{p},i}$ (corresponding to size parameters $x_i = \pi D_{\text{p},i}/\lambda$), is characterized by the occupation numbers n_i of individual bins. Assuming single scattering, the total intensity scattered by

an angle θ is just the sum of intensities scattered by individual droplets

$$I_{\mathrm{sca,total}}(\theta) \propto \left(\frac{1+\cos(\theta)}{\sin(\theta)}\right)^2 \sum_i n_i \, (x_i \, J_1(x_i \, \sin(\theta)))^2,$$

Knowing the angular distribution of the total scattered intensity from the measurement, the set of occupation numbers of the bins leading to best agreement with the measurement can be searched for. The angularly resolved scattering intensity data allows to determine the n_i up to a common multiplicative constant. Finally, the measured total extinction allows to fix this constant, and to obtain the absolute number of scatterers contained in each size bin.

5.1.3. Results and interpretation

Camera images

CCD camera Images of the volume around the centre of chamber #1, illuminated by the green continuous wave laser beam, show the efficient production of scatterers upon transmission of the filamenting Teramobile beam (see Fig. 5.4).

The bright and fuzzy millimeter-sized clouds, partially leading to overexposure of the detector, most probably stem from filament interaction with droplets from the unavoidable thin background haze, permanently present in the chamber, despite the regular 'cleaning cycles'. Picture series acquired with the CCD camera consistently show that additional scattering strong enough to be detectable with the camera, quite generally appears in a pattern similar to that shown in Fig. 5.4.

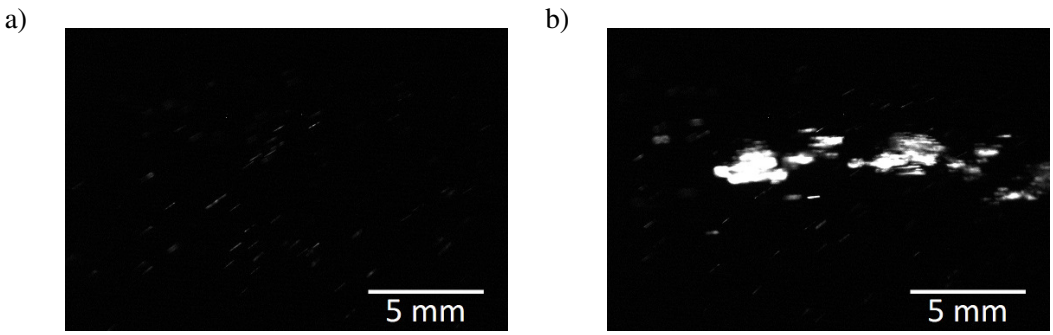

Figure 5.4.: Pictures taken with the CCD camera **a)** before and **b)** after a triple of Teramobile laser shots through chamber #1.

The low dynamic range of the CCD detector prevents quantitative evaluation of the scattering, and judging whether scattering increased also outside those localized regions.

Noting that the presence of background haze particles has strong influence in the particular situation, the question is to what extent the increase of scattering could be caused by mere multiplication the number of scattering bodies (see also the discussion in Sec. 5.2 below) and their subsequent growth, or if the formation of new scatterers is triggered by a different mechanism. Any of the pathways discussed

in the previous Sec. 4.2.2, most importantly those involving *gaseous* products of the filament-droplet interaction, may equally well cause the locally enhanced obvious production of new formed scatterers.

One especially clear example for observed events particularly supporting this interpretation is presented in Fig. 5.5. The sequence of camera frames shows the impact of a double shot from the Teramobile laser (separated by the repetition period of 100 ms) photographed at a rate of 15 frames per second.

Frame a) shows the situation immediately before the first shot, characterized by a low background concentration of preexisting scatterers. The first laser shot occurs during the exposure time of frame b), where a small number of scatterers invisible in the cw illumination beam show up in the strong light of the Teramobile laser. Bright illumination by the second Teramobile pulse shows that apparently two of these scatterers have been seriously hit during the first pulse, most probably by filaments, as the other scatterers appear to have remained intact. Two horizontally elongated plumes show up at the previous positions of these two former scatterers. Moreover, during the second Teramobile shot, the plume located close to the image centre is strongly impacted again, which may be explained by the presence of an "optical pillar" (Bergé et al., 2004; Skupin et al., 2004a) or persistent "mother filament", recurring at the same position in the beam in both laser shots.

Obviously the second shot causes very efficient absorption in the cigar-shaped central plume, as it gets completely erased and instead of it there appears a vortex ring of ≈ 3 mm diameter, centered around the former long axis of the plume. The vortex ring most likely originates from rapidly expanding hot gas, indicating the ignition of an extended and relatively dense plasma. This could be explainable by a high concentration of water vapour in the plume remaining from the first filament impact, together with the lower ionization potential of water vapour as compared to air (approx. 7 eV vs. 12 eV (Bergé et al., 2007; Couairon and Mysyrowicz, 2007)).

Well in accord with this interpretation, in frames e) to j) it can be seen that this ring has initially faint appearance, indicating low content of particles, and scatterers only start to grow after frame e).

Concluding, findings from the examination of images from the centre of chamber #1 suggest that in the presence of preexisting water aerosol a combination of processes discussed in Secs. 4.2.2 and 4.3 is likely to be at play. The efficient plasma-chemical production of precursor substance appears to dominate the effect of laser- or filament-induced production of new scatterers, especially when filaments impact the same volume in more than one laser shot.

Analysis of angularly resolved scattering

In Fig. 5.6 plots of typical background-corrected angularly and time-resolved scattering by aerosol in the centre of the chamber are shown. Measurements were conducted during the fading of an initially present thin background haze. The panels are ordered by decreasing visual observability of the haze in the illumination beam and in almost forward direction, from "visible" (panel (a)) to "almost invisible" (panel (e)). The Spraytec instrument acquired angular scattering data at a rate of 10 kHz.

The plots show the change of scattered intensities relative to their average before firing the laser, in order to visually emphasize the laser effect. In the retrieval of the size distribution, the absolute

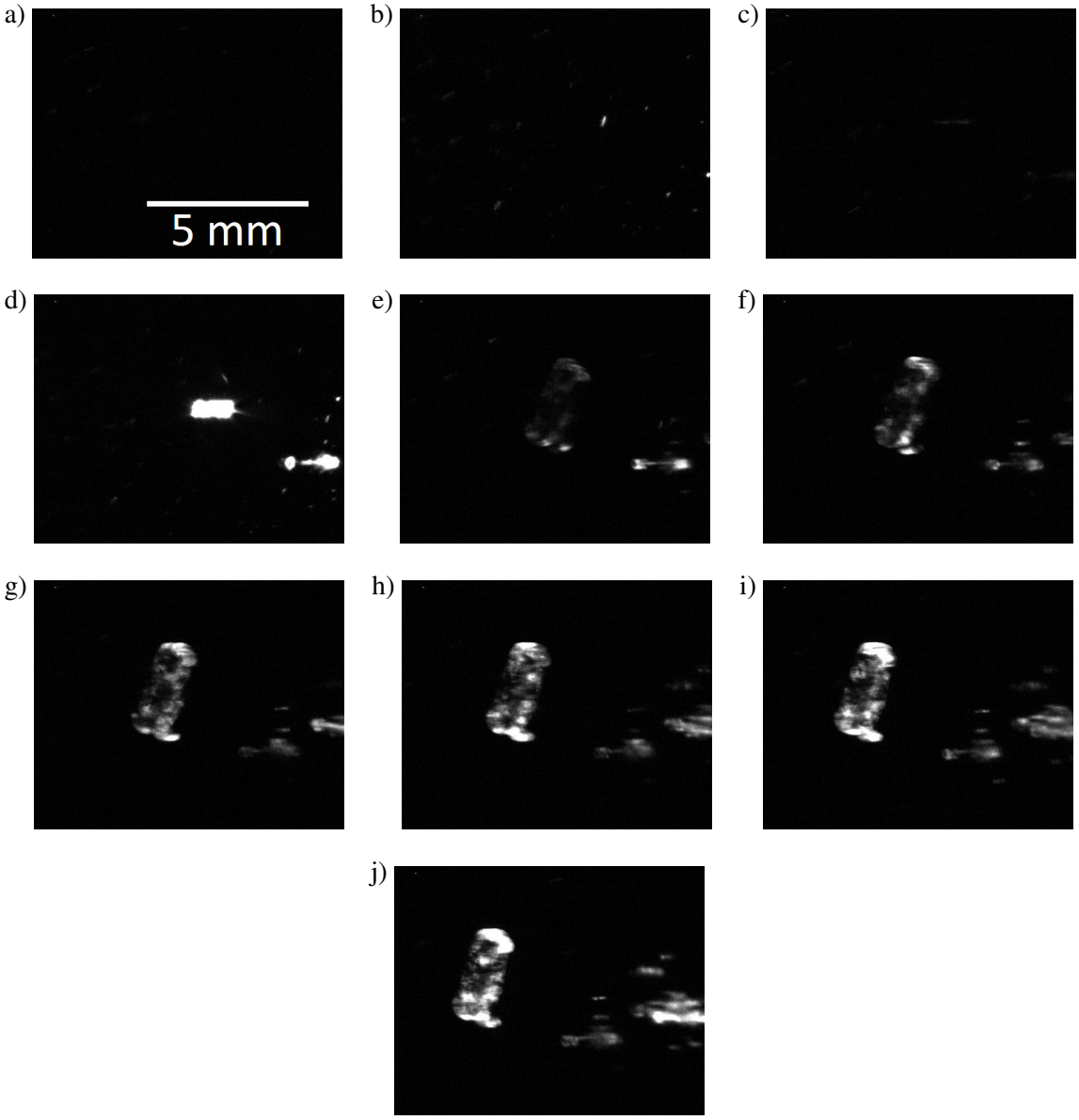

Figure 5.5.: One of the events observed in chamber #1, particularly pointing to gaseous substance, resulting from the evaporative explosion of tiny background fog droplets, as the cause for the localized creation of new scatterers observable by the CCD camera. Subsequent frames are separated in time by $1/15\,\mathrm{s} \approx 66.7\,\mathrm{ms}$. Details are given in the text.

scattering data was used.

It can be seen that the change of the scattering properties of the probed volume follows a distinct pattern, with a temporary increase of scattering at an angular range around detector element #10, as well as around detector element #30. The additional signal in the lower index channels consistently follows a trend to shift to even lower indices with progressing time, indicating growth of this mode in all cases. A less pronounced apparent growth can be seen also in the signal of the smaller mode (higher index detector elements).

Figure 5.7 presents the time dependent size distribution plot resulting from of inverting the angular scattering data corresponding to panel b) in Fig. 5.6.

Three initially present modes of droplets are found by the inversion routine, located at about $4\,\mu$m, $50\,\mu$m, and $250\,\mu$m, respectively, totalling to a liquid water content of about $100\,\mu$g cm^{-3}. The double laser shot at $t = 0$ s initiates a reduction of the particle number in the smallest mode and a slight increase of particle number in the intermediate mode. The main observed effect is the fast growth of the droplets contained in the intermediate mode from about $50\,\mu$m diameter to $80\,\mu$m within only 3 s.

When interpreting the outcome of this evaluation one has to take into account the mainly horizontal drift of the slowly settling smaller droplets, and the increasingly strong sedimentation of droplets exceeding about $100\,\mu$m diameter. One generally has to be aware that the probed sample to some extend changes with ongoing time of measurement. However the clear trend of the time evolution of the centre of the intermediate mode, that is, the observed quick growth of the initially $50\,\mu$m large droplets, visible already in the unprocessed data shown in Fig. 5.6, is certainly not an artefact caused by the relatively small probed volume.

This growth velocity can be compared to that predicted by a growth model describing the condensation of pure water vapour onto an isolated droplet, as it was outlined in Sec. 4.1.4. It is found that, at the temperature prevailing in the observed volume of the chamber, such a rate of vapour uptake would require a water vapour saturation ratio $S > 10$, far in excess of the threshold for homogeneous nucleation. Alternatively, supposing realistic levels of supersaturation ($S \approx 2-3$), the observed grotwh would imply a temperature higher than about 265 K. Both cases can be ruled out, as supersaturations so much beyond the threshold for homogeneous nucleation are fundamentally unattainable (at least, for durations longer than required for the formation of critical clusters – much shorter than the second timescale), and the temperature at the level of the laser beams was permanently monitored and was found to remain constant at $T = 244$ K throughout the experiment.

This indicates that the intermediate size mode grows involving more than just the diffusive transport and condensation of water substance. For example, the observed reduction of particle number in the small mode could mean that electrostatically accelerated coagulation of small droplets with those of the intermediate mode contributes to its accelerated growth. Another possibility to explain the unexpectedly fast growth would be the presence of hygroscopic gaseous precursor substance generated by the filaments.

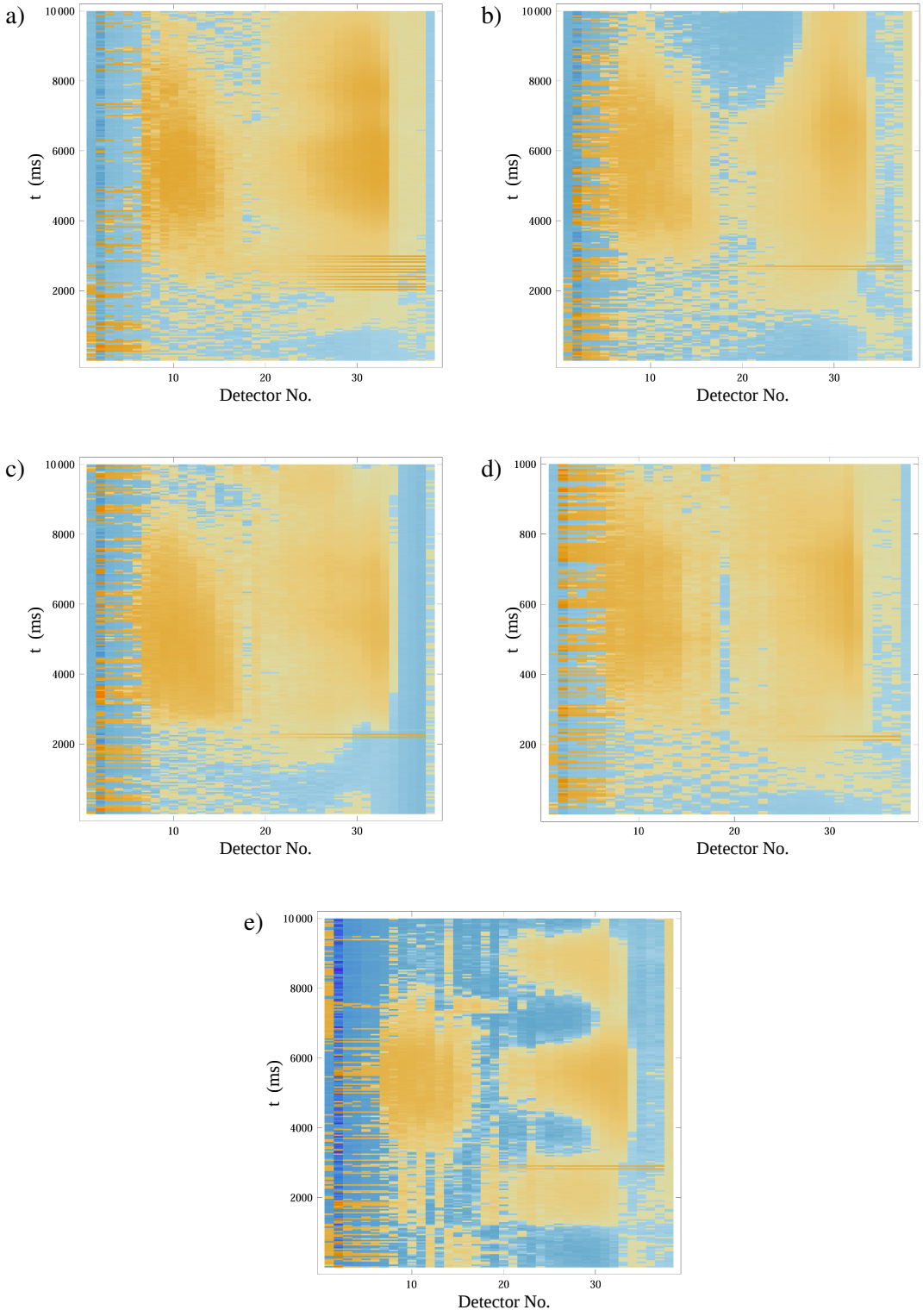

Figure 5.6.: Typical background-subtracted raw angular scattering data, corresponding to the relative change of signal compared to the mean of the interval before firing the laser; each panel shows an independent experiment run. Colour scale from dark blue (negative) to orange (positive); light blue is neutral. Vertical axes show absolute time from start of acquisition; signals measured by individual detector elements are spread along the horizontal axes. Note that the detector element spacing is not equidistant as could be suggested by the plot. Laser flashes are visible mainly in the large angle detectors, defining the actual $t = 0$ time. All panels except a) show double shot events.

Observations in chamber #2

A strong enhancement of total aerosol scattering could be observed in chamber #2, even under conditions of water vapour subsaturation. Figure 5.8 shows the measured change of detected scattered light from the probing laser beam, resulting from firing the filamenting laser beam in a pattern of 30 s long bursts (300 laser shots each), followed by quiet intervals of the same duration. During the displayed time interval the temperature at the level of the Teramobile beam in chamber #2 was about 60 °C, and the relative humidity was around 75 %. The laser ports of the chamber were kept open throughout the entire run. The high contrast of the signal between the intervals with and without firing the laser, respectively, indicates minor impact of this condition on the result.

In Fig. 5.9 the average of signals obtained during the periods of laser firing, indicated by gray bars in Fig. 5.8, is shown at higher time resolution. Despite the increasingly large scatter of the data towards the end of the time interval, an initially rising trend with subsequent saturation can be recognized. The plot additionally includes an exponential curve $f(t) = A\ (1 - \exp\{-(t - t_0)/\tau_{\mathrm{sat}}\})$ with parameters fitted to the data. It serves to estimate the characteristic time of the saturation effect, resulting as $\tau_{\mathrm{sat}} \approx 4$ s. The level of background scattering, as measured before and after the entire firing sequence, is indicated by a dotted line in the plot.

Already in the experiments using chamber #1 it had turned out to be hardly possible to create conditions necessary to enable sufficient production and growth of new droplets to be optically detected with the available instruments, and in the actual detection geometry, without the tradeoff of a nonvanishing background of scatterers.

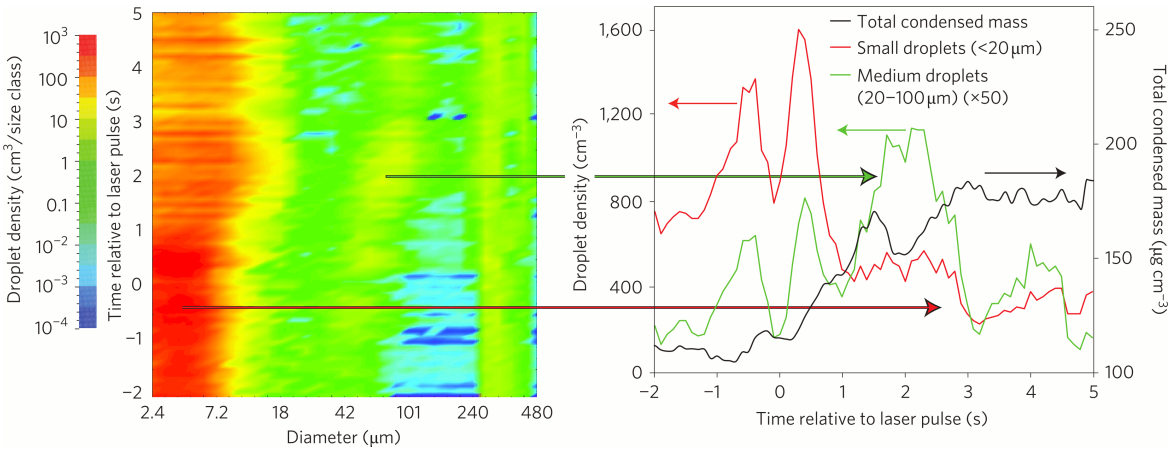

Figure 5.7.: Left: time dependent size distribution in the probed volume in the centre of chamber #1 retrieved from the angularly resolved scattering data corresponding to panel b) of Fig. 5.6, plotted as colour coded number density vs. diameter and meaurement time. Time $t = 0$ indicates the first of two successive filamenting laser shots. The quick growth of the intermediate mode anticipated from Fig. 5.6 is apparent. Right: estimated integrated condensed mass for the 'small' (red) and 'intermediate' (green) size modes indicated by corresponding arrows in the left panel, respectively, and estimated total condensed mass in the probed volume (black). The laser shots initiate loss of small droplets D_{p}, a temporary increase of the occupation of the intermediate mode, and a total gain of condensed mass of about 50 %. Figure from (Rohwetter et al., 2010).

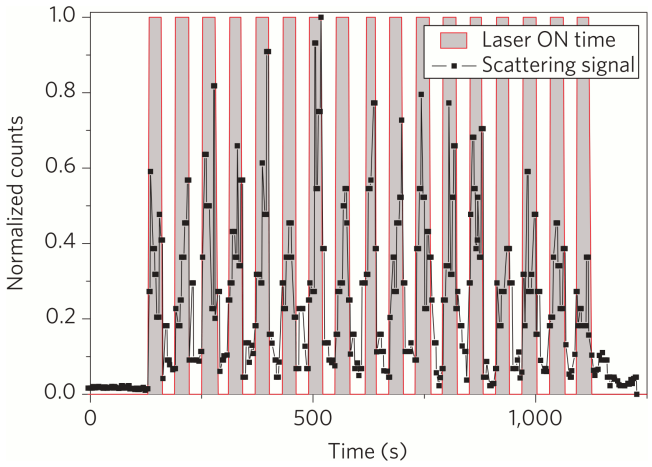

Figure 5.8.: Change of total aerosol scattering induced by the filamenting laser beam passing through chamber #2; Gray bars: 30 s long bursts of 300 laser shots. Signal is plotted as normalized single photon counts.

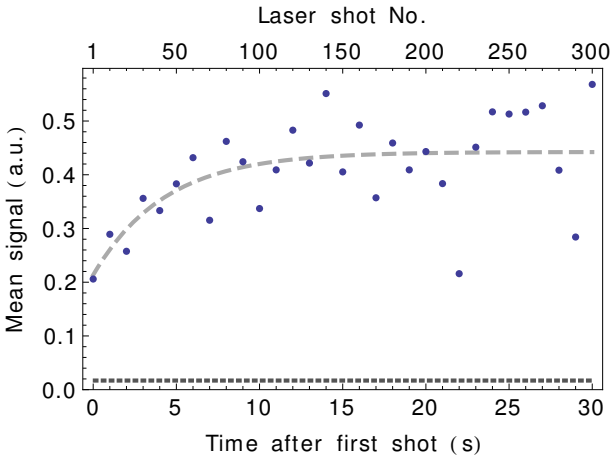

Figure 5.9.: Average of scattering signals during the intervals of laser firing indicated by gray bars in Fig. 5.8, shown at higher time resolution. Dotted line indicates background level; dashed line: exponential fit to estimate the characteristic time for saturation of the signal (see text).

A similar dilemma was encountered with chamber #2. Even worse, its detection system, while being sensitive, provided no information about the sizes of the scattering bodies.

Thus, the cumulative nature of the laser effect seen in Fig. 5.9 *may* indicate sustained laser driven condensation of vapour, but as long as more trivial effects potentially causing overall increase of scattering (which could be simple fragmentation of background haze droplets) cannot be ruled out, no conclusion can be drawn.

The following discussion will show that closer examination of the correlation of signal and background with each other and with relative and absolute humidities yields evidence against the latter trivial scenario.

A series of experiment runs conducted before and during a heating phase and the subsequent relaxation is shown in Fig. 5.10. The whole series, spanning a time of 2:40 hours starting at 00:02 AM, contains four periods of intermittent firing of the Teramobile laser. These are a single burst of 70 s at 00:10, and three periods of 30 s long laser bursts interleaving with 30 s long pauses during the intervals 00:40-00:55, 01:36-01:51, and 02:05-02:22.

In between the measurements the laser ports of the chamber were shut to minimize perturbations of the atmosphere inside. In each measurement run, data acquisition was started while they were still closed. After scattering signal had been acquired for some time from the still closed chamber, they were opened typically $2-3$ minutes before the first laser shot was fired. This was done in order to track any possible influence of opening the ports on the scattering signal. Examination of the data reveals some slight increase of the background scattering due to perturbation via the laser ports, visible in the beginning of the third measurement when data acquisition was started at 01:30, the ports were opened at 01:34, and the first laser shot was fired at 01:36:40 (see Fig. 5.10 b)). The magnitude of the perturbation-induced change of background scattering, compared to that caused by the filamenting laser beam, however turns out to be negligible.

Finally intercomparing trends of filament-affected scattering (red dots), filament-unaffected or background signal (blue dots), and relative and absolute humidities, it can be seen that the background very closely correlates with relative humidity. This becomes especially apparent during the time interval between 00:00 and 01:05, where relative humidity rises steeply. This is due to increased heating of the chamber top starting at at 00:29. It can further be seen that the filament-affected scattering signal (red dots) is entirely uncorrelated with relative humidity, but rather appears to follow the same trend as absolute humidity, that is, the concentration of water vapour.

The first and most important conclusion that can be drawn is that the additional observed scattering is *not* caused by trivial fragmentation of existing scatterers, because in that case background and signal should show similar trends, which they manifestly do not.

As a direct consequence of this, the next conclusion is that the increase of scattering must actually be caused by *growth* of existing scatterers or even the additional formation of new scatterers. Because of the prevailing water vapour subsaturation this implies, as noted before, some efficient growth-enhancing mechanism enabled by the influence of the filamenting laser beam.

Finally, but not less importantly, the approximate correlation of the signal with absolute humidity suggests that water vapour plays a key role in this supposed mechanism, yet other than just being

the primary condensing substance. If only the latter were the case, the *relative* humidity would be expected to be the dominating parameter for the strength of the laser effect, according to the classical model of diffusionally driven droplet growth sketched in Sec. 4.1.4).

The question, which exactly is this process obviously involving water vapour substance, cannot be answered from the present experimental results. Two candidates shall be proposed here to show that there are plausible possible explanations.

Firstly, the lower ionization potential of water as compared to air (as stated before about 7 eV vs. 12 eV for oxygen (Bergé et al., 2007; Couairon and Mysyrowicz, 2007)) suggests that high concentrations of water vapour are likely to lead to more efficient ionization in the filament cores, in two ways. Highly abundant water molecules are expected to directly boost the production of free electrons by multiphoton ionization (which requires only five photons instead of eight in the case of oxygen). These electrons may further play an important role as seed electrons for avalanche ionization, as they are available earlier during the laser pulse, allowing for more efficient deposition of energy due to this process. Then the resulting larger amount of plasma ions could more efficiently trigger subsequent ion-chemical reactions (see sec. 4.2.2). If the role of water vapour as 'accelerant' for avalanche ionization were dominant, one should expect a nonlinear dependence of plasma production on the concentration of water vapour.

Secondly, the influence of absolute humidity could be caused by a step involving a chemical reaction with water vapour as one of the reaction partners. This could be, for example, the ozonolysis of water, leading to the production of ·OH radicals appearing as important agents in several proposed condensation enhancing mechanisms (see Sec. 4.2.2).

5.1.4. Conclusion

Optically detectable production of condensed particles was observed, under quite different but rather extreme atmospheric conditions of either high relative or absolute humidities, in chamber #1 or chamber #2, respectively. In both setups the small observed volume makes optical detection of minor changes of scattering difficult.

The greatest deficiency exposed by both setups was the presence of a background aerosol which could not be avoided under respective suitable atmospheric conditions for producing condensation induced by the filamenting laser beam. In neither of the two chambers used the role of preexisting fog droplets in the observed effect leading to increased scattering could be finally identified.

However, both experiments yielded evidence for an efficient mechanism triggered by the action of the filamenting laser beam, enabling the unusually fast condensational growth of droplets under supersaturated conditions (chamber #1) or even under subsaturated conditions (chamber #2). Growth of scatterers could not be directly observed in chamber #2 due to limitations of the detection scheme, but was inferred indirectly.

Nevertheless the results of these experiments point to the formation of hygroscopic aerosol precursor substance as the origin of the observed phenomenon, most probably induced by plasma chemical reactions.

a)

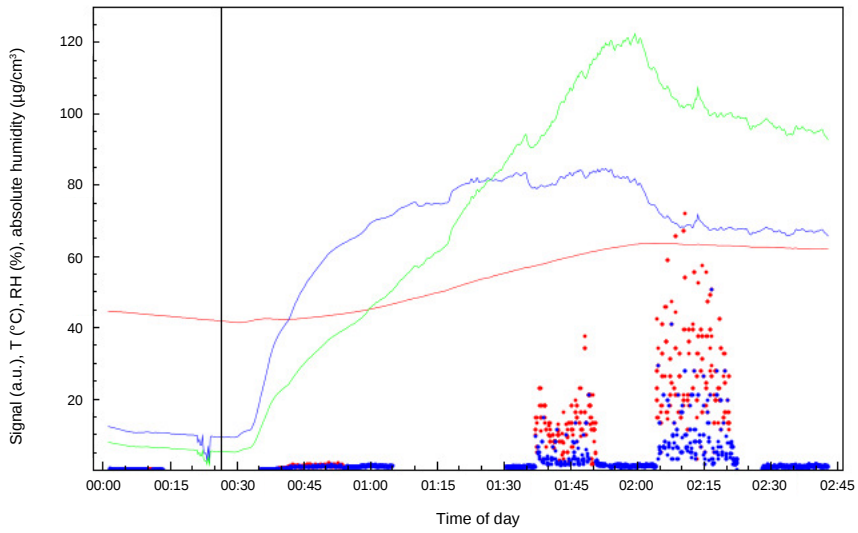

b)

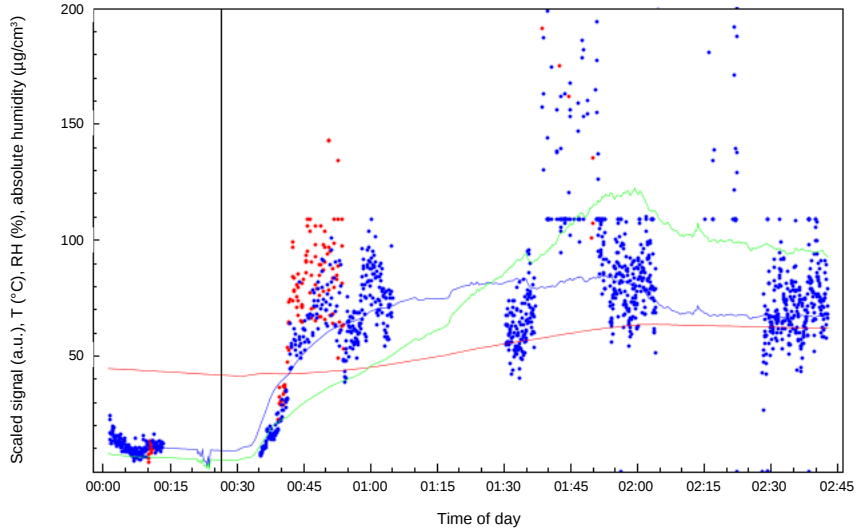

Figure 5.10.: Background scattering signal (blue dots) and filament-affected scattering signal (red dots) during one full series of measurements using chamber #2. Also plotted: temperature (in °C, red line), relative humidity (in % blue line) and absolute humidity (in μg cm^{-3}, green line). Panel a) shows that the magnitude of filament-induced additional scattering roughly follows absolute humidity. In panel b) the same data is plotted, however the plotting scale of the signal is stretched by a constant factor to allow to visually follow the time dependence of the background signal. Apparently the latter is strongly correlated with relative humidity rather than absolute humidity.

5.2. Differential scattering LIDAR experiment

Certainly the atmosphere is *not* a laboratory where an experiment can be conducted under deliberately chosen and stable conditions. These are generally not reproducible day-to-day, and parameters cannot be systemtically scanned. The observations from the cloud chamber under rather extreme conditions indicated that filaments have the potential to enhance aerosol backscattering in the atmosphere, probably by a mix of different mechanisms.

Despite the many uncertainties it was decided to conduct a real-scale LIDAR experiment during November 2008, because the expected weather conditions were considered the most promising to offer an opportunity to observe filament induced atmospheric condensation, and the time in which the Teramobile system would be available was strictly limited.

It is a commonplace that in Autumn high relative humidities, often leading to the formation of fog, occur on a regular basis. This is mainly due to the relatively extreme temperature differences between day and night time. These favourable conditions in terms of available atmospheric humidity were less favourable for operating the Teramobile laser system, which, despite of the thermostated air conditioning system, subtly responded to the sometimes large swings of temperature. As a consequence, the laser had to be freshly warmed up and adjusted before a measurement, and often had to be checked and re-optimized even during measurements.

The strategy consequently amounted to keeping the Teramobile laser performance close to its specifications, and, in case of promising weather forecast for the coming night, to be ready to measure through periods of developing fog.

The aspect of depending on possibly quickly changing weather conditions, together with the need to have the Teramobile laser freshly optimized at night time, and the required number of persons on the site to prepare the experiment quickly and safely made conducting the LIDAR measurements a demanding task.

Suspectedly suitable conditions were met on only a few days during the campaign, most remarkably on Nov. 14$^{\text{th}}$ 2008 when relative humidity was reaching 100 % and outside temperatures reached as low as $\sim 2^{\circ}$ C, resulting in condensing conditions on ground level, but with only slight spontaneous formation of fog. This indicated relatively low abundance of background condensation nuclei, exactly what was supposed to be needed to enable a possible filament effect. However, it turned out that even the presence of slight fog induced strong and variable background backscattering, so that any possible effect of the Teramobile laser was buried in the fluctuating strong background signal.

The measurement setup was improved during the campaign, specifically the single shot acquisition was implemented after learning from experience that even short contiguous periods of averaging caused too much pickup of atmospheric drift to result in usable data even under seemingly quiet conditions.

Finally and unsatisfactorily only one of the nights provided low enough background to result in data where, as it turned out, the remaining still strong fluctuations were amenable to statistical analysis.

The evaluation of this peculiar measurement, conducted under quite special atmospheric conditions during the early morning of Nov. 21$^{\text{st}}$ 2008, will be presented in the following. This example provides

indication that a filament-induced effect on atmospheric aerosol backscattering might occur under real atmospheric conditions, and that it is in principle detectable with the described setup. It also shows that the effect might be subtly sensitive to the interplay of several atmospheric parameters, and indicates possible improvements to the technique.

First of all the evaluation of the LIDAR equation will be adapted to the problem of detecting a change of atmospheric backscattering properties under the specific conditions of the experiment.

5.2.1. Differential Scattering LIDAR equation

In sec. 3.2.1 the classical procedure of retrieving information about particulate (aerosol) scatterers from atmospheric LIDAR return was outlined. The primary goal of the present studies was not to infer specific aerosol properties, but first of all to obtain from the return signals evidence for – or against – a possibly very small effect of a filamenting laser beam on the scattering properties of the aerosol in the traversed air volume. The optimum configuration of the experimental setup for this task deviates from the 'classical' LIDAR configuration, introducing additional, poorly controlled range dependence of the received return (see the explanations on the experimental setup in sec. 5.2.2). Altogether this motivates the derivation of an alternative method, adapted to the situation.

Consider the range-corrected LIDAR equation. Note that range correction here just entails multiplication with the geometrical factor r^2,

$$\begin{aligned} s(r) &= c(r)[\beta_\mathrm{R}(r) + \beta_\mathrm{A}(r)] \exp\left\{-2\int_0^r [\alpha_\mathrm{R}(r') + \alpha_\mathrm{A}(r')]\mathrm{d}r'\right\} \\ &= c(r)[\beta_\mathrm{R}(r) + \beta_\mathrm{A}(r)] f(r) \end{aligned}$$

where

$$f(r) = \exp\left\{-2\int_0^r [\alpha_\mathrm{R}(r') + \alpha_\mathrm{A}(r')]\mathrm{d}r'\right\}.$$

As before, extinction due to absorption by gas molecules or aerosol is neglected. For the actual experimental situation this assumption is very well justified, especially because of the relatively low and short probed height interval. The function $c(r)$ contains the range-dependence caused by the geometry of the setup, except of the already corrected factor of r^{-2}.

After in some way altering the aerosol in the probed volume, the aerosol volume backscattering and extinction coefficients may have changed expressed by the replacements

$$\alpha_\mathrm{A}(r) \to (1 + \delta_{\alpha\mathrm{A}})\, \alpha_\mathrm{A}(r) \qquad\qquad \beta_\mathrm{A}(r) \to (1 + \delta_{\beta\mathrm{A}})\, \beta_\mathrm{A}(r),$$

resulting in an analogous LIDAR equation for the signal $s^*(r)$ and a similar definition of $f^*(r)$ after the replacement. The quantity

$$F(r) = \frac{s^*(r) - s(r)}{s(r)} = \frac{s^*(r)}{s(r)} - 1 = \left(1 + \frac{\beta_\mathrm{A}(r)\, \delta_{\beta\mathrm{A}}}{\beta_\mathrm{R}(r) + \beta_\mathrm{A}(r)}\right) \frac{f^*(r)}{f(r)} - 1. \tag{5.4}$$

has the nice property of being fully range corrected, as the common factor $c(r)$ cancels out. It is also a meaningful quantity as it expresses the relative change of LIDAR signal as a function of the range coordinate r.

The relative change of aerosol extinction in the total probed volume upon laser interaction is expected to be small, which allows to approximate the term $f^*(r)/f(r)$:

$$\frac{f^*(r)}{f(r)} = \exp\left\{-2\int_0^r \alpha_\mathrm{A}(r')\,\delta_{\alpha\mathrm{A}}(r')\mathrm{d}r'\right\} \simeq 1 - 2\int_0^r \alpha_\mathrm{A}(r')\,\delta_{\alpha\mathrm{A}}(r')\mathrm{d}r' \tag{5.5}$$

Similar to the inversion of the usual elastic backscattering LIDAR equation, one has to plug in the functional relationship between the aerosol scattering parameters, i.e. the aerosol LIDAR ratio $g_\mathrm{A}(r) = \alpha_\mathrm{A}(r)/\beta_\mathrm{A}(r)$. As it was pointed out in sec. 3.2.1 this quantity may in principle be derived from auxiliary measurements, or in the worst case has to be chosen according to an aerosol model.

The corresponding situation is more difficult in the case of the analogous relationship of the relative changes of these quantities, $\delta_{\alpha\mathrm{A}}(r)$ and $\delta_{\beta\mathrm{A}}(r)$. The number density as well as the size distribution of the scatterers may be changed due to the interaction with the filamenting laser beam, and both of these effects can possibly depend on the range coordinate in unknown ways. Formally expressing this in the form of a LIDAR ratio of relative changes of the scattering coefficients,

$$g_{\delta\mathrm{A}}(r) = \frac{\delta_{\alpha\mathrm{A}}(r)}{\delta_{\beta\mathrm{A}}(r)},$$

Using this and the approximate expression Eqn. 5.5, Eqn. 5.4 reads

$$F(r) = \left(1 + \frac{\beta_\mathrm{A}(r)\,\delta_{\beta\mathrm{A}}(r)}{\beta_\mathrm{R}(r) + \beta_\mathrm{A}(r)}\right)\left(1 - 2\int_0^r g_\mathrm{A}(r')\,g_{\delta\mathrm{A}}(r')\,\beta_\mathrm{A}(r')\,\delta_{\beta\mathrm{A}}(r')\mathrm{d}r'\right) - 1,$$

and slightly rearranging this leads to

$$\delta_{\beta\mathrm{A}}(r) = \frac{F(r)+1}{1 - 2\int_0^r g_\mathrm{A}(r')\,g_{\delta\mathrm{A}}(r')\,\beta_\mathrm{A}(r')\,\delta_{\beta\mathrm{A}}(r')\mathrm{d}r'}\left(\frac{\beta_\mathrm{R}(r)}{\beta_\mathrm{A}(r)} + 1\right) =: T(\delta_{\beta\mathrm{A}})(r). \tag{5.6}$$

The sought for quantity $\delta_{\beta\mathrm{A}}(r)$ appears on both sides of the equation. If the equation is interpreted as an iteration prescription, starting from a 'not-too-badly' guessed function $\delta_{\beta\mathrm{A},0}(r)$, repeated calculation of $\delta_{\beta\mathrm{A},n+1}(r) = T(\delta_{\beta\mathrm{A},n})(r)$ was checked to lead to quick convergence to a solution $\delta_{\beta\mathrm{A}}(r)$, for 'reasonably' chosen functions appearing in T.

When the observed range interval is shorter than the typical length scales on which the atmospheric scattering parameters change with height, the next step of simplification consists in assuming constant $\beta_\mathrm{A}(r) = \beta_\mathrm{A}$ and $\beta_\mathrm{R}(r) = \beta_\mathrm{R}$ throughout this interval. Another, less physically grounded step of simplification consists in also assuming constant $g_{\delta\mathrm{A}}(r) = g_{\delta\mathrm{A}}$, and setting his constant equal to 1. In principle the value of $g_{\delta\mathrm{A}}$ should depend on the initial aerosol size distribution (which depends on height) and the type of interaction. Setting $g_{\delta\mathrm{A}} = \text{const.}$ corresponds to the assumption that the number density as well as the ensemble averaged phase function change homogeneously in the whole observed interval, while setting $g_{\delta\mathrm{A}} = \text{const.}$ even assumes that the ensemble-averaged phase function remains

unchanged. This surely is a strong simplification that will generally be violated, but considering the smallness of the change of extinction of the probed volume associated with this, it is appropriate.

A last simplification is permitted if the denominator of the first term in Eqn. 5.6 is practically equal to 1. This is the case if the change to the total optical thickness due to laser filament interaction up to the top of the observed interval can be neglected. Then the approximate solution $\delta_{\beta\mathrm{A}}^{\mathrm{App}}(r)$ is

$$\delta_{\beta\mathrm{A}}^{\mathrm{App}}(r) = \left(\frac{\beta_{\mathrm{R}}(r)}{\beta_{\mathrm{A}}(r)} + 1\right) F(r). \tag{5.7}$$

If necessary the relative error due to above assumptions can be estimated by relating Eqns. 5.6 and 5.7:

$$\frac{\delta_{\beta\mathrm{A}}(r) - \delta_{\beta\mathrm{A}}^{\mathrm{App}}(r)}{\delta_{\beta\mathrm{A}}^{\mathrm{App}}(r)} \simeq 2(1 + F^{-1}(r)) \int_0^r g_{\mathrm{A}}(r')\, g_{\delta\mathrm{A}}(r')\, \beta_{\mathrm{A}}(r')\, \delta_{\beta\mathrm{A}}(r')\, \mathrm{d}r'.$$

Letting $\delta_{\beta\mathrm{A}}(r)$ and the other unknowns assume worst case combinations consistent with the observation, that lead to extremal values of the integral can be used to obtain an upper bound of the approximation error.

5.2.2. Experimental setup

Components

Teramobile laser At the time of experiment the Teramobile laser delivered pulses with an average energy of $E_0 = 220\,\mathrm{mJ}$ with a minimal duration of about $\tau_0 = 100\,\mathrm{fs}$. The pulse energy as stated is the one measured directly after compression. With help of the built in sending telescope the Teramobile laser beam was expanded to a diameter of approximately 10 cm, slightly focussed and directed vertically upward through the larger roof port of the container by a large elliptical dichroic mirror, where it was superimposed on the low power visible probing beam (see below).

LIDAR Transmitter The LIDAR setup was installed in the 'detection box', located outside the laser compartment of the Teramobile container. Its stiff frame is made of aluminium profiles, and is rigidly fixed to the main Teramobile laser table. This warrants that the relative alignment of the Teramobile laser beam and any optics installed in the detection box remains unchanged, even if the laser table should move on its suspension: It is obvious that otherwise even minute changes of relative pointing of the two laser beams would lead to loss of geometrical overlap of the two beams. The Lidar transmitter consisted of a flash-lamp pumped YAG laser (BigSky CFR 200). This particular laser delivered light at the fundamental, the second and the third harmonic of the fundamental emission wavelength of 1064 nm. The three wavelengths were separated using dichroic mirrors, and just the second harmonic at 532 nm was transmitted into the atmosphere. A reverse-biased fast photodiode was used to monitor the pulse energies of the LIDAR YAG laser. The photocurrent was digitized with 2 ns temporal resolution and the obtained transient was stored together with the LIDAR return signals. The monitor photodiode was operated at peak currents well below saturation of the signal. The initial

beam diameter of 6 mm was expanded to 40 mm using an adjustable Galilean telescope. This mainly reduced beam divergence and allowed for full overlap with the volume traversed by filaments, even at lower heights. Finally the beam was bent vertically upward by 90° and transmitted centered through the back of the combining mirror. This mirror consisted of a plane-parallel elliptical window substrate (BK7,220 × 150 mm, thickness 15 mm, planarity $\lambda/10$) with a broadband high reflectivity multilayer coating centered around $\lambda_C = 800$ nm for an angle of incidence of 45° on the front face. There the Teramobile beam, which entered the detection box horizontally through an opening to the laser room of the Teramobile container, was superposed with the LIDAR beam and reflected upward coaxially. The combination mirror was mounted on a 4 ” Gimbal mount which allowed for fine adjustment of the pointing of the Teramobile beam. The pointing of the LIDAR YAG beam was adjusted using the last bending mirror located below the combining mirror.

Receiver The height range in which a possible laser effect on atmospheric backscattering was expected to be strongest prescribed the choice of detection optics and geometry: Below and above the height interval where the laser beam propagates within the full field of view (field of view) of the detection optics, the LIDAR signal suffers from so-called ‘geometrical compression’. This simply means that a substantial fraction of the backscattered light that is intercepted by the receiving telescope’s primary mirror simply misses the detector, leading to a distortion of the LIDAR return signal.

The height range in which the laser beam propagates within the full field of view is determined by the inclination angle between the optical axis of the telescope and the laser, the distance between both on ground level, the laser beam initial diameter and its divergence, but also by the focal length of the telescope, the effective detector area, and the position of the effective detector relative to the focal plane of the telescope. The effective detector area can be constituted by a diaphragm, the input aperture of an optical fibre bundle, or simply the physical area of the true detector.

Ray optical treatment of the image formation of the propagating laser pulse with a flat circular transverse intensity profile onto the detector pupil yields an analytical expression for the geometrical compression as a function of height (Stelmaszczyk et al., 2005). This was used in the design of the setup (see also Fig. 5.2.2).

In common atmospheric (aerosol-) LIDAR setups, the alignment is chosen in a way that the laser beam will eventually enter the field of view of the detection optics at some height and after that remain within. The main reason for this choice of geometry is that the inversion of aerosol LIDAR returns requires an intact return signal from the free troposphere, above the planetary boundary layer, where reasonable assumptions about the background aerosol can be made. The field of view is usually kept small to keep the contrast of backscattered return signal and continuous background light as high as possible up to large distances.

This choice generally does not minimize the lower boundary of the height interval of full overlap.

As a compromise between all tradeoffs, a 500 mm focal length, 114 mm aperture Newtonian telescope was used as the primary receiving optic. Its optical axis was offset by 210 mm from the laser beam axis, the minimum allowed by geometrical constraints. However, these were not critical,

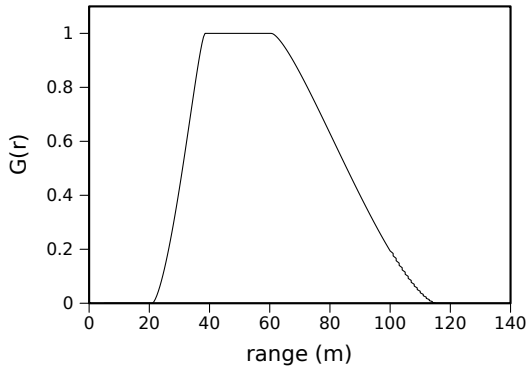

Figure 5.11.: Calculated range-dependent overlap function $G(r)$ ("geometrical compression") of the actual setup geometry, using the relationships derived in (Stelmaszczyk et al., 2005).

as there was no primary need to reach very high altitudes, and a relatively large inclination of the optical axes was permissible.

The collected light was imaged onto the input of a 2 mm diameter silica fibre bundle. In Figure 5.2.2 the calculated overlap function for the idealized actual setup geometry is shown. Note however that this calculation is based on idealized assumptions, and that the true geometrical form factor cannot easily be extracted from measured data. Especially in the present case the calculation can only serve as a guide for design and alignment.

At the output of the fibre bundle the collected light was collimated by a $f = 25$ mm anti-reflection coated plano-convex lens, passed a dielectric multilayer bandpass filter (Andover, $\lambda_c = 532.0 + 0.2/-0$ nm, $\Delta\lambda_{\mathrm{FWHM}} = 1 \pm 0.2$ nm) and finally was detected by a Licel detector module based on a Hamamatsu R7400-P03 photomultiplier tube. The bandpass filter blocked daylight other than that of the laser wavelength by a factor of 10^{-4}. Because of this, and as the experiments described here were done at night/during dawn, the measurement was unaffected by daylight related background or noise.

Data acquisition Unlike in standard atmospheric LIDAR measurements where return signals may be averaged over hundreds of laser shots, corresponding to time intervals of several minutes, one had to prepare for looking for presumably small differences of LIDAR signal hidden under a large atmospheric variability. It was not clear a priori on which time scales an effect – if detectable – could be expected, and how strong the contrast to the natural variability of the background signal would be. This means there was little knowledge which intervals of measurement time would be most adequate for averaging.

The first attempts to observe an influence of filaments on LIDAR backscattering were done acquiring averaged signals of contiguous bunches of 20 or 50 LIDAR shots. In this case the acquisition software operated a shutter in the Teramobile laser to change between intervals where the LIDAR probed a completely unaffected atmosphere, and intervals where the probed column had just previously been traversed by the filamenting Teramobile beam. This approach turned out to be inadequate because averaging over intervals of even only several seconds duration precluded sufficiently detailed account

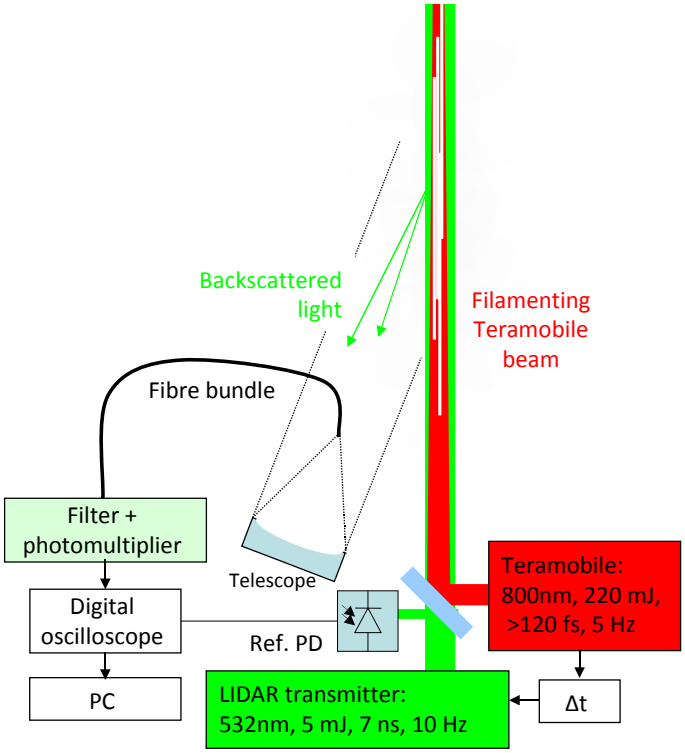

Figure 5.12.: Schematic of the LIDAR experimental setup

of the ever changing background conditions. As a consequence the setup had to be adapted for single shot resolution.

The available transient recorders were not suitable for soingle-shot data acquisition. However, the ability to synchronously record single-shot full resolution LIDAR signals together with the laser pulse energies and the type of LIDAR shot (with or without a preceding filamenting femtosecond pulse), was required.

Therefore, the Lidar signals were digitized using a 500 MHz / 500 MS/s digital oscilloscope with 8 bit A/D dynamic range (LeCroy). As mentioned above, a second channel of the oscilloscope was used for measuring the individual laser pulse energies together with the corresponding LIDAR signals. Sequences of 50 consecutive Lidar shots were sampled between data transfers to the data acquisition computer via GPIB interface. Consequently, the final data set consisted of chunks of consecutive shots, interleaving with gaps due to data transfer time.

Figure5.2.2 shows a schematic of the experimental setup.

Experiment synchronization By construction the Teramobile laser fires at a fixed repetition rate of 10 Hz. Specifically the flashlamp-pumped Nd:YAG pump lasers require to be operated at the specified repetition rate to ensure output mode quality and reliable thermal conditions in the pumped Ti:Sa rods of the amplification stages which are important for safe amplification to high pulse energies. The available LIDAR transmitter laser was limited to a maximum repetition rate of 15 Hz. To achieve

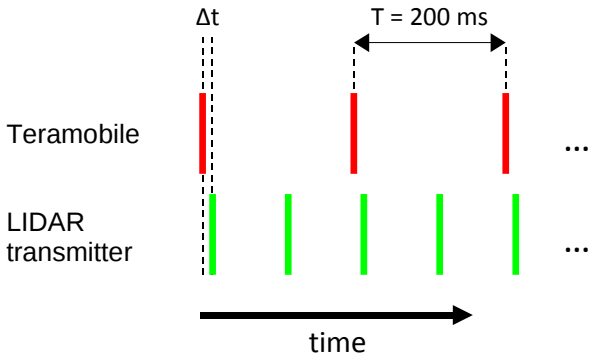

Figure 5.13.: Intermittent firing pattern with the Teramobile laser firing at 5 Hz and a LIDAR repetition rate of 10 Hz.

an interleaving firing pattern as shown in Figure 5.13 the pulse train emitted by the Teramobile laser had to be reduced to 5 Hz by an optical chopper, rotating in phase with the laser pulse train. This leaves unaffected the pumping of the amplifiers and enables stable operation of the laser system.

The chopper (Oriel) was installed right after the output of the compressor and synchronized with the 10 Hz master clock of the Teramobile laser, resulting in a 5 Hz train of femtosecond terawatt laser pulses. For each Teramobile laser trigger the state of the chopper wheel (open or closed) was stored together with the corresponding LIDAR signal.

The Teramobile laser acted as the clock of the experiment. Depending on the phase shift between the Teramobile and the LIDAR laser pulse trains, triggers for the LIDAR laser's flash lamp, the Q-switch and the data acquisition were derived from trigger signals available from the Teramobile laser, using one or, depending on the situation, two additional delay generators (Stanford Research Systems DG535 and Berkeley Nucleonics 565).

The resulting firing pattern is shown in Fig. 5.13.

Alignment procedure

In a 'classical' multi-wavelength atmospheric LIDAR measurement where the atmosphere is only probed, an absolute overlap in space of the different laser beams is not an as strict criterion as in the present case, where *exactly* the same column of air that has interacted with the first laser pulse was to be probed by the second one.

The classical strategy for the alignment of a multi-wavelength LIDAR system is about the following: each beam is aligned separately for best centering in the field of view of the (most commonly) vertically pointing receiving telescope at the largest possible distance, which is usually done by constraining the detector pupil by means of an adjustable iris diaphragm or a pinhole, and optimising for maximum range of detectable signal. Providing that the beams are emitted at the same distance from the telescope axis, such individual optimisation leads to sufficiently good alignment.

Here the required precision of beam overlap required a different strategy:

1. Fine adjust pointing of LIDAR YAG beam looking at the LIDAR signal. Find best geometrical overlap ensuring both
   a) full geometrical overlap at low altitude, typically as close as 35..40 m;

	Measurement tower Fichtenberg	Station Botanischer Garten
Position:	52°27′28.50” N 13°18′36.36” E	52°27′13.36” N 13°18′06.23” E
Height AMSL:	66 m	51 m
Measurements:	wind speed, wind direction (39 m above ground), global irradiance, visibility (33 m above ground)	temperature and relative humidity (2 m above ground)

Table 5.1.: Berlin Dahlem measurement sites of FU Berlin meteorological insitute.

b) at the same time good overlap up to at least $\simeq 100$ m.

This is: come close to the theoretically optimum conditions for the region of full overlap of the LIDAR laser beam and the telescope's field of view, as depicted in Fig. 5.2.2.

2. Install a large mirror above the combining mirror, forming a periscope with the sending mirror, and folding both beams by 90° .

3. Send both beams out horizontally (at much reduced pulse energies).

4. Overlap the beams at $\simeq 65$ m distance (the maximum obtainable propagation distance at the experiment location), by optimizing the pointing of the Teramobile beam by fine adjusting the combining mirror.

5. Remove the additional folding mirror.

This procedure guarantees perfect overlap up to at least twice the distance accessible for direct check, i.e. up to 130 m. Practically one could expect the actual range of perfect overlap to even exceed this distance.

The duration of the emitted Teramobile laser pulses was set to $\tau \approx 800$ fs by applying negative chirp, while the focus of the sending telescope was adjusted to yield the minimum achievable beam diameter of 20 mm at a distance of 65 m. These settings optimized the perceived strength of filamentation at this distance, ensuring that the interval of strongest filamentation longitudinally overlapped well with that observable by the receiving optics.

Auxiliary measurements

Local meteorological data could be obtained from the Meteorological Institute of Freie Universität Berlin, acquired at two locations close to the experiment site (see table 5.1). The Teramobile container was located at 55 m above mean sea level. Wind parameters and standard visibility were measured at a site 1140 m east of the experiment site at heights comparable to the centre of the height interval observed in the LIDAR experiment.

Standard visibility was measured using a visibility meter based on measurement of short-range atmospheric backscattering ('Videograph, Impulsphysik GmbH')

5.2.3. LIDAR data evaluation

Data structure

The measured data was saved in chunks C_i each consisting of n shots Σ_j.

$$C_i = (\Sigma_1 \dots \Sigma_n) .$$

Each shot contained the following data: a timestamp t_k, the raw LIDAR transient $\mathbf{T}_k$, the reference energy measurement photodiode transient $\mathbf{R}_k$, and an indicator f_k telling if the shot was preceded by a filamenting Teramobile laser pulse (from now on termed 'on'-shot) or if it was a reference shot without the preceding laser pulse ('off'-shot). Note that transients (tuples of floating point numbers) are typeset in boldface.

$$\Sigma_j = \left\{ t_j, \mathbf{T}_j, \mathbf{R}_j, f_j \right\} .$$

Within one chunk the shots are separated by the LIDAR laser firing period,

$$t_{j+1} - t_j = T_{\mathrm{LIDAR}} = 100\,\mathrm{ms}.$$

LIDAR laser pulse energy and jitter correction

To adequately correct the raw LIDAR signals $\mathbf{T}_j$ for the actual transmitted laser pulse energies E_j, the latter were obtained from the photodiode signals $\mathbf{R}_j$. Every such transient consisted of 1000 data points sampled with a period of 2 ns. The baseline level b_j of each transient was calculated as the arithmetic mean of samples 700..1000, where inspection of the data showed that the photocurrent due to the respective laser pulse had effectively decayed to zero. A quantity E_j, representative of the laser pulse energy of shot j, then was determined from the numerical integral over the transient $\mathbf{R}_j - \mathbf{b}_j$, where $\mathbf{b}_j = \left(b_j, b_j, \dots, b_j\right)$. The numerical integration used a 2^{nd} order polynomial interpolation of the discrete data. It was checked that further increase of the interpolation order did not improve the precision of the result.

The baseline values b_j are assumed to be composed of two contributions, according to

$$b_j = \overline{b}(t_j) + \epsilon_j .$$

Here, $\overline{b}(t_j)$ represents any long term drift of the background. Such drift could possibly result from changing background light flux at the photodetector (for example due to variation of daylight conditions), and/or minute slow changes in the data acquisition electronics due to thermal drift of electronic gains. The noise component ϵ_j is related to random electromagnetic noise picked up by the circuits.

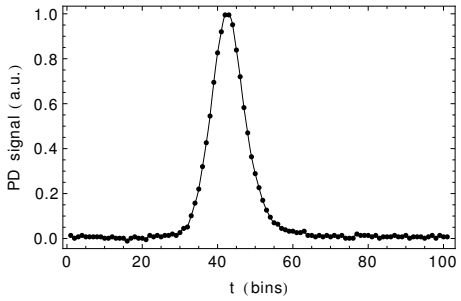

Figure 5.14.: Typical reference photodiode signal. Sampled data is plotted as points, the interpolation as a line.

Based on a 20-point moving average for estimating $\overline{b}(t_j)$, the shot-to-shot noise ϵ_j was isolated from the slowly changing part $\overline{b}(t_j)$, and it was found to result in a *baseline-related*, normally distributed shot-to-shot relative error of the LIDAR laser energy measurement of about 0.5 %. The internal synchronization scheme of the Teramobile laser caused a uniformly distributed relative jitter between the LIDAR laser trigger and the acquisition trigger of 13 ns or ≃ 2 m LIDAR range. Additional, more normally distributed jitter on a scale of several nanoseconds entered by the limited accuracy of the LIDAR laser Q-switch electronics. The total timing uncertainty was reduced to less than ±2 ns or 0.3 m LIDAR range by referencing to the true time of emission relative to the acquisition trigger, $t_{0,j}$, as obtained from the maxima of the interpolated photodiode signals. A typical reference photodiode signal transient is shown in Fig. 5.14 together with its interpolation.

All LIDAR signals were scaled with the inverse of the measured LIDAR laser pulse energy, shifted in time according to the measured true time of emission, and range-corrected by multiplying with r^2 (see sec. 3.2.1). For the l^{th} sample in the resulting transient representing the corrected LIDAR transient, $\mathbf{T}_j^{\text{corr}}$, and as $r(l) = l\,\Delta t_{\text{sample}}$, this reads:

$$T_{j,l}^{\text{corr}} = E_j^{-1}\,\left(l\,\Delta t_{\text{sample}}\right)^2\,T_{j,l+i(t_{0,j})},$$

where $i(t_{0,j})$ is the (rounded) index in the original transient $\mathbf{T_j}$, corresponding to time $t_{0,j}$.

Triple LIDAR transients

The symmetrically intermittent firing pattern, (see preceding section) was dictated by the capabilities of the available laser hardware. This sort of pattern was *not* the most desirable one. It allowed for tracking of slow drift of atmospheric scattering properties, but it was potentially receptible for the influence of fast microscale turbulence on LIDAR signals, that happens on timescales comparable to, or below, the LIDAR firing period of 100 ms (see Sec. 3.3).

In spite of this, the most straightforward estimator for the reference LIDAR signal, that would have been obtained at the times of the 'on'-shots *without* a preceding filamenting Teramobile shot, is given by the linear interpolation between those of the directly preceding and succeeding 'off'-shots. Such a sequence of shots will be called 'triple' from now on.

The acquisition of chunks C_i was not synchronized with the laser clock, which means that for a small fraction of 'on'-shots no triple could be formed, and these shots were discarded to ensure equal

statistical weights.

Organizing the data in triples facilitates book-keeping and proper account of background signal when averaging over random subsets of shots.

Given a triple $(\mathbf{T}'_{\text{off}}, \mathbf{T}_{\text{on}}, \mathbf{T}''_{\text{off}})$ the 'differential LIDAR transient' $\mathbf{T}_{\text{diff}}$ is defined as

$$T_{\text{diff},i} = T_{\text{on},i} - \overline{T_{\text{off},i}} = T_{\text{on},i} - \frac{1}{2}(T'_{\text{off},i} + T''_{\text{off},i}). \tag{5.8}$$

The corresponding 'relative triple differencial LIDAR transient' $\mathbf{T}_{\text{reldiff}}$ is defined as

$$T_{\text{reldiff},i} = \frac{T_{\text{on},i} - \overline{T_{\text{off},i}}}{\overline{T_{\text{off},i}}} = \frac{T_{\text{on},i}}{\overline{T_{\text{off},i}}} - 1 = \frac{2\,T_{\text{on},i}}{T'_{\text{off},i} + T''_{\text{off},i}} - 1, \tag{5.9}$$

which is the discrete counterpart of the function $F(r)$ defined in Eq. (5.4) applied to the triple, and using the mean of the sandwiching 'off'-shots, $\overline{\mathbf{T}_{\text{off}}}$, to represent the reference signal $s(r)$.

Second order LIDAR laser pulse energy correction

Ideally, after normalization of the LIDAR return signals with respect to the measured laser pulse energies E_j, all information about these carried by the signals has been erased – provided that the relationship between the measured E_j and the 'true' laser pulse energies is strictly linear. However, imperfect linearity of any of the involved components will result in a deviation from this ideal relationship. The photodiode used for the pulse energy measurement, the photodetector measuring the LIDAR return signal, as well as the entire signal paths through amplification and A/D conversion for either channel, are potential sources of such nonlinearity.

In the present situation an absolute calibration of the entire setup under realistic conditions was impractical. Nevertheless, to be able to directly compare any two lidar signals, any spurious influence of laser pulse energy measurement error had to be assured, based on a criterion using only the available data. Such criterion was formulated according to the following argument: Provided that the LIDAR signals are perfectly energy-corrected, the differential transients and the analogously defined differential LIDAR laser pulse energies must be statistically independent. Any detectable statistical dependence would indicate imperfect energy correction.

The magnitude of the $T_{\text{diff},i}$ was quantified by their mean value in the height interval between 45 m and 75 m. The resulting plot obtained from actual data is shown in Fig. 5.15. If both quantities were only contaminated with symmetrically distributed, random, uncorrelated noise, the point cloud would be mirror symmetric with respect to both axes. This clearly was not the case. Instead the point cloud indicated some degree of mutual correlation of both quantities, as the points were concentrated around a straight line clearly not parallel to either of the orthogonal coordinate axes. A linear least squares fit could be applied to quantifiy this.

Having identified the correlation, the attempt was made to reduce it with help of the reasonable assumption of a slight nonlinearity in the relationship between 'true' and measured LIDAR laser pulse energy. Note that this is to be understood as a lumped net nonlinearity of the whole system, including

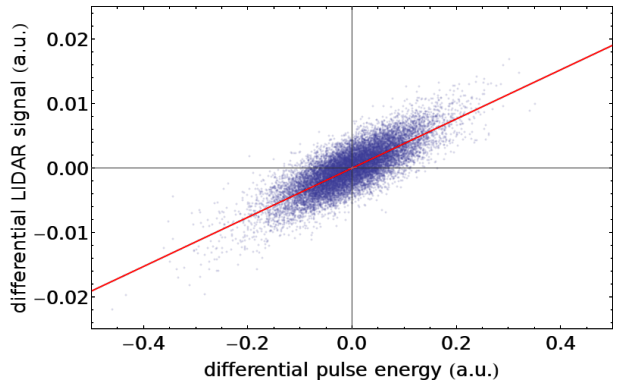

Figure 5.15.: Plot of differential LIDAR signal magnitude vs. corresponding differential LIDAR laser shot energies. The red line corresponds to the linear least squares fit. The slanted shape of the point cloud indicates imperfect energy correction of the LIDAR signals (see text).

both involved photodetectors as well as both signal pathways, without even trying to identify which component contributes exactly in which way.

As a starting point the following form of the relationship between measured and 'true' LIDAR laser energies E_{measured}, and E_{true}, respectively, was assumed:

$$E_{\text{measured}} = E_{\text{true}} + \alpha E_{\text{true}}^2.$$

Tests with artificially generated noisy data (representing reference photodiode signal and LIDAR signal, contaminated by the nonlinearity due to nonvanishing α) showed, that under relatively general conditions the value of the parameter α could be found by numerical optimization, seeking for the value that nullified the slope of the linear fit to the corresponding point cloud. Application of the same algorithm to the real data succeeded in the sense that an α_0 nullifying the slope of the linear fit was found. The resultant point cloud and corresponding relationship $E_{\text{true}}(E_{\text{measured}})$ are shown in Fig. 5.16 .

The much improved shape of the point cloud and the observation that the obtained α_0 represents a unique optimum was taken as justification for this rather heuristical approach. It was also checked that removing that part of the residual nonlinearity which was detectable by the described method, did not qualitatively influence the outcome of the evaluation presented in the following. This was mainly due to the fact that the correction had more of an impact later in the measurement, when the overall LIDAR signal strength had increased, and more importantly, had become more variable shot-to-shot. As will be detailed below, the most interesting observations were made under conditions of weaker LIDAR signal, where the correction had less noticeable effect.

Statistical data analysis

In sec. 3.3 it was discussed how a LIDAR measurement is affected by atmospheric turbulence-induced noise. Such noise with a priori unknown properties and time dependence could not be eliminated by

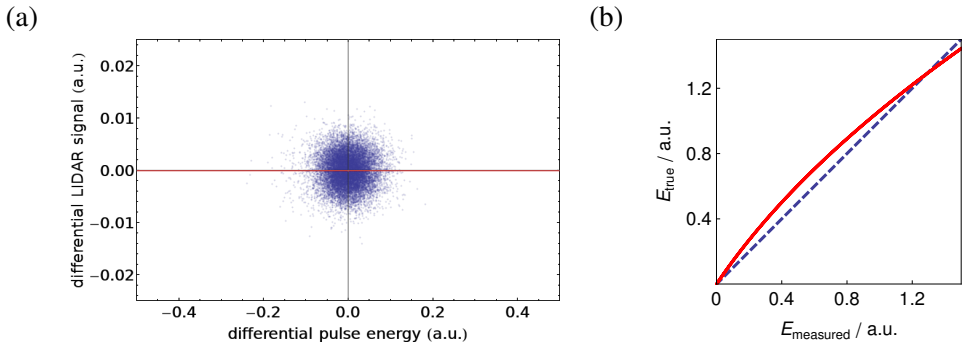

Figure 5.16.: (a) Plot corresponding to that shown in Fig. 5.15 *after* inclusion of nonlinearity in the laser pulse energy measurement. The symmetry axes of the point cloud are parallel to the coordinate axes; (b) resulting relationship $E_{\text{true}}(E_{\text{measured}})$, both in the same a.u.; Additionally the nonlinearity-corrected function was scaled by a constant factor to yield equal mean pulse energies, also facilitating visual assessment of the magnitude of the applied correction.

other methods, and had to be dealt with using statistical means.

The fundamental task was to find evidence whether the filamenting laser beam had an effect on atmospheric backscattering properties, or not. Such effect should cause a systematic difference of backscattering signals between the two classes of LIDAR shots, 'off' and 'on'. This would have to be isolated from strong background noise.

The Wilcoxon-Mann-Whitney (WMW) rank-sum test (Wilks, 2005) was chosen as a sensitive method to accomplish this task. Given two samples of data the WMW test estimates how 'safe' it is to reject the null hypothesis that both samples were drawn from one single population.The test returns a p-value equivalent to the probability under the null hypothesis to obtain the actually observed data or an even more extreme outcome. The two-sided alternative to the null hypothesis of the WMW test states that one of the samples was drawn from a distribution with mean μ_0 and the other from a distribution with mean μ, and $|\mu - \mu_0| > 0$. Choosing the two-sided alternative hypothesis in this specific case corresponds to not being prejudical about the sign of a possible Teramobile laser effect.

The WMW test is known to be resistant to outliers and almost as powerful as the related (parametric) two-sample t-Test. In contrary to the t-Test it does not require that the underlying distribution(s) be normal, which is not guaranteed in many situations. The WMW test works by ranking the data of the combined sample, containing all observations from both samples. In the case of numerical data this amounts to sorting all observations by magnitude. The observations, tagged according to their sample of origin, are sorted irrespective of the sample they belong to. The *rank* of each observation is determined by its position in the sorted row. The *rank sums* are calculated by simply summing up the ranks of the observations, now again distinguishing between the two original samples (this is why the observations were initially tagged). The idea of the WMW test consists in treating the rank sum of one of the samples as a new random variable, and comparing its actually observed value to its probability distribution assuming the null hypotesis holds.

One prerequisite of the WMW test cannot be strictly fulfilled in the present situation: The sampled

probability distribution(s) have to be constant. In reality, any sample of data spans a certain interval in time, during which the probability distribution of the random variable may change. Serial correlation of time series data can lead to false results of the WMW test. Yang and Yue have shown this for a test case where a step of the mean in a sequence of noisy measurements showing serial correlation had to be detected (Yue and Wang, 2002). Under conditions of positive serial correlation, and for said test case, false rejection of the null hypothesis could result. In the latter publication the assumed form of the time series is

$$X_t = \mu_X + \varepsilon_t + \rho(X_{t-1} - \mu_X).$$

X_t is the observation at time t, μ_X the population mean, ε_t a random one-element sample from a ideal gaussian distribution (white noise), and ρ is the serial correlation coefficient. The term proportional to ρ implements serial correlation by introducing 'memory' or persistence to the time series.

Such type of serial correlation is almost certain to occur in the time-resolved differential scattering LIDAR data. Larger-scale turbulent structures (see sec. 3.3) have the potential to generate a similar type of fluctuations persistent over relatively long times (on the order of several LIDAR shots, for structures on the 100 m scale maybe several seconds).

One however has to be aware that the structure of the data to which the WMW test was applied in our context was fundamentally different from that in the study reported in (Yue and Wang, 2002), as there the samples to be tested for equality of the underlying populations corresponded to two temporally *contiguous* blocks of data points, whereas in our case the samples were interleaved in time, and the impact of positive correlation, should it occur, would rather make both samples more *similar* than distinct, leading to a tendency towards false *acceptance* of the null hypothesis rather than false rejection. This means that serial correlation could rather obscure a present effect of laser-induced backscattering enhancement (Type II error) than produce a false positive (Type I error). Of course this constellation is the more favourable from the point of view of 'onus of proof'.

Retrieval of average β_A from standard visibility data

In the present case the independently measured standard visibility was obtained from an instrument that effectively measures short-range atmospheric *backscatter*, not directly *extinction* (Quenzel et al., 1975). To derive the standard visibility, the measured backscatter is internally processed by the instrument, according to an assumed fixed aerosol LIDAR-ratio (see sec. 3.2.1) and standard sea-level Rayleigh atmosphere. Straightforward reversal of this processing yields an approximate value for the aerosol volume backscattering coefficient.

Using the definitions of the scattering parameters (Sec. 3.2.1) the corresponding expression is

$$\beta_{\pi,\mathrm{A}} = \frac{\alpha_\mathrm{A}}{\alpha_\mathrm{R}} \frac{F_\mathrm{A}}{F_\mathrm{R}} \beta_{\pi,\mathrm{R}} = \left(\left(1 - \frac{\alpha_{\mathrm{abs,A}}}{\alpha_\mathrm{A}}\right) \frac{v_\mathrm{R}}{v} - 1\right) \frac{F_\mathrm{A}}{F_\mathrm{R}} \frac{3}{8\pi} \alpha_\mathrm{R}, \tag{5.10}$$

where $v_\mathrm{R} = 336.7\,\mathrm{km}$ and $\alpha_\mathrm{R} = 1.162 \times 10^{-2}\,\mathrm{km}^{-1}$ are the standard visibility and extinction coefficient in a pure Rayleigh atmosphere, respectively. The factor $\frac{\alpha_{\mathrm{abs,A}}}{\alpha_\mathrm{A}}$ represents the fraction of aerosol extinction that is due to absorption, which for clear air can be assumed on the order of 10 % (Quenzel

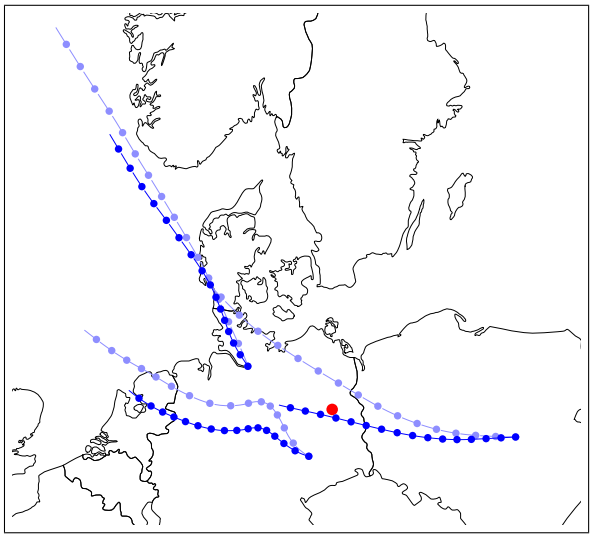

Figure 5.17.: Backtrajectories for Aeronet stations Hamburg, Leipzig, and Belsk ending on Nov. 21,12:00 UTC. Dark blue: 950 hPa level; Light blue: 850 hPa level. Dots are spaced by 1 h; experiment location is indicated by a red circle.

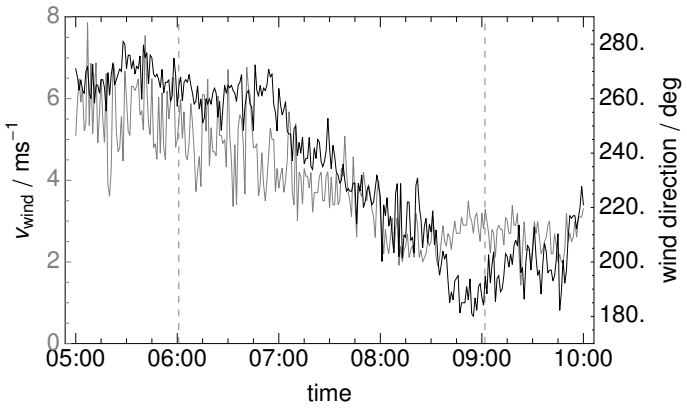

Figure 5.18.: Local wind speed (gray), and wind direction (black); The time for which LIDAR data is available is indicated by vertical dashed lines.

et al., 1975), and $\frac{F_A}{F_R}$ is an instrument-dependent constant, which for the actually used instrument is $\frac{F_A}{F_R} \simeq 0.18$ (Quenzel et al., 1975).

5.2.4. Results

Meteorological conditions

During the night between Nov. 20th and 21st cold maritime air was moving in over Germany from the north. In Fig. 5.17 backtrajectories calculated for air parcels at 950 hPa (blue) and 850 hPa (light blue), corresponding to altitudes of approximately 500 m and 1500 m, respectively, are shown (Kucsera, 2008). According to the backtrajectories, the incoming air masses had spent several days over the North Atlantic, and after crossing the shoreline, had taken a relatively direct way over land.

At the experiment site, during the night of Nov. 20th, repeated showers had kept the ground wet. The rainfall possibly also acted as a sink for coarser aerosol (Hobbs, 1993). At about 20:30 PM, long after sunset, cloud coverage began reducing to partly cloudy. The last light shower before measurement start was registered at 01:30 AM. Consequently there was plenty of moisture on ground. Temperature was dropping and relative humidity measured close to ground was rising, reaching 90 % around

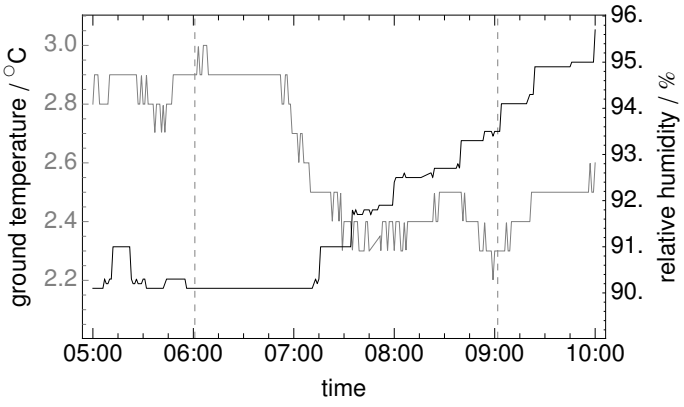

Figure 5.19.: Temperature (gray) and relative humidity (black). The time for which LIDAR data is available is indicated by vertical dashed lines.

04:30 AM (for the trend of relative humidity around the measurement time interval see Fig. 5.19).

At the same time very weak aerosol scattering was observed, expressed by the measured standard visibility. Corresponding data for the morning of Nov. 21st are shown in Fig. 5.20. At around 05:45 AM a maximum standard visibility of more than 70 km was attained, which then dropped at almost constant rate to (still) 30 km until 10:00 AM. In an urban environment standard visibilities greater than 20 km are already considered 'clear'. This means that throughout the measurement time the total amount of suspended particles – including liquid droplets – was surprisingly low, if one considers the moist and cold conditions.

Local wind speed and direction, as registered at measurement tower Fichtenberg, are indicated in Fig. 5.18. While the wind speed gradually settled from around 5 m/s to about 3 m/s the wind direction turned from 270° to about 190° . Wind and the related turbulence may have acted as mixing agent: The same mechanisms that lead to optical turbulence (see Sec.3.3) can induce local fluctuations of vapour saturation around the mean value.

Comparison of the plots of wind direction and speed (Fig. 5.18) and standard visibility (Fig. 5.20) indicates close correlation between the three observables. Especially the plots of wind direction and visibility show common features, justifying the conclusion that, under the prevailing conditions, visibility/aerosol backscattering almost directly reflect the short-term history of the air moving past the observation site.

West of the experimental site (the initial wind direction), at a distance of about one kilometre housing-dominated suburb, Grunewald forest and lake Wannsee constitute many square kilometres of area virtually free from sources of dust or combustion aerosol. Ahead of rush hour motorway A115, passing at a distance of about 4 km west of the site, was propably no strong source of pollution. Air coming in from south of the experiment site has to bridge a considerably wider strip of urban area, possibly influencing its load with aerosol.

Observations

On the morning of Nov. 21st data could be acquired between 06:00'54" AM and 09:13'46" AM. Towards the end of the measurement light sleet started falling, and the data of the terminal ~ 15 min

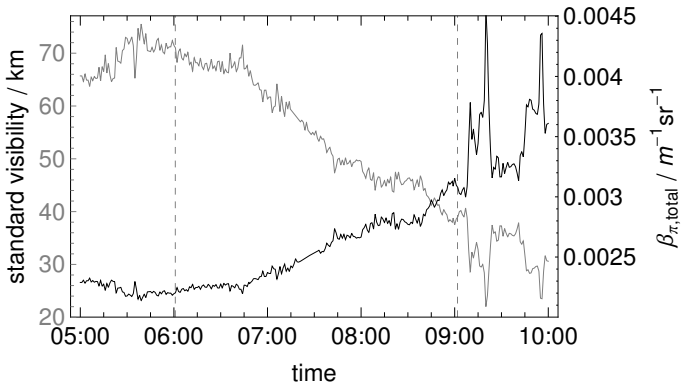

Figure 5.20.: Standard visibility as measured by the Videometer instrument (gray), and the derived local aerosol volume backscattering coefficient β_A (black). The time for which LIDAR data is available is indicated by vertical dashed lines.

was contaminated with sporadic strong scattering events on single larger hydrometeors. This is why only data up to 09:01'49" AM was used for the analysis.

For a total of four times data acquisition was briefly interrupted for checks (each time for about 1 min). It was verified that the interruptions had no influence on the result of the analysis.

As in the present case no independent LIDAR measurement was available, the volume backscattering coefficient β_A was approximately determined from the local visibility measurement, according to Eq. 3.2. The standard visibility was measured at some (horizontal) distance from the LIDAR site (see Tab. 5.1), however at an altitude comparable to that where LIDAR signals were measured. In Figure 5.21 the range-corrected backscattering signal from a height of 60 m above ground at the LIDAR site, and the total backscattering coefficient $\beta_{\mathrm{total}} = \beta_A + \beta_R$ calculated from the standard visibility data according to Eq. 5.10, are shown. Both plots show similar trend and both attain a minimum between about 06:30 AM and 06:45 AM. The relative time lag that gets apparent around the time of the minima is explainable by the downwind location of Fichtenberg measurement tower with respect to the LIDAR site at that specific time.

It should be noted that consequently the earlier stated close correlation between the meteorological observables also extends to the magnitude of LIDAR backscattering signal.

It can be concluded that one can obtain approximate quantitative information about β_{total} at the LIDAR site from the visibility data from Fichtenberg tower. This confirms that, under the prevailing conditions and for the considered short ranges, atmospheric extinction indeed was negligible, and the simplified expression for $\delta^{\mathrm{App}}_{\beta A}(r)$ stated in Eq. 5.7 could be used.

The data analysis was carried out according to the procedure described in Sec. 5.2.3. To start with, the mean relative change of LIDAR signal in the range interval of optimum overlap was examined. Recalling the definition of the function $F(r)$ in eq. 5.4 this corresponds to the discrete counterpart of the integral

$$\overline{F} = (r_{\max} - r_{\min})^{-1} \int_{r_{\min}}^{r_{\max}} F(r)\mathrm{d}r,$$

where $r_{\min} = 45$ m and $r_{\max} = 75$ m.

In Fig. 5.22 the mean relative change of LIDAR signal in the range interval of optimum overlap is shown as a smoothed curve obtained by forming the moving average over 800 triple transients

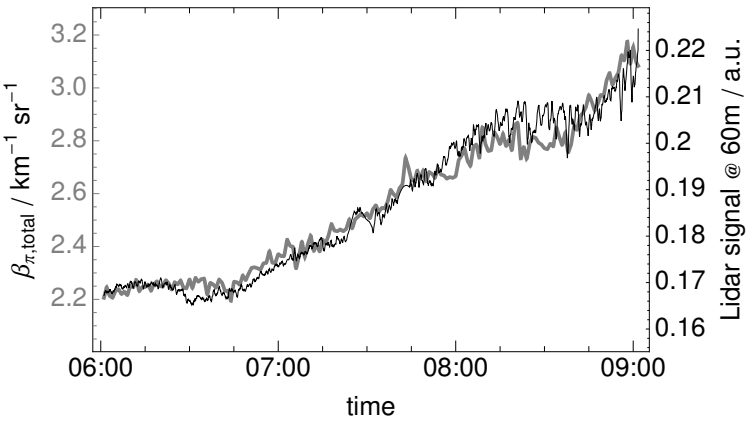

Figure 5.21.: Comparison of total atmospheric volume backscattering coefficient β_{total} as obtained from the measured standard visibility at Fichtenberg measurement tower and the LIDAR signal from an altitude of 60 m above ground at the LIDAR site. The LIDAR signal plot is 50-point moving average smoothed.

corresponding to ∼ 5.5 min of measurement time. Note that the moving average also applies to the time coordinate. Relatively strong shot-to-shot fluctuations of the LIDAR signals that are superimposed on a possible laser effect make indispensible some amount of averaging.

The chosen interval width for the moving average is a compromise between noise suppression and time resolution. Looking at the plots of the meteorological data (Figs. 5.18, 5.19, 5.20), estimating the time scale on which meteorological parameters undergo noticeable changes, suggests, that averaging on a scale of some minutes should preserve enough time resolution to be able to look for coincident features in the outcome of the differential LIDAR analysis and the meteorological data.

The plot in Fig. 5.22 indeed suggests some initial enhancing effect of the Teramobile laser, which seems to fade out later in the measurement, specifically after about 06:30 AM. After this time there are periods of apparently weaker effect taking on either of both signs, probably indicating the noise level due to atmospheric fluctuations. Consequently it was indispensable to quantify the statistical significance of these deviations from neutral.

The Wilcoxon-Mann-Whitney test was applied to this task. As before, and as a compromise between time resolution and sufficiently large sample size, for a given contiguous interval of ∼ 5.5 min measurement time, two samples (*I* and *II*), consisting of subsets of the LIDAR shots in this interval, were compared. The considered interval was shifted in a similar manner as when forming the moving average. The way how samples *I* and *II* were constructed differed between test cases:

1. Samples *I* contained all 'on' shots of the respective time intervals. Samples *II* consisted of the corresponding preceding 'off' shots, exploiting the full available data.

The result of the test indicates a difference ($p \leq 0.01$) between any two corresponding samples *I* and *II* throughout most of the initial ∼ 30 min of measurement (average $\overline{p} = 0.008$). For the data after ∼06:30 AM the WMW test does not detect as significant difference between both types of samples any more. The p-value quite suddenly starts to oscillate to large values, getting larger on average (see

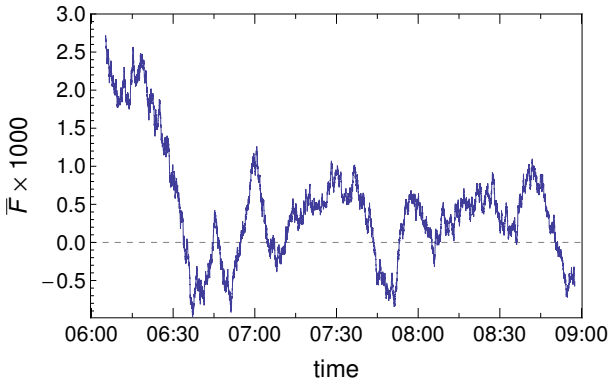

Figure 5.22.: Plot of mean relative change of LIDAR signal in the range interval of optimum overlap; Moving average smoothed over 800 triple transients corresponding to ~ 5.5 min of measurement time

Fig. 5.23). This trend continued until the end of the measurement.

2. As a countercheck, samples *I* and samples *II* were taken from the odd and even 'off' shots, respectively, maintaining the ~ 5.5 min duration of the covered time intervals. The WMW test applied to these pairs of samples resulted in large p-Values throughout the meaurement time (in the critical initial ~ 30 min: average $\overline{p} = 0.47$, minimum $p_{\min} = 0.07$). Of course keeping the interval duration fixed while subsampling the 'off' shots reduced the number of shots in each sample to 400, possibly influencing the result. This is why a final check was done:

3. The first test was repeated on the subsampled dataset, omitting every other 'on' shot and its corresponding 'off' precedessor, in order to consider samples of the same size as in the second case. The p-values resulting from the WMW test remain fairly below 5 % during most of the first ~ 30 min of measurement. One cannot reject the null hypothesis as safely as in the first case, which is not too surprising, regarding that half of the available data were discarded. Still, looking at this result, one can conclude that the observed large p-values in the second test case are *not* an artefact, but they indicate that the 'off' shots of reasonably long time intervals are likely to be sampled from one population. Correspondingly, the very small p-values in the first case, which remain comparatively small even in the third case, are meaningful. The sets of p-values resulting from the three test cases for the first ~ 30 min are plotted in Fig. 5.24.

As a conclusion, during most of the first half hour the total LIDAR signals from the range interval of optimum overlap differ at a significance level of 1 %. The observed difference indicates a backscattering-enhancing effect of the Teramobile laser.

It is clear from the preceding paragraphs that this effect is buried deeply in noise, and can only be detected when considerable spatio-temporal averaging is applied. This is why it was not possible to obtain range *and* time-resolved information on the relative change $\delta^{\mathrm{App}}_{\beta\mathrm{A}}(r)$ of the aerosol volume backscattering coefficient, as would be accessible from less noisy data using eqn. 5.7.

However, the outcome of the statistical analysis is consistent with the visual impression obtainable from plots of time averaged, range resolved differential LIDAR signals. In Fig. 5.25 the time-average

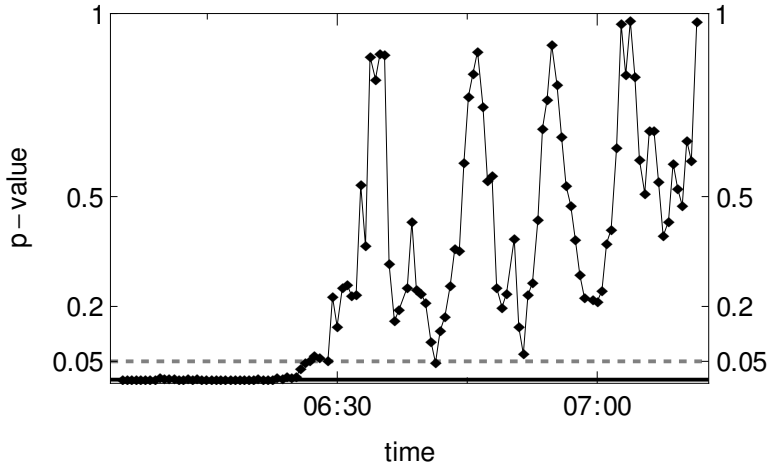

Figure 5.23.: P-values of test case 1 plotted vs. time (details see text). The plotted time interval is truncated as the p-values remain large.

$\langle F(r)\rangle_I$ of the functions $F_i(r)$, where i runs over all triples of shots in time interval I, is plotted along the range interval of optimum overlap and for two averaging time intervals: the 'significant period' where $p \leq 0.01$ (see Fig. 5.23), and its complement. Clearly $\langle F(r)\rangle$ is greater than zero throughout the range interval during the former, indicating a backscattering-enhancing effect of the Teramobile laser, while it is closer to zero during the latter. The curve $\langle F(r)\rangle$ for the 'significant period' suggests that backscattering enhancement was most pronounced around the center of the interval. However, quantiatively interpreting the shape of the curves in terms of effect strength as a function of range would require better signal-to-noise ratio of the measured data.

5.2.5. Discussion and interpretation

In order to estimate the chances that the observed small increase of aerosol backscattering was actually caused by net condensation of vapour out of the gas phase, one has to identify alternative phenomena which could lead to similar measured signals and assess their impact.

Direct effect of fragmentation

One of these potential spurious effects is the bare change of the total backscattering cross section when a larger droplet splits into a number of smaller droplets, assuming conserved liquid volume.

For the simplistic case of a single droplet of diameter $D_{\mathrm{p,before}}$ splitting into N identical droplets of diameter $D_{\mathrm{p,after}}$, mass conservation is expressed as

$$\frac{\pi}{6} D^3_{\mathrm{p,before}} = N \frac{\pi}{6} D^3_{\mathrm{p,after}}.$$

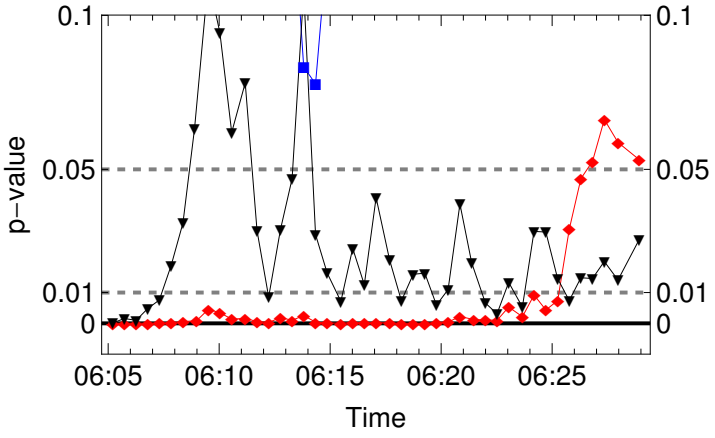

Figure 5.24.: WMW test results for the LIDAR data of the critical initial ~ 30 min of the measurement. Each plot corresponds to one of the three test cases described in detail in the text. Red diamonds: case 1; blue squares: case 2; black triangles: case 3. Note that the p-values of case 2 are out of the plotted range of $p \leq 0.1$ during most of the time.

Then the relative change of the backscattering cross section is given by

$$\frac{C_{\mathrm{b,after}}}{C_{\mathrm{b,before}}} = \frac{N Q_{\mathrm{b}}(D_{\mathrm{p,after}}) D_{\mathrm{p,after}}^2}{Q_{\mathrm{b}}(D_{\mathrm{p,before}}) D_{\mathrm{p,before}}^2} = \frac{Q_{\mathrm{b}}(D_{\mathrm{p,after}})}{Q_{\mathrm{b}}(D_{\mathrm{p,before}})} \frac{D_{\mathrm{p,before}}}{D_{\mathrm{p,after}}},$$

where Q_{b} is the backscattering efficiency factor $Q_{\mathrm{b}} = C_{\mathrm{b}}/(\pi D_{\mathrm{p}}^2/4)$.

The result thus depends on the shape of the function $Q_{\mathrm{b}}(D_{\mathrm{p}})$ and the relative size of the fragments. A generalization of this relation to continuous droplet size distributions is used in the present case.

In sec. 4.3 an estimate for the change of the size distribution of an aerosol of watery droplets undergoing fragmentation due to internal optical breakdown was derived. To recall, the estimate is based on experimental observations of relatively large droplets in a focused beam of near infrared femtosecond pulsed laser light (Lindinger et al., 2004) and their interpretation with the aid of numerical calculations of the onset of internal optical breakdown (Kandidov et al., 2004). The conclusion that in general an impacting filament largely exceeds the threshold for optical breakdown and efficient absorption of energy in large droplets was extrapolated to droplets down to micrometer size based on the comparison of the internal intensity distributions calculated using Mie theory.

In the following this estimate is used to assess to which extent simple fragmentation of preexisting fog or cloud droplets could have had an effect on the measured LIDAR return signal.

Justified by the observed high visibility and the air mass backtrajectories (see Fig. 5.17) the prevailing very thin haze is assumed to be little polluted with soot and solid particulate matter, and to have a size distribution and chemical composition dominated by maritime influence. This entails that most of the dry mass is water soluble sea salt aerosol (Kokhanovsky, 2008; Seinfeld and Pandis, 2006). From the measured high relative humidity it the follows that practically all aerosol particles have deliquesced, which justifies to treat the aerosol particles as spherical droplets.

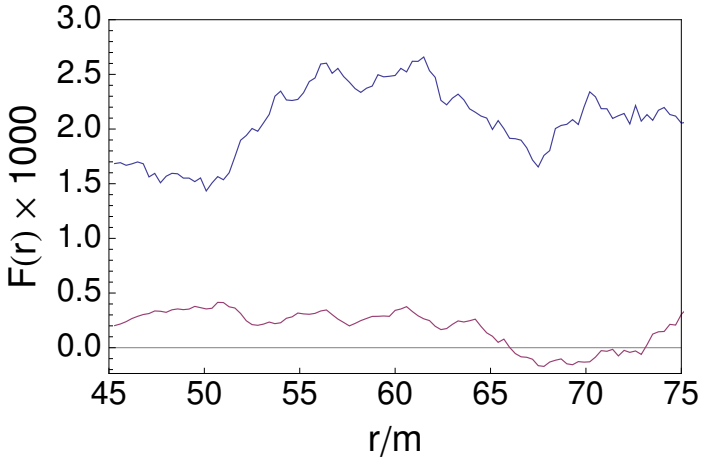

Figure 5.25.: time-averaged $\langle F(r)\rangle_{t\varepsilon I}$ along the range interval of optimum overlap. Red: initial 'significant period' ($p \leq 0.01$, see Fig. 5.23); green: its complement.

The size distribution of the aerosol is assumed to have the shape of a representative maritime haze model size distribution (Jaenicke, 1993) in the following calculations, which is widely used in the literature and in the evaluation of LIDAR measurements. Furthermore the refractive index of the droplet material at the LIDAR laser wavelength of 532 nm is chosen here as that of pure water, $n_\mathrm{p} = 1.337$, adequate for mainly oceanic aerosol at very high RH. (Kokhanovsky, 2008; Seinfeld and Pandis, 2006).

First of all the question is addressed if droplet fragmentation caused by the low intensity 'photon bath' background, propagating in between the filaments could have happened in the particular experimental situation.

Assuming a Gaussian temporal pulse shape and approximating the super-Gaussian Teramobile beam profile by a flat top shape, the peak intensity in the beam cross sectional area in between the filaments can be estimated as

$$I_\mathrm{peak} \approx \frac{P_\mathrm{peak}}{A_\mathrm{beam}} = \frac{2\sqrt{\ln 2}}{\tau\sqrt{\pi}} E_\mathrm{pulse}/(\frac{\pi}{4} d^2_\mathrm{beam}).$$

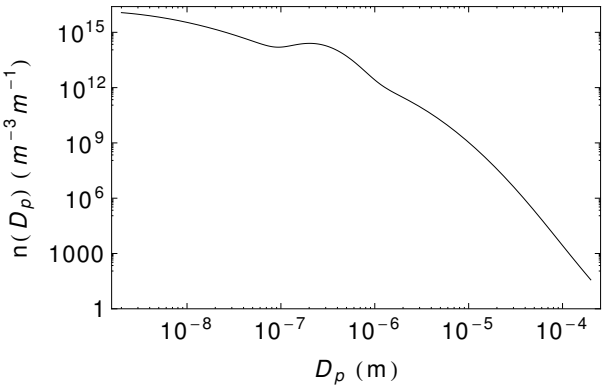

Figure 5.26.: Frequently used model haze size distribution representative for maritime type aerosol (Jaenicke, 1993) parametrized as the sum of three log-normal modes.

Inserting the actual laser pulse and beam parameters ($E_{\mathrm{tot}} = 220\,\mathrm{mJ}$, $\tau_{\mathrm{FWHM,chirped}} = 800\,\mathrm{fs}$) and the minimal beam diameter of $d_{\mathrm{beam}} = 2\,\mathrm{cm}$ at about 65 m distance, one arrives at an estimated peak intensity of $\tilde{I}_{\mathrm{peak}} \approx 8 \times 10^{10}\,\mathrm{W/cm^2}$, which is about half the threshold intensity $I_{\mathrm{thresh},100\,\mu\mathrm{m}}$ for the onset of plasma formation in droplets of around $D_{\mathrm{p}} = 100\,\mu\mathrm{m}$ diameter (see Tab. 4.3.4).

Some caution must be taken here: as the intensity profile in between the actual filaments is affected by nonlinear self-focussing as well, after some propagated distance the distribution of light energy between the filaments deviates from the original beam profile. This transverse energy redistribution must be taken into account when the off-filament peak intensity is estimated.

For a situation resembling the present case there exist numerical simulations of nonlinear multifilamenting laser pulse propagation by Bergé, Skupin et al., backed by experimental data obtained with the Teramobile system (Bergé et al., 2004; Skupin et al., 2004a), from which an upper bound for this redistribution can be estimated. The initial beam profile entering these calculations was obtained from images of the original Teramobile output beam profile. Thus, the shape and the amplitude of initial modulations of the intensity profile, governing the initial phase of transverse energy redistribution are representative for the Teramobile output.

Calculations presented in (Bergé et al., 2004; Skupin et al., 2004a) were done for an initially collimated beam of diameter $D_{\mathrm{p}} = 5\,\mathrm{cm}$ for different chirped pulse durations and a pulse energy of $E_0 = 230\,\mathrm{mJ}$, as well as for a slightly focused ($f = 40\,\mathrm{m}$) beam, initially expanded to $d_{\mathrm{beam}} \approx 10\,\mathrm{cm}$, but only for one set of pulse parameters, $E_0 = 250\,\mathrm{mJ}$ and $\tau_{\mathrm{p}} = 100\,\mathrm{fs}$. In the focused case, due to the shorter focal length, the minimum achieved beam diameter was approximately only 1 cm. Because of this and the much higher pulse peak power than in the case of the configuration used in the present setup ($P/P_{\mathrm{crit}} \approx 760$ vs. $P/P_{\mathrm{crit}} \approx 83$ in the latter case) the evolution of the inter-filament transverse intensity distribution in the present longer focal length and 'low power' case with twice the effective beam waist more resembles the "low power filamentation regime" discussed in (Skupin et al., 2004a) for a collimated beam of diameter $d_{\mathrm{beam}} = 5\,\mathrm{cm}$, and laser pulse parameters of $\tau_{\mathrm{pulse}} = 600\,\mathrm{fs}$, and $E_{\mathrm{pulse}} = 230\,\mathrm{mJ}$.

According to the simulation results presented in (Skupin et al., 2004a) in this regime of laser pulse power, and even in the "high power filamentation regime", represented by $P/P_{\mathrm{crit}} = 760$, none of the regions of elevated intensity developing in between the filamentary hot spots ever exceeds the initial maximum intensity of the input beam profile by a factor of ≈ 2, along the entire length of propagation.

As a result, for a realistic worst-case estimate, the initially assumed flat inter-filamentary intensity distribution given by the previous geometrical estimation should be corrected by this factor of 2. Doing so does not essentially change the result: the corrected value of $\tilde{I}_{\mathrm{peak}} \approx 1.6 \times 10^{11}\,\mathrm{W/cm^2}$ still does not exceed the threshold for $D_{\mathrm{p}} = 100\,\mu\mathrm{m}$ droplets to ignite internal breakdown.

To allow for an order of magnitude of safety margin, again referring to Tab. 4.3.4, one should consider droplets larger than $20\,\mu\mathrm{m}$ to be potentially affected already by the non-filamenting part of the beam cross section. It is important to note that the definition of the threshold intensity for internal plasma formation in Tab. 4.3.4 corresponds to a value at which no notable emission of fragments can be observed in the experiment (Lindinger et al., 2004) (compare also Fig. 4.14).

In Tab. 5.2.5 the cumulative number of particles per $\mathrm{m^3}$ of air larger than a diameter $D_{\mathrm{p,min}}$ is

tabulated for the assumed model maritime size distribution. It can be seen from the observed droplet fragmentation dynamics reported in (Lindinger et al., 2004) that, just above threshold for optical breakdown, a large mother droplet emits only a limited number of much smaller fragments, and the largest part of the original mass remains in the mother droplet.

Such a fragmentation pattern, clearly distinct from the case well above threshold, strongly limits the relative change of the overall size distribution. For example, now considering Tab. 5.2.5, if each of the average two particles per m^{-3} of size $D_p > 50\,\mu m$ were to emit even on the order of a hundred of small fragments of micrometer size, this would cause a relative change of the particle count in the size range of the fragments on the order of 10^{-3} or less.

Summarizing, for the laser pulse and beam parameters in the present setup, the non-filament part of the beam cross-section can be considered neutral with respect to inducing fragmentation of watery aerosol particles in the relevant size range up to $D_p \approx 100\,\mu m$. As a consequence, the discussion of the direct effect of fragmentation on aerosol backscattering can be restricted to the filaments alone in which attained intensities reach three orders of magnitude higher levels than in the rest of the beam profile (Skupin et al., 2004a).

$D_{p,min}$ (μm)	$N_{D_p>D_{p,min}}$ (m^{-3})	$N^{beam}_{D_p>D_{p,min}}$ (m^{-1})
1	1.1×10^6	357
10	2900	0.9
20	170	0.05
50	2	0.0006
100	0.05	0.00002

Table 5.2.: Cumulative number $N_{D_p>D_{p,min}}$ of particles larger than $D_{p,min}$ per m^3 of air, and $N^{beam}_{D_p>D_{p,min}}$ contained in the Teramobile beam ($d = 20\,mm$) per meter of propagation, for the assumed maritime haze size distribution (Jaenicke, 1993) shown in Fig. 5.26.

Greater changes of the overall particle size distribution are expected in the case of efficient fragmentation, when most of the original volume of the mother droplet is split into many considerably smaller fragments. According to Tab. 4.3.4 , for a broad range of mother droplet sizes this regime of fragmentation should apply to the case of an impacting filament. It was discussed earlier why in this case the generic fragmentation model introduced in sec. 4.3 is considered adequate for estimating the spectrum of fragment sizes as a function of mother droplet diameter.

The expected relative change of backscattering of the model aerosol due to the modification of its size distribution caused by fragmentation is calculated using Eqs. 3.7 and 3.1, inserting the numerically computed Mie backscattering coefficient C_b. The corresponding backscattering efficiency factor $Q_b = C_b/(\pi D_p^2/4)$ is plotted in Fig. 5.27.

Specifically, the aerosol volume backscattering coefficients before and after the size distribution has changed due to fragmentation are evaluated according to

$$\beta_{A,before} = \int_{D_{min}}^{D_{max}} dD_p\; n(D_p)\, C_b(D_p) \tag{5.11}$$

$$\beta_{A,after} = \int_{D_{min}}^{D_{max}} dD_p\; \left(n(D_p) + \Delta n(D_p)\right) C_b(D_p), \tag{5.12}$$

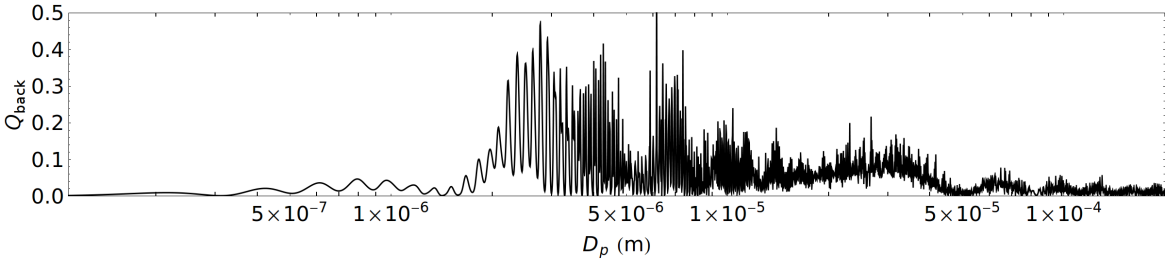

Figure 5.27.: Mie backscattering efficiency factor $Q_\mathrm{b} = C_\mathrm{b}/(\pi D_\mathrm{p}^2/4)$ for a wavelength of $\lambda = 532\,\mathrm{nm}$ and homogeneous spherical water droplets (refractive index $n = 1.337$) as a function f droplet diameter.

where $n(D_\mathrm{p})$ is the initial size distribution and $\Delta n(D_\mathrm{p})$ is its absolute change induced by fragmentation. Because of the mass conservation assumed in the applied estimation of fragmentation $\Delta n(D_\mathrm{p})$ obeys

$$0 = \Delta M_\mathrm{total} = \frac{\pi}{6}\int_{D_\mathrm{min}}^{D_\mathrm{max}} \mathrm{d}D_\mathrm{p}\; D_\mathrm{p}^3\,\Delta n(D_\mathrm{p}).$$

In reality some fraction of the droplet mass is sure to evaporate resulting in $\Delta M < 0$. This leads to a tendency to overestimate the post-fragmentation scattering cross section.

Finally the relative change of the backscattering coefficient is calculated:

$$\delta_{\beta\mathrm{A}} = \frac{\beta_\mathrm{A,after} - \beta_\mathrm{A,before}}{\beta_\mathrm{A,before}} = \frac{\beta_\mathrm{A,after}}{\beta_\mathrm{A,before}} - 1$$

The previous procedure applies to the backscattering properties of the fraction of the aerosol actually contained in the volume traversed by filaments, where the high intensities necessary for efficient explosive fragmentation are reached. Only afterwards this change is related to the overall probed volume contained in the visible LIDAR beam surrounding the filamenting Teramobile beam. This corresponds to finding the effective relative change of the *probed* aerosol backscattering coefficient

$$\delta_{\beta\mathrm{A}}^\mathrm{eff} = \frac{A_\mathrm{filaments}}{A_\mathrm{probed}}\delta_{\beta\mathrm{A}},$$

where $A_\mathrm{filaments}/A_\mathrm{probed}$ is the ratio of the filaments' total cross sectional area over that of the LIDAR probing beam.

Diameters reported in the literature for the cores of strong laser filaments generated from $\lambda_0 = 800\,\mathrm{nm}$ laser pulses range between $50\,\mu$m and $150\,\mu$m(Couairon and Mysyrowicz, 2007), depending on the precise conditions of pulse power and beam convergence. A commonly agreed value for filament diameters under typical multifilamenting conditions is $100\,\mu$m. In the present case where $20-30$ filaments could be observed at the position of strongest filamentation, a conservative estimate of the total beam area covered by filaments would be to assume 100 filaments with a diameter of $200\,\mu$m, resulting in $A_\mathrm{filaments}/A_\mathrm{probed} = 0.0025$. For determining the size distribution change $\Delta n(D_\mathrm{p})$ the estimated fragment size distribution n_frag is evaluated using Eq. 4.26 replacing n_mother by the maritime haze size distribution plotted in Fig. 5.26. Once n_frag is calculated, the resulting absolute

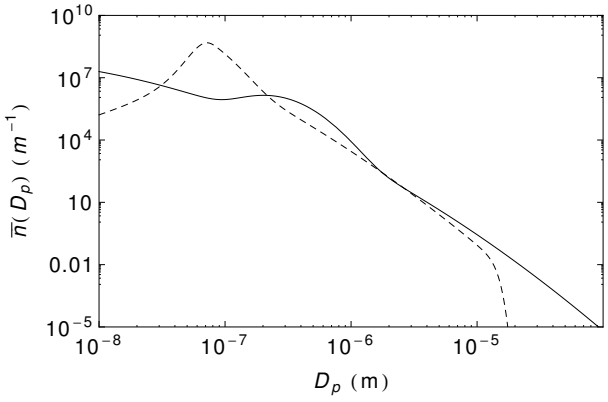

Figure 5.28.: Example for a calculated fragment size distribution (dashed) obtained from the maritime model distribution (solid) for a mean number of fragments per droplet of 480 and assuming all droplets larger than $D_\mathrm{p} = 0.5\,\mu$m undergo fragmentation. To avoid confusion: here the mother distribution has unit m^{-1} and is normalized to 1, in contrary to fig. 5.26.

	$D_{0,\mathrm{thresh}}$ (μm)					
$\bar{N}_\mathrm{frag}$	0.5	0.6	0.8	1	2	4
100	0.03	0.04	0.04	0.04	0.03	0.04
350	-0.01	0.01	0.05	0.05	0.04	0.05
820	-0.04	-0.01	0.03	0.05	0.04	0.05
1600	-0.05	-0.03	0.02	0.04	0.04	0.06
2700	-0.06	-0.03	0.02	0.04	0.04	0.05
4200	-0.07	-0.04	0.01	0.03	0.04	0.05
	$\delta_{\beta\mathrm{A}}^\mathrm{eff}$ (%)					

Table 5.3.: Estimated change in percent of the effective (probed) volume backscattering coefficient $\delta_{\beta\mathrm{A}}^\mathrm{eff}$ due to fragmentation of haze droplets impacted by filaments. $\bar{N}_\mathrm{frag}$ is the approximate mean number of fragments per droplet; $D_{0,\mathrm{thresh}}$ is the assumed minimum diameter necessary for fragmentation.

change of the mother size distribution, $\Delta n(D_\mathrm{p})$, results from counting all generated fragments positive and subtracting all fragmented mother droplets,

$$\Delta n(D_\mathrm{p}) = \begin{cases} n_\mathrm{frag}(D_\mathrm{p}) - n(D_\mathrm{p}) & \text{if } D_\mathrm{p} > D_{0,\mathrm{thresh}} \\ n_\mathrm{frag}(D_\mathrm{p}) & \text{otherwise} \end{cases}.$$

Then the relative change $\delta_{\beta\mathrm{A}}$ of the backscattering coefficient can be evaluated. This was done for different values of the dimensionless absorbed energy $\hat{E}_\mathrm{T}$ corresponding to mean fragment numbers per mother droplet between about 100 and 4000. Also the parameter $D_{0,\mathrm{thresh}}$ corresponding to the minimum diameter necessary for fragmentation was varied between $0.5\,\mu$ and $4\,\mu$m. This was done to explore the effect of a lower size limit of efficient fragmentation, as the estimated brakdown threshold intensity (see Tab. 4.3.4) approaches $I_\mathrm{thresh} \approx 10^{13}\,\mathrm{W/cm^2}$ for droplets below $D_\mathrm{p} \approx 1\,\mu$m size, which is in the range of reported values attained in filament cores in air (Couairon and Mysyrowicz, 2007).

In Tab. 5.3 the calculated effective (probed) $\delta_{\beta\mathrm{A}}^\mathrm{eff}$ for the overestimated 100 filaments of diameter $200\,\mu$m is displayed. The result of the estimation is an expected fragmentation-related relative change of the effective volume backscattering coefficient generally below 0.1 %. If smallest droplets are

assumed to fragment, and for larger average numbers of fragments, the effect may even be a reduction of the backscattering coefficient. Under most conditions, backscattering is slightly enhanced. The dependence on the average number of fragments becomes weaker the larger the assumed threshold droplet diameter for fragmentation.

Based on the estimation, it can be concluded that fragmentation of the background haze most probably cannot explain the observed change of atmospheric backscattering.

On the other hand side it becomes evident from the results of the preceding discussion that fragmentation is sure to have a very substantial effect as soon as large drops are present in the filamenting laser beam, which was not the case under the high visibility, very thin haze conditions. If these large droplets should efficiently fragment outside of genuine filaments, but throughout the whole beam cross sectional area, the expected resulting effect on the volume backscattering coefficient would dominate. Under such conditions the detection of any weaker effect by LIDAR appears hardly feasible.

Filament-induced thermal lensing

Another effect which could lead to an apparent laser-induced change of atmospheric backscattering is related to the transient change of the optical properties of the air, which could be caused by the influence of the filaments, and which may affect the propagation of the light in the LIDAR probing beam. Refractive index changes due to the instantaneous or delayed Kerr effect or due to the free electrons of the plasma channels left behind by the filaments are unimportant here, as they only affect time scales between the laser pulse duration in the former case, and a few nanoseconds, the typical time of the electrons in the filament plasma to undergo recombination or attachment to molecular oxygen (Tzortzakis et al., 2000), in the latter.

However, filaments deposit some amount of energy, mainly in the form of electronic excitation, which is eventually converted to heat. Consequently filaments leave behind meter long tracks of air at a temperature above that of the surrounding. The result is a transient lowering of the air density along the former plasma channels, with a consequent lowering of the refractive index.

The absolute amplitude of the induced index change is small (at the very maximum it could be on the order of $n_{\mathrm{air}} - n_{\mathrm{vacuum}} \lessapprox 3 \times 10^{-4}$). Despite its smallness, prior to being warped and literally blown apart by turbulent mixing with the surrounding air it is well localized along an extended straight path. This is why its potential effect on the propagation of a trailing probe beam should be assessed in the present situation.

From interferometric measurements it is known that the peak temperature of the air in the wake of a representative 800 nm laser filament is about 100 K above ambient and its approximately Gaussian transverse profile has a full width at half maximum (FWHM) of 100 μm. Adiabatic expansion and formation of a shock front occur during about the initial 100 nanoseconds after the passage of the laser pulse, leaving a density depression of about the same diameter as the initial profile of elevated temperature.

As the thermal diffusivity of air $\alpha_{\mathrm{air}} = k_{\mathrm{air}}/(c_{\mathrm{p,air}}\rho_{\mathrm{air}}) \approx 2{\times}10^{-5}\,\mathrm{m^2 s^{-1}}$ (with $k_{\mathrm{air}} \approx 0.024\,\mathrm{J m^{-1} s^{-1} K^{-1}}$

the thermal conductivity, $\rho_{\text{air}} \approx 1290\,\text{kgm}^{-3}$ the density, and $c_{\text{p,air}}$ the specific heat at constant pressure of air, at $T = 273\,\text{K}$ and normal pressure), and the width parameter of the assumed Gaussian temperature distribution increases as $\sigma(t) = \sqrt{\sigma_0^2 + 2\,\alpha_{\text{air}}\,t}$, heat diffusion then flattens out the initial temperature profile relatively slowly. For $t \approx 1\,\text{ms}$ this results in approximately doubling the initial diameter of the density depression of $\approx 100\,\mu\text{m}$.

Here also the induced thermal lens after the millisecond delay is approximated by a Gaussian-shaped refractive index depression. In the present situation this is justified, because the compression wave emitted during the initial fast expansion of the heated channel (Tzortzakis et al., 2001) propagates at the speed of sound, and is outside the observed volume at a time greater than 1 ms after the filament has passed. Then the reduced density of air n_{hot} in the heated region is approximated using the ideal gas law $\frac{\rho_{\text{hot}}}{\rho_0} = \frac{T_0}{T_{\text{hot}}}$, and

$$n_{\text{hot}} = 1 + (n_0 - 1)\left(1 + \left(\frac{T_{\text{hot}}}{T_0} - 1\right)\exp\left\{-\frac{r^2}{2\,\sigma^2}\right\}\right)$$

where n_0 and T_0 are refractive index and temperature of the cooler ambient air, and σ is the $1/e$ width parameter of the radial Gaussian temperature profile. The effect of the heated column of air on light propagation can be thought of as that of a long gradient index lens with a Gaussian radial index modulation.

As the amplitude of the modulation is small and the diameter of the hot air column is considerably larger than a wavelength, its effect on probe laser propagation can be approximately described by ray optics. The general ray equation for the propagation in an inhomogeneous optical medium reads (Born and Wolf, 1993)

$$\frac{\mathrm{d}}{\mathrm{d}s}\left(n(\mathbf{r})\frac{\mathrm{d}\mathbf{r}}{\mathrm{d}s}\right) = \nabla n(\mathbf{r}),$$

where $\mathbf{r}(s)$ is the position vector along the ray parametrized by the coordinate s, and $n(\mathbf{r})$ is the spatially inhomogeneous refractive index.

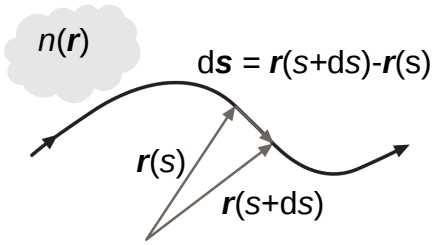

Figure 5.29.: Ray propagating in an inhomogeneous optical medium with position-dependent refractive index $n(\mathbf{r})$, illustrating Eq. 5.2.5; based on a figure from (Träger, 2007).

The radial symmetry of the presently assumed index profile allows to effectively solve the differential equation just for one transverse dimension,

$$\frac{\mathrm{d}^2 x}{\mathrm{d}\tau^2} = \frac{\partial}{\partial x}\left(\frac{1}{2}n^2(\mathbf{r})\right),$$

$$\text{where} \quad \mathrm{d}\tau = \frac{1}{n(\mathbf{r})}\mathrm{d}s, \quad \mathrm{d}s = \sqrt{\mathrm{d}x^2 + \mathrm{d}y^2 + \mathrm{d}z^2},$$

if the contribution of each ray is weighted according to the amount of light flux it represents.

As the refractive index is very close to $n = 1$ and the expected angular deviations of rays from the optical axis are small, in this estimation the approximation $\mathrm{d}\tau \approx \mathrm{d}z$ is applied.

Rays are weighted by partitioning the probing LIDAR beam into concentric rings of inner radius r_i and outer radius $r_i + \Delta r$, where Δr is sufficiently small, and $r_i = i\Delta r$. Approximating the LIDAR beam profile as flat top circular (here of diameter 4 cm) centered around the axis $r = 0$, the total flux of light transmitted through its entire cross sectional area is thus proportional to $\sum_{i=0}^{r_{\mathrm{beam}}/\Delta r} 2\pi\ r_i\ \Delta r$.

The ray launched at a distance r_i from the optical axis (and parallel to it) represents the ring of inner radius r_i and the corresponding transmitted light flux proportional to its cross sectional area $A_{\mathrm{ring},i} = 2\pi r_i \Delta r$.

For simplicity firstly only one channel of hot air is considered, centered in the telescope FOV. This assumption is approximately fulfilled by all filaments, as the telescope FOV is about ten times larger than the filamenting beam diameter. The fraction of light lost from the detection cone is obtained by determining the rays that are deflected out of it by the on-axis hot air channel, and relating the lost light flux, calculated analogously, to the previously determined total flux in the beam. This procedure yields an estimation of the fractional loss of light induced by refraction in the hot air column of the filament, and thus its closely related effective scattering cross section.

In order to estimate an upper boundary of the impact of the filament-induced thermal lens on the propagation of the trailing LIDAR probe pulse, and in consequence on the LIDAR return signal, again a worst case scenario is constructed. In the estimation hot channel diameters of 100 μm and 200 μm are assumed. They represent full width at half maximum (FWHM) parameters of the Gaussian radial temperature profile assumed to peak at the measured maximum 100 K above ambient (Tzortzakis et al., 2001).

The single hot air channel is assumed to start at a range of 60 m, and the range-dependent diameter of the receiving telescope field of view is calculated from its known divergence angle.

Traced rays are launched parallel to the axis of the filament-heated air volume, and the amount of probe light lost from the detection FOV is determined for continuously varying propagated distance.

In Fig. 5.30 the result of the calculation is shown. The plotted graphs correspond to channel diameters of 100 μm and 200 μm, and peak temperatures of 100 K, 80 K, 60 K, and 40 K above ambient, respectively.

It can be seen from the plots that, under the conditions and geometry of the actual experiment, filament-induced thermal lensing is expected to cause loss of LIDAR signal starting from a distance of at least about 16 m from the filament start, and in the case of strongest channel heating. This distance corresponds to about half the extent of the range interval of optimum overlap, and, in this particular case, the thermal lens-induced loss of probing light starts just beyond its far edge (the assumed starting point of the filament at a distance of 60 m is in its center).

The distance from which loss occurs is apparently independent on the diameter of the hot channel, but only depends on its peak temperature. The diameter on the other hand side is important for the amount of light lost at a given distance from the beginning of the hot air column.

The worst case estimate shows that the weak thermal lenses that result from the radial temperature

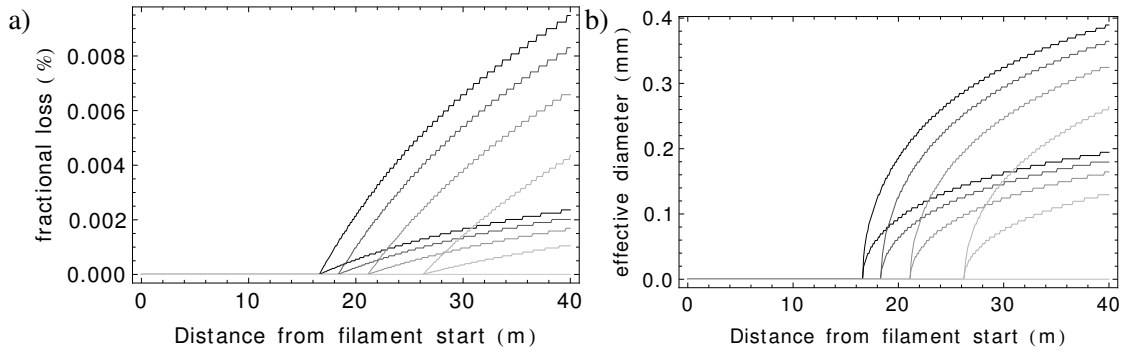

Figure 5.30.: a) Fractional loss of LIDAR probing laser light out of the beam due to action of the filament-induced thermal lens in air, and b) its corresponding effective diameter, plotted as a function of propagation distance relative to the starting point of the filament. The effective diameter is the diameter of an equivalent absorbing disk placed at the position of the filament start, removing the same amount of light from the laser beam (i.e. the detection cone) as the thermal lens. The calculation assumes an axially symmetric index dip with Gaussian shape, representing the hot air column starting at a distance of 60 m from the detection telescope, and a LIDAR configuration as described earlier in the text. Plots show results for channel diameters of 100 μm and 200 μm (upper and lower branches of same shading, respectively), and peak temperatures of 100 K, 80 K, 60 K, and 40 K above ambient (black to light gray).

gradients left behind by laser filaments can in principle affect the LIDAR return picked up by the detection system as used in the present experiment. The fraction of probing light lost from the detection field of view at maximum is on the order of 0.001 % ... 0.007 % per filament (that is, for the propagated distance from filament start of 30 m corresponding to a filament starting right at the beginning of the interval of best overlap). For the 20 to 30 filaments present in the beam this means a signal loss of about 0.02 % ... 0.2 %, approaching the magnitude of the identified effect but remaining below even under almost unrealistic worst case conditions.

It must also be kept in mind that the required distances of propagation along a perfectly straight undisturbed hot air column exceeds typical values reported for the lengths of contiguous filament-generated plasma columns in air, which are on the order of a few meters (Couairon and Mysyrowicz, 2007). This emphasizes the worst case character of the estimation and suggests that in reality thermal lensing of filament-induced hot air channels is way less important, at least in the present situation.

Irrespective of the magnitude of the effect it is obvious from the start that the inward temperature gradient causes near-forward scattering leading to effective *loss* of light from the detection volume. The corresponding additional extinction, if present in the raw LIDAR return, would cause an apparent filament induced *reduction* of the volume backscattering coefficient in the evaluation procedure described above.

To summarize, an effect of thermal lensing may possibly be picked up under the conditions of the experiment, but it is expected to be too small to be clearly identifiable. More importantly, even if present, it should appear as a reduction of backscattering, and thus cannot be made responsible for any observed enhancement. Because of the fluctuation of filament strength and position in a multifilamenting beam, and most of all because of different random warping due to air turbulence of

the initially straight hot channels shot to shot, it is likely to constitute another source of measurement noise, though.

Signature of meteorological trends

Looking at Fig. 5.22 the question arises why the laser effect so abruptly dropped below the noise level. Examination of the data shows that the time interval of about ±3 min around 06:32 AM was especially 'quiet', meaning that the variance of the fluctuations of $\langle F(r) \rangle$ around the moving average was almost constant at a relatively low level. This behaviour went hand in hand with the dropoff of the laser effect.

Comparison with the meteorological observations shows that the fading of laser effect was strikingly coincident with the time of maximum visibility and minimum overall LIDAR signal strength (see Figs. 5.20 and 5.21).

In Sec. 5.2.4 the close correlation between atmospheric scattering and various meteorological parameters during the time of experiment was already discussed. Comparison of Figs. 5.18, 5.19, and 5.20, shows that the fading of the backscattering-enhancing laser effect was accompanied by the onset of respective new trends in background atmospheric backscattering, wind speed, wind direction, temperature, and relative humidity, which could be observed after slightly varying short delays.

This leads to the interpretation that the time of minimum total backscattering coincides with the moment at which a different air mass started to gain influence. This air mass was distinguished from the previous one by even higher relative humidity, slightly lower temperature, and, according to the LIDAR data and the visibility measurement, higher aerosol content. The additional aerosol was very likely water haze precursing the sleet that eventually set an end to the measurement. In the light of these observations a considerable change of laser effect at the observed time is most likely related to meteorological processes.

Summary

The simple multiplication of scatterers by fragmentation could be shown to be of minor importance under clear atmospheric conditions. Also thermal lensing induced by the filament traces cannot be made responsible for any observed increase of backscattering. Thus, the chances increase to have observed an actual and non-trivial increase of the number of aerosol scatterers and/or an increase of the scattering efficiency of existing aerosol particles caused by condensation of vapour out of the gas phase.

Indication for a less trivial role of fragmentation and evaporation of existing aerosol, more precisely, the accompanying formation of locally elevated densities of excited or ionized molecules, was found in the diffusion cloud chamber experiment described in a previous section. There, the formation and growth of new scatterers could be seen to be enhanced around what was supposed to be plumes of fragmented droplets hit by a filament. A similar role could be played by preexisting aerosol in the natural atmosphere, however the presence of even modest levels of background scattering was found to cause too much LIDAR signal variability to be able to isolate a possibly present effect of

the filamenting beam, at least using the presently available detection system. Thus there remain open questions regarding the origin of the observed weak enhancement of backscattering.

The fact that the observability of an effect of the filamenting beam on atmospheric scattering by LIDAR was limited to conditions of exceptionally low background scattering does not necessarily mean that these are the only conditions under which filament-induced condensation can possibly happen. It mainly indicates that a number of noise sources which are of lesser impact in classical aerosol LIDAR have to be dealt with in this new scheme. To continue the development of this new kind of active atmospheric remote sensing, these noise sources, mainly related to atmospheric turbulence, but also the uncertain and fluctuating properties of the filaments in the beam, would have to be better controlled.

Technical issues related to the special requirements towards the LIDAR setup, especially to the needed high quality single-shot performance, would have to be solved. Highest possible dynamic range and accuracy of both detector and data acquisition would have to be provided, and as importantly, the probing LIDAR laser pulse energy would have to be stable, or at least accurately known to the sub-percent level.

The impact of turbulence may be reduced by acquiring LIDAR signals at much higher rate, probably as high as a kilohertz, in order to gain full information about the time dependence of the turbulence induced fluctuations of the background scattering. Alternatively one could use a two beam LIDAR transmission setup where two independent probing laser pulses, in shortest possible temporal succession, sweep out slightly offset volumes, only one of them containing the filamenting beam, and the other, propagating slightly shifted, serving as the reference. Such a scheme could provide for a more accurate reference signal without the need for a full high repetition rate LIDAR transmission and detection system, as both probing beams would ‘see’ approximately the same turbulent modulations of the scattering atmosphere.

The relatively poor knowledge about the prevailing background aerosol obtainable by LIDAR poses a source of uncertainty inherent in this detection scheme, which can be reduced but not eliminated by using, for instance, multiple wavelengths for probing atmospheric scattering.

Improvements may as well be necessary with regard to the system for creating the filamenting laser radiation. The means to actively control high power multiple filamentation are still not advanced enough to precisely set the filament properties in a high power multifilamenting laser beam. Being able to control for instance the exact position of filamentation onset on a shot-by-shot basis would provide additional means to better discriminate filament-induced effects from random background fluctuations. Another couple of ‘simple’ parameters to be changed are the pulse energy and repetition rate of the laser system providing the filamenting beam. The cloud chamber experiments (Sec. 5.1) indicate a considerable enhancement of filament-induced water condensation when multiple successive laser shots are applied. It may turn out that to achieve sufficiently massive particle formation and growth to be optically discriminated from background scattering in a less clear atmosphere the 10 Hz repetition rate of the Teramobile laser system is plainly not enough.

Summarizing, in this section the realization of an active differential backscattering LIDAR scheme was described, and a strategy for the evaluation of the acquired data strongly affected by noise of

mostly atmospheric origin, containing a weak signal, was formulated. A just detectable increase of atmospheric backscattering induced by a filamenting terawatt laser beam could be observed in one occasion during the campaign, characterized by the unusual combination of an exceptionally low background of aerosol scattering and at the same time a high relative humidity. While useful for identifying the difficulties which have to be mastered before this scheme could be used as a tool for probing the atmosphere, the experiences made during the campaign indicate that, for actually learning more about the atmospheric condensation of water induced by laser filaments, a different approach should be taken first.

5.3. In situ observations of particle production in real atmosphere

The goal of the subsequently described experimental campaign was to eventually explore and characterize filament-induced condensation under natural atmospheric conditions, while avoiding the many unknowns involved in real scale atmospheric LIDAR, and especially reducing the fraction of potential measurement time lost because of unfavourable weather.

Motivated by what was learned from the cloud chamber experiments, and also because the natural conditions of temperature and humidity permitted it, the measurement method was not a priori restricted to relatively large working distance optical detection, but could be chosen freely, aiming on increased sensitivity for all potentially relevant particle sizes. The results obtained with the subsaturated cloud chamber #2 had shown that the action filaments can induce the formation and growth of droplets already in subsaturated atmospheres, which can become massive when the water vapour concentration is very high. Not even invoking the singular observation from the LIDAR experiment, it was almost certain that some signature of filament-induced particle formation would be observable under not too extreme natural atmospheric conditions.

5.3.1. Experimental setup

In order to have the chance to measure during periods of elevated atmospheric humidity as often as possible the Teramobile container was placed on a pier on the Rhone, located on the site of a waste water plant at Aïre run by the city of Geneva.

The river coming from Lake Geneva was supposed to act as a water vapour reservoir, providing humidity independent of the weather conditions. It was also expected to act as heat reservoir even at lower air temperatures, pushing air saturation with water vapour close to 100 %. The hope was to have more occasions to experiment under expectedly favourable atmospheric conditions than at the previous experimental site in Berlin.

The campaign spanned the time between autumn 2009 and spring 2010, allowing to examine very different combinations of temperature, humidity, but also chemical composition of the ambient air as well as its aerosol content. The resulting data spans 133 hours in total sampled in 28 sessions.

The aim was to get as direct and detailed information about possibly generated aerosol as possible, and to be able to characterize it also by single particle sensitive methods, not just by its averaged

scattering properties. To avoid the imponderables and difficulties of remote detection which were encountered in the preceding Berlin campaign, and to be able to directly sample the air possibly created particles.

A box was used to protect the sampling volume against wind. In initially experiments the box of the diffusion cloud chamber was reused, because it was already equipped with ports for optical access. Later it was replaced by a less bulky box ($32 \times 36 \times 56\,\mathrm{cm}^3$). In either case the front and back ports of the boxes were kept open to allow for continuous air exchange with the outside. Besides shielding against wind the box allowed to have well defined 'filament affected' and 'filament unaffected' air sampling inlets while keeping pipe lengths short. Any effect of the box other than ensuring some amount of wind protection and thus stabilization of the observed signal was ruled out.

The instruments used for in situ sampling of aerosol size distributions were an aerosol spectrometer (Grimm Aerosol Technik EDM 107) based on the measurement of the single particle light scattering cross section, and a nanoparticle sizer (Grimm Nanocheck 1.320) working on the principle of diffusion charging of aerosol particles.

The EDM 107 classifies single particles traversing a diode laser beam according to the intensity of the flash of light scattered into an angular range of about ±30 degrees around the perpendicular direction, the laser beam lying in the scattering plane. The corresponding electrical pulses are discriminated according to their height and classified in 31 discrete bins. The instrument handles partially volatile aerosol by maintaining precisely controlled internal conditions of temperature and humidity. It covers a diameter range between 230 nm and 32 μm.

Smaller particles can be detected with the Nanocheck instrument, attached downstream the EDM 107, in which the collected aerosol is charged by passing through a corona discharge. A proprietary measurement scheme allows the instrument to simultaneously detect the total particle concentration ($500\,\mathrm{cm}^{-3}$ to $5 \times 10^5\,\mathrm{cm}^{-3}$) and the particle mean diameter in a range between 25 nm and 300 nm. In order to make sure that no measurement artefact results from possibly precharged aerosol particles a condensation particle counter (TSI model 3007) was used for cross checking. In this instrument particles in a laminar air flow grow to optically detectable sizes by supersaturating the air with isopropanol. According to the manufacturer the smallest detectable size is 10 nm.

Air was sampled typically 2 cm below the Teramobile laser beam, as well as outside the shielding box at the same height above ground. Data from the Nanocheck instrument is available for less sessions than it is from the EDM 107 particle counter because the former instrument was only available during part of the campaign.

The Geneva Teramobile team carried out further valuable investigations to determine the nature of the particles detected by the counters. They used an ionic chromatograph (Dionex ICS 3000) to analyze the water-soluble fraction of aerosol collected on track-etched polycarbonate membrane filters (Nuclepore) with pore sizes of 15 nm, 50 nm, and 1 μm, respectively. The EDM 107 instrument provided an internal filter holder for this purpose.

In laboratory experiments involving the stationary Helvetera amplifier system they used a ozone analyzer (Horiba APOA-350E), measuring absorption of UV light, and a chemiluminescence-based NOx analyzer (Monitor laboratories 8840)(Petit et al., 2010).

In a series of sessions of the real atmosphere experiments, conceptually equivalent instruments were used to monitor the same trace gases in the vicinity of the filaments inside the shielding box. Although designed for long term environmental monitoring the ozone analyzer (UV Photometric Analyser Model 49, Thermo Environmental Instruments Inc.) and the NO_2/NO analyzer (AC 31 M, Environnement S.A.) had reasonably short reaction times of 20 s and 15 s, respectively.

To have most convenient access to the Teramobile laser beam it was expanded to a diameter of about 10 cm and guided out of the side exit port onto a large periscope, lowering the beam to a height of about 1.2 m and sending it towards the instrumented wind shielding box located at a distance of approximately 15 m. In general the laser beam was sent slightly focused to place the onset of filamentation a few meters before the experiment setup, yielding about 10 strong filaments close to the inlet of the particle counters.

During the campaign the Teramobile laser pulse energy was limited to about 160 mJ because the pump laser of the first amplification stage was operating below its specified performance. The pulse energy was however sufficient to generate sufficiently strong and many filaments for the present experimental setup.

5.3.2. Results

The most important and initially surprising result obtained during the Aïre campaign is the eventual proof that laser filaments are able to induce condensation of particles up to micrometer size at water vapour saturation ratios far below saturation.

The detected number of sub-300 nm particles typically increased by a factor of 5-10, while the number of additionally detected larger particles increased by up to about 30 %, dependent on the environmental conditions.

In Figure 5.31 the outcome of a typical measurement sequence under manifestly water-subsaturated conditions is shown. The curves show the particle mass concentrations determined by the EDM 107 and Nanocheck instruments, alternatively sampling air affected by the filamenting laser beam (shaded background) as well as unaffected by it. In this plot the data are presented in terms of standard 'Particulate Matter' (PM) values which are commonly used to quantify dust and particulate aerosol in the context of air quality assessment. To a good approximation they reflect the integrated mass per unit volume present as particles of an aerodynamical diameter smaller than the size (in micrometers) indicated by the index. The figure thus gives an impression of the laser effect on the accumulated condensed mass. A clear synchronicity of signal change with the switching between the sampling inlets can be seen in all included PM classes.

Although the amplitude of the signal of the Nanocheck instrument looks most impressive, the accumulated additional mass condensed due to influence of the laser in the corresponding size interval (25 nm–300 nm) is small. This is reflected in the comparatively small amplitude of the PM1 signal (relative to the background mass concentration in this class). It is important to note that the relative humidity at the time of this particular measurement was only 75 %. It will be seen later that these additional particles, showing up in this size range up to 200 nm, are quite stable and may have the

potential to grow larger once the ambient relative humidity rises.

Three examples of particularly efficient production of larger particles are shown in Fig. 5.32. The relative change $n_f(D_p)/n_0(D_p)$ of the size distributions obtained by the EDM 107 instrument are plotted vs. the particle diameters, where the indices 'f' and '0' mean 'affected by the filamenting beam' and 'unaffected', respectively.

Panel a) shows the overview up to very large particle sizes. Above $D_p \approx 4\,\mu$m their number concentrations ranged between a few to a few tens per cm^3, and the sometimes large amplitudes of the relative changes correspond to just a few additional counts. In the present example, below about $D_p = 1.5\,\mu$m between typically 100 and 1000 cm^{-3} particles were counted, and the corresponding relative changes represent relatively good statistical averages.

Note that these specific samples do not show any obvious dependence on the environmental conditions. In addition to showing random variability especially affecting the larger size classes, the samples were measured at different days and at different times of day, with consequences for other parameters influencing the magnitude of the filament effect, also dependent on the particle size under consideration, which will be discussed in the following.

A grand overview of the laser effect on the number of particles in different size intervals is presented in Fig. 5.3.2, comprising sampling data from the Nanocheck instrument together with EDM 107 data. The originally 31 size channels of the EDM 107 instrument were summed to effective 5 larger classes in order to make the figure more readable. Every data point in each panel represents the cycle-averaged net change of particle counts, comparing laser-affected with laser-unaffected samples, for the respective conditions. One cycle corresponds to a pair of gray and white bars along the time axis of Fig. 5.31. Each individual measurement (that is, each complete cycle) corresponds to a point in a multidimensional parameter space. Each column in the grid of panels shown in Fig. 5.3.2 projects

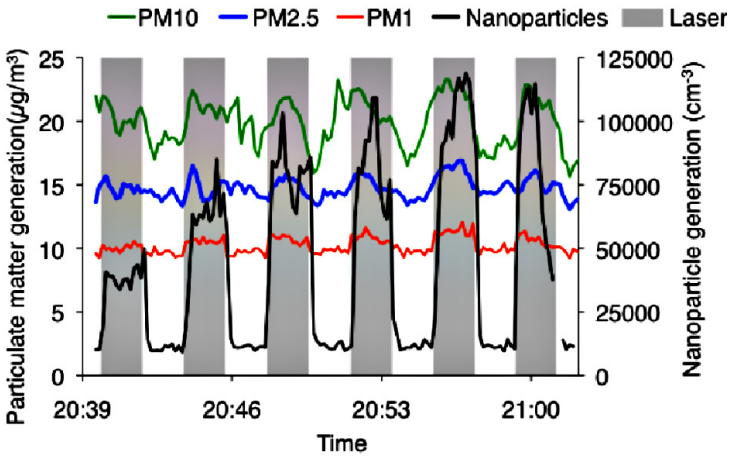

Figure 5.31.: Typical particle sizer signals clearly showing laser induced particle formation under conditions of water vapor subsaturation (RH=75 %, T=13 °C). Data are presented as standard PM values PM10, PM2.5, and PM1 (see text) for the optically detectable size ranges, and in terms of number concentration for the size interval between 25 nm and 300 nm measured by diffusion charging.

the measured data on a different parameter coordinate (temperature, relative humidity, water vapour mass concentration, and SO_2 concentration, respectively), while each row corresponds to a different size class.

It is readily seen in Fig. 5.3.2 that, independent of size class, the majority of points lies above zero, showing that filament induced condensation happens under very general environmental conditions, however varying in efficiency. Obviously the data show strong random variability, but the shapes of the point clouds already visually suggest certain correlations between the 'laser effect' on particle counts and environmental conditions. In some cases the effect appears to be practically quenched when a parameter exceeds a certain threshold value, for example the production of smallest particles at the lowest assumed values of RH of about 20 % (topmost panels b,f,j in the second column).

The figure contains even more information: comparing panels from different rows of a single column, in some cases a reversal of trend can be observed starting from some specific pivot size class, that is, the sign of the apparent correlation may change when going from small to larger particle sizes, moving down in a specific column. For example, the apparent anticorrelation with temperature (first column) of the laser effect for particles up to the 325 nm interval (panel (i)) seems to gradually turn into a positive correlation most pronounced in the size class of largest diameters (panel (u)). The opposite is seen for the dependence on relative humidity (compare first and second columns). Indeed, the point clouds in panels corresponding to the same size classes are almost mirror symmetric, indicating a (not surprising) anticorrelation of both quantities.

The visually apparent trends also show up when the sample correlation coefficients of the laser effect in the individual size classes (of the EDM 107 instrument) and the respective environmental parameters are plotted as in Fig. 5.34. Relative humidity is positively correlated with the generation of particles below $D_p \approx 400$ nm, and negatively correlated for larger diameters. Correlations with temperature and water vapour concentration follow a different pattern, where temperature correlations are practically opposite with respect to those of the RH, and almost no correlation is found with water vapour concentration throughout the interval of particle sizes between about $D_p \approx 600$ nm and $D_p \approx 3\,\mu$m.

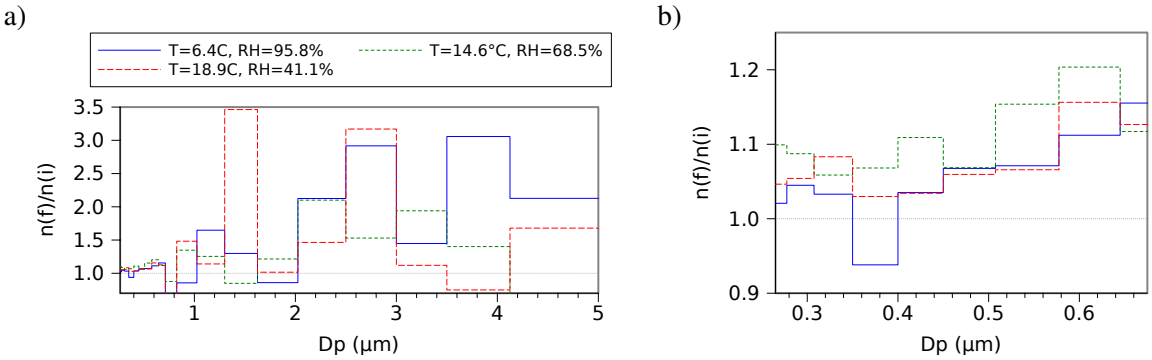

Figure 5.32.: Examples for the relative change of the measured particle concentrations as a function of diameter, comparing aerosol samples affected by laser filaments vs. unaffected samples. Panel b) shows a closeup of the smaller size channels, showing a systematic increase of particle number by about 5 % to 10 %.

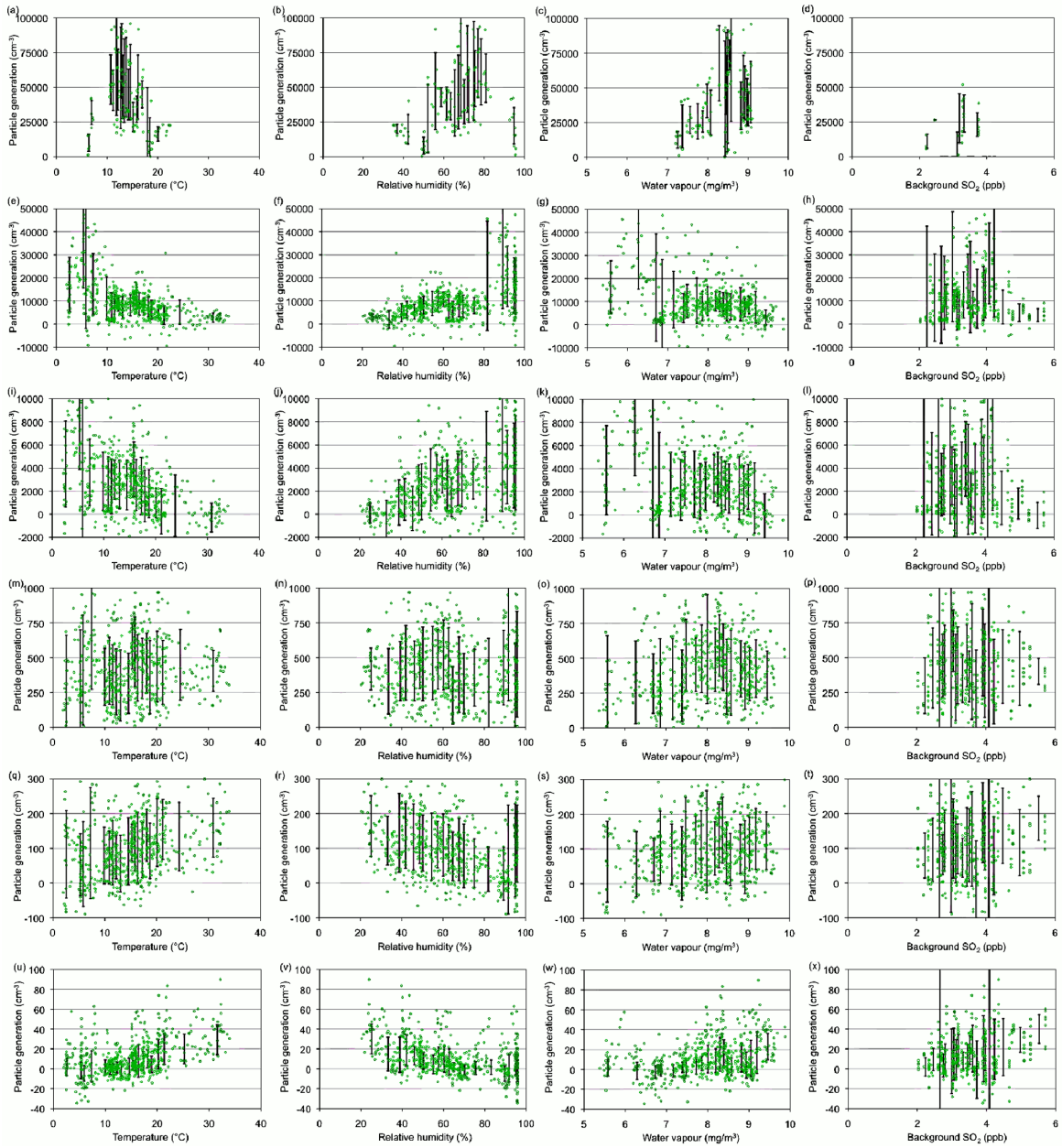

Figure 5.33.: Projections of differential particle concentration measurements (comparison of laser affected samples with corresponding laser unaffected samples) for all available experimental data. Rows top to bottom: Nanocheck data (25 nm–300 nm), EDM 107 data (265 nm $\leq D_p <$ 325 nm, 325 nm $\leq D_p <$ 540 nm, 540 nm $\leq D_p <$ 1.15 μm, 1.15 μm $\leq D_p <$ 4.5 μm, 4.5 μm $\leq D_p <$ 32 μm). Columns: projections on different parameter coordinates (temperature, relative humidity, water vapour mass concentration, SO_2 concentration). Representative error bars illustrate the local scatter of the data points. They correspond to the standard deviations of chunks of data each containing 5 % of the data points.

Although not plotted in Fig. 5.34, there is a strong positive correlation between the generation of particles detected by the Nanocheck instrument and relative as well as absolute humidity. Somewhere in the range between D_p = 265 nm, which is the lower end of the detection range of the optical particle counter, and D_p = 1 μm the sign of the correlation with absolute humidity reverses.

Some features visible in the data presented in Fig. 5.3.2 are missed when forming the correlation coefficients, and Fig. 5.34 must be interpreted with a bit of caution. The notable rise of particle production in most size bins when RH exceeds about 80 % is a priori discarded by computing a linear correlation, but it may have essential physical meaning, as it will turn out subsequently. To be sure that the filaments actually caused condensation, that is net production of new particles and/or growth of existing ones, it is important to certify that the appearance of nanometric particles and at the same time a reduction of particle counts in the intermediate size range is not caused simply by fragmentation of background aerosol due to influence of the laser. This is why it is important to note that actually no correlation of the laser effect with the background concentration of particles could be detected in the data.

It can be observed that, as expected, the size distribution of the background aerosol varies with the environmental conditions, causing corresponding correlations observable in the data of individual size channels. Especially relative humidity is expected to have an effect, as it determines the equilibrium sizes of wettable and soluble aerosol particles of the background aerosol. The recorded data show no correlation with relative or absolute humidity of larger size channels (D_p > 500 nm), while such correlations exist for the smaller size channels. Considering this it is interesting to note that the signals in size channels below 500 nm recorded from the background aerosol show opposite signs of correlation with relative and absolute humidity than those from the filament-affected aerosol. Although difficult to interpret, this observation somehow indicates that the particles created by the filaments may have properties quite different from the background aerosol.

Trace gas measurements sampling air close to the filaments in the wind shielding box were conducted simultaneously with aerosol sampling during one early series of outdoor experiments. They showed high concentrations of O_3, NO and NO_2 as soon as filaments were present. The production rate of these gases was found to be independent of temperature and humidity and amounted to typically 200 ppb, 25 ppb and 1 ppb for the respective gases, where especially the O_3 concentration

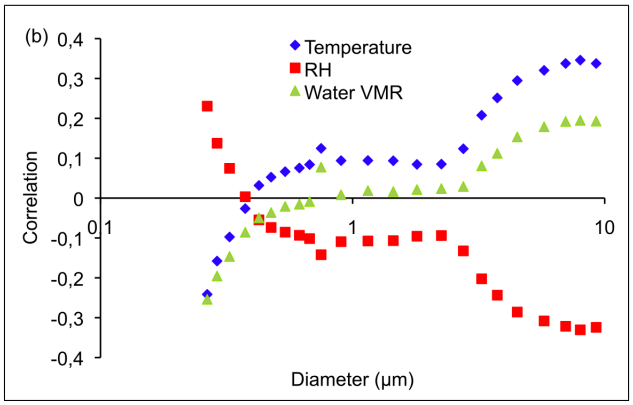

Figure 5.34.: Correlation of the laser effect with environmental parameters, plotted individually for each size class.

exhibited a large random variability between approximately 100 ppb and 300 ppb. The measured NO_2 concentrations scattered about half as much about the mean. Note that these are the steady state concentrations after typically 2 min of continuously firing the laser at 10 Hz repetition rate.

A clear and close relationship between trace gas concentrations and the number density of small particles sampled by the Nanocheck instrument were observable. In Fig. 5.35 the time dependent decay of sampled trace gas concentrations and nanoparticle number density with time is shown, starting from about the time when the Teramobile laser was stopped after a phase of continuous firing. Because the air in the shielding box cannot be assumed homogeneously mixed at all times,

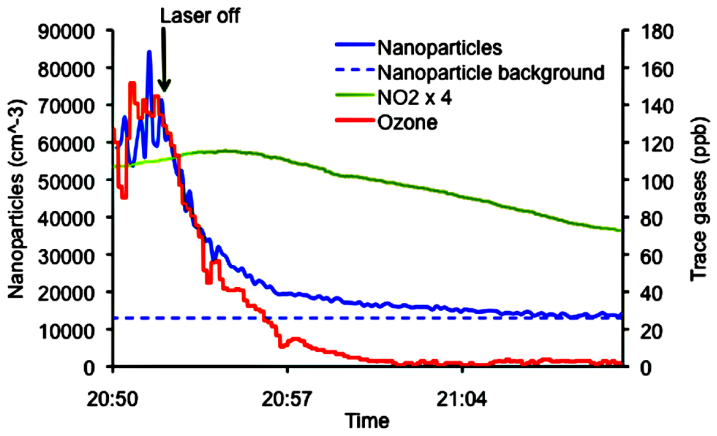

Figure 5.35.: Typical decay of nanoparticle number concentration and trace gas volume concentrations sampled close to the filamenting beam shortly before and after the laser is switched off (time indicated by vertical arrow).

it is difficult to separate effects of local sampling, effective dilution with air entering via the ports of the box, and consumption by chemical reactions. It is however evident that NO_2 concentration peaks at a retarded time, which can be explained by an ongoing production. Also, assuming that the non-sedimenting nanoparticles of 25 nm mean diameter freely drift with the motion of the air, the effects of local sampling and turbulent dilution should lead to similar curve shapes of ozone and nanoparticle concentrations. Apparently ozone decays faster, meaning that it is consumed, likely for the benefit of NO_2.

In order to quantify the amounts of these gases generated in laser filaments, without the mentioned uncertainties, an indoor laboratory experiment was designed by the Geneva Teramobile team (Petit et al., 2010). They were able to show that filaments created with near infrared sub-picosecond laser pulses generate unexpectedly large amounts of ozone and oxides of nitrogen. Filaments were created in a Plexiglass pipe used as a flow cell, and the volume averaged concentrations of ozone (O_3), nitric oxide (NO), and nitrogen dioxide (NO_2) were measured at constant airflow. A plate capacitor setup was used to estimate the total amount of free charges generated in the filament plasma. This method provided a relative measure for intercomparing the amount of ionization resulting from different sets of laser parameters (Henin et al., 2009).

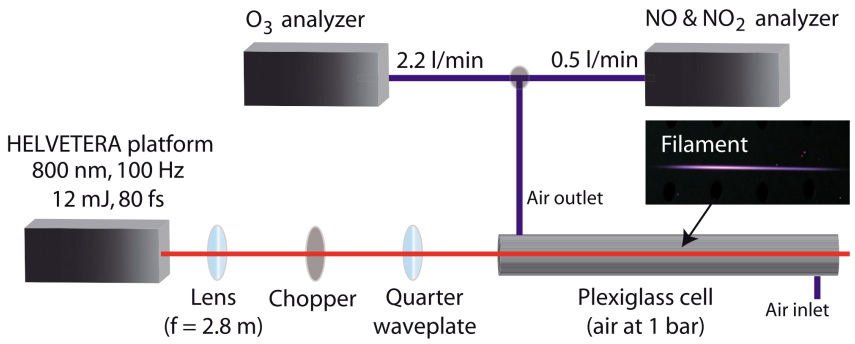

Figure 5.36.: Setup used by Petit et al. for determining the production rates of trace gases generated in near infrared laser filaments. (Fig. 1 from (Petit et al., 2010))

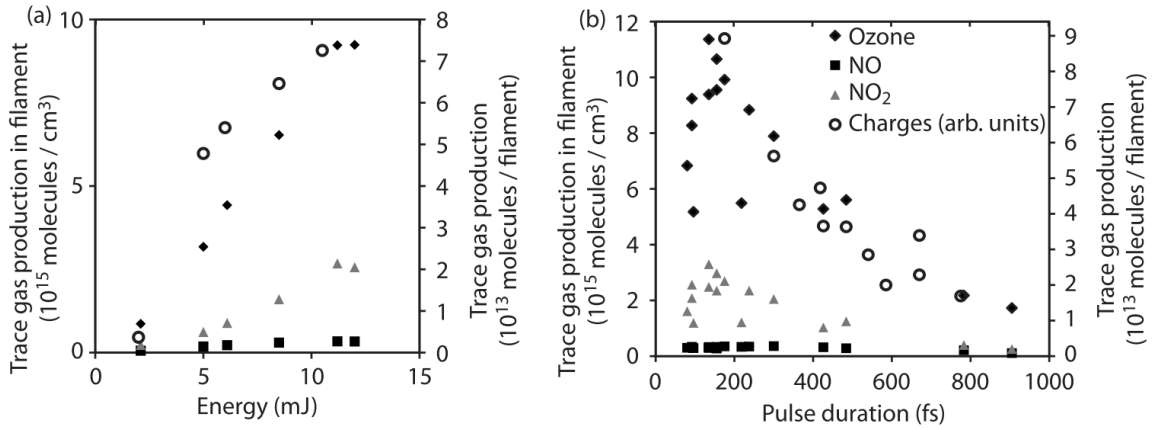

Figure 5.37.: Concentrations and total number of produced molecules of O_3, NO, and NO_2 in laser filaments. Displayed concentrations were estimated from the respective steady-state concentrations in the cell, extrapolating to the estimated total source volume. In panel (a) the pulse duration of 80 fs is held constant and the pulse energy is varied, while in panel (b) the duration is varied for a fixed pulse energy of 11.2 mJ. (Fig. 2 from (Petit et al., 2010))

The experimental setup is shown in Fig. 5.3.2. The gas sensors attached to the interaction cell (length 2 m, diameter 2 cm) were drawing air through it at a constant volume flow rate. A focused laser beam of initially $2.0 \times 2.4\,cm^2$ cross section created typically two filaments at a chopped-down rate of just 2.5 Hz with pulse energies up to 12 mJ and a Fourier limited duration of 80 fs. Additionally a quarter wave plate inserted in the optical path could be used to switch the polarization of the laser beam between linear and circular.

The steady-state production rates of the trace gases were determined and extrapolated to the assumed filament volume, leading to concentrations as high as 400 ppm or $10^{16}\,cm^{-3}$ molecules O_3 and 100 ppm or $3 \times 10^{15}\,cm^{-3}$ molecules NO_2. Regarding what is known about the plasma dynamics in a filament from the few theoretical calculations (see sec. 4.2.3) this suggests a very efficient conversion of ionic species to reactive neutrals in the filament volume, even if the filament volume

was underestimated.

Indication was found that the production of trace gases must be especially efficient in the filaments as compared to the surrounding photon bath: circularly polarized laser light yielded half as much outcome of trace gases than linearly polarized light with the same pulse energy and duration. As the type of polarization mainly affects the process of (especially multi-) filamentation (Fibich and Ilan, 2003), by modulating the effective strength of self-focusing, this shows that the filament plasma is the dominant source of the trace gases or their precursors.

Observing this, Petit et al. identified a set of reactions starting from the singly charged nitrogen ion N^+, the singly charged nitrogen molecule ion N_2^+ and excited atomic and molecular states of nitrogen, N^* and N_2^*, resulting in the production of mainly nitric oxide NO and oxygen radicals ·O, most of which quickly react with molecular oxygen to form ozone: $\cdot O + O_2 + M \rightarrow O_3 + M$. The previously cited numerical study of filament plasma dynamics by Gordon et al. (Gordon et al., 2003) indeed shows initial concentrations of atomic oxygen as high as $10^{16}\,\mathrm{cm}^{-3}$ in almost perfect accordance with the ozone concentrations of 400 ppm in the filament core, inferred from the experimental results.

Furthermore Petit et al. showed that the observed high concentrations of ozone and nitric oxide can lead to efficient production of NO_2 (which is directly observed) and drive its further oxidation into the highly reactive nitrate radical NO_3:

$$\begin{aligned} NO + O_3 &\longrightarrow NO_2 + O_2 \\ NO_2 + O_3 &\longrightarrow NO_3 + O_2 \end{aligned} \tag{5.13}$$

where NO_2 is constantly replenished by oxidation of NO. The nitrate radical together with another NO_2 molecule take part in the equilibrium

$$NO_2 + NO_3 + M \overset{k_1}{\rightleftharpoons} N_2O_5 + M, \tag{5.14}$$

where the equilibrium constant is $k_1 = 3 \times 10^{-11}\,\mathrm{cm}^3$. With a reaction rate of $k_2 = 3 \times 10^{-4}\,\mathrm{s}^{-1}$ (at about room temperature) the unstable dinitric pentoxide quickly reacts with highly abundant water to form HNO_3 in the gas phase:

$$N_2O_5 + H_2O \xrightarrow{k_2} 2\ HNO_3 \tag{5.15}$$

From the expected reaction velocities, assuming the precursor gas concentrations in the filament volume deduced from the steady state measurements, the authors conclude that gaseous HNO_3 may easily be produced at ppm levels in the plasma channel of a filament.

In this context also the formation of ·OH radicals by positive ion transfer reactions with water molecules, and their further reaction with NO_2 discussed in Sec. 4.2.2 should be recalled, which offer another pathway for the formation of HNO_3. The effective rate of the initial step, the reaction of positive ions with water molecules, should depend at least linearly on the water vapour concentration, and it could explain the dependence on absolute humidity of filament-induced condensation observed in the subsaturated cloud chamber #2 (see earlier Sec. 5.1.3). It follows that, although not detectable by the instruments in the present setup, ·OH radicals produced by O_2^+ ions present in the filament core

may additionally contribute to an efficient production of nitric acid.

The outcome of the experiment showed no nonlinearity with respect to the effective laser repetition rate. This proves that a subsequent laser shot did not influence the ongoing chemical reactions other than by producing fresh primary reactants.

The trace gas production rates determined in the laboratory are compatible with the observed mean concentrations in the outdoor experiment, taking into account uncertainties due to the poorly known rate of air exchange with the environment in the latter case. It is thus justified to assume multi-ppm concentrations of HNO_3 in the gas phase were present in the filament volume also in the outdoor experiment.

Knowing that the filaments leave behind highly concentrated precursors of HNO_3, the attempt was made to find out if the laser-generated aerosol has a corresponding chemical composition. The difference of chemical composition of filament-affected aerosol compared to the background aerosol collected under otherwise similar atmospheric conditions becomes obvious from the ionic chromatography traces displayed in Fig. 5.38. The peak corresponding to nitrate ions (NO_3^-) is strongly enhanced for all cutoff sizes, getting stronger when the cutoff size is reduced (going from panel (c) to (a)). A less pronounced excess of nitrite ions (NO_2^-) is detected in the filament-affected samples, while sulphate (SO_2^{2-}) content is essentially unchanged.

Unfortunately it is not possible to draw quantitative conclusions from the ionic chromatography signals. The question whether the highly augmented nitrate content found in the small particle fraction is caused by the formation of new particles by binary nucleation of HNO_3 and water directly out

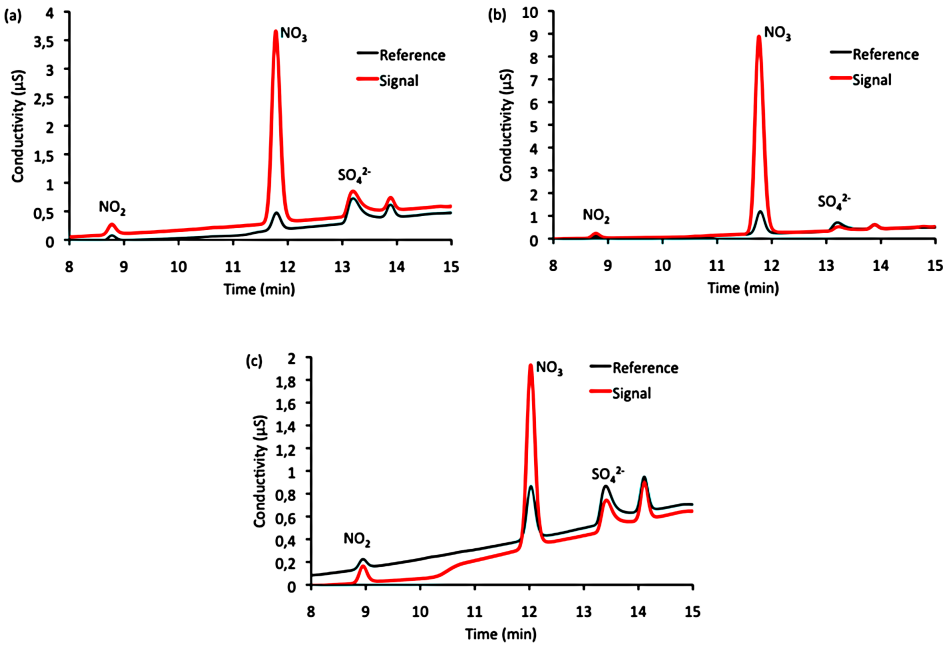

Figure 5.38.: Ionic chromatography traces of the water-soluble fraction of aerosol collected on filter membranes. Panels (a) to (c) show signals corresponding to respective membrane pore sizes of 15 nm, 50 nm, and 1 μm. In each panel background ("Reference") and filament-affected ("Signal") aerosol are compared.

of the gas phase cannot be answered based on the chromatography data and information from the Nanocheck particle counter alone. The scenario of HNO_3 condensing onto already existing particles would be as well compatible with the observations, if the condensation germs initially are just small enough to escape detection (by the Nanocheck particle counter and the membrane filter) – or if they additionally consist of water insoluble material, leaving no trace in the ionic chromatography.

The result is very important and valuable nevertheless, because it yields strong evidence that HNO_3 actually *is* formed as suspected, and that it condenses out of the gas phase.

Once again returning to Fig. 5.3.2 there remains one more feature to be discussed showing up in the second column, panels (b), (f), ..., (v), concerning the dependence of the filament effect on relative humidity. A closer look at panels (n), (r), (u), in the three rows from the bottom, reveals that above about 80 %RH the falling trend of the particle counts with increasing relative humidity, dominating most of the parameter range, is apparently broken. Although they are strongly scattered the data indicate that, beyond approximately 90 %RH, the concentration of filament-generated particles, especially in the size range between 540 nm and 4.5 μm (panels (n) and (r)), eventually starts rising. As this trend reversal concerns only a fraction of the total of data points, and because of the large scatter, it does not have strong impact in the previous correlation analysis. A discontinuity in the RH dependence appears also in the smallest size channel of the EDM 107 instrument (panel (f)), where the detected particle concentration experiences a noticeable boost, which is accompanied by increased random variability as well. The Nanocheck data (panel (b)), between 80 %RH and about 95 %RH, make a jump by a factor of approximately 1/3. There is a gap in the data in between because the Nanocheck instrument was only available in part of the duration of the whole campaign, and unfortunately most of this time the relative humidity remained below 80 %. Still regarding the continuity of trend reversal in the EDM 107 channels across the RH range spanned by the gap, the jump cannot be put aside as a measurement artefact, but has to be considered real and significant.

5.3.3. Model for filament-induced condensation

The strong evidence for HNO_3 as a key substance in filament induced atmospheric condensation lead to the following questions: can the presence of HNO_3 explain the observed production of stable particles far below unity water vapour saturation ratios? If yes, how much time would be required for a droplet to grow to micrometer size in an atmosphere containing the water soluble gas at the observed concentrations? Would then the growth be fast enough to explain the detection of particles of this size in our experimental situation (and even more in the millisecond time between filament action and probing in that of the LIDAR experiment)?

In this section answers to these questions will be developed.

Extended Köhler model calculations

To address the question of the existence of stable particles the extended Köhler theory of Laaksonen et al. (Laaksonen et al., 1998), introduced in Sec. 4.1.3 was applied. It however had to be adapted to be able to describe the present atmospheric conditions. The assumptions entering the derivation of

the original theory restrict it to relative humidities in excess of 99 % and HNO3(g) concentrations not higher than about 10 ppb. These assumptions had to be released to make accessible the local multi-ppm levels potentially caused by laser filaments and the strongly subsaturated water vapour pressures.

A major assumption to be dropped was that of a dilute ionic solution (also underlying the classical Köhler theory) which is sufficiently well fulfilled by atmospheric droplets forming around salt particles, close to water vapour saturation (Seinfeld and Pandis, 2006), but not considerably below. This situation is similar to the case of stratospheric concentrated sulphuric acid aerosol in an atmosphere containing gaseous HNO_3 at ppb levels, treated by Kokkola et al. (Kokkola et al., 2003b). In their case the droplets to be described consisted of concentrated $H_2SO_4 - HNO_3 - H_2O$ acid, which cannot be realistically described as an ideal solution.

Equilibrium size and composition of solution droplets

In order to determine the equilibrium water vapour pressure over watery solution droplets in an atmosphere containing a highly soluble trace gas, one has to consider two simultaneous equilibria: $H_2O(g) \rightleftharpoons H_2O(sol)$ and $HNO_3(g) \rightleftharpoons HNO_3(sol)$ (note: here and from now on the suffix "(sol)" identifies quantities in the mixed liquid solution, "(g)" correspondingly refers to the gas phase).

Both equations

$$p_{\infty,i}(T, m_j) = p_{\mathrm{sat},i}(T, m_j)\ \exp\left(\frac{4\ \sigma(T, m_j)\ v_i(T, m_j)}{k_\mathrm{B}\ T\ D_\mathrm{p}(T, m_j)}\right), \tag{5.16}$$

have to be fulfilled by a droplet to be in equilibrium with the surrounding atmosphere. In Eq. 5.16 the index i enumerates the substances H_2O and HNO_3, and the symbol $p_{\infty,i}(T, m_j)$ on the left hand side denotes the actual vapour pressure of substance i in the reservoir. The right hand side is the product of two terms, namely the saturation vapour pressure $p_{\mathrm{sat},i}(T, m_j)$ of substance i over the flat mixed liquid phase, and the exponential term resulting from the Kelvin effect. The symbolic parameter m_j represents the individual masses of all substances constituting the liquid solution droplet.

Equations 5.16 have the same form and a similar physical interpretation as Eq. 4.5, describing the simpler case of a single pure substance. They can be derived on the basis of the same argument of Gibbs energy minimization leading to the latter equation. The formal similarity becomes more obvious if the term $S_{\mathrm{equ}}(r)$ appearing in Eq. 4.5 is replaced by the respective vapour saturation ratio over the flat mixed liquid phase $S_{\mathrm{equ},i} = p_{\infty,i}(T, m_j)/p_{\mathrm{sat},i}(T, m_j)$, and the droplet radius r_p is expressed in terms of the diameter $D_\mathrm{p} = 2\ r_\mathrm{p}$.

Besides water and the dissociating highly soluble gas, the particular form of extended Köhler theory used here considers a spherical mixed liquid phase additionally containing a fixed amount of a fully dissolving nonvolatile substance. In the following this substance is represented by NH_4NO_3 (ammonium nitrate) salt. It is a typical constituent of atmospheric water-soluble aerosol acting as germs for heterogeneous nucleation (see sec. 4.1.1). This particular salt was chosen for two reasons: first of all it is sufficiently common in the troposphere (Jaenicke, 1993; Seinfeld and Pandis, 2006) to be considered representative. Second, but technically more important, the necessary data about the

ternary solution of H_2O, HNO_3, and NH_4NO_3 are available.

Ammonium nitrate deliquesces at a RH of between 58.3 % at 30 °C% and 76.6 % at 0 °C (Seinfeld and Pandis, 2006), but once it has deliquesced it can exist as a supersaturated liquid phase at RH considerably below the respective deliquescence point. The assumption of liquid NH_4NO_3 aerosol under practically all encountered experimental situations is thus physically unproblematic. Note that 'supersaturation' in this context refers to crystallization of solid salt out of the liquid phase.

In the whole required parameter range the system $H_2O - HNO_3 - NH_4NO_3$ is described by the semi-empirical Extended Aerosol Inorganics Model (E-AIM) of Clegg et al. (Clegg and Wexler, 2010; Clegg et al., 1998; Dutcher et al., 2010). Some further details are given in the appendix.

Similar to the approach taken in (Laaksonen et al., 1998) the present model takes into account the consumption of vapour substance from the gas phase by assuming a monodisperse droplet size distribution and a fixed particle number concentration C_p. As the vapour reservoirs are limited, the number density of droplets in equilibrium with the atmosphere has an effect on the position of the equilibrium in terms of droplet size and composition. The dependence of the reservoir vapour pressures $p_{\infty,i}(T, m_j)$ on the m_j expresses the vapour depletion effect. The assumption of a monodisperse droplet size distribution makes this dependence particularly simple. The extension to arbitrary size distributions is straightforward (Kokkola et al., 2003b) but avoided here as the simplified system should already give reasonable answers to the questions posed in the beginning of this section (Laaksonen et al., 1998).

In the following results obtained from extended Köhler theory will be presented, while more details on the implementation can be found in the appendix. The plots presented in this section are to be interpreted exacly as Fig. 4.7.

Panels (a), (b), (c) of Fig. 5.39 correspond to temperatures 273 K, 279 K, and 303 K, respectively, spanning about the range encountered during the outdoor experiments. Each of the panels shows curves for a set of initial background HNO_3(g) vapour pressures up to 4 ppm, being on the order of magitude expected in the volume of a filament. The dry diameter of the salt core was chosen as 15 nm to simulate condensation nuclei at the lower edge of the detection range of the Nanocheck instrument, the growth of which would contribute to a measured net increase of particle concentration. This is why, in particular, the maxima of the Köhler curves are located at a smaller diameter as compared to the 50 nm diameter salt core. The 'zero HNO_3' curves are plotted as a visual reference in each panel .

Comparing to the case of ppb-level HNO_3(g) concentration (Figs. 4.7 and A.1 in the appendix) the shallow depression around the local minimum, as the HNO_3(g) vapour pressure is increased, becomes more and more a plateau in the semi-logarithmic plot. The local maximum in the Köhler curve, defining the critical water saturation ratio for the first activation of initially nanometric aerosol is shifted downwards far below $S_{\mathrm{H_2O}} = 1$. The term 'first activation' expresses that there are two threshold saturation ratios. After the first activation threshold is overcome, droplet growth to sizes much larger than the size of the unactivated nuclei is enabled, however limited by the second barrier. After the second activation step is overcome, growth is basically unlimited, corresponding to the traditional use of the term activation.

The amount of depression of the threshold water saturation ratio for the first activation is highly

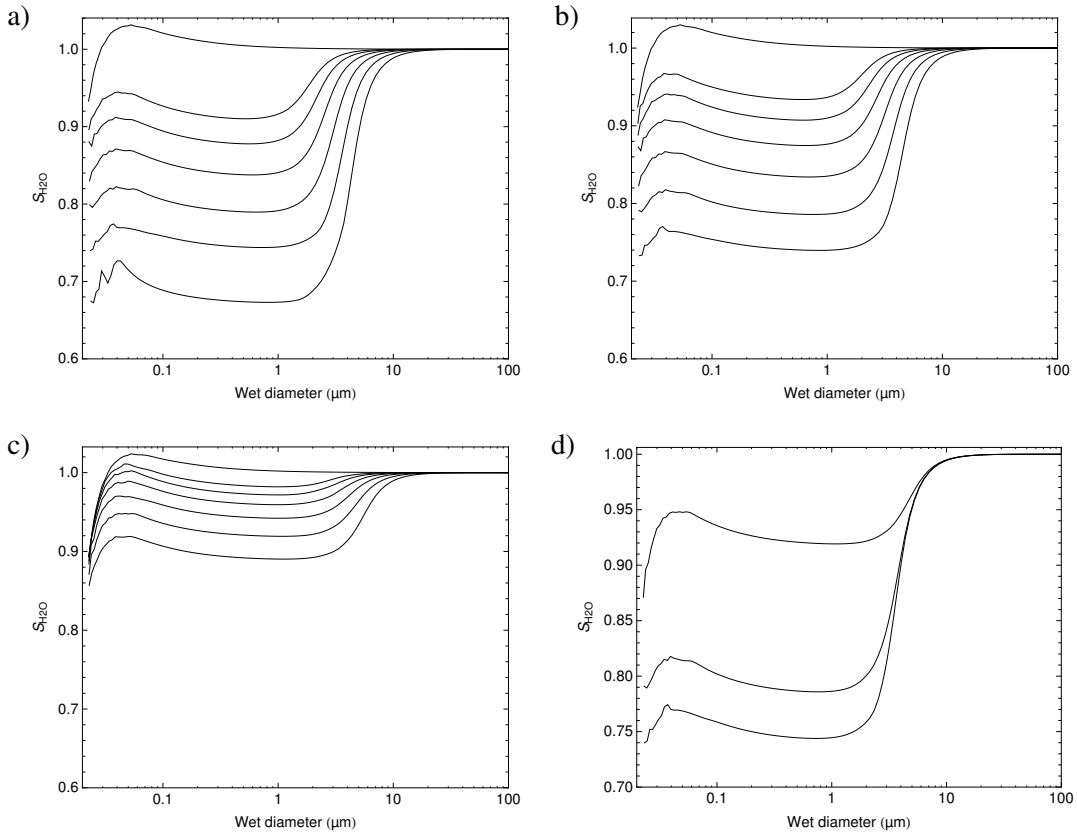

Figure 5.39.: Köhler curves for a) $T = 273$ K, b) $T = 279$ K, c) $T = 303$ K; HNO_3 concentrations are 0, 0.125, 0.25, 0.5, 1, 2, 4 ppm (top to bottom, 0 ppm is plotted as visual reference). d) curves for 2 ppm HNO_3(g) and each of the temperatures of panels a)-c) (bottom to top). Dry diameter of NH_4NO_3 core is 15 nm, atmospheric pressure is 101325 Pa, assumed droplet number concentration is $C_p = 1000\,\mathrm{cm}^{-3}$.

dependent on temperature. While at $T = 273\,\mathrm{K}$ a concentration of 4 ppm HNO_3(g) is sufficient to depress it down to about 72 %RH, the threshold is only down to about 92 %RH at $T = 303\,\mathrm{K}$. For a direct comparison in panel (d) of Fig. 5.39 the curves corresponding to 2 ppm HNO_3(g) at each of the temperatures are plotted in one graph.

On the large diameter end the Köhler curves steeply rise and converge towards the curve valid in absence of HNO_3. Under otherwise similar external conditions the position of this steep rise depends on the amount of available HNO_3(g).

To illustrate the influence of the size of the initial salt core in Fig. 5.40 Köhler curves for the conditions of Fig. 5.39, but for salt cores of 30 nm and 60 nm dry diameter, respectively, are plotted. A larger dry diameter mainly shifts the first activation barrier, increasingly eroding the associated local maximum. This is qualitatively similar to the situation of low HNO_3 concentrations considered n (Laaksonen et al., 1998).

A Köhler curve by definition is constructed without taking into account the depletion of water vapour. It is imaginable that, if the droplet cloud is large enough, and the HNO_3(g) concentration is high, also the water liquid and gaseous phases have to be treated as a closed system. This results in a limitation of the water vapour pressure in the reservoir that can be maintained given the amount of water already present in the condensed phase. The effect of a depleting water vapour reservoir on the effective size limit for the monodisperse droplet cloud is illustrated in Fig. 5.41.

Starting from the same water vapour saturation ratio $S_{\mathrm{H_2O}} = 0.99$ at two different temperatures the dashed curves represent the hypothetical $S_{\mathrm{H_2O}}$ as a function of droplet diameter D_p that would result if the droplet cloud strictly followed the Köhler curve while moving along the diameter coordinate. Note that this type of 'growth' is *not* physical at all, because the water vapour pressure would be grossly in excess of its equilibrium value (designated by the Köhler curve) most of the time. The dashed curves

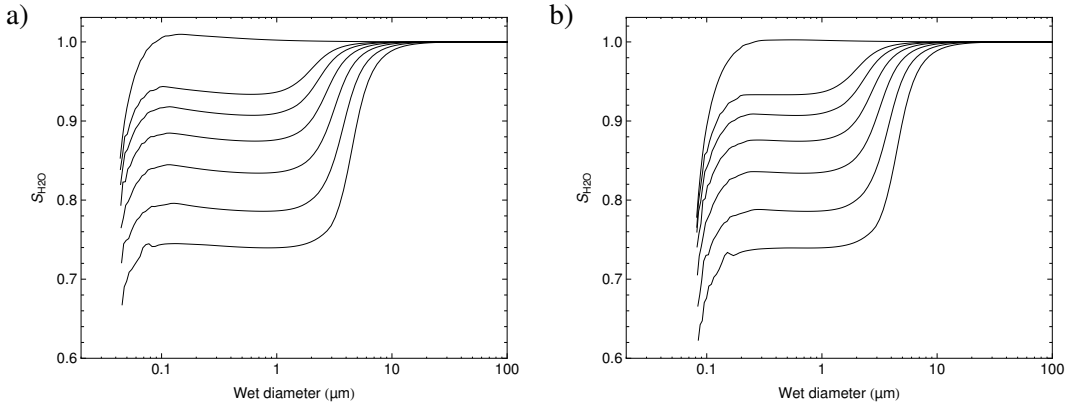

Figure 5.40.: Köhler curves for different salt core diameters ; a) dry diameter 30 nm b)dry diameter 60 nm for initial HNO_3 concentrations of 0, 0.125, 0.25, 0.5, 1, 2, 4 ppm (respective curves top to bottom). Atmospheric pressure is 101325 Pa, assumed droplet number concentration is $C_\mathrm{p} = 1000\,\mathrm{cm}^{-3}$, and $T = 279\,\mathrm{K}$. To be compared with Fig. 5.39
b) for a dry diameter of 15 nm.

thus are physically meaningful only at their respective intersection with the corresponding Köhler curve.

The intersections indicate the droplet diameter at which the water vapour reservoir is depleted to a level which it cannot provide vapour for further condensation while maintaining the vapour at stable equilibrium with the monodisperse droplet cloud.

Time-dependent growth model calculations

Having shown that the presence of HNO_3 at reasonable levels can explain the formation and stabilization of ternary solution droplets by diffusional equilibration of the compositions of the liquid and gaseous phases the question remains to be answered if this equilibration happens fast enough to explain the observed quick formation of aerosol particles. If this were not the case, additional or alternative mechanisms would have to be considered.

Starting from the classical expressions for diffusional growth or evaporation of an isolated spherical liquid droplet, including the release of latent heat of condensation and temperature equilibration with the surrounding by heat conduction (Pruppacher and Klett, 1997), and the detailed model for the ternary solution $H_2O - HNO_3 - NH_4NO_3$ already used in the calculation of the Köhler curves, the coupled time dependent changes of water and HNO_3 partial masses in the mixed droplet liquid phase were integrated. Again, the model equations and more details regarding the implementation are provided in the appendix.

In Fig. 5.42 the time evolution of an ammonium nitrate aerosol particle of dry diameter $D_{p,dry}$ = 25 nm is shown for an ambient temperature of 2 °C, relative humidities of 75 %, 90 %, and 99 %, as well as HNO_3(g) concentrations between 2 ppm and 8 ppm.

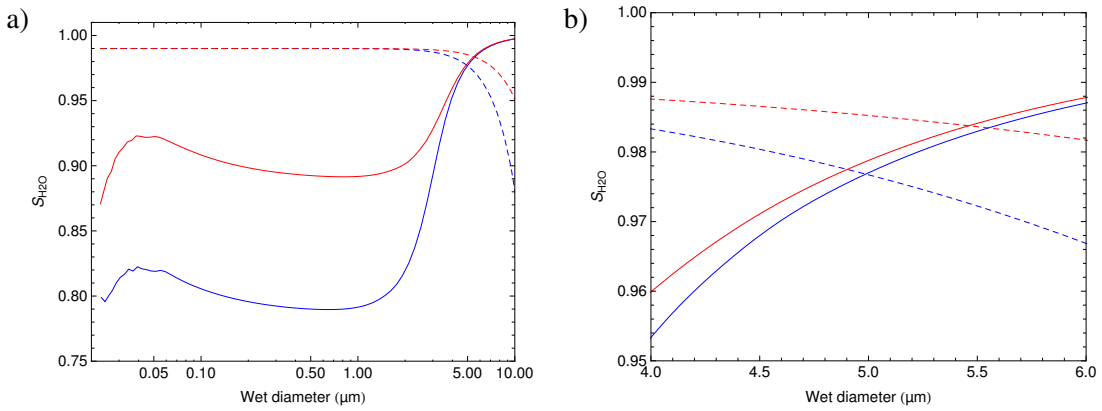

Figure 5.41.: Effect of limited total amount of water substance on the maximum attainable droplet size of a monodisperse cloud in equilibrium with both H_2O(g) and HNO_3(g). Initial concentration of HNO_3(g): 2ppm, dry diameter of the NH_4NO_3 core: 15 nm, droplet number concentration C = 1000 cm^{-3}, initial water saturation ratio S_{H_2O} = 0.99; atmospheric pressure 101325 Pa; blue: T = 273.15 K, red: T = 289 K; Köhler curves drawn solid, depletion-limited water saturation ratios dashed; Panel b) shows linear scale closeup of the intersections. The depletion-limited diameter at T = 289 K (approx. 5.5 μm) is about 10 % larger than at T = 273.15 K (approx. 5.0 μm) for the same initial S_{H_2O}. More detailed explanation in the text.

In the calculation, up to the time $t = 0$ s the initially deliquesced salt particle is at equilibrium with the respective ambient water vapour pressure, resulting in different initial wet diameters taken on at different levels of RH. At $t = 0$ the atmosphere surrounding the particle is assumed to instantly contain the respective concentration of HNO_3(g), and the diffusional equilibration of the gas and liquid phase concentration of the trace gas begins.

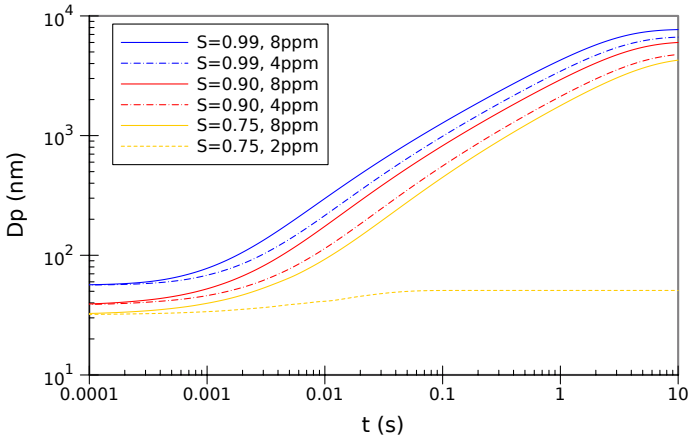

Figure 5.42.: Time dependence of the droplet diameter under conditions of various combinations of water saturation ratio and initial HNO_3(g) concentration (as stated as 'ppm' in the legend) as obtained from the binary diffusive growth model described in the text. Assumed temperature is $T = 2\,°C$, and droplet number concentration is $C_p = 1000\,cm^{-3}$. Both water vapour and HNO_3(g) are subject to depletion. Note the case '$S = 0.75$, 2 ppm', where growth stops at the first slope of the Köhler curve (see text).

The assumed number concentration of aerosol particles is fixed at $C_p = 1000$. It can be seen from the previously discussed Köhler curves that HNO_3 depletion becomes notable only in the later growth stages, when the rate of mass uptake becomes larger, eventually decelerating and stopping growth.

Results obtained for the initial growth stages thus depend relatively little on the number of particles per unit volume, growing simultaneously.

Fig. 5.43 shows, as an example, the time dependence of the partial masses of water and HNO_3 in the liquid phase for the case $RH = 90\,\%$ and [HNO_3(g)] = 4 ppm. It can be seen that only after sufficient HNO_3 has accumulated in the liquid phase, the ambient water vapour becomes supersaturated enough to start condensing onto the droplet. The concentration of HNO_3 in the droplet rises until $t \approx 10$ ms, peaking at about 20 wt% in this specific case, and then slightly decreases until the end of the growth, when it is still about 18 wt%.

This pattern of growth is relatively common among situations when growth is possible, while the velocity of growth and the final size, as well as the final composition of the droplet depend somewhat on the ambient conditions.

The curve 'S=0.75, 2 ppm' in Fig. 5.42 exemplifies the case where the initially growing nucleus encounters the first ascending slope of the Köhler curve, left of its maximum (see for example Fig. 5.39), and stable equilibrium is established already at a droplet diameter of $D_p \approx 50$ nm, corresponding to a growth factor of just $D_{p,final}/D_{p,initial} \approx 1.5$. Additionally, the gain in size is much

slower than in the other cases, when both water saturation ratio and the concentration of HNO_3(g) are sufficient for growth.

In general, at the assumed ppm levels of HNO_3(g) concentration, growing droplets attain micrometer size on the order of a second after the exposure to the trace gas begins.

The timescale on the order of a second for growth to (sub-)micrometer size is compatible with the in situ observations of filament-induced particle formation using the sampling particle counters.

Another question which can be posed is, whether diffusional growth, as described by the model discussed here, can result in an increase of total optical backscattering of the prevailing background aerosol as it is displayed by the LIDAR data. Fig. 5.44 presents the time dependent growth factors $D_p(t)/D_p(0)$ for the growth curves displayed in Fig. 5.42.

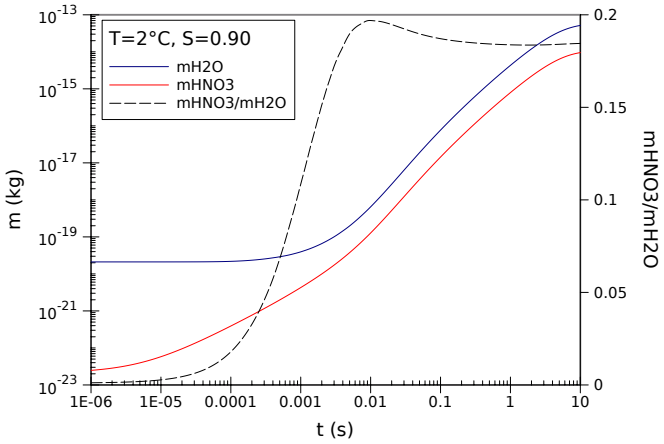

Figure 5.43.: Condensed partial masses of water and HNO_3 substance exemplified for the situation $T = 2\,°C$ and an initial concentration $[HNO_3(g)] = 4$ ppm. Also shown the ratio of dissolved HNO_3 and liquid water, increasing strongest during about the initial 10 ms, and then remaining below 20 wt%. The pattern of initial accumulation of HNO_3, and subsequent growth at relatively constant concentration appears to be general for binary droplet growth in a water-subsaturated atmosphere.

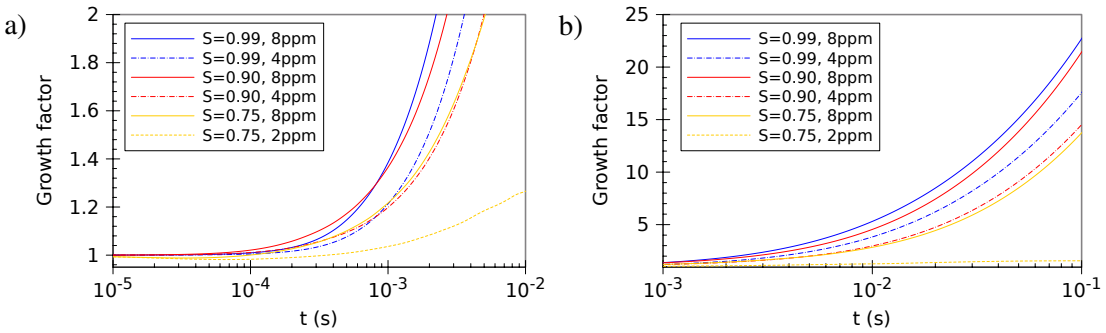

Figure 5.44.: Time dependent Growth factor $D_p(t)/D_p(0)$ for conditions of $T = 2\,°C$ and the previous combinations of relative humidity and initial HNO_3(g) concentrations. Dry particle diameter is $D_{p,dry} = 25$ nm again. Panels a) and b) show different time intervals.

The plot shows that the growing particles of a dry diameter $D_{p,dry} = 25\,nm$ (but different wet diameters between about 33 nm and 56 nm, depending on relative humidity) have gained between 20 % and 40 % in diameter within the interval of 1 ms duration after the HNO_3 trace gas became available at $t = 0$.

For assessing the impact on the backscattering cross section at the LIDAR wavelength, the more favourable value of 40 % for the growth factor of the initially wet salt particles is assumed. Using backscattering efficiency factors obtained from Mie theory, for example as plotted for water in Fig. 5.27, for initial wet particle diameters around $D_{p,wet} \approx 40\,nm$, and for a refractive index between $n = 1.33$ and $n = 1.5$, an increase of the backscattering cross section by a factor of approximately 7 to 7.5 can be estimated. This reflects the approximate proportionality of the scattering cross section to D_p^6 valid in the limit of particle sizes considerably smaller than the scattered wavelength (Bohren and Huffmann, 1983).

Additionally including the observation that the number of sub-300 nm typically increased by a factor of about 3 in the in situ sampling data (see previous Sec. 5.3.2), the increase of backscattering due to of particles in this size class undergoing diffusional growth may be as large as a factor of 20 after the initial millisecond.

In naturally occuring tropospheric aerosol particles of this size range are present in number concentrations between some tens per cm^3 (in clean maritime air) up to several tens of thousands per cm^3 (in urban aerosol) (Jaenicke, 1993). Their contribution to the total backscattering coefficient at the laser wavelength of 532 nm is minor because of their small total cross section and the low backscattering efficiency when $D_p < \lambda$ (see Fig. 5.27).

Consequently, the results of the model calculations suggest that the diffusive growth of initially wetted salt particles (some tens of nanometers initial size) during a time of only 1 ms , exposed to ppm levels of HNO_3(g), cannot explain the increase of the backscattering coefficient inferred from the LIDAR data.

The existence of other mechanisms happening on shorter timescales, able to quickly increase the number of particles in the sub-μm size range would have to be postulated to explain a more substantial increase of scattering. These can not be identified from the in situ sampling measurement, and can only be speculated about. Further experimental investigation of the initial fractions of a second after the action of a filamenting laser beam would be needed to find a definitive answer.

In Fig. 5.45 finally, as an example, the enhancement factor of the particle backscattering cross section C_b for an initially $D_p = 33\,nm$ particle is shown as a function of the growth factor. Considering Fig. 5.44 b), it can be seen that already after $t = 100\,ms$ diffusive growth could have enhanced the backscattering cross section of an initially nanometric particle by a factor of 10^5 or more.

This illustrates that with regard to future attempts to use filament induced condensation as a tool for probing the atmosphere, the delay between the filament action and the probing may be the most important factor to increase any present signal related to diffusive growth.

5.3.4. Discussion

The experimental evidence gained by in situ sampling of filament-affected aerosol very clearly proves that laser-induced water condensation even under conditions below water vapour saturation is possible. It is also becomes evident that the strength of the effect, and its expression in different aerosol particle size ranges, depends on various parameters. The most important of these is – not surprisingly – the relative humidity.

However, the data suggest that also the absolute water vapour content may play a role on its own, but with quite different consequences on the change of the particle counts measured in different aerosol size ranges. While there is positive correlation with the filament effect in the large ($D_p \gtrapprox 1\,\mu$m) size classes, the opposite is the case in the small size classes ($D_p \lessapprox 500$ nm), specifically pronounced in the nanoparticle counter signal.

Ion chromatographic analysis of the laser-generated aerosol showed that it is strongly enriched with nitrate. Based on the measurement of trace gases produced in filaments under well defined conditions, showing high levels of mainly O_3, and NO_2 a possible pathway for the generation of ppm-levels of HNO_3 in the filament volume could be identified

Application of extended Köhler theory shows that indeed the observed production of HNO_3 by laser filaments is a very good candidate for the explanation of the observed filament-induced condensation. At temperatures close to 0 °C already low ppm levels of the soluble gas may explain the lowering of the 'first activation' barrier way below water saturation. This lowering, however, shows a pronounced temperature dependence.

The results also indicate that a certain indirect influence of temperature on the growth limit for big droplets may be observable, caused by the lower water vapour volume mixing ratio at lower temperatures for similar initial vapour saturation ratios. The terminal stage of growth may thus be affected by the finite supply of water vapour.

Besides limiting the maximum growth capacity the water vapour concentration may also have a direct impact on the processes leading to the production of HNO_3, according to the interpretation of the cloud chamber experiments proposed in Sec. 5.1.3.

In this context and in general it must be kept in mind that the underlying assumptions, especially those of a monodisperse droplet size distribution, a fixed concentration of identical soluble nucleation

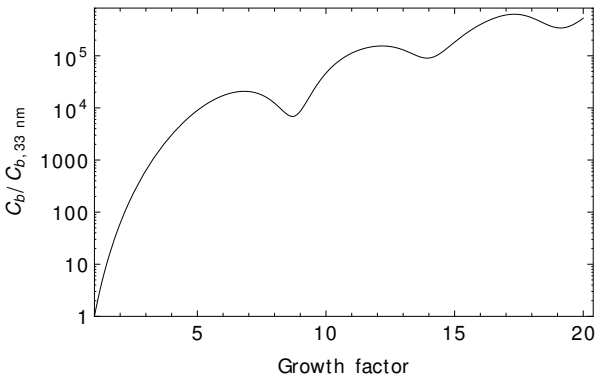

Figure 5.45.: Dependence of the enhancement of the backscattering cross section on the growth factor of an exemplary initially D_p = 33 nm droplet (refractive index n=1.33).

germs, and most importantly, thermodynamic equilibrium, probably do not describe the actual experimental conditions very well. The equilibrium model is a tool to delineate the conditions under which filament-induced aerosol growth can possibly happen, but the results must be interpreted with sufficient caution.

The results of time dependent growth calculation showed that the observed rise times of particle counts on the order of seconds are in accord with the scenario of binary diffusional growth. This is even valid for the observation of sub-micrometric or even micrometer size particles in response to firing the laser.

One explanation for the opposite trend of the filament effect with increasing relative humidity in the different size ranges considered so far was based on the argument that in a depleted vapour reservoir the initial volume mixing ratio becomes important after the (assumed monodisperse) cloud has passed the first activation barrier. The appearance of an increasing number of large particles with increasing water vapour mixing ratio would be interpreted as a delayed depletion of the reservoir once the droplets in the cloud have grown to a size where depletion becomes notable (see Fig. 5.41).

In the case of the monodisperse model aerosol the effect is notable but not very pronounced in terms of the difference of the maximum attainable particle diameters. One reason for the actually observed correlation could thus simply be that the assumption of a monodisperse cloud eventually fails in describing the final state of a droplet cloud growing in a depleting atmosphere.

In a polydisperse cloud where the chemical composition of the particles is the large droplets is the same irrespective of size, large droplets would tend to grow at the cost of smaller ones, caused by the reduced surface energy (Kelvin-) effect for the larger droplets. Such competition on the other hand should be strongest under conditions of *reduced* vapour mixing ratio.

An amplification of the effect of the competition for soluble trace gas between different size classes of cloud droplets has previously been identified by Kokkola et al. (Kokkola et al., 2003a). They were concerned with the situation of a cooling air parcel containing a polydisperse aerosol and HNO_3 present at ppb levels. In this situation the competition was reinforced by limited diffusional transport of HNO_3.

As it was shown earlier in this section, the interpretation as binary condensation of HNO_3 is compatible with the observations in many regards. There are however more aspects o be considered. First of all it seems straightforward to include other than liquid salt aerosol in the discussion. While soluble ionic compounds constitute a large fraction of the tropospheric aerosol, there are other major constituents which are much less water soluble or insoluble.

To initiate the growth of a droplet on an insoluble particle, a layer of water has to be deposited. The initial steps of formation of this layer are governed by processes such as adsorption, desorption, and surface diffusion, determined by the interaction of gas phase molecules with the surface.

An important quantity in this regard is the uptake coefficient $\gamma = J_{\mathrm{transf}}/J_{\mathrm{coll}}$ which is defined as the ratio of the net flux J_{transf} of molecules eventually sticking to the particle (leading to mass transfer) and the ideal gas-kinetic collision rate J_{coll} of molecules with the particle surface.

In Fig. 5.46 the uptake coefficient for HNO_3 on relatively inert silica-rich mineral dust with a mean particle diameter of about 200 nm is shown as as a function of relative humidity, as it was

experimentally determined by Vlasenko et al. (Vlasenko et al., 2006). In their experiment, a flow tube reactor was used to expose the aerosol to HNO_3(g) at a concentration of 10^{12} cm^{-3}, corresponding to about 40 ppb, for a duration of 1.9 s. This was done for different levels of water vapour saturation. The figure shows that even chemically inert aerosol (with respect to reaction with HNO_3) is efficiently wetted in the presence of the soluble gas under clearly subsaturated conditions.

It is also evident from the figure that the uptake coefficient has a positive dependence on relative humidity, which gets increasingly stronger towards 80 %RH. It can be concluded that the co-adsorption of gaseous HNO_3 on insoluble, inert particles thus facilitates their initial wetting. Once wetting progresses further diffusive growth is facilitated, because the particles become more and more similar to pure solution droplets.

Similar conclusions can be drawn for another important class of aerosol. Organic and elementary carbon constitute a major fraction to the total aerosol mass (see Tab. 5.3.4), especially in urban, but also in continental rural areas. These particles are rather hydrophobic, which means that the adhesive forces acting on water molecules in contact with the surface are generally too weak to form a liquid phase easily enough below considerable water vapour saturation. These particles consequently are less efficient condensation nuclei.

From atmospheric measurements and laboratory experiments on model carbon aerosol particles it is known that soot aerosol from jet aircraft plumes (with sizes of typically a few tens of nm) is hygroscopicised by adsorption of sub-monolayer amounts of H_2SO_4. Wyslouzil et al. (Wyslouzil et al., 1994) treated larger black carbon particles ($D_p \approx 125 - 150\,\mu$m) with gaseous sulphuric acid and studied their water adsorption properties compared to untreated particles. They could observe that a surface coverage with typically 0.1 monolayer of H_2SO_4, comparable to their estimate for

		composition (%)				
Region	mass (μg m^{-3})	C(elem)	C(org)	$NH4^+$	NO_3^-	SO_4^{2-}
remote	4.8	0.3	11	7	3	22
nonurban continental	15	5	24	11	4	37
urban	32	9	31	8	6	28

Table 5.4.: Typical total mass concentrations and chemical compositions of tropospheric aerosol; C(elem) means 'elementary carbon' or 'black carbon' from combustion; C(org) are all other carbon containing compounds. after (Seinfeld and Pandis, 2006), Table 2.19.

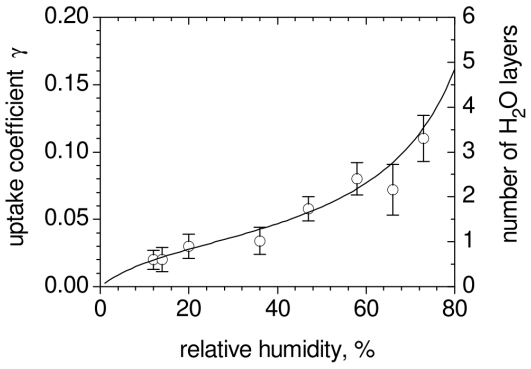

Figure 5.46.: HNO_3 uptake coefficient and deduced coverage of a chemically inert silica aerosol ($\bar{D}_p \approx 200$ nm) after exposure to about 40 ppb HNO_3(g) for 1.9 s, as a function of relative humidity. Fig. 8 From (Vlasenko et al., 2006).

actual aerosol from jet plumes, yields strongly hydrophilic surface properties. These enable efficient adsorption of water already under water vapour subsaturated conditions (see Fig. 5.47). In their publication the authors of (Wyslouzil et al., 1994) explicitly consider HNO_3 as another candidate substance for soot surface hydrophilization. As their goal was to investigate processes happening in jet exhaust gas plumes, where H_2SO_4 from oxidized SO_2 is much more abundant than HNO_3, they chose this gas for their investigations. Consequently, also with regard to black carbon aerosol particles, the high local concentrations of HNO_3 in the wake of a filament may lead to a change of the surface properties, permanently enhancing their efficiency as condensation nuclei.

Finally, the ozone generated in filaments at high concentrations is probably as important for the processing of condensation nuclei as the HNO_3 itself. It is known that already at common atmospheric concentrations the strong oxidizer O_3 chemically processes the surfaces of hydrophobic organic aerosol (Seinfeld and Pandis, 2006), adding polar groups to unpolar carbon compounds.

The oxidizing effect of ozone could have an impact on the number of suitable condensation germs for the proposed binary heterogeneous condensation of water and HNO_3. From the experiments described in this section it was seen that filament generated ozone is available in excess of the amount needed to explain the formation of sufficient HNO_3 (Petit et al., 2010). It could thus take part in the initial steps of processing of the background aerosol.

The Köhler curves in Fig. 5.39 show that the first activation barrier raises with increasing temperature. This means that at the same relative humidity and HNO_3 concentration, at a higher temperature fewer small particles get activated to grow up to the second barrier.

Thus less HNO_3(g) is consumed than if many smallest particles would pass the first barrier and start to grow. This could increase the effective time for which HNO_3 concentrations remain high, prolonging the exposure of initially non-wetted (organic or mineral) larger aerosol particles to the trace gas, and probably leading to the above described hydrophilization.

This means that at higher temperatures the processing of initially hydrophobic aerosol gets facilitated because of less loss of HNO_3 to many small activated particles.

Again returning to the LIDAR experiment, the straightforward interpretation of the in situ measured particle creation and growth can not be transferred to explain the sub-percent increase of the volume backscattering coefficient observed there.

The distance between the filaments and the sampling inlet in the in situ measurements was approximately equal to the LIDAR probing beam radius, which gives some confidence that the sampled

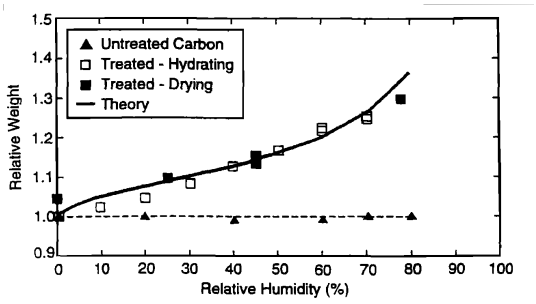

Figure 5.47.: Mass gain of the spherical carbon particles that were chemically processed with H_2SO_4(g), resulting in about 0.1 monolayer of acid molecules, exposed to different ambient relative humidities. Fig. 2 from (Wyslouzil et al., 1994).

volumes in both cases are about equivalent with regard to their mixing with unaffected background aerosol.

Supposing this, the in situ observed relative gain of particles of sub-μm to several micrometers size is fairly sufficient to explain an increase of the volume backscattering coefficient even of several percent. This can be estimated by considering the change of the aerosol backscattering coefficient analogous to Eq. 5.11, which is given by

$$\Delta\beta_{\mathrm{A}} = \frac{\pi}{4} \int_0^\infty \mathrm{d}D_{\mathrm{p}}\; D_{\mathrm{p}}^2\; \Delta n(D_{\mathrm{p}})\; Q_{\mathrm{b}}(D_{\mathrm{p}}).$$

The new large particles, adding up to 30 % to the background concentration under favourable conditions (see also Fig. 5.32), can be seen to strongly dominate the integral and to lead to the strong increase of aerosol backscattering.

Under low background conditions several percent of increase of total atmospheric backscattering appear possible to reach by diffusive growth alone – however only after a time delay up to a second or so.

It remains to be checked if other mechanisms exist, like charge-accelerated coagulation of particles of sub-100 μm size, which could serve to explain the required fast appearance of even only a few micrometer sized paricles per cm^3 of air. Before any new attempt to remotely detect filament-induced condensation is made, a deeper understanding of it is necessary.

5.4. Outlook: the TerAIDA campaign

It had become clear already after the initial weeks of the real-atmosphere campaign at Aïre that, to gain further insight in the nature of filament-induced condensation, full control of all experimental conditions would be required, in addition to more sensitive instrumentation, extending the range of detectable sizes and concentrations of particles.

Besides that, especially full knowledge and control of the chemical composition of the atmosphere would be desirable. The presence of other trace substances, such as volatile organic compounds (VOC), could not even be detected during the Aïre campaign. Additionally the background aerosol, apart from its known size distribution in the detection range of the available instruments, could not be characterized and was not controllable.

For these reasons, right in succession to the measurement campaign at Geneva the Teramobile system was moved to the aerosol and cloud research facility ‘AIDA’. The acronym AIDA is for Aerosol Interaction and Dynamics in the Atmosphere, which is one of the main fields of research of the Institute for Meteorology and Climate Research (IMK-AAF) at the Karlsruhe Institute of Technology.

The IMK-AAF, headed by T. Leisner, hosted the campaign spanning three weeks of installation and preparation, and finally two weeks of experiment.

At the time this text is written the evaluation of the outcome of the experiments conducted during the ‘TerAIDA’ campaign has not been completed yet, and here mainly an overview of the goals,

the strategy and the actual conduction of the experiments is given, together with some preliminary qualitative results.

5.4.1. The AIDA cloud chamber

The AIDA cloud chamber is an almost cylindrical steel vessel (inner diameter 4 m, height ≈ 7.5 m) in an insulating housing which can be precisely thermally controlled throughout a temperature range between 60 °C and −90 °C. The chamber can be filled with an atmosphere of pure synthetic air or nitrogen, and pressurized between 10^5 Pa and 100 Pa.

The atmosphere of the chamber can be saturated with water vapour, and trace gases like SO_2, NO/NO_2 or O_3 can be added at precisely controlled concentrations.

Also a variety of volatile organic compounds can be mixed into the artificial atmosphere, allowing to study their role in aerosol formation processes. These are, for example, α-pinene representing biogenic terpene VOC, or toluene as a common aromatic atmospheric trace constituent.

Finally, aerosol can be created in situ or injected into the chamber atmosphere, in order to prepare a pool of well characterized particles for the study of their interaction with the atmosphere.

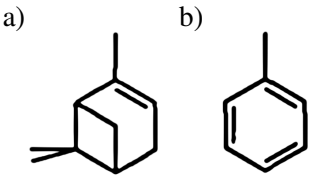

Figure 5.48.: Structure diagrams of the volatile organic compounds a) α-pinene and b) toluene (images from (Seinfeld and Pandis, 2006)).

A pump is used to depressurize the AIDA chamber at typical pumping rates of 50 m^3/h, leading to adiabatic expansion and cooling of its atmosphere. As a consequence of this, an initially water-saturated atmosphere eventually supersaturates with respect to condensation.

The adiabatic expansion in the cloud chamber simulates the rising of an air parcel in the natural atmosphere. If the cloud chamber is pumped sufficiently fast the transport of vapour to the walls and the exchange of heat with them is negligible. Under such conditions natural nucleation and cloud formation processes can be studied.

A fan located at the chamber bottom can be rotated at variable speed in order to evenly distribute trace substances. This is important in general cloud chemistry experiments in order to avoid artefacts caused by inhomogeneous distribution of reacting substances.

Besides its well-controlled atmosphere, also the arsenal of instruments attached to the AIDA chamber make it ideally suited to investigate filament-induced condensation.

The water vapour concentration is determined with high precision by 'direct Tunable Diode Laser Absorption Spectroscopy' (dTLAS) where a single absorption line of water at about $\lambda = 1.37\,\mu$m is constantly scanned by a tunable diode laser, and the wavelength-dependent absorption of water vapour along a multiply folded path across the chamber is measured. The detection limit for water vapour is 0.1 ppm with a response time of 1 s.

Alternatively, a dew point mirror is used to determine the relative humidity in an independent measurement. The measurement principle of this device is based on modulating the temperature

of a highly reflective mirror surface around the dew point, that is, the temperature leading to water supersaturation at the ambient water vapour concentration. The dew point is indicated by sudden loss of mirror reflectance due to scattering on droplets condensing on the mirror surface.

Trace gas monitors for ozone, SO_2, and NO/NO_x are part of AIDA's standard instrumentation. During the TerAIDA campaign they were sampling air via Teflon tubes guided to the (radial) centre of the chamber, about 7 cm below the level where the Teramobile beam propagated (see the description below). This allowed to relatively locally measure filament-affected trace gas concentrations while the air in the chamber was at rest. Ozone and SO_2 could be detected down to concentrations of 1 ppb with a response time of 20 s, while the detection limit for NO/NO_x was 2 ppb for an exposure of 20 s.

AIDA is also equipped with a variety of aerosol sensing, sizing and characterization instruments, only some of which were used in the experiments to be described in the following. Here only the instruments are listed which were actually used: Sampling instruments for aerosol characterization include condensation particle counters (CPC) for particles between 3 nm and 1 μm size, a scanning mobility particle sizer (SMPS), and the 'small ice detector' (SID) which collects 2-dimensional angle resolved scattering patterns and can discriminate spherical droplets (radially symmetric scattering pattern) from non-spherical ice particles (radially non-symmetric scattering).

The in-situ scattering particle counter SIMONE measures near-forward ($\theta = 1.8\,°$) and polarization-resolved near-backward scattering ($\theta = 178.2\,°$) and yields the ratios of forward- to backward scattered total intensity (conveying size information) as well as the backscattering depolarization ratio (conveying shape information) as measured quantities.

5.4.2. TerAIDA setup

The Teramobile container was placed next to the hall enclosing AIDA. In Fig. 5.49 b) a schematic drawing of its position relative to the building is shown.

The position of the Teramobile container had to be precisely set within a few centimeters, next to a port in the outer wall of the hall, specifically made for the purpose of as directly as possible coupling the laser beam into the cloud chamber. The beam was guided out of the Teramobile container via the roof port and reflected once more by the roof periscope mirror, pointing it directly through the AIDA chamber.

Two exisiting ports to the AIDA chamber were used for optical access. Extension steel tubes of 1 m length each and an inner diameter of 150 mm were used to mount optical glass windows outside the insulating housing (see sketch), kept at room temperature in order to prevent fogging when the interior of the chamber was cooled below ambient temperature.

The presence of the input window required to guide the Teramobile beam as directly as possible and with the maximum possible beam diameter from the laser output to the chamber port, in order to prevent premature filamentation and destruction of the input window. Another requirement was to guide the beam out of the chamber safely without causing ablation on any metal part of the chamber, or on the output window.

These boundary conditions left only one practical option to produce filamentation inside the

chamber, which was to place a geometrical focus close to the centre of the chamber, suppressing filamentation by the divergence of the beam until it reached the output window. This allowed to safely dump the transmitted light outside the chamber. An $f = 4\,\mathrm{m}$ fused silica lens was placed in the beam path next to the input window to achieve this goal.

Figure 5.50 shows a sketch of the AIDA chamber and the beam path, together with a photograph of the filamenting beam taken during the initial beam alignment, when the interior of the chamber was still accessible. An axial view of the Teramobile beam path inside the chamber is also shown.

After the initial alignment and tests the chamber was sealed, cleaned, and purged, and it remained inaccessible for the rest of the campaign. Opening it again, and therewith polluting it, would have caused inacceptable delay.

To ensure that the beam path remained unchanged throughout the campaign, the alignment target of the SIMONE instrument, visible on the photograph in Fig. 5.50 b), was used for checking the Teramobile beam alignment as part of the daily routine, using weak unamplified leakage radiation from the Teramobile regenerative amplifier, observed with the video camera which is part of the SIMONE instrument.

During experiments the presence of the filamenting beam could be directly observed with SIMONE's alignment cameras.

5.4.3. Objectives and strategy of the TerAIDA campaign

The objectives of the campaign were to study filament-induced condensation under a variety of well controlled physical atmospheric parameters, specifically at different temperatures and water vapour saturation ratios, and first of all in an ideally clean, virtually aerosol-free artificial atmosphere.

The production of particles and trace gases depending on these environmental parameters, but also on the properties of the laser pulses, their duration and energy, were to be examined.

In order to investigate the role of the action of filaments in cloud formation, two different kinds

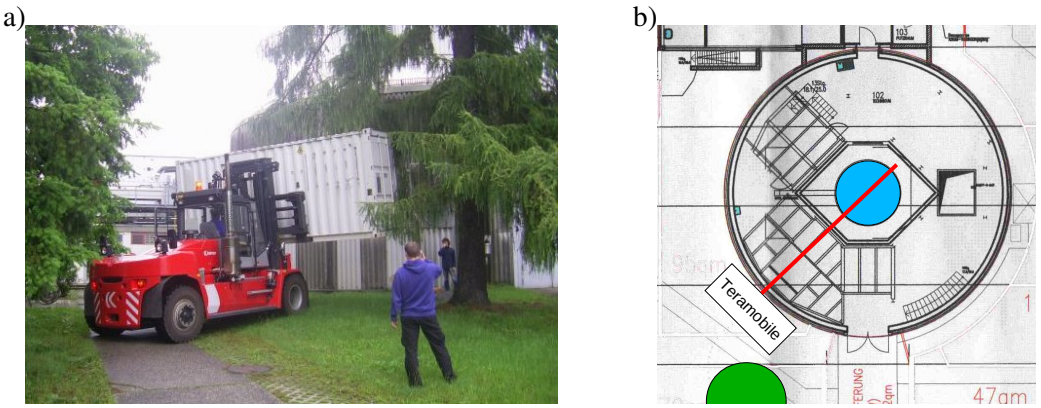

Figure 5.49.: a) Placement of the Teramobile container next to the AIDA hall. b) sketch of the container position relative to the building and the AIDA chamber (blue circle). The laser beam path is already indicated by a red line.

of experiments were planned: 'static' experiments where filaments were fired through a prepared atmosphere for a certain extended time interval, and 'dynamic' experiments where the filaments acted upon a changing atmosphere of increasing water saturation ratio, in order to observe activation of filament-generated aerosol, or any other direct effect of filament plasma (or photochemical) products on the activation and growth of cloud droplets.

Because of the specific capability of the AIDA chamber to prepare conditions where direct nucleation of ice particles is possible, and the availability of instruments to identify it, experiments for the investigation of possible filament-induced ice nucleation could be included in the planning of the campaign.

The other main objective however was to gain insight in the role of the chemical composition of the atmosphere in filament-induced condensation. The roles played by the trace gases previously identified as important, most importantly of those generated by the filaments themselves (NO_x, O_3). Besides, the influence of externally added SO_2, and very importantly, the role of volatile organic compounds was a main focus.

One experiment was included in the planning where the main component of the atmosphere was pure nitrogen instead of artificial air. The reason to include this experiment was to look for indication of any of the processes specifically involving the atmospheric molecular oxygen, and in particular to find evidence for or against a contribution of a multiphoton-activated Byers Brown-type process (see

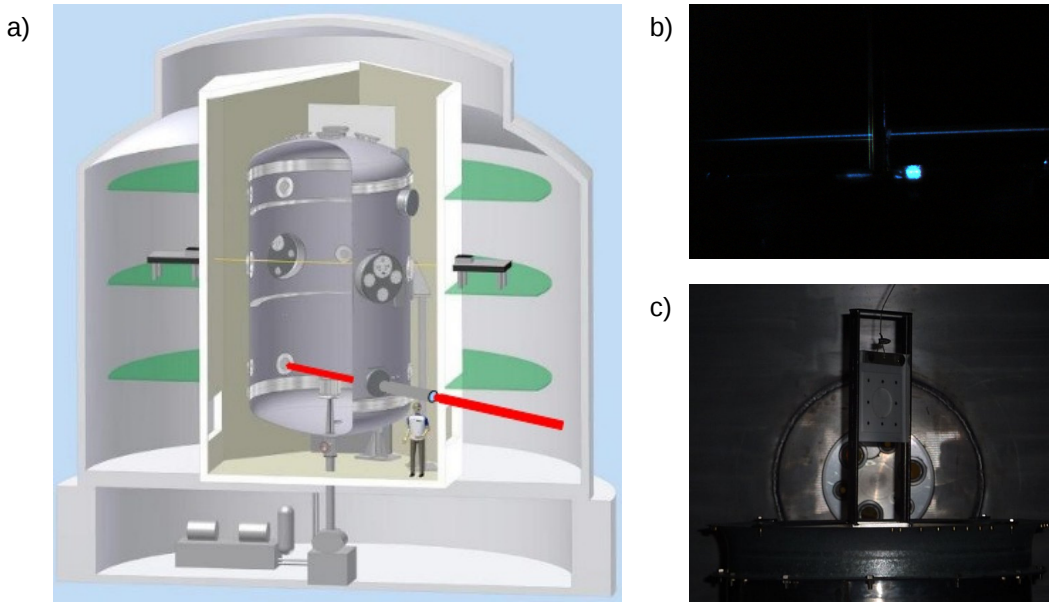

Figure 5.50.: a) sketch of the AIDA chamber in the insulating housing, surrounded by access platforms (green), and enclosed by the hall (image source: IMK-AAF). The Teramobile beam (red line), extension pipe and input window are added; b) the filamenting Teramobile beam close to the radial centre of the AIDA chamber, passing just above the mixing fan (visible at the base of panel c)) and between the rails of the SIMONE alignment target, also visible in panel c) showing the view through the chamber from the perspective of the beam. Note that in c) the output pipe and window are not yet mounted.

atmosphere	temperature (°C)
'synthetic air'	10
'synthetic air + SO_2'	10
'synthetic air + VOC + SO_2'	10
'pure nitrogen'	10
'synthetic air'	-10
'synthetic air + VOC'	-28
'synthetic air'	-48

Table 5.5.: Sequence of atmospheres investigated during the TerAIDA campaign. In experiment sessions involving trace compounds these were typically added in sequence, and one or more experiments were conducted with each cumulative atmospheric composition.

Sec. 4.2.2).

Another goal included in the design of the experiments was to evaluate the influence of turbulent mixing of filament-plasma products with the surrounding air, and their consequent dilution, on the production of particles and droplets. For this reason experiments were planned to be conducted alternatively in stagnant or in strongly turbulent air, mixed by the fan located just below the filamenting beam (see Fig. 5.50).

A total of 43 experiments of both types ('static' and 'dynamic') were conducted during the two scheduled weeks. For most of the experiments the temperature of the chamber was stabilized at 10 °C, and was gradually decreased in steps of 20 K for the last three days of the campaign. Because of the time required for temperature stabilization of the chamber, a temperature change had to be initiated after the last experiment of a day's session. The sequence of atmospheres investigated during the campaign is liste.d in Tab. 5.5

5.4.4. Preliminary results

As the evaluation of the experimental results obtained during the TerAIDA campaign is still in progress, only some preliminary and qualitative results can be formulated here. A detailed analysis will most probably appear in the dissertation of Teramobile team member S. Henin.

Nucleation and condensation of particles and droplets induced by the action of filamenting ultrashort laser pulses could be produced and observed under controlled conditions. Especially the nucleation of fresh particles could be confirmed with great confidence, thanks to the well characterized low background of particles down to 3 nm size.

Also the efficient production of ozone (O_3), NO and NO_2 by filaments, as reported for a smaller scale laoratory experiment in (Petit et al., 2010), was reproduced.

A clear effect of mixing dilution of gaseous products of the filament plasma on the number and size spectrum of produced particles was observed. As most of the aerosol counting instruments of AIDA are installed at a level above the Teramobile beam, quantifying the mixing effect is a bit more

involved.

It could be observed that atmospheric oxygen plays an important role, mainly as the basis for the production of O_3 and NO_x. Experiments in pure nitrogen atmosphere still showed production of new sub-50 nm particles under subsaturated conditions (RH >= 70 %), which could be activated to droplets detected by SIMONE, just above water saturation. No definitive answer can be given yet if part of the particle production observed in oxygen-containing atmosphere can be attributed to multiphotonic Byers Brown-type production and aggregation of charge transfer complexes $H_2O^+ \cdot O_2^-$, or if mainly NO, NO_x, respectively their oxidation product HNO_3, are the only important substances for aerosol nucleation.

A strong impact of the presence of SO_2, VOC, and their combination on particle production could be observed. In the case of α-pinene observations indicated that major part of the particle formation is indirectly triggered by its ozonolysis, which is a well-known process in the formation of secondary organic aerosol, as well as the enhancing effect of strong acids such as H_2SO_4 (Seinfeld and Pandis, 2006). Toluene rather appeared to show a more direct effect of laser irradiation, indicating a different mechanism than mere ozonolysis.

Experiments involving the activation of ice nuclei indicate that laser-produced aerosol is water soluble, which was to be expected owing to its known high content of nitrate ions (see Sec. 5.3).

Intercomparison of laser parameters, trace gas and particle production under various atmospheric conditions may give further hints on the mechanisms underlying laser- or filament-induced nucleation and condensation.

Concluding, the ongoing detailed analysis of the large amount of data collected during the TerAIDA campaign is expected to yield further and more quantitative insight in the phenomenon.

6. Conclusion

In the experimental part of this work femtosecond filament-induced formation of aerosol particles was investigated in different artificially prepared and natural atmospheres, spanning a broad range of temperatures, relative and absolute humidities. Condensing particles were detected by light scattering, either with or without angularly resolved detection, or by in situ sampling detectors.

Additionally, a real-scale atmospheric backscattering LIDAR experiment was designed and performed with the aim of remotely detecting filament-induced atmospheric condensation by means of a time-differential LIDAR scheme. It could be shown that the action of laser filaments can cause a detectable increase of atmospheric backscattering. However, the other important result from this experiment is the persistence of fundamental difficulties arising from the necessarily short time delays between filamenting and probe laser pulses, from turbulence-induced measurement noise, and the evidently required simultaneously clear and humid atmospheric conditions. Although a number of potential sources of error could be ruled out, there is some remaining uncertainty if the remotely detected increase of atmospheric backscattering is exclusively due to the filament-induced condensational growth of new scatterers.

Such uncertainty is eliminated when filament-generated aerosol is sampled in situ and analyzed by sampling particle counters. With regard to gaining an understanding of the nature of filament-induced condensation, a campaign with corresponding instrumentation yielded the most conclusive results. The acquired data provided detailed information on the dependence of particle production on the main parameters temperature, relative humidity and water vapour concentration, all within typical atmospheric parameter ranges, and relative humidity generally below unity. The sheer amount of data which could be acquired during this campaign, as well as the extended detectable particle size range of the sampling instruments make it superior to the data collected using the optical detection methods of the experiments performed in artificial atmospheres.

The ion-chromatographic analysis of in situ sampled filament-produced aerosol particles, performed by the Geneva Teramobile team during the same campaign, as well as experimental data on the production of ozone and NO_x in femtosecond near-infrared laser filaments allowed to narrow the choice from several candidate mechanisms rewieved in the introductory part of this work.

Motivated my these findings a model for the binary condensation of water vapour and gaseous HNO_3 was implemented. Assuming realistic levels of $HNO_3(g)$ concentration the predicted threshold humidities for particle growth, the expected qualitative shape of the resulting size distributions as well as growth velocities produced by the model were found to compare well with experiment.

Also the experimental observations made under the more extreme artificial atmospheric conditions support a chemo-physical pathway to condensation, however less directly and clear than the results

obtained with the sampling particle counters.

Finally, at the state of knowledge gained in this work, the binary homogeneous condensation of water vapour and nitric acid onto nanometric background aerosol particles appears to be the most plausible candidate for the dominating mechanism underlying filament-induced formation of aerosol particles.

Considering the simplicity of the applied model, it is well possible that nitric acid plays its most important role only during a certain phase of particle growth. Other chemical compounds known to be present at high concentrations (for instance, O_3) are ignored in this model, and it may turn out that a better picture can only be gained if they are included together with a more realistic preexisting background aerosol.

The experiments described in this text depend a lot on the mobility of the Teramobile system. In particular the realization of the TerAIDA experiment described last would have been very unlikely without it (the same holds for the chances to operate a terawatt class laser on a ship dock, one or two meters above the surface of a river). The TerAIDA experiment produced some promising results which await completion in an already scheduled follow-up campaign, and which will certainly refine our knowledge about filament-induced atmospheric condensation.

List of publications

P. Rohwetter, J. Yu, G. Méjean, K. Stelmaszczyk, E. Salmon, J. Kasparian, J.-P. Wolf, and L. Wöste, *Remote LIBS with ultra-short pulses: characteristics in picosecond and femtosecond regimes*, J. Anal. Atom. Spectrom., vol. 19, pp. 437-444 (2004)

K. Stelmaszczyk, P. Rohwetter, G. Méjean, J. Yu, E. Salmon, J. Kasparian, R. Ackermann, J.-P. Wolf, L. Wöste, *Long-distance remote laser-induced breakdown spectroscopy using filamentation in air*, Appl. Phys. Lett., vol. 85, 18, pp. 3977-3979 (2004)

P. Rohwetter, K. Stelmaszczyk, L. Wöste, R. Ackermann, G. Méjean, E. Salmon, J. Kasparian, J. Yu and J.-P. Wolf, *Filament-induced remote surface ablation for long range LIBS operation*, Spectrochim. Acta B, vol. 60, pp. 1025-1033 (2005)

R. Ackermann, K. Stelmaszczyk, P. Rohwetter, G. Méjean, E. Salmon, J. Yu, J. Kasparian, G. Méchain, V. Bergmann, S. Schaper, B. Weise, T. Kumm, K. Rethmeier, W. Kalkner, J.-P. Wolf, L. Wöste, *Triggering and guiding of MV discharges by laser-induced filaments under rain conditions*, Appl. Phys. Lett., vol. 85, 23, pp. 5781-5783 (2004)

G. Méchain, G. Méjean, R. Ackermann, P. Rohwetter, Y.-B. André, J. Kasparian, B. Prade, K. Stelmaszczyk, J. Yu, E. Salmon, W. Winn, L.A. (Vern) Schlie, A. Mysyrowicz, R. Sauerbrey, L. Wöste, J.-P. Wolf, *Propagation of fs TW laser filaments in adverse atmospheric conditions*, Appl. Phys. B, vol. 80, 7, pp. 785-789 (2005)

K. Stelmaszczyk, P. Rohwetter, R. Ackermann, G. Méjean, J. Yu, E. Salmon, J. Kasparian, J.-P. Wolf, and L. Wöste, *Non-linear effects accompanying terawatt laser-pulse in air and their applications*, Proc. SPIE, vol. 61580, pp. 61580F1-12 (2006)

G. Méjean, R. Ackermann, J. Kasparian, E. Salmon, J. Yu, J.-P. Wolf, K. Rethmeier, W. Kalkner, P. Rohwetter, K. Stelmaszczyk, L. Wöste, *Improved laser triggering and guiding of megavolt discharges with dual fs-ns pulses*, Appl. Phys. Lett. vol. 88, 2, pp. 1101-1103 (2006)

R. Ackermann, E. Salmon, N. Lascoux, J. Kasparian, P. Rohwetter, K. Stelmaszczyk, S. Li, A. Lindinger, L. Wöste, P. Bejot, L. Bonacina, and J.-P. Wolf, *Optimal Control of Filamentation in Air*, Appl. Phys. Lett. vol. 89, 17, pp. 11171-11173 (2006)

J. Kasparian, R. Ackermann, Y.-B. André, G. Méchain, G. Méjean, B. Prade, P. Rohwetter, E. Salmon, K. Stelmaszczyk, J. Yu, A. Mysyrowicz, R. Sauerbrey, L. Wöste, and J.-P. Wolf,

Electric events synchronized with laser in thunderclouds, Optics Express vol. 16, 8, pp. 5757-5763 (2008)

J. Kasparian, R. Ackermann, Y.-B. André, G. Méchain, G. Méjean, B. Prade, P. Rohwetter, E. Salmon, K. Stelmaszczyk, J. Yu, A. Mysyrowicz, R. Sauerbrey, L. Wöste, and J.-P. Wolf, *Progress towards lightning control using lasers*, J. Eur. Opt. Soc. vol. 3, pp. 08035 1-6 (2008)

P. Rohwetter, M. Queißer, K. Stelmaszczyk, M. Fechner, and L. Wöste, *Laser multiple filamentation control in air using a smooth phase mask*, Phys Rev. A vol. 77, 013812 (2008)

P. Rohwetter, K. Stelmaszczyk, M. Queißer, M. Fechner, and L. Wöste, *Relative merit of $\chi^{(3)}$ and $\chi^{(3)}$ SHG by charged water microdroplets - Implications for LIDAR*, Opt. Comm., vol. 281, 4, pp. 797-802 (2008)

K. Stelmaszczyk, P. Rohwetter, Y. Petit, M. Fechner, J. Kasparian, J.-P. Wolf, and L. Wöste, *White-light symmetrization by the interaction of multifilamenting beams*, Phys. Rev. A vol. 79, pp. 053856 1-5 (2009)

K. Stelmaszczyk, M. Fechner, P. Rohwetter, M. Queißer, A. Czyzewski, T. Stacewicz and L. Wöste, *Towards Supercontinuum Cavity Ring-Down Spectroscopy*, Appl. Phys. B, vol. 94, 3, pp. 369–373 (2009)

K. Stelmaszczyk, P. Rohwetter M. Fechner, M. Queißer, A. Czyzewski, T. Stacewicz and L.Wöste, *Cavity Ring-Down Absorption Spectrography based on filament-generated supercontinuum light*, Optics Express vol. 17, 5, pp. 3673-3678 (2009)

P. Rohwetter, J. Kasparian, K. Stelmaszczyk, Z. Hao, S. Henin, N. Lascoux, W. M. Nakaema, Y. Petit, M. Queißer, R. Salamé, E. Salmon, L. Wöste and J.-P. Wolf, *Laser-induced water condensation in air*, Nature Photonics 4, 451 (2010)

S. Henin, Y. Petit, J. Kasparian, J.-P. Wolf, A. Jochmann, S. D. Kraft, S. Bock, U. Schramm, R. Sauerbrey, W. M. Nakaema, K. Stelmaszczyk, P. Rohwetter, L. Wöste, C.-L. Soulez, S. Mauger, L. Bergé and S. Skupin , *Saturation of the filament density of ultrashort intense laser pulses in air*, Appl. Phys. B, 100 (2010)

Y. Petit, S. Henin, W.M. Nakaema, P. Béjot, A. Jochmann, S.D. Kraft, S. Bock, U. Schramm, K. Stelmaszczyk, P. Rohwetter, J. Kasparian, R. Sauerbrey, L. Wöste, and J.-P. Wolf. *1-J white-light continuum from 100-TW laser pulses.* Physical Review A 83, 013805 (2011)

Y. Petit, S. Henin, J. Kasparian, J.P. Wolf, P. Rohwetter, K. Stelmaszczyk, Z.Q. Hao, W.M. Nakaema, L. Wöste, A. Vogel, T. Pohl, and K. Weber. *Influence of pulse duration, energy, and focusing on laser-assisted water condensation.* Applied Physics Letters 98, 041105 (2011)

Acknowledgements

I want to thank Prof. Dr. Ludger Wöste for supervising this dissertation project. His enthusiasm always was a reward and also a source of motivation, especially during times of difficulties. I would also like to thank Prof. Dr. Jean-Pierre Wolf for inspiring discussions and for valuable feedback. The frequent and often intense conversation with Dr. Jérôme Kasparian was highly appreciated.

I would like to cordially thank Dr. Kamil Stelmaszczyk for his continuous support and encouragement, as a boss and as a friend.

Thanks go to all people with whom I had the honour and pleasure to spend many hours of work in the lab and on the Teramobile. These are Dr. Walter Morinobu Nakaema, Dr. Zuoqiang Hao, Manuel Queißer and Martin Fechner (Berlin), Stefano Henin, and Dr. Yannick Petit (Geneva), Dr. Rami Salamé, Dr. Noelle Lascoux, and Dr. Estelle Salmon (Lyon). Most of the experimental results reported in this work wouldn't have been obtained without everyone's commitment and endurance (and the ability to stand long cold nights of field measurement).

I'd also like to thank Prof. Dr. Konradin Weber, Andreas Vogel and Tobias Pohl of FH Düsseldorf for providing their gas and aerosol sensing equipment and expertise, as well as Dr. Friedhelm Schneider of Grimm Aerosol Technik for additional instruments.

The friendly collaboration with the AIDA team of IMK-AAF of Karlsruhe Institute of Technology lead by Prof. Dr. Thomas Leisner is gratefully acknowledged.

Much would have been more difficult without the support by the administrative and technical staff of the physics department of FU Berlin.

Very special thanks go to current and former members of the Wöste group . It was an experience to be part of this "emergent system", scientifically and personally.

Finally I thank Dr. Bruno E. Schmidt for many insightful discussions.

Besonders dankbar bin ich meiner Lebensgefährtin Stephanie Schwarz und unseren Söhnen Anton und Jakob für die Geduld, die sie für mich aufgebracht haben. Sie haben mich während der ganzen Zeit getragen und sicher manchmal auch ertragen.

A. Appendix

A.1. Model for the binary condensation of H_2O and filament-generated HNO_3

A.1.1. Implementation of extended Köhler theory

For constructing the Köhler curves both equations 5.16 are solved under the constraint of conserved total mass of HNO_3 per unit volume of the system. All gases are assumed ideal, and in the calculation of the remaining gas phase HNO_3 the liquid phase is assumed to occupy a negligible fraction of the total system volume.

As the number concentration C_p of identical droplets per unit volume is fixed, conservation of mass is included by varying the reservoir vapour pressure according to the respective condensed mass:

$$p_{\infty,i}(m_i) = p^0_{\infty,i} - C_\mathrm{p}\frac{R\,T}{M_i}m_i. \tag{A.1}$$

The term $p^0_{\infty,i}$ denotes the initial vapour pressure. In the equilibrium calculations only $p_{\infty,\mathrm{HNO_3}}$ is constrained. For each fixed $m_{\mathrm{H_2O}}$ the HNO_3 atmosphere is equilibrated and once the (unstable) equilibrium point is found, the water equilibrium vapour pressure over the thus determined droplet is calculated from Eq. 5.16. Finally the droplet diameter D_p is determined from the total mass and the composition-dependent density.

The graph in Fig. A.1 shows the Köhler curves obtained for a droplet containing a NH_4NO_3 core in pure moist air (the 'classical' Köhler curve) and in an atmosphere containing a total of 10 ppb of HNO_3(g). This situation is almost the same as that depicted in Fig. 4.7 (cases "No soluble gas" and "10 ppb HNO_3, with depletion"), where the salt core consists of $(HN_4)_2SO_4$. Comparison shows that the numerical code yields results consistent with the analytical expressions from the original theory for dilute solutions. The curves are expected to lie close as both salts dissociate to similar numbers of ions per volume solid ($(HN_4)_2SO_4$: $\sim 2.0\,\mathrm{mol\ m^{-3}}$, HN_4NO_3 : $\sim 2.2\,\mathrm{mol\ m^{-3}}$), and the solutions are dilute.

Slight error due to imperfect interpolation of the finite sampling points is apparent, and could certainly be improved by avoiding the interpolation. The level of accuracy (sub-permille) is however sufficient to expect meaningful results.

A.1.2. Model for the diffusional growth of ternary $H_2O - HNO_3 - NH_4NO_3$ droplets driven by binary condensation of water and $HNO_3(g)$

In the approximation of independent diffusion of both condensing vapour substances equations similar to Eq. 4.19 hold for each component independently, which read, expressed in terms of the respective partial condensed mass m_i:

$$\frac{\mathrm{d}m_i}{\mathrm{d}t} = \frac{2\pi\ D_i\ M_i\ D_\mathrm{p}}{R}\ f(Kn, \alpha_{\mathrm{m},i})\left(\frac{p_{\infty,i}}{T_\infty} - \frac{p_{\mathrm{sat},i}}{T_\mathrm{p}}\ \exp\left\{\frac{4\ \sigma\ v_i}{k_\mathrm{B}\ T_\mathrm{p}\ D_\mathrm{p}}\right\}\right) \tag{A.2}$$

As in Eq. 5.16, the index i enumerates the substances H_2O and HNO_3, and the symbols $p_{\infty,i}(T, m_j)$ and $p_{\mathrm{sat},i}(T, m_j)$ denote the vapour pressure in the reservoir, and its saturation vapour pressure of substance i over the flat mixed liquid phase, respectively. Further, M_i denotes the molar mass, v_i the respective partial molecular volume, and D_i the diffusivity of vapour substance i in air.

The temperature change of the droplet is coupled to the mass change rates by the latent heat released or consumed, and by heat diffusion according to

$$\begin{aligned}\frac{\mathrm{d}T_\mathrm{p}}{\mathrm{d}t} &= \left(c_\mathrm{sol}(m_{\mathrm{H_2O}} + m_{\mathrm{HNO_3}} + m_{\mathrm{NH_4NO_3}})\right)^{-1} \\ &\left(q_{\mathrm{H_2O}}\frac{\mathrm{d}m_{\mathrm{H_2O}}}{\mathrm{d}t} + q_{HNO_3}\frac{\mathrm{d}m_{HNO_3}}{\mathrm{d}t} - 2\pi D_\mathrm{p}\ f(\mathrm{Kn}, \alpha_\mathrm{T})\ k_{air}(T_\mathrm{p} - T_\infty)\right),\end{aligned} \tag{A.3}$$

where c_sol is the specific heat capacity of the liquid phase, q_i are the respective latent heats of evaporation, and k_air is the thermal conductivity of air.

The functions $f(\mathrm{Kn}, \alpha)$ are the Fuchs-Sutugin correction factors necessary to match the continuum

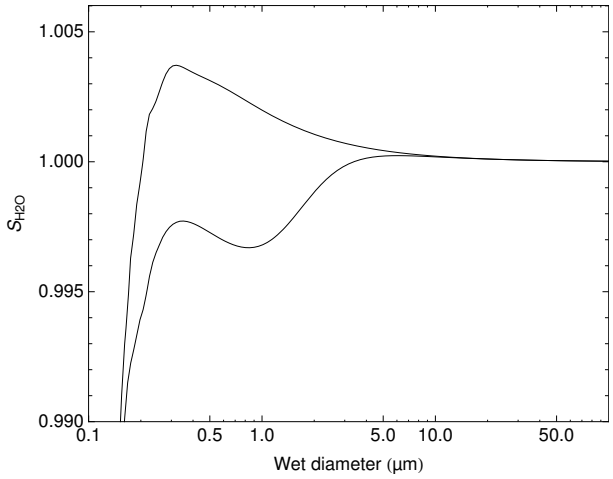

Figure A.1.: Köhler curves for deliquesced ammonium nitrate (NH_4NO_3) particles of dry diameter 50 nm at $T = 293$ K and 101325 Pa. Upper curve: no $HNO_3(g)$ present; lower curve: 10 ppb $HNO_3(g)$ present, assuming conserved total amount of HNO_3 per unit volume. Droplet number concentration $C_\mathrm{p} = 1000\,\mathrm{cm}^{-3}$; to be compared with Fig. 4.7.

description strictly valid only for particles large compared to the gas mean free path with the kinetic regime valid for small particles (see also Sec. 4.1). The correction factors have the form (Seinfeld and Pandis, 2006)

$$f(\mathrm{Kn}, \alpha) = \frac{0.75\,\alpha\,(1 + \mathrm{Kn})}{\mathrm{Kn}^2 + \mathrm{Kn} + 0.283\,\alpha\,\mathrm{Kn} + 0.75\,\alpha}, \tag{A.4}$$

where the Knudsen number $\mathrm{Kn} = 2\lambda_i/D_\mathrm{p}$ compares the free mean path of gas i in air with the characteristic length of the particle. The definition of the gas molecule mean free path used here is

$$\lambda_i = \frac{3D_i}{\bar{c}_\mathrm{i}}$$

with the mean thermal velocity of the vapour molecules $\bar{c}_i$ defined as

$$\bar{c}_i = \left(\frac{8\ k_\mathrm{B}\ T}{\pi\ m_i}\right)^{\frac{1}{2}}.$$

Following the argument of Winkler et al (Winkler et al., 2004) and Laaksonen et al. (Laaksonen et al., 2005) the mass and thermal accomodation coefficients are assumed unity.

Parametrizations for the D_i and k_air are taken from the literature (Durham and Stockburger, 1986; Pruppacher and Klett, 1997; Seinfeld and Pandis, 2006).

A.1.3. Thermodynamic model for the ternary $H_2O - HNO_3 - NH_4NO_3$ solution

The submodel "model II" of the Extended Aerosol Inorganics Model (E-AIM) of Clegg et al. (Clegg and Wexler, 2010; Clegg et al., 1998; Dutcher et al., 2010). was used to calculate the physical properties of the ternary watery solution of HNO_3 and NH_4NO_3. The data obtained from E-AIM are the common basis for both the construction of the Köhler stability curves as well as for the calculations of the growth dynamics. The model was used to sample various quantities for a discrete set of solution compositions and temperatures, which then were interpolated. The interpolations were then used in the actual calculations.

Composition-dependent equilibrium vapour pressures $p_{\mathrm{sat},i}(T, m_j)$ over the flat solution, density $\rho(T, m_j)$ and and surface tension $\sigma(T, m_j)$ of the mixed solution were calculated for a broad range of concentrations of HNO_3(sol) as well as NH_4NO_3(sol). The molar ratio $n_{\mathrm{NH_4NO_3(sol)}}/n_{\mathrm{H_2O(sol)}}$ for which the quantities were calculated spanned the range between 0 and 0.6, in order to also cover highly concentrated deliquesced salt nuclei. The molar ratio $n_{\mathrm{HNO_3(sol)}}/n_{\mathrm{H_2O(sol)}}$ was sampled up to values corresponding to concentrated nitric acid of about 62 wt% to cover mixtures with very low water content as they were suspected to occur for small solution drops under conditions of low relative humidity, and at the same time high HNO_3 vapour pressures. The same calculations were done for a set of temperatures covering the whole range for which measured data exist, that is, from 0 °C up to 36 °C.

To obtain values for intermediate points in 'composition' space the discrete data were interpolated on a two dimensional grid. In a second step interpolation was done also in the temperature coordinate. As an example Fig. A.2 shows $p_{\mathrm{sat,H_2O}}(T, m_j)$ where the composition dependence is expressed in

terms of the water mole fraction in the solution $x_{H_2O} = n_{H_2O}/(n_{H_2O} + n_{H^+} + n_{NH_4^+} + n_{NO_3^-})$ and the mole ratio $n_{NH_4^+}/n_{H_2O}$ as two independent coordinates.

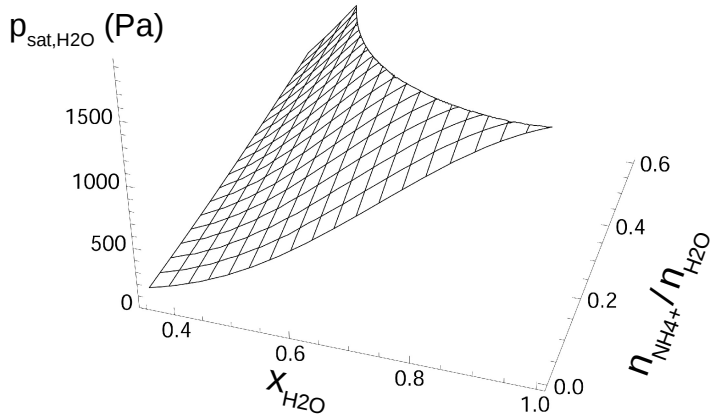

Figure A.2.: Example for interpolated E-AIM model results (see text). The graph shows p_{sat,H_2O} over a ternary $H_2O - HNO_3 - NH_4NO_3$ solution at $T = 290\,K$.

For quantities not directly obtainable from the model output approximate values were derived from it. The partial molecular volumes v_i of water and HNO_3 in the mixed liquid phase were obtained from the density estimation provided by the E-AIM model, according to the relationship

$$v_i = \frac{M_i}{N_A}\frac{\partial V_p}{\partial m_i} = \frac{M_i}{N_A}\frac{\partial}{\partial m_i}\left[(m_{H_2O} + m_{HNO_3} + m_{NH_4NO_3})\ \rho^{-1}\right],$$

where the density ρ depends on the composition of the solution.

The latent heat of evaporation q_i of either substance with respect to the flat mixed solution was obtained from the equilibrium vapour pressures using the integrated version of the Clausius-Clapeyron equation

$$\begin{aligned} \ln\left(\frac{p_{i,1}}{p_{i,2}}\right) &= -\frac{\Delta H_{evap}}{R}\left(\frac{1}{T_1} - \frac{1}{T_2}\right) \\ q_i = \frac{\Delta H_{evap,i}}{M_i} &= -\frac{R}{M_i}\ln\left(\frac{p_{i,1}}{p_{i,2}}\right)\left(\frac{1}{T_1} - \frac{1}{T_2}\right)^{-1}, \end{aligned} \tag{A.5}$$

for each vapour substance where $p_{i,j}$ are the equilibrium vapour pressures of substance i at two close discrete temperatures T_1 and T_2.

As the Kelvin effect distorts the evaporation/condensation equilibrium, it also affects the latent heats of evaporation. In first order approximation the corrected expression for the latent heat of evaporation reads

$$q_i' = q_i - \frac{N_A}{M_i}\frac{4\sigma v_i}{D_p}. \tag{A.6}$$

Like the causing Kelvin effect this correction gains importance with decreasing droplet size. Its

relative impact on the latent heat is however small for droplets in the size range considered here. At $D_p = 10\,\text{nm}$, it has just reached the order of a percent, which is why it is neglected in the present calculations.

Bibliography

Adachi, M., Okuyama, K. and Seinfeld, J.H. *Experimental studies of ion-induced nucleation*. Journal of Aerosol Science (1992); 23:327–337.

Alexander, D.R., Barton, J.P., Schaub, S.A. and Holtmejer, G.M. *Nonlinear interaction of KrF laser radiation with small water droplets*. Applied Optics (1991); 30:1455–1460.

Almaev, R.Kh., Volkovitsky, O.A., Sedunov, Yu.S., Semenov, L.P. and Slesarev, A.G. *Laser beam propagation in a cloud under droplet shattering conditions*. Infrared Physics (1985); 25:475–478.

Andrews, L.C. *Field Guide to Atmospheric Optics*. Bellingham, Washington: SPIE Press (2004).

Astafieva, L.G. and Prishivalko, A.P. *Heating of solid aerosol particles exposed to intense optical radiation*. International Journal of Heat and Mass Transfer (1998); 41:489–499.

Banakh, V.A., Smalikho, I.N. and Werner, C. *Numerical Simulation of the Effect of Refractive Turbulence on Coherent Lidar Return Statistics in the Atmosphere*. Applied Optics (2000); 39:5403–5414.

Barber, P.W. and Hill, S.C. *Light Scattering by Particles: Computational Methods*. World Scientific (1990).

Becker, A., Aközbek, N., Vijayalakshmi, K., Oral, E., Bowden, C.M. and Chin, S.L. *Intensity clamping and re-focusing of intense femtosecond laser pulses in nitrogen molecular gas.* Applied Physics B: Lasers & Optics (2001); 73:287.

Béjot, P., Kasparian, J., Henin, S., Loriot, V., Vieillard, T., Hertz, E., Faucher, O., Lavorel, B. and Wolf, J.-P. *Higher-Order Kerr Terms Allow Ionization-Free Filamentation in Gases*. Physical Review Letters (2010); 104:103903.

Belmonte, A. *Coherent DIAL profiling in turbulent atmosphere*. Optics Express (2004); 12:1249–1257.

Bergé, L., Skupin, S., Lederer, F., Méjean, G., Yu, J., Kasparian, J., Salmon, E., Wolf, J.-P., Rodriguez, M., Wöste, L., Bourayou, R. and Sauerbrey, R. *Multiple Filamentation of Terawatt Laser Pulses in Air*. Physical Review Letters (2004); 92:225002.

Bergé, L., Skupin, S., Nuter, R., Kasparian, J. and Wolf, J.-P. *Ultrashort filaments of light in weakly ionized, optically transparent media*. Reports on Progress in Physics (2007); 70:1633–1713.

Bohren, C.F. and Huffmann, D.R. *Absorption and Scattering of Light by Small Particles*. New York: Wiley (1983).

Born, M. and Wolf, E. *Principles of optics*. Oxford: Pergamon (1993).

Boyd, R.W, Lukishova, S.G. and Chen, Y.R. *Self-focusing: Past and Present*. New York: Springer (2009).

Brabec, T. and Krausz, F. *Nonlinear Optical Pulse Propagation in the Single-Cycle Regime*. Physical Review Letters (1997); 78:3282.

Braun, A., Korn, G., Liu, X., Du, D., Squier, J. and Mourou, G. *Self-channeling of high-peak-power femtosecond laser pulses in air*. Optics Letters (1995); 20:73–75.

Bucholtz, A. *Rayleigh-scattering calculations for the terrestrial atmosphere*. Applied Optics (1995); 34:2765–2773.

Bukatyi, V.I. and Pogodaev, V.A. *Evaporation of a water drop by IR radiation*. Soviet Physics Journal (1970); 13:119–120.

Byers Brown, W. *Photonucleation of water vapour in the presence of oxygen*. Chemical Physics Letters (1995); 235:94–98.

Byers Brown, W., Vincent, M.A., Trollope, K. and Hillier, I.H. *Van der Waals and charge-transfer complexes of molecular oxygen and water*. Chemical Physics Letters (1992); 192:213–216.

Byers Brown, W., Hillier, I.H., Masters, A.J., Palmer, I.J., Santos, D.H.V. Dos, Stein, M. and Vincent, M.A. *Modelling the photonucleation of water vapour by UV in the presence of oxygen and the absence of pollutants*. Faraday Discussions (1995); 100:253–267.

Cacace, F. *Discovery and characterization of atmospherically relevant inorganic species by structurally diagnostic mass spectrometric techniques*. International Journal of Mass Spectrometry (2001); 212:403–411.

– *Erratum to "Discovery and characterization of atmospherically relevant inorganic species by structurally diagnostic mass spectrometric techniques" [Int. J. Mass Spectrom. 212 (2001) 403-411]*. International Journal of Mass Spectrometry (2002); 218:197–198.

Cacace, F., de Petris, G., Pepi, F. and Troiani, A. *Direct Experimental Evidence for the* $H_2O^+O_2^-$ *Charge Transfer Complex: Crucial Support to Atmospheric Photonucleation Theory*. Angewandte Chemie International Edition (2000); 39:367–369.

Campillo, A.J. *Periodic breakup of optical beams due to self-focusing*. Applied Physics Letters (1973); 23:628.

Caramana, E.J., Webster, R.B., Quigley, G.P. and Morse, R.L. *Theoretical and experimental studies of* CO_2 *laser evaporation of clouds*. Journal of Applied Physics (1991); 70:4601–4616.

Carls, J.C. and Brock, J.R. *Explosive vaporization of single droplets by lasers: comparison of models with experiments*. Optics Letters (1988); 13:919–921.

Champeaux, S., Bergé, L., Gordon, D., Ting, A., Peñano, J. and Sprangle, P. *(3+1) -dimensional numerical simulations of femtosecond laser filaments in air: Toward a quantitative agreement with experiments*. Physical Review E (2008); 77:036406.

Chen, P. and Viñals, J. *Pattern Selection in Faraday Waves*. Physical Review Letters (1997); 79:2670.

Chiao, R.Y., Garmire, E. and Townes, C.H. *Self-Trapping of Optical Beams*. Physical Review Letters (1964); 13:479.

– *Self-Trapping of Optical Beams.* Physical Review Letters (1965); 14:1056.

Chin, S.L. *The Physics and the Challenge of the Propagation of Powerful Femtosecond Laser Pulses in Optical Media*. Physics in Canada (2004); 60:273–281.

Chin, S.L., Talebpour, A., Yang, J., Petit, S., Kandidov, V.P., Kosareva, O.G. and Tamarov, M.P. *Filamentation of femtosecond laser pulses in turbulent air*. Applied Physics B: Lasers and Optics (2002); 74:67–76.

Chrzanowski, J., Kirkiewicz, J. and Kravtsov, Yu. A. *Influence of enhanced backscattering phenomenon on laser measurements of dust and aerosols content in a turbulent atmosphere*. Physics Letters A (2002); 300:298–302.

Clark, I.D. and Noxon, J.F. *Particle Formation during Water-Vapor Photolysis*. Science (1971); 174:941–944.

Clegg, S.L. and Wexler, A.S. *Densities and apparent molar volumes of atmospherically important electrolyte solutions. I. The solutes* H_2SO_4, HNO_3, HCl, Na_2SO_4, $NaNO_3$, NaCl, $(NH_4)_2SO_4$, NH_4NO_3, *and* NH_4Cl *from 0 to 50* °C, *including extrapolations to very low temperature and to the pure liquid state, and* $NaHSO_4$, NaOH *and* NH_3 *at* 25 °C. Journal of Physical Chemistry (2010).

Clegg, S.L., Brimblecombe, P. and Wexler, A.S. *Thermodynamic Model of the System* H^+–NH_4^+–SO_4^{2-}–NO_3^-–H_2O *at Tropospheric Temperatures*. The Journal of Physical Chemistry A (1998); 102:2137–2154.

Cohen, R.D. *Shattering of a Liquid Drop due to Impact*. Proceedings of the Royal Society of London. Series A: Mathematical and Physical Sciences (1991); 435:483 –503.

Couairon, A. and Bergé, L. *Modeling the filamentation of ultra-short pulses in ionizing media*. Physics of Plasmas (2000); 7:193.

Couairon, A. and Mysyrowicz, A. *Femtosecond filamentation in transparent media*. Physics Reports (2007); 441:47–189.

Couairon, A., Gaizcaronauskas, E., Faccio, D., Dubietis, A. and Di Trapani, P. *Nonlinear X-wave formation by femtosecond filamentation in Kerr media*. Physical Review E (2006); 73:016608.

Courvoisier, F., Boutou, V., Kasparian, J., Salmon, E., Méjean, G., Yu, J. and Wolf, J.-P. *Ultraintense light filaments transmitted through clouds*. Applied Physics Letters (2003); 83:213.

Cross, M.C. and Hohenberg, P.C. *Pattern formation outside of equilibrium*. Reviews of Modern Physics (1993); 65:851.

DeForest, C.L., Qian, J. and Miller, R.E. *Time-Resolved Studies of the Interactions between Pulsed Lasers and Aerosols*. Applied Optics (2002); 41:5804–5813.

Diels, J.-C., Yeak, J., Mirell, D., Fuentes, R., Rostami, S., Faccio, D. and Di Trapani, P. *Air filaments and vacuum*. Laser Physics (2010); 20:1101–1106.

Dos Santos, D.H.V., Vaughn, S.J., Akhmatskaya, E.V., Vincent, M.A. and Masters, A.J. *Computer simulation of water clusters containing an* $H_2O \cdot O_2$ *charge-transfer complex*. Journal of the Chemical Society, Faraday Transactions (1997); 93:2781–2785.

Durham, J.L. and Stockburger, L. *Nitric acid-air diffusion coefficient: Experimental determination*. Atmospheric Environment (1986); 20:559–563.

Dutcher, C.S., Wexler, A.S. and Clegg, S.L. *Surface Tensions of Inorganic Multicomponent Aqueous Electrolyte Solutions and Melts*. The Journal of Physical Chemistry A (2010); 114:12216–12230.

Eickmans, J.H., Hsieh, W.-F. and Chang, R.K. *Plasma spectroscopy of H, Li, and Na in plumes resulting from laser-induced droplet explosion*. Applied Optics (1987); 26:3721–3725.

Farley, F.J.M. *Clouds Produced in an Expansion Chamber by Ultra-Violet Light*. Proceedings of the Royal Society of London. Series A. Mathematical and Physical Sciences (1951); 207:527–539.

Feit, M.D. and Fleck, J.A. *Effect of refraction on spot-size dependence of laser-induced breakdown*. Applied Physics Letters (1974); 24:169.

Fibich, G. and Ilan, B. *Self-focusing of circularly polarized beams*. Physical Review E (2003); 67:036622.

Fibich, G., Sivan, Y., Ehrlich, Y., Louzon, E., Fraenkel, M., Eisenmann, S., Katzir, Y. and Zigler, A. *Control of the collapse distance in atmospheric propagation*. Optics Express (2006); 14:4946–4957.

Goodman, J.W. *Statistical Optics*. John Wiley & Sons (1985).

Gordon, D.F., Ting, A., Hubbard, R.F., Briscoe, E., Manka, C., Slinker, S.P., Baronavski, A.P., Ladouceur, H.D., Grounds, P.W. and Girardi, P.G. *Streamerless guided electric discharges triggered by femtosecond laser filaments*. Physics of Plasmas (2003); 10:4530.

Gurvich, A.S. and Kashkarov, S.S. *Problem of enhancement of scattering in a turbulent medium*. Radiophysics and Quantum Electronics (1977); 20:547–549.

He, F. and Hopke, Ph. K. SO_2 *Oxidation and* H_2O–H_2SO_4 *Binary Nucleation by Radon Decay*. Aerosol Science and Technology (1995); 23:411–421.

Heidt, L.J. and Ekstrom, L. *Influence of dissolved air on optical density measurements of water solutions*. Journal of the American Chemical Society (1957); 79:1260–1261.

Heidt, L.J. and Johnson, A.M. *Optical Study of the Hydrates of Molecular Oxygen in Water1*. Journal of the American Chemical Society (1957); 79:5587–5593.

Henderson, S.W., Gatt, Ph., Rees, D. and Huffaker, R.M. 'Wind Lidar'. In: *Laser Remote Sensing*. Ed. by T. I. Fujii and T. Fukuchi. Boca Raton, FL: CRC Press (2005).

Henin, S., Petit, Y., Kiselev, D., Kasparian, J. and Wolf, J.-P. *Contribution of water droplets to charge release by laser filaments in air*. Applied Physics Letters (2009); 95:091107.

Henin, S., Petit, Y., Kasparian, J., Wolf, J.-P., Jochmann, A., Kraft, S. D., Bock, S., Schramm, U., Sauerbrey, R., Nakaema, W. M., Stelmaszczyk, K., Rohwetter, P., Wöste, L., Soulez, C.-L., Mauger,

S., Bergé, L. and Skupin, S. *Saturation of the filament density of ultrashort intense laser pulses in air*. Applied Physics B (2010); 100:77–84.

Hill, S.C., Boutou, V., Yu, J., Ramstein, S., Wolf, J.-P., Pan, Y.-l., Holler, S. and Chang, R.K. *Enhanced Backward-Directed Multiphoton-Excited Fluorescence from Dielectric Microcavities*. Physical Review Letters (2000); 85:54.

Hitschfeld, W. and Bordan, J. *Errors inherent in the RADAR measurement of rainfall at attenuating wavelengths*. Journal of Meteorology (1954); 11:58–67.

Hobbs, P. V. 'Aerosol-Cloud Interactions'. In: *Aerosol–Cloud–Climate Interactions*. Ed. by P. V. Hobbs. Burlington, MA: Academic Press (1993), 33–73.

Hoppel, W.A. and Dinger, J.E. *Production of Cloud Nuclei by Ultraviolet Radiation*. Journal of the Atmospheric Sciences (1973); 30:331–334.

Jaenicke, R. 'Tropospheric Aersosols'. In: *Aerosol–Cloud–Climate Interactions*. Ed. by P. V. Hobbs. Burlington, MA: Academic Press (1993), 1–31.

Kafalas, Peter and Herrmann, Jan. *Dynamics and Energetics of the Explosive Vaporization of Fog Droplets by a* 10.6μ*m Laser Pulse*. Applied Optics (1973); 12:772–775.

Kandidov, V.P. and Militsin, V.O. *Intensity of light field and electron concentration in the laser-induced plasma in a droplet of water aerosol exposed to a femtosecond laser pulse. Geometric optics analysis*. Atmospheric and Oceanic Optics (2004); 17:46–53.

Kandidov, V.P., Aközbek, N., Scalora, M., Kosareva, O.G., Nyakk, A.V., Luo, Q., Hosseini, S.A. and Chin, S.L. *A method for spatial regularisation of a bunch of filaments in a femtosecond laser pulse*. Quantum Electronics (2004); 34:879–880.

Kandidov, V.P., Shlenov, S.A. and Kosareva, O.G. *Filamentation of high-power femtosecond laser radiation*. Quantum Electronics (2009); 39:205–228.

Kashchiev, D. *On the relation between nucleation work, nucleus size, and nucleation rate*. The Journal of Chemical Physics (1982); 76:5098.

Kasparian, J. and Wolf, J.-P. *Physics and applications of atmospheric nonlinear optics and filamentation*. Optics Express (2008); 16:466–493.

Keldysh, L.V. *Ionization in the Field of a Strong Electromagnetic Wave*. Soviet Physics JETP (1965); 20:1307–1314.

King, L.V. *On the Complex Anisotropic Molecule in Relation to the Dispersion and Scattering of Light*. Proceedings of the Royal Society of London. Series A, Containing Papers of a Mathematical and Physical Character (1923); 104:333–357.

Klett, J.D. *Stable analytical inversion solution for processing lidar returns*. Applied Optics (1981); 20:211–220.

Köhler, H. *The nucleus in and the growth of hygroscopic droplets*. Transactions of the Faraday Society (1936); 32:1152–1161.

Kokhanovsky, A.A. *Aerosol optics : light absorption and scattering by particles in the atmosphere*. New York: Springer (2008).

Kokkola, H., Romakkaniemi, S. and Laaksonen, A. *Köhler theory for a polydisperse droplet population in the presence of a soluble trace gas, and an application to stratospheric STS droplet growth*. Atmos. Chem. Phys. (2003); 3:2139–2146.

– *On the formation of radiation fogs under heavily polluted conditions*. Atmos. Chem. Phys. (2003); 3:581–589.

Kolesik, M., Wright, E.M. and Moloney, J.V. *Femtosecond filamentation in air and higher-order nonlinearities*. Optics Letters (2010); 35:2550–2552.

Kruer, W.L. *The Physics of Laser Plasma Interactions*. Reading, MA: Addison-Wesley (1988).

Kucsera, T. L. Backtrajectories generated and published by T. L. Kucsera (GEST) at NASA/Goddard, available at `http://croc.gsfc.nasa.gov/aeronet/`.

Kusaka, I., Wang, Z.-G. and Seinfeld, J.H. *Ion-induced nucleation: A density functional approach*. The Journal of Chemical Physics (1995); 102:913.

Kuzikovskii, A.V. and Khmelevtsov, S.S. *Kinetics of evaporation of water aerosol in the field of optic radiation*. Izvestiya Akademii Nauk SSSR, Fizika Atmosfery i Okeana Izvestiya Akademii Nauk SSSR, Fizika Atmosfery i Okeana (1968); 4:363.

Kuzikovskii, A.V., Pogodaev, V.A. and Khmelevtsov, S.S. *Evaporation of a drop of water under influence of a pulse of light*. Inzhenerno-Fizicheskii Zhurnal (1971); 20:21–25.

Laaksonen, A., Korhonen, P., Kulmala, M. and Charlson, R.J. *Modification of the Köhler Equation to Include Soluble Trace Gases and Slightly Soluble Substances*. Journal of the Atmospheric Sciences (1998); 55:853–862.

Laaksonen, A., Vesala, T., Kulmala, M., Winkler, P.M. and Wagner, P.E. *Commentary on cloud modelling and the mass accommodation coefficient of water*. Atmos. Chem. Phys. (2005); 5:461–464.

Langsdorf, A. *A Continuously Sensitive Diffusion Cloud Chamber*. Review of Scientific Instruments (1939); 10:91.

Lenard, Ph. and Wolf, M. *Zerstäuben der Körper durch das ultraviolette Licht*. Annalen der Physik (1889); 273:443–456.

Lindinger, A., Hagen, J., Socaciu, L.D., Bernhardt, T.M., Wöste, L., Duft, D. and Leisner, T. *Time-Resolved Explosion Dynamics of* H_2O *Droplets Induced by Femtosecond Laser Pulses*. Applied Optics (2004); 43:5263–5269.

Liu, J., Duan, Z., Zeng, Z., Xie, X., Deng, Y., Li, R., Xu, Z. and Chin, S.L. *Time-resolved investigation of low-density plasma channels produced by a kilohertz femtosecond laser in air*. Physical Review E (2005); 72:026412.

Liu, W., Hosseini, S.A., Luo, Q., Ferland, B., Chin, S.L., Kosareva, O.G., Panov, N.A. and Kandidov, V.P. *Experimental observation and simulations of the self-action of white light laser pulse propagating in air*. New Journal of Physics (2004); 6:26412.

Liu, W., Théberge, F., Arévalo, E., Gravel, J.-F., Becker, A. and Chin, S.L. *Experiment and simulations on the energy reservoir effect in femtosecond light filaments*. Optics Letters (2005); 30:2602–2604.

Luderer, J.C. 'Untersuchung der Ionisationsspur in einem Weißlichtkanal mit einer Nebelkammer'. Diplom thesis. Freie Universität Berlin.

Lushnikov, A.A. and Negin, A.E. *Aerosols in strong laser beams*. Journal of Aerosol Science (1993); 24:707–735.

Marburger, J.H. *Self-focusing: Theory*. Progress in Quantum Electronics (1975); 4:35–110.

Measures, R.M. *Laser Remote Sensing: Fundamentals and Applications*. New York: Wiley (1984).

Méchain, G., Couairon, A., Franco, M., Prade, B. and Mysyrowicz, A. *Organizing Multiple Femtosecond Filaments in Air*. Physical Review Letters (2004); 93:035003.

Méchain, G., Méjean, G., Ackermann, R., Rohwetter, P., André, Y.-B., Kasparian, J., Prade, B., Stelmaszczyk, K., Yu, J., Salmon, E., Winn, W., Schlie, L. A., Mysyrowicz, A., Sauerbrey, R., Wöste, L. and Wolf, J.-P. *Propagation of fs TW laser filaments in adverse atmospheric conditions*. Applied Physics B (2005); 80:785–789.

Méchain, G., C. D'Amico, André, Y.-B., Tzortzakis, S., Franco, M., Prade, B., Mysyrowicz, A., Couairon, A., Salmon, E. and Sauerbrey, R. *Range of plasma filaments created in air by a multi-terawatt femtosecond laser*. Optics Communications (2005); 247:171–180.

Méjean, G., Kasparian, J., Yu, J., Frey, S., Salmon, E. and Wolf, J.-P. *Remote detection and identification of biological aerosols using a femtosecond terawatt lidar system*. Applied Physics B: Lasers and Optics (2004); 78:535–537.

Méjean, G., Ackermann, R., Kasparian, J., Salmon, E., Yu, J., Wolf, J.-P., Rethmeier, K., Kalkner, W., Rohwetter, P., Stelmaszczyk, K. and Wöste, L. *Improved laser triggering and guiding of meqavolt discharges with dual fs-ns pulses*. Applied Physics Letters (2006); 88:021101.

Metzger, A., Verheggen, B., Dommen, J., Duplissy, J., Prevot, A.S.H., Weingartner, E., Riipinen, I., Kulmala, M., Spracklen, D.V., Carslaw, K.S. and Baltensperger, U. *Evidence for the role of organics in aerosol particle formation under atmospheric conditions*. Proceedings of the National Academy of Sciences (2010); 107:6646–6651.

Middleton, W.E.K. and Spilhaus, A.F. *Meteorological Instruments*. University of Toronto Press (1953).

Mie, G. *Beiträge zur Optik trüber Medien, speziell kolloidaler Metallösungen*. Annalen der Physik (1908); 330:377–445.

Mishchenko, M.I., Travis, L.D. and Lacis, A.A. *Scattering, Absorption, and Emission of Light by Small Particles*. Cambridge: Cambridge University Press (2002).

Morse, P.M. and Feshbach, H. *Methods of theoretical physics*. New York: McGraw-Hill (1953).

Nibbering, E.T.J., Curley, P.F., Grillon, G., Prade, B.S., Franco, M.A., Salin, F. and Mysyrowicz, A. *Conical emission from self-guided femtosecond pulses in air*. Optics Letters (1996); 21:62–65.

Nuter, R., Skupin, S. and Bergé, L. *Chirp-induced dynamics of femtosecond filaments in air*. Optics Letters (2005); 30:917–919.

Orlando, J.J., Tyndall, G.S. and Wallington, T.J. *The Atmospheric Chemistry of Alkoxy Radicals*. Chemical Reviews (2003); 103:4657–4690.

Oxtoby, D.W. and Kashchiev, D. *A general relation between the nucleation work and the size of the nucleus in multicomponent nucleation*. The Journal of Chemical Physics (1994); 100:7665.

Palmer, I.J., Byers Brown, W. and Hillier, I.H. *Simulation of the charge transfer absorption of the* H_2O/O_2 *van der Waals complex using high level ab initio calculations*. The Journal of Chemical Physics (1996); 104:3198.

Park, B.-S. and Armstrong, R.L. *Laser droplet heating: fast and slow heating regimes*. Applied Optics (1989); 28:3671–3680.

Peñano, J. R., Sprangle, P., Hafizi, B., Manheimer, W. and Zigler, A. *Transmission of intense femtosecond laser pulses into dielectrics*. Physical Review E (2005); 72:036412.

Petit, Y., Henin, S., Kasparian, J. and Wolf, J.-P. *Production of ozone and nitrogen oxides by laser filamentation*. Applied Physics Letters (2010); 97:021108–021108–3.

Piironen, P. and Eloranta, E.W. *Demonstration of a high-spectral-resolution lidar based on an iodine absorption filter*. Optics Letters (1994); 19:234–236.

Pinnick, R.G., Hill, S.C., Pan, Y.-L. and Chang, R.K. *Fluorescence spectra of atmospheric aerosol at Adelphi, Maryland, USA: measurement and classification of single particles containing organic carbon*. Atmospheric Environment (2004); 38:1657–1672.

Pruppacher, H.R. and Klett, J.D. *Microphysics of Clouds and Precipitation*. 2nd Ed. Dordrecht: Kluwer (1997).

Pustovalov, V.K. and Khorunzhii, I.A. *Thermal and optical processes in shattering water aerosol droplets by intense optical radiation*. International Journal of Heat and Mass Transfer (1992); 35:583–589.

Quenzel, H., Ruppersberg, G.H. and Schellhase, R. *Calculations about the systematic error of visibility-meters measuring scattered light*. Atmospheric Environment (1975); 9:587–601.

Quickenden, T.I. and Irvin, J.A. *The ultraviolet absorption spectrum of liquid water*. The Journal of Chemical Physics (1980); 72:4416.

Reiss, H. *The Kinetics of Phase Transitions in Binary Systems*. The Journal of Chemical Physics (1950); 18:840.

Reiss, H., Marvin, D.C. and Heist, R.H. *The use of nucleation and growth as a tool in chemical physics*. Journal of Colloid and Interface Science (1977); 58:125–141.

Robinson, .W. and Kjaergaard, H.G. *High level ab initio studies of the low-lying excited states in the* $H_2O \cdot O_2$ *complex*. The Journal of Chemical Physics (2003); 119:3717.

Rodriguez, M. 'Terawatt-Femtosekunden-Laserpulse in der Atmosphäre: Phänomene und Anwendungen'. PhD thesis. Freie Universität Berlin.

Rodriguez, M., Bourayou, R., Méjean, G., Kasparian, J., Yu, J., Salmon, E., Scholz, A., Stecklum, B., Eislöffel, J., Laux, U., Hatzes, A.P., Sauerbrey, R., Wöste, L. and Wolf, J.-P. *Kilometer-range nonlinear propagation of femtosecond laser pulses*. Physical Review E (2004); 69:036607.

Rohwetter, P., Queißer, M., Stelmaszczyk, K., Fechner, M. and Wöste, L. *Laser multiple filamentation control in air using a smooth phase mask*. Physical Review A (2008); 77:013812.

Rohwetter, P., Kasparian, J., Stelmaszczyk, K., Hao, Z.Q., Henin, S., Lascoux, N., Nakaema, W.M., Petit, Y., Queißer, M., Salamé, R., Salmon, E., Wöste, L. and Wolf, J.-P. *Laser-induced water condensation in air*. Nat Photon (2010); 4:451–456.

Roskey, D.E., Kolesik, M., Moloney, J.V. and Wright, E.M. *The role of linear power partitioning in beam filamentation*. Applied Physics B (2006); 86:249–258.

Saavedra, I. *On the theory of the diffusion cloud chamber*. Nuclear Instruments (1958); 3:85–89.

Sabu, A., Kondo, S., Miura, N. and Hashimoto, K. *Potential energy surface and intermolecular vibrations of* H_2O–O_2. Chemical Physics Letters (2004); 391:101–105.

Salamé, R., Lascoux, N., Salmon, E., Ackermann, R., Kasparian, J. and Wolf, J.-P. *Propagation of laser filaments through an extended turbulent region*. Applied Physics Letters (2007); 91:171106.

Schmelzer, J.W. P. *Comments on the Nucleation Theorem*. Journal of Colloid and Interface Science (2001); 242:354–372.

Schmidt, B.E., Unrau, W., Mirabal, A., Li, S., Krenz, M., Wöste, L. and Siebert, T. *Poor man's source for sub* 7 fs*: a simple route to ultrashort laser pulses and their full characterization*. Optics Express (2008); 16:18910–18921.

Seinfeld, J.H. and Pandis, S.N. *Atmospheric Chemistry and Physics*. 2nd edition. Hoboken, NJ: John Wiley & Sons (2006).

Sennikov, P.G., Ignatov, S.K. and Schrems, O. *Complexes and Clusters of Water Relevant to Atmospheric Chemistry:* H_2O *Complexes with Oxidants*. ChemPhysChem (2005); 6:392–412.

Shim, B., Schrauth, S.E., Hensley, C.J., Vuong, L.T., Hui, P., Ishaaya, A.A. and Gaeta, A.L. *Controlled interactions of femtosecond light filaments in air*. Physical Review A (2010); 81:061803.

Skupin, S., Bergé, L., Peschel, U., Lederer, F., Méjean, G., Yu, J., Kasparian, J., Salmon, E., Wolf, J.-P., Rodriguez, M., Wöste, L., Bourayou, R. and Sauerbrey, R. *Filamentation of femtosecond light pulses in the air: Turbulent cells versus long-range clusters*. Physical Review E (2004); 70:046602.

Skupin, S., Bergé, L., Peschel, U. and Lederer, F. *Interaction of Femtosecond Light Filaments with Obscurants in Aerosols*. Physical Review Letters (2004); 93:023901.

Spracklen, D.V., Carslaw, K.S., Kulmala, M., Kerminen, V.-M., Sihto, S.-L., Riipinen, I., Merikanto, J., Mann, G.W., Chipperfield, M.P., Wiedensohler, A., Birmili, W. and Lihavainen, H. *Contribution of particle formation to global cloud condensation nuclei concentrations*. Geophysical Research Letters (2008); 35:L06808.

Sprangle, P., Peñano, J. R. and Hafizi, B. *Propagation of intense short laser pulses in the atmosphere*. Physical Review E (2002); 66:046418.

Stelmaszczyk, K., Dell'Aglio, M., Chudzynski, S., Stacewicz, T. and Wöste, L. *Analytical function for lidar geometrical compression form-factor calculations*. Applied Optics (2005); 44:1323–1331.

Stibenz, G., Zhavoronkov, N. and Steinmeyer, G. *Self-compression of millijoule pulses to* 7.8 fs *duration in a white-light filament*. Optics Letters (2006); 31:274–276.

Strickland, D. and Mourou, G. *Compression of amplified chirped optical pulses*. Optics Communications (1985); 56:219–221.

Talebpour, A., Yang, J. and Chin, S.L. *Semi-empirical model for the rate of tunnel ionization of* N_2 *and* O_2 *molecule in an intense Ti:sapphire laser pulse*. Optics Communications (1999); 163:29–32.

Thomson, J. J. *Conduction of Electricity through Gases*. Cambridge, UK: Cambridge University Press (1906).

Tohmfor, G. and Volmer, M. *Die Keimbildung unter dem Einfluß elektrischer Ladungen*. Annalen der Physik (1938); 425:109–131.

Träger, F., ed. (2007). *Springer Handbook of Lasers and Optics*. New York: Springer (2007).

Tyndall, J. *On the Blue Colour of the Sky, the Polarization of Skylight, and on the Polarization of Light by Cloudy Matter Generally*. Proceedings of the Royal Society of London (1868); 17:223–233.

Tzortzakis, S., Franco, M.A., André, Y.-B., Chiron, A., Lamouroux, B., Prade, B.S. and Mysyrowicz, A. *Formation of a conducting channel in air by self-guided femtosecond laser pulses*. Physical Review E (1999); 60:3505.

Tzortzakis, S., Prade, B., Franco, M. and Mysyrowicz, A. *Time-evolution of the plasma channel at the trail of a self-guided IR femtosecond laser pulse in air*. Optics Communications (2000); 181:123–127.

Tzortzakis, S., Prade, B., Franco, M., Mysyrowicz, A., Hüller, S. and Mora, P. *Femtosecond laser-guided electric discharge in air*. Physical Review E (2001); 64:057401.

Vaida, V. and Headrick, J.E. *Physicochemical Properties of Hydrated Complexes in the Earth's Atmosphere*. The Journal of Physical Chemistry A (2000); 104:5401–5412.

Varma, S., Chen, Y.-H. and Milchberg, H.M. *Trapping and Destruction of Long-Range High-Intensity Optical Filaments by Molecular Quantum Wakes in Air*. Physical Review Letters (2008); 101:205001.

Villermaux, E. *Fragmentation*. Annual Review of Fluid Mechanics (2007); 39:419–446.

Vlasenko, A., Sjogren, S., Weingartner, E., Stemmler, K., Gäggeler, H.W. and Ammann, M. *Effect of humidity on nitric acid uptake to mineral dust aerosol particles*. Atmos. Chem. Phys. (2006); 6:2147–2160.

Wagner, W.G., Haus, H.A. and Marburger, J.H. *Large-Scale Self-Trapping of Optical Beams in the Paraxial Ray Approximation*. Physical Review (1968); 175:256–266, Erratum Phys. Rev. A, 3, 2150 (1971).

Walter, D., Bürsing, H. and Ebert, R. *Emission of spiral patterns from filaments in the infrared*. Optics Express (2010); 18:24258–24263.

Weise, F. and Lindinger, A. *Full parametric pulse shaping in phase, amplitude, and polarization using an effective four-array modulator*. Applied Physics B (2010); 101:79–91.

Weitkamp, C., ed. (2005). *Lidar*. Vol. 102. New York: Springer-Verlag (2005).

Wen, F.C., McLaughlin, T. and Katz, J.L. *Photoinduced Nucleation of Water Vapor*. Science (1978); 200:769–771.

– *Photoinduced nucleation of supersaturated vapors in the presence of carbon disulfide*. Physical Review A (1982); 26:2235.

Wilks, D.S. *Statistical methods in the atmospheric sciences*. 2nd Ed. Burlington, MA: Academic Press (2005).

Wille, H., Luderer, J.C., Krenz, M., Rodriguez, M. and Wöste, L. 'Water droplet formation in a cloud chamber induced by ultra short laser Pulses'. In: *CLEO 2001, Postconference Technical Digest*, 409.

Wilson, C.T.R. *On the Condensation Nuclei Produced in Gases by the Action of Rontgen Rays, Uranium Rays, Ultra-Violet Light, and Other Agents*. Philosophical Transactions of the Royal Society of London. Series A, Containing Papers of a Mathematical or Physical Character (1899); 192:403–453.

– *On a Method of Making Visible the Paths of Ionising Particles through a Gas*. Proceedings of the Royal Society of London. Series A (1911); 85:285 –288.

Winkler, P.M., Vrtala, A., Wagner, P.E., Kulmala, M., Lehtinen, K.E. J. and Vesala, T. *Mass and Thermal Accommodation during Gas-Liquid Condensation of Water*. Physical Review Letters (2004); 93:075701.

Wöste, L., Wedekind, C., Wille, H., Rairoux, P., Stein, B., Nikolov, S., Werner, C., Niedermeier, S, Ronneberger, F., Schillinger, H. and Sauerbrey, R. *Femtosecond atmospheric lamp*. Laser und Optoelektronik (1997); E 2688.

Wu, J., Cai, H., Peng, Y., Tong, Y., Couairon, A. and Zeng, H. *Control of femtosecond filamentation by field-free revivals of molecular alignment*. Laser Physics (2009); 19:1759–1768.

Wyslouzil, B.E., Carleton, K.L., Sonnenfroh, D.M., Rawlins, W.T. and Arnold, S. *Observation of hydration of single, modified carbon aerosols*. Geophys. Res. Lett. (1994); 21:2107–2110.

Yoshihara, K. *Laser-induced Mist and Particle Formation from Ambient Air: A Possible New Cloud Seeding Method*. Chemistry Letters (2005); 34:1370.

Yoshitake, M. *On the Vapor Pressure Gradient in the Layer Near the Cooled Surface of a Dew-Point Hygrometer*. Journal of the Meteorological Society of Japan 11th ser. (1961); 39:97–102.

Young, A.T. *On the Rayleigh-Scattering Optical Depth of the Atmosphere*. Journal of Applied Meteorology (1981); 20:328–330.

– *Rayleigh scattering*. Physics Today (1982); 35:42.

Yu, F. *Modified Kelvin–Thomson equation considering ion-dipole interaction: Comparison with observed ion-clustering enthalpies and entropies*. The Journal of Chemical Physics (2005); 122:084503–8.

– *From molecular clusters to nanoparticles: second-generation ion-mediated nucleation model*. Atmos. Chem. Phys. (2006); 6:5193–5211.

Yu, F. and Turco, R.P. *On the contribution of lightning to ultrafine aerosol formation*. Geophysical Research Letters (2001); 28:155–158.

Yue, S. and Wang, C. *The influence of serial correlation on the Mann-Whitney test for detecting a shift in median*. Advances in Water Resources (2002); 25:325–333.

Zhang, J.-Z., Lam, J.K., Wood, C.F., Chu, B.-T. and Chang, R.K. *Explosive vaporization of a large transparent droplet irradiated by a high intensity laser*. Applied Optics (1987); 26:4731–4737.